2017

Predictive Modeling of Functional Materials for Catalytic and Sensor Applications

Takat Rawal
University of Central Florida

PREDICTIVE MODELING OF FUNCTIONAL MATERIALS FOR CATALYTIC AND SENSOR APPLICATIONS

by

TAKAT BAHADUR RAWAL
B.Sc., Physics, Tribhuvan University, 2001
M.Sc., Physics, Tribhuvan University, 2007
M.S., Physics, University of Central Florida, 2012

A dissertation submitted in partial fulfillment of the requirements
for the degree of Doctor of Philosophy
at the Department of Physics
in the College of Science
in the University of Central Florida
Orlando, Florida

Summer Term
2017

Major Professor: Talat S. Rahman

ABSTRACT

The research conducted in my dissertation focuses on theoretical and computational studies of the electronic and geometrical structures, and the catalytic and optical properties of functional materials in the form of nano-structures, extended surfaces, two-dimensional systems and hybrid structures. The fundamental aspect of my research is to predict nanomaterial properties through *ab-initio* calculations using methods such as quantum mechanical density functional theory (DFT) and kinetic Monte Carlo simulation, which help rationalize experimental observations, and ultimately lead to the rational design of materials for the electronic and energy-related applications.

Focusing on the popular single-layer MoS_2, I first show how its hybrid structure with 29-atom transition metal nanoparticles (M_{29} where M=Cu, Ag, and Au) can lead to composite catalysts suitable for oxidation reactions. Interestingly, the effect is found to be most pronounced for Au_{29} when MoS_2 is defect-laden (S vacancy row). Second, I show that defect-laden MoS_2 can be functionalized either by deposited Au nanoparticles or when supported on Cu(111) to serve as a cost-effective catalyst for methanol synthesis *via* CO hydrogenation reactions. The charge transfer and electronic structural changes in these sub systems lead to the presence of 'frontier' states near the Fermi level, making the systems catalytically active.

Next, in the emerging area of single metal atom catalysis, I provide rationale for the viability of single Pd sites stabilized on ZnO($10\bar{1}0$) as the active sites for methanol partial oxidation, an important reaction for the production of H_2. We trace its excellent activity to the modified electronic structure of the single Pd site as well as neighboring Zn cationic sites. With the DFT-calculated activation energy barriers for a large set of reactions, we perform *ab-initio* kMC simulations to determine the selectivity of the products (CO_2 and H_2). These findings offer

an opportunity for maximizing the efficiency of precious metal atoms, and optimizing their activity and selectivity (for desired products).

In related work on extended surfaces while trying to explain the Scanning Tunneling Microscopy images observed by our experimental collaborators, I discovered a new mechanism involved in the process of Ag vacancy formation on Ag(110), in the presence of O atoms which leads to the reconstruction and eventually oxidation of the Ag surface. In a similar vein, I was able to propose a mechanism for the orange photoluminescence (PL), observed by our experimental collaborators, of a coupled system of benzylpiperazine (BZP) molecule and iodine on a copper surface. Our results show that the adsorbed BZP and iodine play complimentary roles in producing the PL in the visible range. Upon photo-excitation of the BZP-I/CuI(111) system, excited electrons are transferred into the conduction band (CB) of CuI, and holes are trapped by the adatoms. The relaxation of holes into BZP HOMO is facilitated by its realignment. Relaxed holes subsequently recombine with excited electrons in the CB of the CuI film, thus producing a luminescence peak at ~2.1 eV. These results can be useful for forensic applications in detecting illicit substances.

To the memory of my Late Father

Rup Singh Rawal

ACKNOWLEDGMENT

I would like to take an opportunity to express my sincere thanks to those who have helped me to achieve the significant milestone in my educational journey. Without their help, support, and guidance, this dissertation work would not have been ever possible.

First of all, I would like express my sincere gratitude to my advisor Pegasus Professor Talat S. Rahman for the incessant guidance, invaluable advice, support, patience and the encouragement throughout my Ph.D study. She is a great advisor. Her efforts to provide an atmosphere of seeking knowledge oneself freely also helped me to gain unique experience that will guide and myself to conduct the research in the future. Moreover, not only her motivation, enthusiasm, and wide scientific knowledge on the subject matters make easier to tackle the problems during my research, but her critical approaches to the problems also helped me to explore new ideas for the advancement in research. In both personnel and professional windows, I greatly appreciate her for all contributions that helped me to work better during the course of my Ph.D. work.

I thank to my dissertation committee members Professor Zhengu Chang, Professor Michael A. Leuenberger, and Professor Shengli Zou for the evaluation of my work and insightful comments and suggestion.

I would like to thank Professor Mario Rocca (Italy) and his group members, Professor Matti Alatalo (Finland), Professor Peter A. Dowben (USA), Professor Ludwig Bartels (USA), and Professor Donna A. Chen (USA) for offering me the opportunities to involve in the collaborative projects during the course of my dissertation. I am indebted to Professor Mario for his insightful suggestions and encouragement, but also for the comments which incented me to widen my research from various perspectives.

I thank Dr. Volodymyr Turkowski, Dr. Sampyo Hong, Dr. Marisol Alcantra, and Dr. Duy Le for providing much insightful comments and suggestion, and for their support in the collaborative projects I worked on, for having helpful scientific discussions and efforts to make things simple to understand the physics problems. Dr. Duy and Dr. Sampyo taught me many computational techniques, and the necessary tools for doing the theoretical calculations. Working together with them was constructive and directional to the progressive achievement. I also would like to thank Dr. Alfredo Ramiraz (Mexico), and Mr. Aki Pulkinenen (Finland) for fruitful discussions.

Many thanks to all the Ph.D. students of professor Rahman's group: Dr. Syd Islammudin Shah, Dr. Maral Amounpuor, Dr. Neha Shokeen, Dr. Alamgir Kabir, Dr. Ghazal Safai, Shree Ram Acharya, Zahra Hoosmand, Naseem, and Jiang Tao for being so friendly and helpful, and for creating the nice working atmosphere and for the very good scientific discussions. I greatly enjoyed my time as a member of the group. It was a pleasant and inspiring experience.

I sincerely thank Professor Lyman A. Baker for his insightful comments and fruitful discussions during the course of preparing the manuscripts. I learned the efficient way of writing the reports, manuscripts, and the way to think critically for logical writing.

Finally, I would like to thank my parents, elder brothers and the family members for their invaluable support and love. Without their sacrifice of providing me the opportunity for education, it would not have been possible to pursue my advanced degree. My sincere thanks goes to my lovely wife Mrs. Samjhana Tamang for helping and supporting me during my PhD study.

TABLE OF CONTENTS

LIST OF FIGURES

LIST OF TABLES

CHAPTER 1 INTRODUCTION

After the discovery of graphene [1-3], there is a considerable interest in other two-dimensional (2D) materials, e.g. see Refs. [4-6]. One such large family is that of the layered transition metal dichalcogenides (TMDs) with the formula MX_2 ,('M' being a transition metal and 'X' a chalcogen atom), which has attracted a good deal of attention in the scientific community because of unique physical and chemical properties of its constituents, and their wide potential applications in electronics [5,7,8], opto-electronics [9-11], catalysis [12,13], and electro-catalysis [14-17].

New physics and chemistry may emerge upon functionalization of the TMDs and other nano-structured materials because of the entirely different physical and chemical properties of the end products. These functional materials represent a new class of materials for exploring fundamental physics and chemistry at the atomic scale, for which basic research may lead to exciting novel technological applications beyond the reach of traditional materials, thereby enabling advancement in the field of materials for the next-generation energy-related applications.

As a motivation for the work in this thesis, catalysis research is being intensified in all disciplines – physics, chemistry, engineering, and industrial technology. Modern heterogeneous catalysis research is directed to the development of novel catalysts by varying their size, shape, composition, and structure. It invokes variation of the local atomistic environment to produce new functionality. Surface-sensitive experimental techniques have been critical in unveiling the reaction mechanisms. However, experiments alone cannot provide insights into understanding complexities of the reaction mechanisms. Close coupling between theory, modeling, simulation and experiment is required to understand catalytic processes and to predict new catalysts. Thus, it

is critical to have atomistic level understanding of the underlying mechanisms from both physics and chemistry points of view.

Among the materials of interest in this dissertation, MoS_2 exhibits tunable bandgaps that can undergo transition from an indirect band gap in the bulk material to a direct band gap for a single layer. There is thus a widening of the band gap with decreasing atomic layers because of quantum confinement. Single-layer MoS_2 is chemically inert, similar to the graphene which can be made catalytically active by functionalizing with molecules [18]. But the functionalizing of graphene with molecules can result in the loss of its exotic properties. On the other hand, 2D TMDs exhibit versatile chemical properties [19,20] when functionalized, for example with other nanomaterials or by other techniques. For instance, the basal plane of MoS_2 is catalytically inert. One way of making it active is through creating S vacancies. Energetics for the formation of S vacancies on single-layer MoS_2, plotted in Figure 1.2 from our work, indicate that as the S vacancies grow on MoS_2 they prefer to align in a row. As we have shown [13], such a defect-laden single layer MoS_2 is chemically active.

In the work leading to this dissertation, my premise was that the description of the chemical bond between atom/gas molecules adsorbates and the catalyst surface is the fundamental basis for understanding surface chemical reactivity in heterogeneous catalysis. The reactivity of the catalysts can be determined by its electronic structure. For example, the location of the frontier orbital of the catalyst materials, whether it is close to the Fermi level (E_F) or further away (deep) from the E_F, determines whether there is bond formation with adsorbates. For understanding the bond formation and trends in reactivity of transition metals, the *d*-band model [21-23] has also

been proposed, according to which the closer the d-band center to the Fermi level, the higher the anti-bonding states and the stronger the bond.

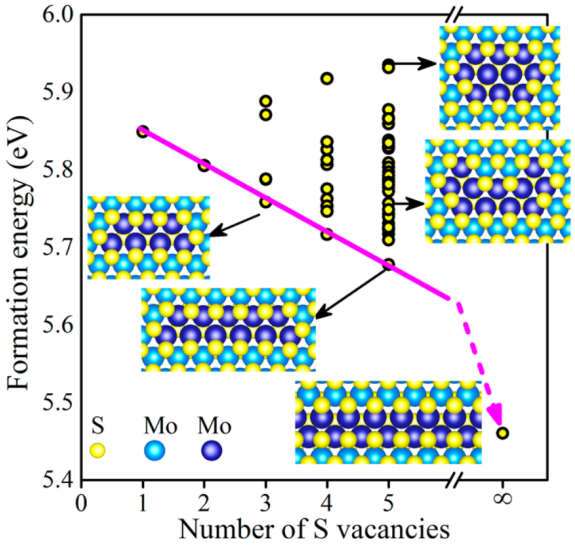

Figure 1.1 Formation energy of S vacancies on MoS_2. Each data point (circle) represents the formation energy of a vacancy structure. The magenta line connects the data of S-vacancy row [Ref. D. Le, T. B. Rawal, and T. S. Rahman, J. Phys. Chem. C, **118**, 5346 (2014)]. (Copyright: American Chemical Society 2014).

As for reactions of interest in this dissertation, a significant one in the catalytic conversion of syngas into alcohol which is of great importance in industrial processes with potential applications in hydrogen storage and conversion of renewable energy. It demands the design of cheap and efficient catalyst materials and a prudent way to achieve this goal is through predictive modeling employing modern quantum mechanical methods and powerful computational techniques. Further improvement of present-day catalysts and the design of novel catalysts require the atomistic level understanding of the processes involved. With the development of modern electronic structure theory and computer science, it is possible to understand the structure and

properties of catalyst material at the atomic scale and elucidate the detailed mechanisms of chemical reactions.

Very relevant to the work presented here are a variety of nanostructured materials of great importance to emerging nanoscience and nanotechnology. These materials possess fascinating size-related electronic (quantum size effect) and catalytic properties and find applications in electronics [24], catalysis [25-27], and bio-medicine [28], thereby fulfilling the promise of the 'bottom-up' approach of nanotechnology. As I will show, these encapsulated metal nanoparticles can greatly optimize the electronic structure of the single-layer MoS_2, and enhance the latter's catalytic activity, as a result of electron transfer from the metal particles to the MoS_2 surface.

Also relevant to this dissertation is heterogeneous catalysis by singly-dispersed precious metal atoms on non-metallic support which greatly maximizes the efficiency of these metal atoms, and allows several ways of designing novel catalysts with high activity and selectivity for the desired products. This single-site catalyst approach addresses the issue that while precious-metal-based catalysts show good catalytic performance for various chemical reactions, their cost hinders effective utilization in large scale industrial applications. By downsizing particles to single metal atom, such catalysts are highly desirable not only to maximize atom efficiency but also to optimize their activity and selectivity [29-31]. Our aim herein is to predict a new catalyst, which can offer high activity and selectivity for conversion of methanol (CH_3OH) to carbon dioxide (CO_2) and hydrogen (H_2).

In predictive modeling of material functionalities, it is critical to understand and predict the properties of materials at the nanoscale for which one needs to perform electronic structure calculation at the quantum mechanics level. In the solid-state community, a most commonly

adopted *ab-initio* approach is density functional theory (DFT) [32], which can serve to validate the conclusions that are drawn from analysis of experimentally measured data. The DFT-based calculation of the properties of a wide range of material systems leads to the establishment of a close coupling between theory and experiment. Most often, DFT-based calculations provide an important information about the geometry, electronic structures, adsorption properties, activation energy barriers, and reaction pathways for reactions on solid surfaces. In this dissertation, I have heavily utilized the *ab-initio* DFT theory to calculate the properties such as geometry, energetics, electronic structures, activation barriers, and the reaction pathways.

Van der Waals interaction is a relatively weak interaction as compared to covalent interactions, however, it plays an important role in condensed-matter physics, surface physics, and nanoscience. It is an ubiquitous quantum mechanical phenomenon originating from the response of electrons in one region of a system (atoms or molecules) to instantaneous charge density fluctuations at other parts of the system. Such interaction comes into play between atoms and molecules or between atoms and molecules on solid (catalyst) surfaces, and therefore can contribute to the binding of the atoms and molecules to the surface. Correspondingly, the adsorption energy and the electronic structures of adsorbed atoms/molecules on solid systems can be affected by van der Waals interaction [33]. In this dissertation, van der Waals interaction are taken into consideration on a regular basis.

An understanding of the kinetics of catalytic reactions (an important property) is a key to the rational design of catalysts. As a first step, useful information about catalysts can be achieved from physical quantities (adsorption energy, reaction energies and activation energy barriers) that can be obtained from DFT. However, catalysts working under realistic conditions of temperature,

and pressure should also meet the requirements of suitable kinetics associated with the specific reaction. For the description of kinetics, one needs to evaluate the reaction rates, turnover frequency and selectivity for the desired products. One of the efficient way to calculate these quantities is by using *ab-initio* Kinetic Monte Carlo (kMC) method [34-36] – so-called the *ab-initio* DFT+kMC, which is the combined form of quantum- and statistical-mechanical approaches. This method has the capability to describe the kinetics of the processes – comprising of simple adsorption and desorption, dissociation, diffusion, and reactions of chemical species – on solid catalyst surface in realistic experimental conditions, as we shall show. For such simulations, we obtain the kinetic parameters from *ab-initio* DFT, and then apply standard kMC algorithm that satisfies the master equation to perform long-time (seconds) simulations.

One of the goals of theoretical surface science is to understand the underlying principles which govern the geometric and electronic structure of surfaces, and processes (e.g. adsorption and reactions) occurring on them. Experimental surface science techniques have thus been crucial in contributing a quantitative description of a wide range of surface phenomena. One of the techniques is scanning tunneling microscope (STM) [37], which can provide high-resolution images of atoms on solid surfaces. This technique has been essential in benchmarking computational surface science and in providing experimental guidance and verification of the concepts developed. As I will show, theoretical modeling in conjunction with STM measurements can provide a fundamental understanding of processes such as adsorption of reactants, diffusion, breaking of some bonds of the reactants, and the creation of new ones to form the product molecules on the solid surface. An understanding of such complexities is critical for designing efficient catalysts.

This dissertation is mainly focused on understanding the geometry and electronic structure of two-dimensional materials, metallic nanostructures, and solid surfaces by means of state-of-art modern quantum-mechanical theory and computational approaches, as a first step toward the predictive modeling of functional materials. The ultimate goal of the projects undertaken in this dissertation is to design a new material for technologically important energy-related and sensor applications. The rest of the dissertation is organized as follows:

Chapter 2 introduces the theoretical methods employed in the present work to calculate the properties of the materials of interest here. The chapter discusses the methods for performing electronic structure calculations based on density functional theory, for calculating the vibrational frequencies, and for determining the kinetics of rare-event of the dynamical systems of interest.

Chapter 3 describes an *ab initio* study of the geometry, electronic structure, and the propensity for adsorption and dissociation of oxygen molecule on a set of metallic nanoparticles, P_{29} (P=Cu, Ag, Au) supported on single-layer MoS_2, both pristine and defect-laden, using density functional theory with the inclusion of van der Waals interactions. Our results point out that the defect-laden MoS_2 has relatively larger effect in enhancing the catalytic properties of the investigated nanoparticles.

Chapter 4 deals with the electronic structure and the reactivity of 13-atom gold nanoparticle on a single-layer MoS_2 with an S vacancy. I show that the electronic interaction as wells as charge transfer between Au_{13} and MoS_2 helps shift frontier orbitals, which are localized on Au atoms away from the interface, closer to the Fermi level. Such modified electronic structure remarkably enhances the chemical activity of the Au-MoS_2 toward methanol synthesis from syngas, i.e,

$CO+2H_2 \rightarrow CH_3OH$ (systematic representation is depicted in Figure 1.2) – a very different activity from that of the Au-TiO_2 nanocatalyst which promotes methanol decomposition.

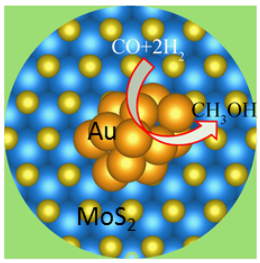

Figure 1.2 Schematic representation of computational-predicted Au-MoS_2 catalyst for methanol synthesis reaction.

Chapter 5 explains the strategy for enhancing the reactivity of MoS_2 by manipulating the electronic structure using Cu(111) as its support. I argue that significant charge transfer from Cu to MoS_2 and strong interaction between them leads to a shift of the Mo unoccupied d states closer to the Fermi level, thereby making defective MoS_2 on Cu(111) more active than when it is unsupported. On the basis of calculated potential energy profile with activation energy barriers for each reactions, I show that the Cu(111) substrate remarkably promotes methanol synthesis from CO hydrogenation on defective MoS_2. On the other hand, I show that water-gas shift reaction is not thermodynamically favorable, but some intermediate species can be formed via the reverse process.

Chapter 6 is dedicated to a detailed study of the atomic and electronic structures, and the energetics for O induced effects on Ag(110), as well as for CO oxidation on the surface. The main idea in this chapter is to enlighten the basic understanding of the physical and catalytic properties of Ag(110) in oxygen environment. This chapter contains three sub-chapters as follows.

Part I contains the DFT-based results for adsorption, dissociation, diffusion and vibration of oxygen on Ag(110). In addition, the results indicate that O_2 dissociation on Ag(110) is coupled with the surface Rayleigh mode (~4meV) and O_2[001] dissociation is more strongly coupled with the substrate motion than $O_2[1\bar{1}0]$, suggesting that the former process can be activated by surface phonon even at low temperature. The results from diffusion barriers calculations reveal that atomic oxygen, produced from O_2 dissociation, can diffuse from short-bridge site to either three-fold or four-fold hollow site owing to the downhill potential along the diffusion path.

Part II mainly discusses the reactivity of disordered Ag(110) for CO oxidation, which is an important reaction for environmental concerns. The results show that the weakly-bound singly dispersed O species at the four-fold hollow of the ordered Ag(110) has more reactive nature than the tightly-bound O species embedded into the O-Ag-O chain of the disordered surface. The former species spontaneously reacts with CO whereas the latter species needs a barrier for the reaction.

Part III deals with investigation of the structural evolution of the O/Ag(110) system by means of DFT and kMC simulations. We propose a new mechanism involved in the process of Ag vacancy formation on Ag(110). The formation of Ag vacancy and O-Ag-O structures act as the building blocks for the added-row reconstruction on Ag(110), thereby explaining experimental observations, which were registered many years ago. Insights into these properties are potentially helpful for comprehending the catalytic behaviour of Ag(110).

Chapter 7 is mainly focused on the exploration of single-metal atom catalyst for specific reaction by means of multi-scale modeling. High activity and cost effectiveness of single-atom catalysts hold practical implication for the desired reaction, for instance, methanol partial oxidation (MPO) with overall reaction: $CH_3OH+½O_2 \rightarrow CO_2+2H_2$, which is an industrially important reaction

for H_2 production. The main goal of this study is thus to design of single-atom catalyst for MPO. Since Pd/ZnO catalysts exhibit excellent thermal stability, and are not pyrophoric, these catalysts can be better choice for methanol-based fuel cell applications. In order to maximize the efficiency of Pd particles, one needs to go to the limit of single Pd atom. By doing so, we can alter the local environment as well as the electronic structure of ZnO surface in the vicinity of single Pd site. In this study, we first examine the geometric and electronic structures of Pd_1/ZnO. Then we look into the adsorption of reactants (CH_3OH, O_2) and products (CO, H_2O, H_2, CO_2) involved in the reaction on Pd_1/ZnO, and the potential energy profile with activation energy barriers for each intermediate reaction. Through our *ab-initio* DFT+kMC Simulation, we show that Pd_1/ZnO has the higher activity and selectivity for formation of H_2 and CO_2 over that of formation of H_2O and CO.

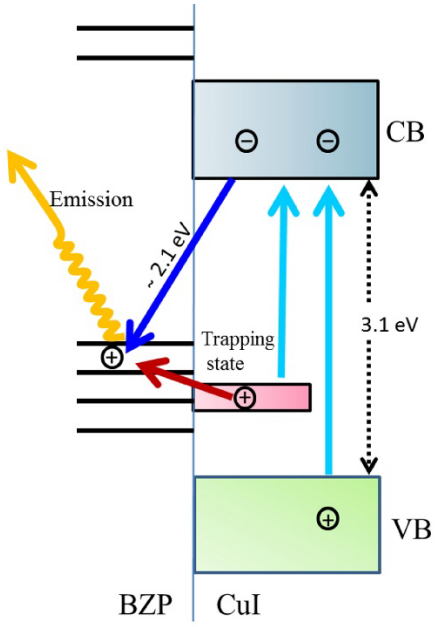

Figure 1.3 The photoluminescence mechanism for the BZP/CuI(111) in the presence of an iodine adatom. [Ref. T. B Rawal, V. Turkowski, T. S Rahman, J. Phys. Condens. Matter **26**, 185005, (2014)] (Copyright IOP Publishing).

Chapter 8 discusses the optical properties of CuI. In this chapter, I describe the mechanism behind the orange photoluminescence (PL) from a system of benzylpiperazine (BZP)/CuI(111) in the presence of an iodine 'vapor' atom. The results show that the adsorbed BZP and the iodine ad-atom play complimentary roles in producing the PL in the visible range. Upon photo-excitation, excited electrons are transferred into the conduction band (CB) of CuI, and holes are trapped by the 'vapor' atoms. These holes then relax into the BZP HOMO state, and finally recombine with excited electrons in the CB of the CuI film (the mechanism is presented in Figure 1.3), thereby producing a luminescence peak at ~2.1 eV.

The conclusions derived from this dissertation work are presented in Chapter 9.

CHAPTER 2 THEORETICAL METHODS

2.1 Many Body Problem

The physical and chemical properties of a quantum mechanical system can be obtained by solving the quantum mechanical wave equation, the so-called the many-particle Schrödinger equation, which governs the dynamics of the system. To solve this equation exactly is practically impossible due to the many-particle effects caused by interaction among many particles. This is referred as the many-body problem. To describe the properties of matter (gas, liquid or condensed phase) at the atomic scale, we can now imagine an ensemble of those interacting particles, i.e. nuclei and electrons, under the influence of an external field. According to Born-Oppenheimer (BO) approximation [38], one can then simplify the many-body problem by decoupling it into nuclear and electronic parts.

2.1.1 Born-Oppenheimer Approximation

The Hamiltonian of a system of N electrons and M ions, assuming the nuclei and electrons to be point masses, can be written as

$$\hat{H} = -\sum_{\alpha=1}^{M} \frac{\hbar^2}{2M'} \nabla_\alpha^{\,2} - \sum_{i=1}^{N} \frac{\hbar^2}{2m} \nabla_i^{\,2} + \frac{e^2}{2} \sum_{\alpha=1}^{M} \sum_{\beta>\alpha}^{M} \frac{Z_\alpha Z_\beta}{\vec{r}_{\alpha\beta}} - e^2 \sum_{\alpha=1}^{M} \sum_{i=1}^{N} \frac{Z_\alpha}{\vec{r}_{i\alpha}} + \frac{e^2}{2} \sum_{j=1}^{N} \sum_{j>i}^{N} \frac{1}{\vec{r}_{ij}} \qquad (2.1)$$

where the first and second terms represent the kinetic energy of the nuclei and electrons, respectively. The third, fourth, and fifth terms represent the nuclei-nuclei repulsion, the electron-nuclei attraction, and the electron-electron repulsion, respectively.

Time-independent Schrödinger equation is given by

$$\hat{H}\left|\Psi(\vec{r},\vec{R})\right\rangle = E\left|\Psi(\vec{r},\vec{R})\right\rangle \tag{2.2}$$

where E are the energy eigenvalues and $\Psi(\vec{r},\vec{R})$ are the corresponding wave functions.

To obtain the many-body wave function of a system it is required to solve the time-independent Schrödinger equation (2.2) in the spatial coordinates of the electrons and the nuclei. Solving this equation exactly is already quite challenging. So, approximation has to be made. Born-Oppenheimer introduced an idea of separating the total wave function into nuclear and electronic parts:

$$\Psi = \Psi_{elec} \times \Psi_{nucl} \tag{2.3}$$

The BO approximation rests on the fact that ions are much heavier than electrons, indicating the ions are nearly fixed with respect to the motion of electrons. Thus, in the many-body Hamiltonian of Eq. (2.1) there is a large asymmetry in the kinetic energy of the electrons as compared to that of the ions due to $M' >> m$. We can therefore solve for the electronic wave function assuming that the nuclei are static.

The Schrödinger equation for electrons is given by

$$\hat{H}_{elec}(\vec{r},\vec{R})\left|\Psi_{elec}(\vec{r},\vec{R})\right\rangle = \varepsilon(\vec{R})\left|\Psi_{elec}(\vec{r},\vec{R})\right\rangle \tag{2.4}$$

where $\vec{r}$ and $\vec{R}$ are the coordinates of the electrons and nuclei, respectively. The electronic eigenvalues (ε) are dependent on the ionic positions $(\vec{R})$. Once the equation for electrons is solved one can then use it to generate the potential for the Schrödinger equation involving only the nuclei. The Schrödinger equation for the nuclei is given by

$$\hat{H}_{nucl}(\vec{r},\vec{R})\left|\Psi_{nucl}(\vec{R})\right\rangle = E\left|\Psi_{nucl}(\vec{R})\right\rangle \tag{2.5}$$

Since the nuclei are far more massive than the electrons, the nuclear positions ($\vec{R}$) are updated in small increments and the electronic wave functions are completely recomputed for each step. This is reminiscent of the adiabatic theorem so the BO approximation is often referred to as the adiabatic approximation.

Although the BO approximation has made the problem simpler by excluding the nuclear degrees of freedom, the remaining many-electron problem is still complicated.

2.1.2 Electronic Problem

In quantum mechanics, the key challenge of the electronic problem is to solve exactly the electronic Schrödinger equation for a system of N interacting electrons in the external field produced by the nuclei. This equation can be given as

$$\hat{H}_{elec}\left|\Psi(\vec{r},\vec{R})\right\rangle = \varepsilon(\vec{R})\left|\Psi(\vec{r},\vec{R})\right\rangle \tag{2.6}$$

where $\Psi(\vec{r},\vec{R})$, $\vec{R}$ and $\varepsilon(\vec{R})$ are the many-electron wave function, the nuclear coordinates, and the eigenvalues of the electrons, respectively.

The electronic Hamiltonian can be written as

$$\hat{H}_{elec} = -\frac{\hbar^2}{2m}\sum_{i=1}^{N}\nabla_i^2 - e^2\sum_{\alpha=1}^{M}\sum_{i=1}^{N}\frac{Z_\alpha}{\vec{r}_{i\alpha}} + \frac{e^2}{2}\sum_{j=1}^{N}\sum_{j>i}^{N}\frac{1}{\vec{r}_{ij}} \tag{2.7}$$

The ground state energy is given by:

$$E = \left\langle\psi\left|\hat{T}\right|\psi\right\rangle + \left\langle\psi\left|\hat{U}_{eN}\right|\psi\right\rangle + \left\langle\psi\left|\hat{U}_{ee}\right|\psi\right\rangle \tag{2.8}$$

where $|\psi\rangle$ is the N-electron ground state wave function, $\hat{\mathbf{T}}$ is the kinetic energy operator, $\hat{U}_{eN}$ is the nuclear-electron interaction, and $\hat{U}_{ee}$ is the electron-electron interaction.

2.2 Density Functional Theory

Density Functional Theory (DFT) is one of the most widely used quantum mechanical tool in the electronic structure calculations of atoms, molecules, solid crystals and surfaces, and of their electronic interactions which determine the structure and properties of the matter from molecules to solids. The main idea of DFT is to solve the many-electron Schrödinger equation by replacing the full wave function with the much simpler electron density as the fundamental variable. The total ground-state energy of the system is then a functional of ground-state electron density, and contains the unknown part of the interaction energy of electrons, the exchange-correlation functional, which has been a subject of many investigations.

2.2.1 Thomas-Fermi Model

One of the earliest approach for solving the many-electron problem was proposed by Thomas and Fermi [39,40]. Thomas and Fermi (TF) suggested that atoms are homogeneous gas of electrons distributed around the nuclei in a six dimensional phase space (momentum and coordinates). This is a nice simplification of the actual many-electron problem. TF proposed an idea of calculating the energy of the electronic system by the use of electron density $n(\vec{r})$, which is the central variable rather than the wave function. One can then derive an approximate expression for the total energy of the homogenous gas of non-interacting electrons, which move in the given external field generated by the nuclei.

For a homogenous electron gas, the relation between the electron density and the Fermi energy (ε_F) can be written as

$$n(\vec{r}) = \frac{1}{3\pi^2}\left(\frac{2m}{\hbar^2}\right)^{3/2} \varepsilon_F^{3/2}, \tag{2.9}$$

Thus, the kinetic energy density at any point is approximated by that of a homogeneous electron gas of non-interacting electrons for a spin unpolarized system:

$$T_{TF}[n(\vec{r})] = a_s \int d^3r\, n^{5/3}(\vec{r}), \quad \text{where } a_s = \frac{3}{10}\left(3\pi^2\right)^{2/3} \tag{2.10}$$

This expression is the well-known TF kinetic energy functional, which is a function of the local density $n(\vec{r})$.

The repulsive electron-electron interaction is approximated by the classical electrostatic Coulomb repulsion between electrons, called the Hartree energy:

$$U_{ee} = \frac{1}{2}\int d^3r \int d^3r' \frac{n(\vec{r})\, n(\vec{r}')}{\left|\vec{r} - \vec{r}'\right|} \tag{2.11}$$

The attractive interaction between electrons and nuclei is

$$U_{eN} = \left\langle \hat{U}_{eN} \right\rangle = \int d^3r\, n(\vec{r})\, \upsilon_{ext}(\vec{r}) \tag{2.12}$$

$$\upsilon_{ext}(\vec{r}) = -\frac{Ze^2}{\vec{r}} \tag{2.13}$$

The TF energy functional then is given by

$$E^{TF} = T_{TF}[n(\vec{r})] + U_{ee}[n(\vec{r})] + U_{eN}[n(\vec{r})] \tag{2.14}$$

Subsequently, one can minimize this total functional under the physical constraint that the correct total number of electrons is given:

$$\int d^3r\, n(\vec{r}) = N \tag{2.15}$$

Using the Lagrange multiplier (μ) for the constraint, one can obtain the stationary condition:

$$\delta\left\{E^{TF}[n(\vec{r})]-\mu\left(\int d^3r\, n(\vec{r})-N\right)\right\}=0 \tag{2.16}$$

which yields the so-called the well-known TF equations:

$$\frac{5}{3}a_s n(\vec{r})^{2/3}+\upsilon_{ext}(\vec{r})+\int d^3r\frac{n(\vec{r})}{|\vec{r}-\vec{r}|}-\mu=0 \tag{2.17}$$

These equations can be solved directly to obtain the ground-state density.

The TF model provides reasonably good prediction for atoms. However, this method is considered rather crude for more complex systems because it does not incorporate the actual orbital structure of electrons. Furthermore, it does not predict bonding between atoms in the solids. The main source of errors arise from the approximation of kinetic energy in a crude way, the over-simplified description of electron-electron interaction, and the exclusion of exchange interaction.

2.2.2 Hohenberg-Kohn Theorems

In 1964, Hohenberg and Kohn (H-K) [41] had shown that it was possible to calculate any ground-state property through the knowledge of only the electron density. In fact, the H-K theorems [41] provide the fundamental mathematical basis for the modern forms of the density functional theory.

Theorem I

For any system of N interacting electrons in an external potential, there is one-to-one correspondence between the external potential and the ground state density. In other words, the external potential is a unique functional of the ground state density.

The first H-K theorem permits the use of electron density $n(\vec{r})$ as the basic variable. Then, the external potential $\upsilon_{ext}(\vec{r})$ is determined by the electron density $n(\vec{r})$. Since $n(\vec{r})$ determines the number of electrons, it also determines the ground state wave function ψ and all other electronic properties of the ground state system.

The total Hamiltonian is

$$\hat{H} = -\frac{\hbar^2}{2m}\sum_{i=1}^{N}\nabla_i^2 + \sum_{i=1}^{N}\upsilon_{ext}(\vec{r}_i) + \upsilon(\vec{r}_1, \vec{r}_2, ...\vec{r}_N) \tag{2.18}$$

They proved that, for the given electron density $n(\vec{r})$ of the ground state for a system, we cannot have two different external potentials, $\upsilon_{ext}^{(1)}(\vec{r})$ and $\upsilon_{ext}^{(2)}(\vec{r})$. For the proof, let us assume that we have two different potentials, which are differed by more than additive constant. Then, we have two different wave function for the ground states,

$$\hat{H}^{(1)}\left|\psi_0\right\rangle = E_0\left|\psi_0\right\rangle \tag{2.19}$$

$$\hat{H}^{(2)}\left|\psi_0\right\rangle = E_0'\left|\psi_0'\right\rangle \tag{2.20}$$

where

$$\hat{H}^{(1)} = -\frac{\hbar^2}{2m}\sum_{i=1}^{N}\nabla_i^2 + \sum_{i=1}^{N}\upsilon_{ext}^{(1)}(\vec{r}_i) + \upsilon(\vec{r}_1, \vec{r}_2, ...\vec{r}_N) \tag{2.21}$$

$$\hat{H}^{(2)} = -\frac{\hbar^2}{2m}\sum_{i=1}^{N}\nabla_i^2 + \sum_{i=1}^{N}\upsilon_{ext}^{(2)}(\vec{r}_i) + \upsilon(\vec{r}_1, \vec{r}_2, ...\vec{r}_N) \tag{2.22}$$

Variational principle tells us that

$$E_0 = \left\langle\psi_0\left|\hat{H}^{(1)}\right|\psi_0\right\rangle < \left\langle\psi_0'\left|\hat{H}^{(1)}\right|\psi_0'\right\rangle \tag{2.23}$$

Then one can obtain

$$E_0 < \left\langle\psi_0'\left|\hat{H}^{(1)}\right|\psi_0'\right\rangle = \left\langle\psi_0'\left|\hat{H}^{(1)} - \hat{H}^{(2)} + \hat{H}^{(2)}\right|\psi_0'\right\rangle$$

$$= \langle \psi_0' | \hat{H}^{(1)} - \hat{H}^{(2)} | \psi_0' \rangle + \langle \psi_0' | \hat{H}^{(2)} | \psi_0' \rangle \tag{2.24}$$

The ground-state energy is

$$E_0 = \int d^3r \left[\upsilon_{ext}^{(1)}(\vec{r}) - \upsilon_{ext}^{(2)}(\vec{r}) \right] n(\vec{r}) + E_0' \tag{2.25}$$

Eq. (2.25) can be written as

$$E_0 - E_0' = \int d^3r \left[\upsilon_{ext}^{(1)}(\vec{r}) - \upsilon_{ext}^{(2)}(\vec{r}) \right] n(\vec{r}) \tag{2.26}$$

Now, interchanging the labels in Eq. (2.23), we can rewrite the expectation value as

$$E_0' = \langle \psi_0' | \hat{H}^{(2)} | \psi_0' \rangle < \langle \psi_0 | \hat{H}^{(2)} | \psi_0 \rangle \tag{2.27}$$

Again, we can write

$$E_0' = \int d^3r \left[\upsilon_{ext}^{(2)}(\vec{r}) - \upsilon_{ext}^{(1)}(\vec{r}) \right] n(\vec{r}) + E_0 \tag{2.28}$$

Eq. (2.28) can be written as

$$E_0' - E_0 = \int d\vec{r} \left[\upsilon_{ext}^{(2)}(\vec{r}) - \upsilon_{ext}^{(1)}(\vec{r}) \right] n(\vec{r}) \tag{2.29}$$

Adding eq. (2.26) and (2.29), we get

$E_0 + E_0' < E_0' + E_0$, which is clear contradiction. Therefore, two ground state wave functions ψ_0 and ψ_0' yield two different ground state densities $n(\vec{r})$ and $n'(\vec{r})$, but not the same density. This means there is a one-to-one correspondence between potentials and ground-state densities.

Theorem II

The ground state energy can be obtained by variation method: the density that minimizes the total energy is the exact ground state density.

For a given external potential $\upsilon_{ext}(\vec{r})$, the ground state energy can be written as a functional of $n(\vec{r})$ by defining an energy functional as,

$$E[n(\vec{r})] = F[n(\vec{r})] + \int d^3r\, \upsilon_{ext}(\vec{r})\, n(\vec{r}) \tag{2.30}$$

where $F[n(\vec{r})]$ is a universal functional which is independent of the external potential $\upsilon_{ext}(\vec{r})$ and is sum of the kinetic energy functional $T[n(\vec{r})]$ and the electron-electron interaction functional $U_{ee}[n(\vec{r})]$, i.e.

$$F[n(\vec{r})] = T[n(\vec{r})] + U_{ee}[n(\vec{r})] \tag{2.31}$$

The second H-K theorem tells that for a trial density the energy functional $E_v[n(\vec{r})]$ assumes its minimum for the correct ground-state electron density $n'(\vec{r})$.

By applying the variational principle, one can obtain a different electron density $n'(\vec{r})$ that will provides the higher energy.

$$E_v[n(\vec{r})] = F[n(\vec{r})] + \int d^3r\, \upsilon_{ext}(\vec{r})\, n(\vec{r}) < F[n(\vec{r})] + \int d^3r\, \upsilon_{ext}(\vec{r}) n'(\vec{r}) = E'_v\left[n'(\vec{r})\right] \tag{2.32}$$

i.e.,

$$E'_v[n'(\vec{r})] \geq E_v[n(\vec{r})] \tag{2.33}$$

The variational principle allows us to write

$$\delta\left\{E_v[n(\vec{r})] - \mu\left(\int d^3r\, n(\vec{r}) - N\right)\right\} = 0 \tag{2.34}$$

which simplifies to

$$\mu = \frac{\delta E_v[n(\vec{r})]}{\delta[n(\vec{r})]} = \upsilon_{ext}(\vec{r}) + \frac{\delta F[n(\vec{r})]}{\delta n(\vec{r})} \tag{2.35}$$

Thus, by minimizing the total energy with respect to the electron density, one can find the total energy of the ground state. The true density that minimizes the energy is the ground state density.

Although the explicit form of the universal functional $F[n(\vec{r})]$ is not known, the coulomb part of the electron-electron interaction can be extracted as,

$$U_{ee}[n(\vec{r})] = J[n(\vec{r})] + E_c[n(\vec{r})] \tag{2.36}$$

where the first term is the classical Coulomb part and the second term is the non-classical contribution to the electron-electron interaction which is the major part of the exchange-correlation energy. The determination of $F[n(\vec{r})]$ is very important in DFT calculations and unfortunately the H-K theorems give no idea of determining these functionals.

2.2.3 Kohn-Sham Formalism

The way of finding good approximations to the energy functional is greatly simplified by Kohn and Sham in 1965 [32]. They put a major step toward a quantitative modeling of the electronic structure problems. The main advantages of the Kohn-Sham formalism is that it allows a simplistic approach of determining the kinetic energy in a simple manner, and that it also provides an exact single-electron picture of interacting electronic systems. The beauty of Kohn-Sham DFT [32] is that it is exact, efficient, and able to solve the Schrödinger equation by replacing the many-electron wave function by the single-electron density as a fundamental variable. However, there are complexities hidden in the exchange-correlation functional. The success or failure of DFT thus depends upon the accurateness of the exchange-correlation functional. Therefore, the determination of exchange-correlation functional has been a subject of many investigations in the solid-state physics community [42-48]. Once a particular exchange-

correlation functional has been chosen, the mathematical problem is completely specified as a set of Kohn-Sham equations, whose solution yields orbitals and energies from which the total electronic energy can be evaluated. The great success of DFT is that simple approximations perform remarkably well for a wide range of problems in physics and chemistry [49,50], particularly for the prediction of the properties of molecules and solids.

Electronic structure calculations based on KS DFT become quite popular in condensed matter physics, material science, and quantum chemistry. It is usually called the first-principle or *ab initio* method, because it allows us to determine many ground-state properties of a condensed matter system by just giving some basic structural information without any adjustable parameter. Let us introduce a non-interacting system of N electrons with the Hamiltonian as

$$\hat{H}_{eff} = \sum_{i=1}^{N} \left\{ -\frac{\hbar^2}{2m} \nabla_i^2 + \upsilon_{eff}(\vec{r}_i) \right\} \tag{2.37}$$

where $\upsilon_{eff}(\vec{r})$ is the effective potential such that the ground-state density of the Hamiltonian $\hat{H}_{eff}$ equals to the electron density. This density is constructed according to

$$n(\vec{r}) = \sum_{i=1}^{N} \left| \phi_i(\vec{r}) \right|^2 \tag{2.38}$$

where $\phi_i(\vec{r})$ are the single-electron orbitals, and are the solutions of the single-electron Schrödinger equation:

$$\hat{H}_{KS} \phi_i(\vec{r}) = \varepsilon_i \phi_i(\vec{r}) , \tag{2.39}$$

where ε_i are the single-particle energies, and $\hat{H}_{KS}$ is the Kohn-Sham Hamiltonian which is given by

$$\hat{H}_{KS} = \left\{ -\frac{\hbar^2}{2m} \nabla^2 + \upsilon_{eff}(\vec{r}) \right\} \tag{2.40}$$

Kohn-Sham expressed the total energy functional in terms of the single-electron orbitals that minimize the kinetic energy of non-interacting electrons under the fixed density constraint.

$$E_{KS}[n(\vec{r})] = -\frac{\hbar^2}{2m}\sum_{i=1}^{N}\left\langle \phi_i(\vec{r})\middle|\nabla^2\middle|\phi_i(\vec{r})\right\rangle + \int d^3r\, n(\vec{r})\, \upsilon_{ext}(\vec{r}) + \frac{1}{2}\int d^3r \int d^3r' \frac{n(\vec{r})\, n'(\vec{r})}{|\vec{r}-\vec{r}'|} + \int \tilde{E}_{XC}[n(\vec{r})] \qquad (2.41)$$

We now define a functional $G[n(\vec{r})]$ with the variational principle as

$$G[n(\vec{r})] = E[n(\vec{r})] - \mu\int d^3r\, n(\vec{r}) \qquad (2.42)$$

where μ is the chemical potential of the interacting system.

Taking the variation of $G[n(\vec{r})]$ with respect to $n(\vec{r})$, and setting $\delta\vec{G}$ to zero for minimum of $G[n(\vec{r})]$, we get

$$\frac{\delta T[n(\vec{r})]}{\delta n(r)} + \left[\upsilon_{ext}(\vec{r}) + \int d^3r \frac{n(\vec{r})\, d\vec{r}'}{|\vec{r}-\vec{r}'|} + \frac{\delta E_{XC}[n(\vec{r})]}{\delta n(\vec{r})}\right] = \mu \qquad (2.43)$$

Since the electrons in the effective potential only interact with the effective potential, the non-interacting Hamiltonian, Eq. (2.40), corresponds to the energy functional:

$$E_{eff}[n(\vec{r})] = T_{eff}[n(\vec{r})] + \int d^3r\, n(\vec{r})\, \upsilon_{eff}(\vec{r}) \qquad (2.44)$$

Applying the variational principle to this energy functional, we get

$$\frac{\delta T[n(\vec{r})]}{\delta n(\vec{r})} + \upsilon_{eff}(\vec{r}) = \mu_{eff} \qquad (2.45)$$

where μ_{eff} is the chemical potential of the non-interacting system, which must coincide with that of the interacting system.

Now, comparing two Eqs. (2.43) and (2.45), we obtain the expression for the effective potential:

$$\upsilon_{eff}(\vec{r}) = \upsilon_{ext}(\vec{r}) + \int d^3r \frac{n(\vec{r})}{|\vec{r}-\vec{r}'|} + \frac{\delta E_{XC}[n(\vec{r})]}{\delta n(\vec{r})} \qquad (2.46)$$

Thus, we see that there are extra terms $\int d^3r \frac{n(\vec{r})}{|\vec{r}-\vec{r}'|}$ and $\frac{\delta E_{XC}[n(\vec{r})]}{\delta n(\vec{r})}$ added with the external potential $\upsilon_{ext}(\vec{r})$ for the real interacting system. For a real interacting system, the external potential can be characterized by the Coulomb attraction between electrons and nuclei.

The third term on the RHS of Eq. (2.46) represents the exchange-correlation potential given as

$$V_{XC}\left[n(\vec{r})\right] = \frac{\delta E_{XC}[n(\vec{r})]}{\delta n(\vec{r})} \tag{2.47}$$

The single-electron Schrödinger equations are

$$\sum_{i=1}^{N}\left[-\frac{\hbar^2}{2m}\nabla_i^2 + \upsilon_{eff}(\vec{r})\right]\phi_i(\vec{r}) = \varepsilon_i\phi_i(\vec{r}) \tag{2.48}$$

The set of equations in Eq. (2.48) are called the Kohn–Sham equations of DFT. These equations are solved self-consistently to obtain the ground-state density $n(\vec{r})$: First, the initial electron density is constructed using the external potential $\upsilon_{ext}(\vec{r})$. Together with any explicit approximation for the exchange-correlation term, the effective potential $\upsilon_{eff}(\vec{r})$ is then calculated. From this calculated effective potential, the new density is obtained. If the density is converged, the self-consistent loop is terminated. If not, again the potential is calculated until the self-consistency is reached. It provides an efficient scheme for calculating the electron density and the ground-state energy for a system of N identical electrons. The flow chart of self-consistent loop is shown in Figure 2.1.

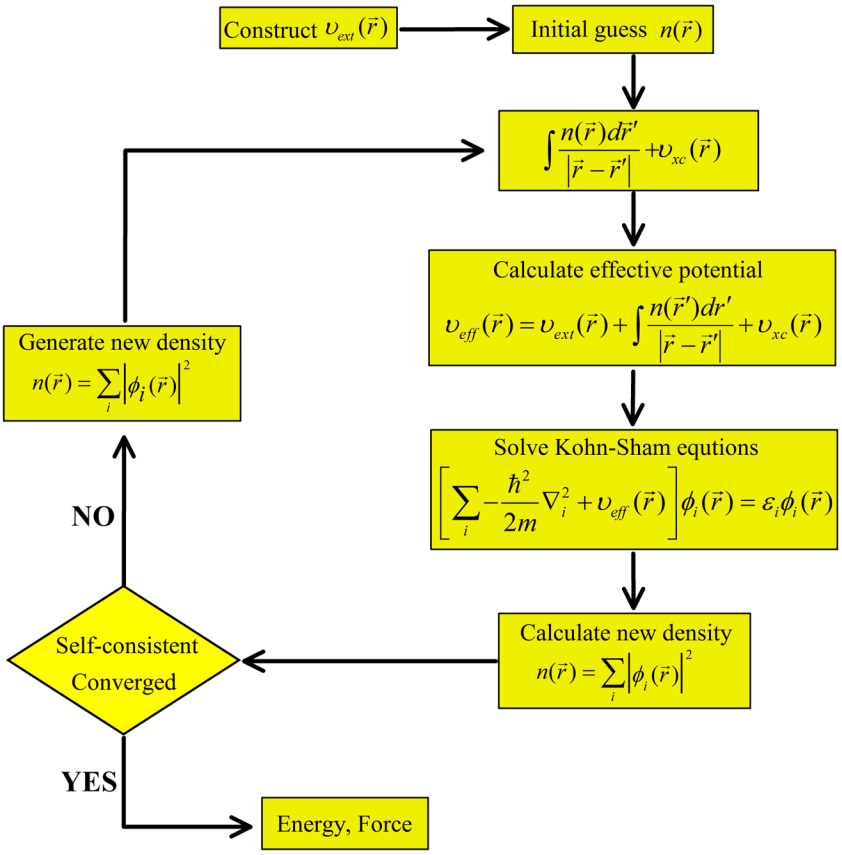

Figure 2.1 Kohn-Sham DFT self-consistent loop.

2.2.4 Spin-Polarized Density Functional Theory

Spin-polarized density functional theory has the capability to solve the ground-state problem related to the systems which have spin-polarization. For a spin-polarized system, the occupancy of electrons in any orbitals is not necessarily to be equal, i.e. $N_{\uparrow} \neq N_{\downarrow}$. These electrons are known as spin-up (↑) and spin-down (↓) electrons, whose corresponding densities satisfy the following self-consistent Kohn-Sham equations:

$$\sum_{i=1}^{N_{(\uparrow,\downarrow)}} \left\{ -\frac{\hbar^2}{2m} \nabla_i^{\,2} + \upsilon_{\mathrm{eff},(\uparrow,\downarrow)}(\vec{r}) \right\} \phi_{i,(\uparrow,\downarrow)}(\vec{r}) = \varepsilon_{i,(\uparrow,\downarrow)} \phi_{i,(\uparrow,\downarrow)}(\vec{r}) \tag{2.49}$$

where $\varepsilon_{i,(\uparrow,\downarrow)}$ are the single-electron Kohn-Sham eigenvalues, and $\upsilon_{\mathrm{eff},(\uparrow,\downarrow)}$ is the effective potential given by

$$\upsilon_{\mathrm{eff},(\uparrow,\downarrow)}(\vec{r}) = \upsilon_{\mathrm{ext}}(\vec{r}) + \int d^3r' \frac{n(\vec{r})}{|\vec{r} - \vec{r}'|} + \frac{\delta \tilde{E}_{XC}[n_\uparrow(\vec{r}), n_\downarrow(\vec{r})]}{\delta n_{(\uparrow,\downarrow)}(\vec{r})} \tag{2.50}$$

The last term of Eq. (2.50) is the exchange-correlation potentials which depend upon the spin densities, – constituting the total electron density $n(\vec{r}) = n_\uparrow(\vec{r}) + n_\downarrow(\vec{r})$, and the spin-polarization (or magnetization) density $\xi(\vec{r}) = \xi_\uparrow(\vec{r}) - \xi_\downarrow(\vec{r})$ – which are constructed using Kohn-Sham spin orbitals as

$$n_{(\uparrow,\downarrow)}(\vec{r}) = \sum_{i=1}^{N_{(\uparrow,\downarrow)}} \left| \phi_{i,(\uparrow,\downarrow)}(\vec{r}) \right|^2 \tag{2.51}$$

In SDFT, one can write the total energy of the spin-polarized system:

$$E_{KS}[n_\uparrow(\vec{r}), n_\downarrow(\vec{r})] = -\frac{\hbar^2}{2m} \sum_{\mathrm{spin}}^{2} \sum_{i=1}^{N_{(\uparrow,\downarrow)}} \left\langle \phi_{i,(\uparrow,\downarrow)}(\vec{r}) \middle| \nabla^2 \middle| \phi_{i,(\uparrow,\downarrow)}(\vec{r}) \right\rangle + \int n(\vec{r}) \upsilon_{\mathrm{ext}}(\vec{r}) d^3r + \frac{1}{2} \int \int \frac{n(\vec{r})\, \upsilon_{\mathrm{ext}}(\vec{r})\, d^3r\, d^3r'}{|\vec{r} - \vec{r}'|} + \tilde{E}_{XC}[n_\uparrow(\vec{r}), n_\downarrow(\vec{r})] \tag{2.52}$$

Subtracting the double counting terms, the total energy of the system can be written as

$$E_{KS}[n_\uparrow(\vec{r}), n_\downarrow(\vec{r})] = -\sum_{\mathrm{spin}}^{2} \sum_{i=1}^{N_{(\uparrow,\downarrow)}} \varepsilon_{i,(\uparrow,\downarrow)} + \int n(\vec{r}) \upsilon_{\mathrm{ext}}(\vec{r}) + \frac{1}{2} \int \int \frac{n(\vec{r}) \upsilon_{\mathrm{ext}}(\vec{r})\, d^3r\, d^3r}{|\vec{r} - \vec{r}'|} + \left\{ \tilde{E}_{XC}[n_\uparrow(\vec{r}), n_\downarrow(\vec{r})] - \int n(\vec{r}) \frac{\delta \tilde{E}_{XC}[n_\uparrow(\vec{r}), n_\downarrow(\vec{r})]}{\delta n_{(\uparrow,\downarrow)}(\vec{r})} d\vec{r} \right\} \tag{2.53}$$

2.3 DFT+U

DFT with common approximations such as LDA or GGA for exchange-correlation of electrons does not properly account the electron-electron interaction for the "strongly correlated" systems that have localized d- or f-electrons, thereby leading to the failure in describing the physics of correlated systems. It is therefore necessary to include the correction using the Hubbard model [51,52] – the so-called the Hubbard correction, "+U". In this model, the Coulomb interaction between localized d or f electrons is treated in a mean-field approximation, whereas the interaction between delocalized s, p electrons is described by LDA or GGA functionals.

In DFT+U formulation [53-55], the total energy functional can be written as:

$$E_{DFT+U}[n(\vec{r})] = E_{DFT}[n(\vec{r})] + E_{Hub}[\{n^{l\sigma}_{mm}\}] = E_{dc}[\{n^{l\sigma}\}] \tag{2.54}$$

where E_{DFT} is the DFT total energy functional, E_{Hub} is the interaction energy for strongly correlated electrons (Hubbard term), and E_{dc} is the correction energy for the double counting.

The equation (2.54) can be written as

$$E_{DFT+U}[n(\vec{r})] = E_{DFT}[n(\vec{r})] + \sum_{l}\left[\frac{1}{2}U^{l}\sum_{m,\sigma^{l}m',\sigma'} n^{l\sigma}_{m} n^{l\sigma'}_{m'} - \frac{1}{2}U^{l}n^{l}(n^{l}-1)\right] \tag{2.55}$$

with $n^{l} = \sum_{m,\sigma} n^{l\sigma}_{m}$

Here, $n^{l\sigma}_{m}$ represent the occupation numbers of strongly localized orbitals with orbital quantum number l, magnetic quantum number m, and the spin quantum number σ, and are calculated from the projection of Kohn-Sham orbitals on the localized atomic states as follows:

$$n^{l\sigma}_{mm'} = \sum_{k,\eta} f^{\sigma}_{k\eta} \left\langle \psi^{\sigma}_{k\eta} \middle| \varphi^{l}_{m'} \right\rangle \left\langle \varphi^{l}_{m} \middle| \psi^{\sigma}_{k\eta} \right\rangle \tag{2.56}$$

where $f_{k\eta}^{\sigma}$ are the occupation of Kohn-Sham states, with the labels for k-point, band and the spin indices.

The orbital energies are obtained by differentiating equation (2.55) with respect to orbital occupation, n^l as follows:

$$\varepsilon_{dc} = \frac{\partial E_{DFT+U}}{\partial n^l} = \varepsilon_{DFT} + U^l\left(\frac{1}{2} - n^l\right) \tag{2.57}$$

Here, the second term is the correction to the atomic orbital energy.

The orbital-dependent potential can be obtained as:

$$V_m^{l\sigma} = \frac{\delta E}{\delta n^l} = V_{DFT} + \sum_{l,m} U^l\left(\frac{1}{2} - n_m^{l\sigma}\right)\left|\varphi_m^l\right\rangle\left\langle\varphi_m^l\right| \tag{2.58}$$

According to Eq. (2.58), the Hubbard potential turns out to be repulsive for less than half-filled orbitals, attractive in all the other cases. In addition, the above potential, Eq. (2.58), gives the upper and lower Hubbard bands with the energy separation between them equal to the Coulomb parameter, U. The difference between the potential acting on occupied and unoccupied states (~ U) associate with some discontinuity in the potential. Such discontinuity is responsible for opening the fundamental gap of the correlated system.

2.4 Exchange-Correlation Functional

In DFT, the biggest challenge is to accurately approximate the exchange-correlation term. Although the exchange term can be treated exactly as a functional of the orbitals (computationally expensive), it however will not help to compensate for any errors generated while approximating

the correlation term. Both terms have to be treated at the similar level of approximation for consistently approximating the exchange-correlation of electrons.

2.4.1 Local Density Approximation (LDA)

In DFT, LDA is the simplest approximation used for constructing exchange-correlation functional. In this approximation, the exchange-correlation energy per electron at a point in space, where the electron density is slowly varying, is assumed to be same as that for a locally homogeneous electron gas of the same electron density. This concept was initially propounded by Kohn and Sham [32] in 1965.

Within this approximation, one can write the exchange-correlation energy as

$$E_{xc}^{LDA}[n(\vec{r})] = \int d^3r\, n(\vec{r})\, \varepsilon_{xc}^{LDA}[n(\vec{r})] \tag{2.59}$$

where ε_{xc}^{LDA} is the exchange-correlation energy density of a homogeneous gas of electrons. Since ε_{xc}^{LDA} is considered to be a functional of the local electron density, one can write

$$\varepsilon_{xc}^{LDA}[n(\vec{r})] = \varepsilon_{xc}^{hom}[n(\vec{r})] \tag{2.60}$$

Now, the expression for the exchange-correlation energy density is

$$\varepsilon_{xc}^{LDA}[n(\vec{r})] = \frac{1}{2}\int d^3r \frac{n_{xc}^{LDA}(\vec{r}, \vec{r}')}{|\vec{r} - \vec{r}'|} \tag{2.61}$$

where exchange-correlation energy density is calculated as the linear sum of exchange energy and correlation energy densities:

$$\varepsilon_{xc}^{LDA}[n(\vec{r})] = \varepsilon_{x}^{LDA}[n(\vec{r})] + \varepsilon_{c}^{LDA}[n(\vec{r})] \tag{2.62}$$

For the exchange energy density ε_x^{LDA} of a homogenous electron gas, the analytical expression is given by Dirac:

$$\varepsilon_x^{LDA}\left[n(\vec{r})\right] = -\frac{3}{4}\left(\frac{3}{\pi}\right)^{1/3} n^{1/3}(\vec{r}) = -\frac{0.458}{r_s} \text{ a.u. } \left(\text{where 1 a.u. = 0.529 angstrom}\right) \quad (2.63)$$

where r_s is the effective radius of a single-electron sphere, and is defined by

$$r_s = \left(\frac{3}{4\pi n(\vec{r})}\right)^{1/3} \quad (2.64)$$

Since calculation of the correlation energy density ε_c^{LDA} is not simple, various approximations, for example, Vosko-Wilk-Nusiar (VWN) [56], Perdew-Zunger (PZ81) [48], Perdew-Wang (PW92) [57] have been made.

Although LDA has certain limitations of accurately predicting a number of important features such as bond dissociation energies, binding energies of atoms and molecules on solid surfaces, bond-lengths of van der Waals systems, but in some cases it performs very well. It is also important in the construction of more sophisticated approximations – generalized gradient approximations or hybrid functional – to the exchange-correlation energy.

2.4.2 Generalized-Gradient Approximation (GGA)

The failure of LDA in describing the effects of inhomogeneous electron gas on the real systems is overcome by an alternative approach. The approach was first proposed by Hohenberg and Kohn [41], who made the extension of LDA functional. This is known as gradient-expansion approximation (GEA). The idea behind this approximation is to use the first or higher order of derivatives of electron density with respect to the spatial coordinates so that one can capture the

inhomogeneity effects. The first order density gradient subsequently implemented and tested for atoms and molecules; however testing was a complete failure.

Subsequently, several modified version of approximations [58-61] were proposed to address the issue of inhomogeneities in the electron density. These all modified gradient expansions collectively known as generalized-gradient approximation (GGA). GGA can be conveniently written in terms of an analytic function known as the enhancement factor, $F_{xc}\left[n(\vec{r}), \nabla n(\vec{r}), \nabla^2 n(\vec{r}) \ldots\ldots\ldots\ldots \right]$, that directly modifies the LDA expression according to the variation of density in the vicinity of the considered point. So, GGA is a semi-local approach that retains the correct features of the LDA (LSDA), and combines them with the inhomogeneity features that are assumed to be energetically the most important ones. In this approach, the exchange-correlation energy is written in the following form:

$$E_{xc}\left[n(\vec{r}) \right] = \int d^3r\, n(\vec{r}) \varepsilon_{xc}\left[n(\vec{r}) \right] F_{xc}\left[n(\vec{r}), \nabla n(\vec{r}), \nabla^2 n(\vec{r}) \ldots\ldots\ldots\ldots \right] \qquad (2.65)$$

In general, GGA functionals are obtained from two different strategies: *Ab-initio* and empirical approaches. An *ab initio* approach involves the theoretical expression of $F_{xc}[n(\vec{r})]$ that requires the functional to satisfy some or all known properties of the exchange-correlation energy. An empirical approach is to fit all parameters of $F_{xc}[n(\vec{r})]$ in such a way that the GGA functional can reproduce a number of experimental results. Though this approach works very well when applied to molecules, the transferability to solid systems is not guaranteed.

The vital steps that led to the GGA were principally made by Perdew and co-workers [57-59] who devised a cutoff procedure that sharply terminates the GEA exchange-correlation hole in

real-space using delta functions, in order to restore the sum rule and non-positivity hole conditions. Considering the gradient of density, the exchange-correlation energy takes the following form:

$$E_{xc}^{PBE}\left[n(\vec{r})\right] = \int d^3r\, n(\vec{r})\, \varepsilon_{xc}^{hom}\left[n(\vec{r})\right] F_{xc}^{PBE}\left[n(\vec{r}), \nabla n(\vec{r})\right] \tag{2.66}$$

The enhancement factor is often written in terms of Wigner-Seitz radius (r_s), and dimensionless reduced density gradient, $s(\vec{r}) = \dfrac{\left|\nabla n(\vec{r})\right|}{\left(2k_F(\vec{r})\, n(\vec{r})\right)}$, and the Fermi-wave vector, $k_F(\vec{r}) = \left(3\pi^2 n(\vec{r})\right)^{1/3}$.

The Perdew, Burke and Ernzerhof (PBE) functional [43] does not contain any free parameters that are fitted to experimental data, but it is determined from the exact quantum-mechanical relations. The PBE functional uses a simplified form of exchange enhancement factor:

$$F_x^{PBE}(s) = 1 + \kappa - \frac{\kappa}{1 + \mu s^2/\kappa} \tag{2.67}$$

$\mu = \beta\left(\pi^2/3\right) = 0.21951$ and $\beta = 0.066725$, and $\kappa = 0.804$

In PBE approximation, correlation energy is defined as

$$E_c^{PBE}\left[n(\vec{r})\right] = \int d^3r\, n(\vec{r})\left[\varepsilon_c^{LDA}[n(\vec{r}), \xi(\vec{r})] + H[n(\vec{r}), \xi(\vec{r}), t]\right] \tag{2.68}$$

where $H[n(\vec{r}), \xi(\vec{r}), t]$ is the correlation correction term and is defined by

$$H\left[n(\vec{r}), \xi(\vec{r}), t\right] = \left(e^2/a_0\right)\gamma\theta^3 \ln\left\{1 + \frac{\beta}{\gamma}t^2\left[\frac{1 + At^2}{1 + At^2 + A^2t^4}\right]\right\} \tag{2.69}$$

with $\beta = 0.066725$, and $\gamma = (1 - \ln 2)/\pi^2 = 0.031091$

Here, t is a dimensionless density gradient:

$$t(\vec{r}) = \frac{\left|\nabla n(\vec{r})\right|}{\left(2\theta k_s(\vec{r}) n(\vec{r})\right)} \tag{2.70}$$

where k_s is the Thomas-Fermi Screening wave number, and $\theta[\xi(\vec{r})]$ is the spin-scaling factor which is given by

$$\theta\left[\xi(\vec{r})\right] = \left((1+\xi(\vec{r}))^{2/3} + (1-\xi(\vec{r}))^{2/3}\right) \tag{2.71}$$

where $$A = \frac{\beta}{\gamma}\left[\exp\left\{\frac{\varepsilon_c^{LDA}[n(\vec{r})]}{\gamma e^2\theta^3/a_0}\right\} - 1\right]^{-1} \tag{2.72}$$

Although GGA functionals are not suitable for strongly correlated systems and for capturing accurately the long-range interactions, these functionals, in comparison to LDA, improve the binding energies, bond lengths, and bond angles of the real solid systems. GGA functionals also predict better gap energies of semiconductors and insulators.

2.5 Van der Waals Interaction

The accurate description of the van der Waals (vdW) interactions is a difficult benchmark problem in many-body theory that should include the vdW interaction in the correlation functional. The vdW interaction is a true quantum phenomenon. The origin of the vdW interaction between two non-covalent bonded ions or solid materials or molecules is the coupling of the electro-static field generated by fluctuations in the correlated electronic density of one fragment with the density of the other fragment, so the interaction exists in all materials. The fluctuation in electron density is a dynamical correlation effect that the LDA or GGA cannot capture. Owing to the correlation effect, vdW interactions must be included in $E_{ex}[n(\vec{r})]$. An accurate way of including vdW interactions (or dispersions) in DFT requires that the total energy functional must include both the long-ranged and medium-ranged nature of vdW interactions.

A very simple and crude approximation is the pair interaction between two ions. In this approximation, the total energy is written as

$$E[n(\vec{r})] = E_{DFT}[n(\vec{r})] + E_{disp} \tag{2.73}$$

where E_{disp} is the dispersion interaction, and is defined as

$$E_{dis} = -\sum_{i,j} \frac{C_6^{ij}}{R_{ij}^6} \tag{2.74}$$

where the dispersion coefficient C_6^{ij} depend on the ion pairs *i* and *j*. Within this approach dispersion is assumed to be pairwise additive and can therefore be calculated as a sum over all pairs of atoms i and j. With the simple $\frac{C^6}{r^6}$ correction schemes the dispersion correction diverges at short inter-atomic separation.

2.5.1 DFT-D

Another empirical approach known as DFT-D [62] is introduced in order to overcome the issue of divergence problem in the dispersion correction term by including the 'damping' function. This method is tested for a wide variety of molecular complexes [62]. The idea is that strong covalent bonds are well described by standard approximation, GGA [43] and a pairwise atomistic correction can be used to account for the vdW forces.

In DFT-D method, the empirical dispersion correction is given as

$$E_{dis} = -s_6 \sum_{i=1}^{N-1} \sum_{j=i+1}^{N} \frac{C_6^{ij}}{R_{ij}^6} f_{dmp}(R_{ij}) \tag{2.75}$$

where N is the number of atoms in the system, C_6^{ij} is the dispersion coefficient for a pair of atoms i and j, s_6 is the global scaling factor, and R_{ij} is the interatomic distance. In this approach, C_6^{ij} coefficients are simply given by the average:

$$C_6^{ij}(R_{ij}) = 2\frac{C_6^i C_6^j}{C_6^i + C_6^j} \tag{2.76}$$

In DFT-D method, a damping function is used to avoid the near-singularities. This function is defined as

$$f_{damp}(R) = \frac{1}{\left(1+e^{-\alpha(R/R_0 - 1)}\right)} \tag{2.77}$$

where R_0 is the sum of atomic van der Waals radii.

2.5.2 DFT-D2

The original DFT-D method has certain limitations: C6 coefficients are only available for elements H, C–Ne. For large molecular systems, many electron correlations exist at intermediate inter-electronic distances that are 'doubly counted' when a $C_6^{ij}.R_{ij}^{-6}$ correction is used together with a standard density functional. This problem can be overcome when a semi-empirical GGA with appropriate options for adjustments is parameterized explicitly together with the vdW correction [63]. This new approach of parametrization is known as DFT-D2 [63], which is less empirical than the original DFT-D. This method is based on Becke's power-series ansatz from 1997 [64], and is explicitly parameterized by including damped atom-pairwise dispersion corrections of the form $C_6^{ij}.R_{ij}^{-6}$.

In DFT-D2 method [63], the empirical D2-dispersion correction is given as

$$E_{dis} = -s_6 \sum_{i=1}^{N-1} \sum_{j=i+1}^{N} \frac{C_6^{ij}}{R_{ij}^6} f_{d,6}(R_{ij}) \tag{2.78}$$

where N is number of atoms in the system, C_6^{ij} is the dispersion coefficient for a pair of atoms i and j, and R_{ij} is the distance between atom *i* located in the reference unit cell L=0 and atom *j* in the unit cell L. s_6 is the global scaling parameter, and it is optimized for different DFT functionals like PBE (s_6 =0.75), BLYP (s_6 =1.2), and B3LYP (s_6 =1.05).

The Fermi-type damping function $f_{d,6}(\vec{R}_{ij})$ is defined as

$$f_{d,6}(R_{ij}) = \frac{1}{\left(1+e^{-d\left(R_{ij}/R_{0ij}-1\right)}\right)} \tag{2.79}$$

where R_{0ij} is the sum of atomic vdW radii.

For heavier atoms, the original DFT-D approach do not provide $C_6^{ij}(R_{ij})$ coefficients. This problem is solved by DFT-D2 method by considering the combination rules according to which $C_6^{ij}(R_{ij})$ coefficients and R_{0ij} vdW radii are computed as

$$C_6^{ij}(R_{ij}) = \sqrt{C_6^i C_6^j} \quad \text{with} \quad R_{0ij} = R_{0i} + R_{0j} \tag{2.80}$$

2.5.3 DFT-D3

In DFT-D3 method [65], atom pair-specific dispersion coefficients and cutoff radii are computed explicitly from *ab-initio* methods. As compared to the original DFT-D versions, it has following advantages: i) It is simple, asymptotically exact for a gas of weakly interacting neutral

atoms, and atomic forces are easy to calculate; ii) It provides a consistent description of all chemically relevant elements of the periodic system nuclear charge Z=1–94; and iii) It provides similar or better accuracy for "light" molecules and a strongly improved description of metallic and "heavier" systems.

In DFT-D3 method [65], the total energy is written as

$$E_{DFT-D3} = E_{KS-DFT} + E_{disp} \tag{2.81}$$

where E_{disp} is the dispersion correction.

The two-body dispersion correction is defined as

$$E_{disp} = -\sum_{i=1}^{N}\sum_{j=1}^{N}\sum_{n=6,8,10,....} s_n \frac{C_n^{ij}}{R_{ij}^6} f_{d,n}(R_{ij}) \tag{2.82}$$

Here, the first sum is over all atom pairs in the system, C_n^{ij} denotes the averaged isotropic nth-order dispersion coefficient orders n=6, 8, 10, ... for a pair of atom i and j, and R_{ij} is their inter-nuclear distance.

The expansion for C_n^{ij} is truncated for n=8, since n>8 do not improve the results considerably for "normal" molecules. In order to avoid near singularities for small R_{ij} and mid-range double-counting effects of correlation at intermediate distances, damping functions $f_{d,n}(R_{ij})$ are used which determine the range of the dispersion correction.

$$f_{d,n}(R_{ij}) = \frac{1}{1 + 6\left\{R_{ij}/\left(R_{0ij}s_{r,n}\right)\right\}^{-\alpha_n}} \tag{2.83}$$

where $s_{r,n}$ is the order-dependent scaling factor of the cutoff radii R_{0ij} to adapt the correction at small and medium range distances, and α_n are the "steepness" parameters that adjusted manually such that the dispersion correction is less than 1% of E_{disp}^{max} for typical covalent bonds.

2.5.4 vdW-DF Functional

The vdW-DF method [47,66-68] does not rely on the external parameters, but rather calculate the dispersion interaction directly from the electron density $n(\vec{r})$. This method adds a description of vdW interaction (or say long-range correlations) directly within a DFT (LDA or GGA) functional and combines correlations of all ranges in a single mathematical formulation. The beauty of vdW-DF method is to include the long-range part of the correlation energy, as a nonlocal functional of the electron density $n(\vec{r})$, as the following fashion:

$$E_{xc}(\vec{r}) = E_x^{GGA}[n(\vec{r})] + E_x^{LDA}[n(\vec{r})] + E_c^{nl}[n(\vec{r})] \tag{2.84}$$

where $E_c^{nl}[(n(\vec{r})]$, a fully non-local correlation energy which can be written as

$$E_c^{nl}[(n(\vec{r})] = \frac{1}{2}\int d^3r_1 d^3r_2 n(\vec{r}_1)\phi(q_1, q_2, \vec{r}_{12})n(\vec{r}_2) \tag{2.85}$$

where $\vec{r}_{12} = \left|\vec{r}_1 - \vec{r}_2\right|$ is a scaling factor, q_1 and q_2 are the values of a universal function $q_0\left[n(\vec{r}), \left|\nabla n(\vec{r})\right|\right]$, and $\phi(q_1, q_2, \vec{r}_{12})$ is the kernel which can be expanded in the following form:

$$\phi(q_1, q_2, \vec{r}_{12}) \cong \sum_{\alpha\beta}\int \phi(q_\alpha, q_\beta, \vec{r}_{12})p_\alpha(q_1)p_\beta(q_2) \tag{2.86}$$

where q_α are the fixed values that give the good interpolation of the function $\phi(q_\alpha, q_\beta, \vec{r}_{12})$, which is called the integration kernel, analogous to the classical Coulomb interaction kernel $\frac{1}{|\vec{r}_1 - \vec{r}_2|}$.

Substituting Eq. (2.86) into Eq. (2.85), one can get

$$E_c^{nl} = \frac{1}{2}\sum_{\alpha\beta}\int\int d^3r_1 d^3r_2 \theta_\alpha(\vec{r}_1)\theta_\beta(\vec{r}_2)\phi_{\alpha\beta}(r_{12})$$

$$E_c^{nl} = \frac{1}{2}\sum_{\alpha\beta}\int d^3k \theta_\alpha^*(\vec{k})\theta_\beta(\vec{k})\phi_{\alpha\beta}(\vec{k}) \qquad (2.87)$$

where $\theta_\alpha(\vec{r}_1) = n(\vec{r}) p_\alpha\left[q_0\left(n(\vec{r}), \nabla n(\vec{r})\right)\right]$ and $\theta(\vec{k})$ is its Fourier transform.

The vdW-DF method improves significantly in predicting the lattice parameters and the binding energy of vdW solid systems as well as other vdW systems.

2.5.5 optB88-vdW Functional

The starting point for this modified new functional is the functional with the B88 exchange enhancement factor:

$$F_x^{B88}(s) = 1 + \frac{\mu s^2}{\left(1 + \beta s \,\mathrm{arcsinh}(cs)\right)} \qquad (2.88)$$

where s is the reduced gradient density, and is given by $s = \frac{|\nabla n(\vec{r})|}{2(3\pi^2)^{1/3} n(\vec{r})^{4/3}}$, and c, μ, and β are the parameters defined as

$$c = 2^{4/3}(3\pi^2)^{1/3},\ \beta = \frac{9\mu(6/\pi)^{1/3}}{(2c)} \text{ with } \mu \cong 0.2743$$

In optB88-vdW functional [69], the ratio of μ/β and μ are changed to 1.2 and 0.22, respectively. As a result, this new functional significantly improves the binding energy of vdW materials.

2.6 Practical Methods in Electronic Structure Calculations

2.6.1 Pseudopotential Approach

For the formation of covalent bond between two atoms, their core electrons do not participate since they are highly localized. Only the valence electrons (outermost electrons) involve in forming the covalent bond between atoms. But, the problem with the valence states is the oscillatory behavior that could result in the slow convergence in the plane wave expansion. To overcome this problem, one needs a good description of the valance wave functions. The full ionic core–electron interaction (often called *ion–electron* interaction), which includes the orthogonality of the valence wave functions to the core states, is replaced by a pseudopotential whose general form can be written as:

$$U_P(\vec{r}) = \sum_{l=0}^{\infty} \upsilon_P^l(\vec{r})\hat{P}_l \qquad (2.89)$$

Here, $\upsilon_p^l(\vec{r})$ is the pseudo potential, and $\hat{\mathbf{P}}_l$ is the projector operator that operates on the l^{th} angular momentum subspace.

For the pseudo potential, the solutions of the atomic Schrödinger equation becomes the pseudo-wave functions which are not the same as true wave functions. The pseudo wave-functions must be smooth in the core region (inside the cutoff radius), and can be used to generate the accurate charge density in the core region. The idea of generating such pseudo potential, first

proposed by Hamann et al. [70], must satisfy the following conditions: i) inside pseudized region (inside the cutoff radius) the core region the total charge generated by pseudo wave functions must be same as that generated by true wave-functions – the so-called norm conserving condition; ii) the eigenvalues of the pseudo-wave functions coincide with those of the all-electron wave functions for a chosen electronic configuration of the atom. The pseudo potential generated under these conditions, is known to be norm-conserving pseudopotential. But, the problem with this pseudo potential is that it requires a larger number of plane wave basis set for obtaining the reasonable accuracy of the calculations.

A very successful effort for reducing the plane wave cut off was made by Vanderbilt [71] in 1990. The proposed method has the ability to produce the much smoother pseudo wave function, and the softer pseudopotential – the so-called the ultrasoft pseudopotential (USPP). The advantage of this scheme is that it substantially leads to reduce the energy cutoff for PW calculations that involved first row and transition metal atoms.

In 1994, Blöchl [72] introduced the projector-augmented wave (PAW) method, which was implemented by Kresse and Joubert [73] in 1999 for the *ab-initio* DFT calculations. This method retains the all-electron character, but it uses a decomposition of the all-electron wave function in terms of a *smooth* pseudo-wave function. All-electron wave function is obtained from the pseudo-wave function via the linear transformation as

$$\left|\Phi_n\right\rangle = \left|\tilde{\Phi}_n\right\rangle + \sum_{J=1}^{P} \sum_{L} \sum_{i} \left(\left|\phi_i^L\right\rangle - \left|\tilde{\phi}_i^L\right\rangle \right) \left\langle \tilde{p}_i \middle| \tilde{\Phi}_n \right\rangle \tag{2.90}$$

Here, ϕ_i^L are the all-electron partial waves, and are obtained for a reference atom, whereas ϕ_i^L are the pseudo-atomic partial waves that are equivalent to the all-electron inside the valence region

(outside the cutoff radius), and match inside the core region (inside the cutoff radius). The sums run over all atom sites J, angular momenta L=(l, m), and the projector functions $\tilde{p}_i$. The projector functions satisfy the following relation:

$$\left\langle \tilde{p}_i \middle| \tilde{\phi}_j \right\rangle = \delta_{ij} \tag{2.91}$$

According to PAW method, the all-electron charge density can be written as

$$n(\vec{r}) = \tilde{n}(\vec{r}) + n_1(\vec{r}) + \tilde{n}_1(\vec{r}) \tag{2.92}$$

Here, $\tilde{n}(\vec{r})$ is the soft- Pseudo charge density that can be calculated from the pseudo wave functions on the plane wave grid as

$$\tilde{n}(\vec{r}) = \sum_n f_n \left\langle \tilde{\Phi}_n \middle| \vec{r} \right\rangle \left\langle \vec{r} \middle| \tilde{\Phi}_n \right\rangle \tag{2.93}$$

$$o_{ij} = \sum_{i,j} f_n \left\langle \tilde{\Phi}_i \middle| \tilde{p}_i \right\rangle \left\langle \tilde{p}_j \middle| \tilde{\Phi}_j \right\rangle \tag{2.94}$$

Using pseudo wave functions being computationally fast, the construction of the true wave functions for calculating the observables in Kohn-Sham DFT are mostly utilized. As such, the PAW method is very flexible, and found to be one of the most powerful techniques, at present, combining the pseudopotential plane wave method with the accuracy offered by augmentation. The details of the methods can be found in [72,73].

2.6.2 Periodic Systems and Plane Wave

For the efficient representation of the electronic orbitals in the Kohn-Sham DFT, and for speeding up the numerical calculations in the self-consistent loop (Figure 2.1), we require a good choice of a set of basis functions. Since the electronic wave functions follow the same periodicity

as the lattice, we can take advantage of using the periodicity for the solid crystals and surfaces. In this regard, the plane waves would be a natural choice for the complete representation of the basis functions of the periodic system using the Fourier series expansion. Blöch's theorem allows us to determine the wave function for all electrons in the periodic solid system by performing the calculation of the electronic wave functions in the unit cell using the finite number of k vectors in the first BZ, and therefore to reproduce the physical properties of the periodic system to the desired numerical accuracy.

Blöch Theorem

In an external periodic potential, the wave function of an electron is given by

$$\psi_k(\vec{r}) = e^{ik.\vec{r}} u_k(\vec{r}) \tag{2.95}$$

where the first part in right hand side is the phase factor coming from the translational symmetry, and the second term is the periodic potential $u_k(\vec{r}) = u_k(\vec{r} + \vec{a}_i)$. In a periodic lattice system, the wave function of the electron can be displaced using the lattice vectors $(\vec{r} + \vec{a}_i)$, i.e.,

$$\begin{aligned} \psi_k(\vec{r} + \vec{a}_i) &= e^{ik.(\vec{r}+\vec{a}_i)} u_k(\vec{r} + \vec{a}_i) \\ &= e^{ik.\vec{a}_i} e^{ik.\vec{r}} u_k(\vec{r} + \vec{a}_i) \\ &= e^{ik.\vec{a}_i} \psi_k(\vec{r}) \end{aligned} \tag{2.96}$$

Therefore, the probability density $|\psi_k(\vec{r})|^2$ is exactly the same for the periodic lattice.

According to the Blöch's theorem, we can determine the electronic wave function of the periodic system by using the wave function of the unit cell since, except for a phase factor $(e^{i\vec{k}.\vec{a}})$,

the wave function in the neighboring cell is exactly the same. We can now exploit Blöch's theorem allows us to write a general form of the electronic wave functions in a periodic potential:

$$\psi_k(\vec{r}) = e^{i\vec{k}.\vec{r}} \sum_{\vec{G}} C_{\vec{k}+\vec{G}} e^{i\vec{G}.\vec{r}} \tag{2.97}$$

Here, $\vec{G} = \vec{n}_i \vec{b}_i$, with i=1,2,3, are the reciprocal lattice vectors.

For a periodic system, the vectors outside the first BZ can be written in the form $\vec{k}' = \vec{k}+\vec{G}$ with k' in the first BZ.

Now, the plane wave basis functions are defined as

$$\phi_G(\vec{r}) = \frac{1}{\sqrt{\Omega}} e^{i.\vec{G}.\vec{r}} \tag{2.98}$$

The normalization conditions gives us $\langle \phi_G(\vec{r}) | \phi_G(\vec{r}) \rangle = \delta_{G,G'}$

Now, the wave functions for the different eigenstates m can be written as

$$\psi^{(k)}(\vec{r}) = e^{i\vec{k}.\vec{r}} \sum_{G=0}^{\infty} C_{mk}(\vec{G}) \phi_G(\vec{r}) \tag{2.99}$$

If we define

$$\phi_G(\vec{r}) = \frac{1}{\sqrt{\Omega}} e^{i(\vec{k}+\vec{G}).\vec{r}}, \tag{2.100}$$

Then the above expression can be written as

$$\psi^{(k)}(\vec{r}) = \sum_{G=0}^{\infty} C_{mk}(\vec{G}) \phi_G^k(\vec{r}) \tag{2.101}$$

where $C_{mk}(\vec{G})$ are the plane wave coefficients.

A periodic Kohn-Sham potential can be written as

$$\langle \phi_G(\vec{k}) | \hat{v} | \phi_{G'}(\vec{k}) \rangle = \frac{1}{\Omega} \int d^3r \, v(\vec{r}) \, e^{-(\vec{G}-\vec{G}').\vec{r}} = v_{eff}(\vec{G}-\vec{G}') \tag{2.102}$$

In a plane wave basis set formulation, the Kohn-Sham eigenvalue equation can be written as

$$H_{G,G'}(\vec{k})C_{m,k}(\vec{G}') = \varepsilon_{mk} C_{m,k}(\vec{G}) \tag{2.103}$$

where $H_{G,G'}(\vec{k})$ are the Hamiltonian matrix elements, and given by

$$H_{G,G'}(\vec{k}) = \sum_{G'}\left[\frac{\hbar^2}{2m}\left|\vec{k}+\vec{G}\right|^2 \delta_{G,G'} + V_{eff}(\vec{G}-\vec{G}')\right] \tag{2.104}$$

For any given $\vec{k}$, the solution of the eigenvalue equation, Eq. (2.107), can be written as

$$\psi_{m,k}(\vec{r}) = \frac{1}{\Omega}\sum_{G} C_{m,k}(\vec{G})\, e^{i(\vec{k}+\vec{G}).\vec{r}} \tag{2.105}$$

According to Blöch's theorem, one can expand the wave function of an electron in a periodic potential using a plane-wave basis set. In the plane-wave expansion, the allowed $\vec{G}$ vectors are the lattice vectors of a periodic system in the reciprocal space. The plane wave expansion can be truncated at a finite number of the basis functions with the kinetic energy less than the cutoff energy as

$$\frac{\hbar^2}{2m}\left|\vec{k}+\vec{G}\right|^2 < E_{cut} \tag{2.106}$$

If $\vec{k} = 0$, then above expression becomes

$$\left|\vec{G}\right| < G_{cut} = \sqrt{\frac{2mE_{cut}}{\hbar^2}} \tag{2.107}$$

In atomic units, $\hbar = m = 1$, the above equation can be written as

$$G_{cut} = \sqrt{2E_{cut}} \tag{2.108}$$

In the Fourier series representation, any periodic function can be represented by

$$\phi^{(k)}(\vec{r}) = \frac{e^{i\vec{k}.\vec{r}}}{\sqrt{\Omega}}\sum_{G=0}^{\infty} C_k(\vec{G}) e^{i\vec{G}.\vec{r}} \tag{2.109}$$

The finite cut-off energy puts the restriction of using the type of functions. Then the plane wave expansion requires a set of integer numbers as

$$\left|n_i b_i\right| = G_{cut} \quad i = 1, 2, 3 \tag{2.110}$$

The maximum number of G-vectors then can be written as $n_i \geq \frac{G_{cut}}{\left|b_i\right|} = \frac{G_{cut}\left|a_i\right|}{2\pi}$ which works for any direction in the BZ.

2.6.3 Sampling of Brillouin Zone

Solving the infinite number of Kohn-Sham equations to obtain the properties of the infinite solid system is not computationally feasible due to the infinite k-vectors. However, the problem can be made simpler by approximating the full Brillouin zone (BZ) integral with a summation over a finite set of k-point, the so-called the BZ sampling. In this approach, the number of k-points is chosen based on the unit-cell size as well as the characteristic of the systems. Metallic systems, for example, require a very fine BZ sampling whereas semiconductors need reasonably a few k-points.

Because of the periodicity of the system, the electron density in each replicas of the unit cell is identical *via* $n(\vec{r} + \vec{L}) = n_k(\vec{r})$, for any linear combination of the lattice vectors, L. The electronic wave function is also periodic in the supercell, i.e. $\phi_k(\vec{r} + n\vec{a}_i) = e^{ink.\vec{a}_i}\phi_k(\vec{r})$. Thus, the wave function at k-point in the whole spatial region of the periodic system will be the same as that in the small unit cell.

Then, one needs to solve a set of single-electron Kohn-Sham equations for each k-point included in the BZ sampling of the system for which the electronic density can be written as

$$n(\vec{r}) = \sum_{k \in BZ} \omega_k \sum_{i=1}^{Nk} f_i^{(k)} \left| \phi_i^{(k)}(\vec{r}) \right|^2 \qquad (2.111)$$

where the sum runs over all k-vectors in the BZ of the unit cell, ω_k are the weight factors that depend on the symmetry of the unit cell, N_k is the number of electronic states occupied at each k-point, and $f_i^{(k)}$ is the occupation number of band i at wave vector k.

The flexible and efficient way to sample the BZ was proposed by Monkhorst and Pack [74]. Their main idea is to use equally spaced mesh, for all symmetries, to sample the BZ according to the following construction:

$$\vec{k} = n_i \vec{G}_i \quad \text{with} \quad i=1, 2, 3 \qquad (2.112)$$

where $\vec{G}_i$ are the reciprocal lattice vectors, and n_i are the integers that are determined as

$$n_i = \frac{2r - q - 1}{2q} \quad \text{with } r = 1, 2, \ldots..q \qquad (2.113)$$

The magnitude of the error introduced by BZ sampling with a finite number of k-points can be reduced by using denser points, and thus the accuracy of calculations can be controlled by the density of k-points.

While BZ sampling close to the Fermi surface of a metallic system, the highest occupied bands can fluctuate during the iterative process due to the adjustment of the Fermi energy – leading to the electronic instability. This causes the convergence problem in the self-consistent procedure. The Gaussian smearing technique [75] has resolved this issue by introducing a distribution of occupation numbers to smear the Fermi surface.

In the case of metallic systems, there is a finite density of states near the Fermi energy due to which the functions to be integrated needs first to be multiplied by a sharp Fermi occupation in

order to reduce the errors during BZ sampling. The Methfessel-Paxton [76] tackled this problem nicely by introducing a smearing scheme in which they propose an approximation to the delta-function by taking finite number of points, and then approximation to the step function by integrating the approximated delta function. Here, the step function that characterizes the Fermi surface and the delta function associated with the BZ sampling using a finite number of points are approximated by smooth approximations based on Hermite polynomials. Under these approximations, values of the following integral can be evaluated with a small number of k-points.

$$I = \int_{-\infty}^{\infty} S(E(\vec{k}) - E_F) \int_{BZ} f(\vec{k})\ \delta(\varepsilon - E(\vec{k}))d\varepsilon \tag{2.114}$$

where $E(\vec{k})$ represents the energy band as a function of the wave vector, and E_F is the Fermi energy. The details of this method can be found in Ref. [78].

2.6.4 Electronic Density of States

The total density of states is given by

$$\rho(\varepsilon) = \sum_{n}^{bands} \sum_{\vec{k}} \delta\left(\varepsilon - \varepsilon_n(\vec{k})\right) \tag{2.115}$$

where $\varepsilon_n(\vec{k})$ is the eigenvalue for a given wave vector $\vec{k}$.

The total density of states can be written as

$$\rho(\varepsilon) = \sum_i \rho_i(\varepsilon) = \sum_i \sum_n^{bands} \sum_{\vec{k}} \left\langle \phi_n(\vec{k}) \middle| Y_{l,m} \right\rangle \left\langle Y_{l,m} \middle| \phi_n(\vec{k}) \right\rangle \delta\left(\varepsilon - \varepsilon_n(\vec{k})\right) \tag{2.116}$$

where $\rho_i(\varepsilon)$ is the projected density of states (PDOS), and can be computed by projecting the wavefunctions onto the spherical harmonics.

2.6.5 Bader's Approach for Estimating Charge Transfer

The charge transfer between atoms provides important information about the electronic properties of the materials. Accurate estimate of the charge transfer thus requires the proper description of the atomic charges, which are not observables. However, atomic charges can be obtained by the decomposition of the electronic density. An efficient approach for partitioning of the electronic density is proposed by Bader [77]. An atom can be defined as a region of real space bounded by surfaces through which there is a "zero flux" in the gradient vector field of the electron density. The topology of the electron density is thus used to define where one atom ends and the next begins. According to the Bader's approach, the whole spatial region of any quantum mechanical molecular system can be divided into smaller sub-systems (called Bader volumes) by the "zero" flux surfaces at which the gradient of the electron density vanishes. Therefore, the "zero flux" surfaces satisfy the boundary condition:

$$\nabla n(\vec{r}).\hat{n}(\vec{r}) = 0\,, \tag{2.117}$$

for every point on the surface.

Here, $n(\vec{r})$ is the electron density and $\hat{n}(\vec{r})$ is the unit vector perpendicular to the dividing surface. The gradient vector field of the charge density is represented by the trajectories. A trajectory of the electron density starts from some arbitrary point $(\vec{r}_0)$, and can be obtained by calculating the gradient of the density and keep iterating the process until the gradient path generated terminates.

A simple and efficient algorithm for partitioning the electron density according to Bader's approach is developed by Henkleman et al.[78]. Later, the same group developed the improved grid-based algorithm [79] for the decomposition of the charge density into Bader volumes.

2.6.6 Tersoff-Hamann Model for Simulation of STM Image

Scanning tunneling microscopy (STM) has profound applications in surface science and nanoscience. Since the invention of STM by Rohrer and Binnig [37], STM has led revolutionary developments allowing us to observe the surface structures at the atomic scale. After the invention of STM, Tersoff and Hamann (TH) formulated a model [80,81] based on Bardeen's formalism, which treats the tip and surface as two non-interacting systems. Then, the electronic wave functions of the sample and tip sub-systems can be obtained separately by solving the Schrödinger equation. TH suggested for replacing the unknown electronic structure of the tip by a simple model system, in which the wave-function of the STM tip atom is assumed to be an atomic s wave function.

The TH approximation is thus based on the s-wave model for the tip with the spherically symmetric wave functions centered at the center of curvature of the tip, $\vec{r}_0$. All other tip wave functions can be neglected.

According to TH [80,81], one can model the STM tip as a locally spherical potential well, centered at $\vec{r}_0$, where it approaches nearest to the surface which is represented by the Z=0 plane. In Bardeen's approach, since the potentials of the sample and the tip are negligible in the separation plane, both the sample and tip wave functions satisfy the following Schrödinger equation:

$$-\frac{\hbar^2}{2m}\nabla^2\psi = E\psi \tag{2.118}$$

$$\nabla^2\psi = \kappa^2\psi \tag{2.119}$$

where $\kappa^2 = \left|\frac{2mE}{\hbar^2}\right|$

Assuming the tip wave-function has the form

$$\psi_{\lambda}^{T}(\vec{r}-\vec{r}_0)=\frac{C}{\kappa\left|\vec{r}-\vec{r}_0\right|}\exp(-\kappa\left|\vec{r}-\vec{r}_0\right|) \tag{2.120}$$

where κ_1 is the Bessel function, and C is a normalization constant.

This is the general form of an atomic s-orbital as wave function, and is characterized by an exponential decay from tip to vacuum. This function can be related to the Green's function of the vacuum Schrödinger equation which can be written as:

$$(\nabla^2-\kappa^2)\,G(\vec{r}-\vec{r}_0)=\delta(\vec{r}-\vec{r}_0) \tag{2.121}$$

Thus, one can write

$$G(\vec{r}-\vec{r}_0)=\frac{\kappa}{4\pi C}\psi^{T}(\vec{r}-\vec{r}_0)\ \text{ with }\ \nabla^2 G(\vec{r}-\vec{r}_0)=-4\pi\delta(\vec{r}-\vec{r}_0) \tag{2.122}$$

The tip wave function is thus given by

$$\psi^{T}(\vec{r}-\vec{r}_0)=\frac{4\pi C}{\kappa}G(\vec{r}-\vec{r}_0) \tag{2.123}$$

Using Green's theorem to transform the integral in the expression for the matrix elements which are defined by

$$M_{\eta\lambda}^{ST}=\frac{\hbar^2}{2m}\int_S(\psi_{\lambda}^{T*}\nabla\psi_{\eta}^{S}-\psi_{\eta}^{S}\nabla\psi_{\lambda}^{T*}).d\vec{S} \tag{2.124}$$

This integral is evaluated for the separation surface between tip and the surface.

If the energies of the tip and sample state are the same the decay constant will be

$$\kappa_{\eta}=\kappa_{\lambda}=\kappa \tag{2.125}$$

Inserting the wave function $\psi^{T}(\vec{r}-\vec{r}_0)$, one can rewrite Eq. (2.124) as

$$M_{\eta\lambda}^{ST} = \frac{4\pi C h^2}{2m\kappa} \int_S \left[G_\lambda(\vec{r} - \vec{r}_0) \nabla \psi_\eta^S - \psi_\eta^S \nabla G_\lambda(\vec{r} - \vec{r}_0) \right] . d\vec{S} \tag{2.126}$$

This equation can be written as:

$$M_{\eta\lambda}^{ST} = \frac{4\pi C \hbar^2}{2m\kappa} \int_{V(tip)} \left[G_\lambda(\vec{r} - \vec{r}_0) \nabla^2 \psi_\eta^S - \psi_\eta^S \nabla^2 G_\lambda(\vec{r} - \vec{r}_0) \right] d^3 r \tag{2.127}$$

From Eqs. (2.121) and (2.127), one can obtain

$$M_{\eta\lambda}^{ST} = \frac{4\pi C \hbar^2}{2m\kappa} \int_{V(tip)} \left[G_\lambda(\vec{r} - \vec{r}_0) \kappa^2 \psi_\eta^S - \psi_\eta^S \left\{ \kappa^2 G_\lambda \vec{r} - \delta(\vec{r} - \vec{r}_0) \right\} \right] d^3 r \tag{2.128}$$

Cancelling the first and second terms in the Eq. (2.128), we get

$$M_{\eta\lambda} = \frac{4\pi C \hbar^2}{2m\kappa} \int_{V(tip)} d^3 r \; \psi_\eta^S \delta(\vec{r} - \vec{r}_0) \tag{2.129}$$

Thus, the final expression for the matrix elements is reduced to

$$M_{\eta\lambda} = \frac{2\pi C \hbar^2}{\kappa m} \psi_\eta^S(\vec{r}_0) \tag{2.130}$$

which is the central result of the TH model of STM.

Using Fermi's golden rule, the tunneling current from the sample to the tip, for a system with negative bias voltage, V_t, can be given as:

$$I_{s\text{-}t} = \frac{4\pi e}{h} \int_{-\infty}^{\infty} \left[\rho_\lambda^T(\varepsilon + eV) \left[1 - f(\varepsilon + eV) \right] |M|^2 \rho_\eta^S(\varepsilon) f(\varepsilon) \right] d\varepsilon \tag{2.131}$$

where $f(\varepsilon)$ represents the Fermi-distribution function.

Similarly, the total current flowing from the sample to the tip can be given as:

$$I_{t-s} = \frac{4\pi e}{\hbar} \int_{-\infty}^{\infty} \left[\rho_\lambda^T(\varepsilon + eV) f(\varepsilon + eV) |M|^2 \rho_\eta^S(\varepsilon) \left[1 - f(\varepsilon) \right] \right] d\varepsilon \tag{2.132}$$

The total current flowing from the sample to the tip is given by

$$I_t = I_{s\text{-}t} - I_{t\text{-}s}$$

$$= \int_{-\infty}^{\infty} \left[\{ f(\varepsilon) - f(\varepsilon + eV) \} |M|^2 \rho_\lambda^T(\varepsilon + eV) \rho_\eta^S(\varepsilon) \right] d\varepsilon \tag{2.133}$$

At the low temperature, the Fermi distribution function becomes the step function, so the expression of the tunneling current becomes:

$$I_t \approx \frac{4\pi e}{\hbar} \int_{\varepsilon_F - eV}^{\varepsilon_F} |M|^2 \rho_\lambda^T(\varepsilon + eV)\, \rho_\eta^S(\varepsilon)\, d\varepsilon \tag{2.134}$$

The differential conductance is then given by

$$\frac{dI_t}{dV_t} = \frac{16\pi^3 C^2 \hbar^3 e}{\kappa^2 m^2} \rho_\lambda^T \rho_\eta^S(\varepsilon_F^S + eV, \vec{r}_0) \tag{2.135}$$

In the limit of small bias voltage and low temperature, one can write

$$dI_t \propto dV_t \sum_{n\vec{q}} \left| \psi_{n\vec{q}}(\vec{r}_0) \right|^2 \delta\left(\varepsilon_{n\vec{q}} - \varepsilon_F \right) = dV_t \rho_{n\vec{q}}^S\left(\varepsilon_F, \vec{r}_0 \right) \tag{2.136}$$

where the sum extends over the states evaluated at $\vec{r}_0$, and $\psi_{n\vec{q}}(\vec{r}_0)$ represent the Kohn-Sham wave functions of the system with band energy $\varepsilon_{n\vec{q}}$, band index n and wave vector $\vec{q}$ in the surface Brillouin zones.

$$I_t = \frac{16\pi^3 C^2 \hbar^3 e}{\kappa^2 m^2} \rho^T \int_0^{eV} d\varepsilon\, \rho^S\left(\varepsilon_F^S, \vec{r}_0 \right) \tag{2.137}$$

The above equation shows that the integral includes all states of the sample at the tip location between the Fermi energy and the Fermi energy shifted by the applied bias voltage. Thus, the tunneling current is proportional to the integrated local density of states.

$$\rho^{S}_{n\vec{q}}\left(\varepsilon_F, \vec{r}_0\right) = \sum_{n\vec{q}} \left|\psi^{S}_{n\vec{q}}\left(\vec{r}_0\right)\right|^2 \delta\left(\varepsilon_{n\vec{q}} - \varepsilon_F\right) \tag{2.138}$$

This is the local density of the sample states at the position $\vec{r}_0$ of the tip apex atom, and is a basic quantity for STM image. The TH model provides a conceptual simple framework for interpreting STM images, and therefore, it is still the widely used.

2.7 Lattice Vibrations

In the adiabatic approximation [82], we assume that electrons are at their equilibrium states for a given nuclear configuration. All of the electron's contribution is contained in the forces acting on the nucleus.

The Hamiltonian for nuclear motions in the crystal can be written as

$$H = \sum_{i,j} \frac{p_{ij}^2}{2m_j} + V \tag{2.139}$$

If each atom i, in the unit cell j, is allowed to vibrate about equilibrium with the displacement $u_{ij}(t)$, one can write the instantaneous position of atoms at time t as

$$\vec{R}_{ij}(t) = \vec{r}_i + \vec{r}_j + \vec{u}_{ij}(t) \tag{2.140}$$

The potential energy of the crystal now can be expanded in a Taylor series of the atomic displacements about $\vec{u}_{ij} = \vec{r}_i + \vec{r}_j = 0$:

$$V = V^{(0)} + \sum_{\alpha ij} \frac{\partial V}{\partial u^{\alpha}_{ij}} u^{\alpha}_{ij} + \frac{1}{2} \sum_{\alpha ij} \sum_{\beta i'j'} \frac{\partial^2 V}{\partial u^{\alpha}_{ij} \partial u^{\beta}_{i'j'}} u^{\alpha}_{ik} u^{\beta}_{i'j'} + \text{.....}, \tag{2.141}$$

where α and β represent the Cartesian directions, i and i' represent the indices of atoms in the unit cell and j and j' represent the indices of the unit cell.

Assuming the adiabatic approximation and keeping the terms up to the second order, one can write the total static energy of the crystal under a small perturbation of ion positions from the equilibrium as:

$$V = V^{(0)} + \sum_{\alpha ij} \Phi_{ij}^{\alpha} u_{ij}^{\alpha} + \frac{1}{2} \sum_{\alpha ij} \sum_{\beta i'j'} \Phi_{ij,i'j'}^{\alpha\beta} u_{ik}^{\alpha} u_{i'j'}^{\beta} \tag{2.142}$$

where $\Phi_{ij}^{\alpha} = \frac{\partial V}{\partial u_{ij}^{\alpha}} = -F_{ij}^{\alpha}$,

The term V_0 is the static potential energy of the crystal. Since the force on any atom vanish in the equilibrium configuration, we have, $\Phi_{ij}^{\alpha} = 0$

The second order term in the above eq. (2.142) is termed the harmonic energy where the expression for $\Phi_{ij,\,i'j'}^{\alpha\beta}$ is given as:

$$\Phi_{ij,i'j'}^{\alpha\beta} = \frac{\partial^2 V}{\partial u_{ij}^{\alpha} \partial u_{i'j'}^{\beta}} = -\frac{\partial F}{\partial u_{i'j'}^{\beta}} \tag{2.143}$$

These are the second-order force constants.

In the harmonic approximation, the equations of motion for all the nuclei can be written as

$$M_i \ddot{\vec{u}}_{ij}(t) = -\sum_{i'j'} \Phi_{ij,i'j'}(t) \vec{u}_{i'j'}(t) \tag{2.144}$$

The solution has the form

$$\vec{u}_{ij}(t) = \hat{e}_{ij}(\vec{k}) e^{(i\vec{k}.\vec{r}_i - \omega t)} \tag{2.145}$$

where M_i is the mass of atom, $\hat{e}$ is the polarization unit vector, and $\vec{k}$ is a vector in the reciprocal space, and $\vec{r}_i$ is the translation vector of the primitive lattice. From equations (2.144) and (2.145), one can obtain the dynamical matrix as:

$$D_{ii'}^{\alpha\beta}\left(\vec{k}\right)=\frac{1}{\sqrt{M_i M_{i'}}}\sum_{j'}\Phi_{i0,i'j'}^{\alpha\beta}e^{i\vec{k}\left(\vec{r}_{i'j'}-\vec{r}_{i,0}\right)} \tag{2.146}$$

Here, j=0 since the summation over j' and the origin is arbitrary.

$$\sum_{ii'}D_{ii'}^{\alpha\beta}(\vec{k})\ e_{\beta}(\vec{k})=\omega^2(\vec{k})\ e_{\alpha}(\vec{k}) \tag{2.147}$$

By diagonalizing the dynamical matrix, one can obtain the harmonic eigen frequencies and eigen modes for the crystals. These eigen modes are the confined motion of ions, the so-called the lattice vibrations.

2.7.1 Linear Response Method

The Linear Response method [83] does not directly compute the force-constant matrix. Within this approach, the dynamical matrix can be obtained using the linear response. In the linear response calculations, there is not a big difference between calculations for a k-point near the zone center and other k-point in the Brillouin zone. This method considers only the linear term, and the anharmonic effect is not included.

2.7.2 Frozen Phonon Method

In the Frozen Phonon method, the perturbation is proportional to any special vibrational mode, and the frequency of this mode is obtained from the change of the total energy. The frozen phonon method is an easy and direct way to evaluate the frequency of lattice vibrations. This method can be used to study the anharmonic effects since the calculated energy change includes all of the higher order terms.

2.7.3 Finite Difference Method

The Finite-Difference method is more suitable than other two methods mentioned above when the system contains more than 200 atoms. We have used this method for our vibrational frequency calculations. In this method, the finite difference is used to construct the force-constant matrix in real space. In real space, the values of the force constant matrix decay with the interatomic distances. Therefore, one can cut the sum for including the number of nearest neighbors as:

$$D_{ii'}^{\alpha\beta}\left(\vec{k}\right) \approx \frac{1}{\sqrt{M_i M_{i'}}} \sum_{j'}^{\text{finite}} \Phi_{i0,i'j'}^{\alpha\beta} e^{i\vec{k}.\left(\vec{r}_{i'j'} - \vec{r}_{i,0}\right)} \tag{2.148}$$

where $\Phi_{i0,i'j'}^{\alpha\beta} = -\frac{F_{i0,i'j'}^{\beta}}{u_{i'j'}^{\alpha}}$ is the force-constant matrix or Hessian matrix.

Since the crystal is invariant under translations of any lattice vector, it is only necessary to displace the atoms in one primitive cell and calculate the forces induced on all the other atoms of the crystal. The force constant matrix can be obtained by displacing each atom of the lattice along the three Cartesian components by $u_{i'j'}^{\alpha}$, and calculating the forces $F_{ij,i'j'}$ induced on each atom. After the computation of these forces, one can evaluate the Hessian matrix using the finite difference procedure as:

$$\Phi_{ij,i'j'}^{\alpha\beta} \approx -\left\{\frac{F_{ij,i'j'}^{\beta(+)} - F_{ij,i'j'}^{\beta(-)}}{2u_{i'j'}^{\alpha}}\right\} \tag{2.149}$$

2.8 Methods for Calculating Activation Energy Barriers

2.8.1 The Drag Method

Drag method is a very simple and crude approximation for finding the minimum energy pathway and the saddle point along that path. In this method, the drag coordinate (x or y or z) (one degree of freedom) is chosen and is held fixed, but other coordinates (remaining N-1 degree of freedom) are allowed to relax. Guessing for the good reaction coordinate can simply be used for choosing the drag coordinate. Constraining the drag coordinate and relaxing the remaining degrees of freedom, the total energy of the system is minimized in the N-1 dimensional hyperplane. The drag coordinate is increased with a small increment along the reaction path from an initial state to the final state. The maximum energy obtained along the reaction path gives the saddle point energy.

2.8.2 Nudged-Elastic Band Method

Nudged elastic band (NEB) [84,85], originally implemented by Henkleman [86], is an efficient method for finding a minimum energy path (MEP) between the initial and the final states involved in the reaction path. Both states are known states, and are at local minima on the potential energy surface (PES). It is widely adopted for estimating the transition rates within the harmonic transition state theory (HTST) approximation, which will be described briefly later. In the NEB method, a set of images that is generated according to the linear interpolation is used to describe the reaction path. Along this path, each image is connected with neighboring image by an artificial spring which keeps the image at equal distance during the energy minimization process. Then, an optimization algorithm is applied to relax all images down toward the MEP. This path passes

through at least one first-order saddle point. Overall, the NEB gives both an estimate of the saddle point and the energy landscape features.

In NEB method, one can consider a set $\{\vec{R}_0, \vec{R}_1, ..., \vec{R}_N\}$ of images along the reaction path. Two endpoints $\vec{R}_0$ and $\vec{R}_N$ are fixed whereas other N-1 intermediate images are relaxed by using different optimization algorithm. The tangent vector at an image i can be estimated by bisecting the two unit vectors as

$$\hat{\tau}_i = \frac{\vec{R}_{i+1} - \vec{R}_i}{\left|\vec{R}_{i+1} - \vec{R}_i\right|} + \frac{\vec{R}_i - \vec{R}_{i-1}}{\left|\vec{R}_i - \vec{R}_{i-1}\right|} \tag{2.150}$$

It is normalized as $\left(\hat{\tau}_i = \frac{\hat{\tau}_i}{|\hat{\tau}_i|}\right)$. The total force acting on image i is the sum of two force components: the spring force along the tangent and the true force perpendicular to the tangent.

$$\vec{F}_i^{NEB} = \vec{F}_i^{\perp} + \vec{F}_i^{\parallel} \tag{2.151}$$

where the first component of true force perpendicular to the band,

$$F_i^{\perp} = \vec{\nabla}V(\vec{r}_i)_{\perp} = \vec{\nabla}V(\vec{r}_i) - \vec{\nabla}V(\vec{r}_i).\hat{\tau}_i\ \hat{\tau}_i \tag{2.152}$$

and, the second component is the spring force parallel to the band

$$F_i^{s\parallel} = k\left(\left|\vec{R}_{i+1} - \vec{R}_i\right| - \left|\vec{R}_i - \vec{R}_{i-1}\right|\right)\hat{\tau}_i \tag{2.153}$$

where R_i is the position of the i_{th} image and k is the spring constant.

In the NEB method, a minimization of an elastic band is carried out when the perpendicular component of the spring force and the parallel component of the true force are projected out. The projection of the perpendicular component of $\vec{\nabla}V(\vec{r}_i)$ and the parallel component of the spring force is known as ‘nudging’.

When the spring force perpendicular to the path is weak as compared to the parallel component of force, and the energy of the system changes rapidly along the path. Then, the intermediate images undergo in 'kinky' region where images fluctuate back and forth. As a result, convergence of the minimization slows down. To reduce this problem of slow convergence of minimization, one has to reduce the magnitude of parallel force and to add some fraction of the perpendicular component of spring force into the expression of Eq. (2.154). A smooth switching function gradually turns on the perpendicular component of the spring force. The force on image i then becomes

$$\mathrm{F}_{\mathrm{i}}^{\mathrm{NEB}} = \vec{\nabla}\mathrm{V}(\vec{\mathrm{r}}_{\mathrm{i}})_{\perp} + \mathrm{F}_{i}^{s\|}.\hat{\tau}_{\mathrm{i}}\ \hat{\tau}_{\mathrm{i}} + f\left(\phi_{i}\right)\left\{\mathrm{F}_{i}^{s\|} - \mathrm{F}_{i}^{s\|}.\hat{\tau}_{\mathrm{i}}\ \hat{\tau}_{\mathrm{i}}\right\} \tag{2.154}$$

where $f\left(\phi\right)$ is a switching function, and is defined by

$$f\left(\phi_{i}\right) = \frac{1}{2}\left(1 + \cos\left(\pi\cos\phi_{i}\right)\right) \tag{2.155}$$

where $\cos\phi_{\mathrm{i}} = \dfrac{\left(\vec{\mathrm{R}}_{\mathrm{i+1}} - \vec{\mathrm{R}}_{\mathrm{i}}\right)\left(\vec{\mathrm{R}}_{\mathrm{i}} - \vec{\mathrm{R}}_{\mathrm{i-1}}\right)}{\left|\left(\vec{\mathrm{R}}_{\mathrm{i+1}} - \vec{\mathrm{R}}_{\mathrm{i}}\right)\right|\left|\left(\vec{\mathrm{R}}_{\mathrm{i}} - \vec{\mathrm{R}}_{\mathrm{i-1}}\right)\right|}$

If $\phi = 90°$, the full perpendicular component of spring force is kept, but if $\phi = 0°$ then none of the perpendicular spring force is kept. A small amount of the perpendicular spring force is often enough to straighten out the path and improve the convergence of minimization. However, the stability of the band varies with the number of images chosen along the path. To deal with this problem, Henklemann [86] proposed a new modified version of NEB method that start with the new definition of local tangent at an image i:

$$\hat{\tau}_{\mathrm{i}} = \begin{cases} \hat{\tau}_{\mathrm{i}}^{+} & \text{if} \quad \mathrm{E_{i+1}} > \mathrm{E_i} > \mathrm{E_{i-1}} \\ \hat{\tau}_{\mathrm{i}}^{-} & \text{if} \quad \mathrm{E_{i+1}} < \mathrm{E_i} < \mathrm{E_{i-1}} \end{cases} \tag{2.156}$$

where E_i is the energy of the image i, and $\hat{\tau}_i^+ = \vec{R}_{i+1} - \vec{R}_i$ and $\hat{\tau}_i^- = \vec{R}_i - \vec{R}_{i-1}$

To find out the true MEP, the intermediate images along the NEB are relaxed through a force projection scheme in which forces are calculated using force-based optimizers using the following optimization methods: Steepest Descent (SD), Quick-Min (QM), Fast-Inertial Relaxation Engine [87], Conjugate-Gradient (CG) [88], and limited memory Broyden-Fletcher-Goldfarb-Shanno (L-BFGS) [89]. These optimizations have been implemented in NEB method by Sheppard et al.[90].

2.8.3 Climbing-Image Nudged Elastic Band Method

Climbing-Image (CI) NEB method [91] is the modified version of the regular NEB [86]. In this method, the higher energy image is allowed to climb to the saddle point. The climbing imaged does not experience the spring forces along the elastic band. Only the true force along the tangent acting on the image is inverted. In this way, the image tries to maximize its energy along the band, and minimize in all other directions. After the convergence of the images, we can obtain the saddle point.

The force on this one image is obtained by

$$F_{i,max}^{climb} = -\nabla E(R_{i,max}) + 2\nabla E(R_{i,max}).\hat{\tau}_{i,max}\hat{\tau}_{i,max} \qquad (2.157)$$

If the initial maximum-energy image is far away from the saddle point, then the minimization of the MEP hardly converge. Therefore, it is always better to proceed with the regular NEB to obtain the preliminary MEPs for the reaction. The subsequent usage of CI-NEB after the

regular NEB will provide the good estimate of the reaction co-ordinate around the saddle point, and hence allows the highest-energy image is close to the saddle point.

In this work, both NEB and CI-NEB methods have been used extensively for calculating the MEPs for various reactions under consideration here.

2.9. Kinetics of the Rare-Event Dynamical Systems

2.9.1 Transition State Theory

Transition-state theory (TST), first proposed by Marcellin in 1915, has been widely employed approximation to determine the chemical reaction rates. It defines the relationship between the activation energy and the frequency associated with a rare event. Along the reaction coordinate, there is a well-defined transition state (saddle-point configuration). The rate constant for escaping from state i to state j can be obtained by determining the equilibrium flux through a dividing surface which separate these two states.

Chemical reactions on the solid surfaces are the typical examples of rare events for which the dynamics are characterized by rare transitions between initial and final states. Such a system appears as largely be inactive, spending a long period of time before any transition occurs, and therefore called the *rare-event* dynamical system**.** In order for a transition to happen from one basin to another, the system has to pass through the saddle point by overcoming the associated energy barrier. Since the system stays for a very long time (relative to the picosecond timescale for one vibrational period) in a particular basin, the state-to-state transition happens rarely. Transition is

defined with a rate constant (k_i or k_j), which depends on the shape of the potential energy surface that constitutes to the basin and that of the saddle-point.

If we count the number of forward transition through a dividing surface separating state i and j that occur per unit time in the equilibrium ensemble, and divide this by the number of trajectories that are on average in state i, this yields the TST approximation to the rate constant, k^{TST}. TST differs from MD, in which the system can undergo transition in each direction, and repeatedly. Realistically, there is always a possibility for the backward transition at the dividing surface.

$$k_{ij}^{TST}(T)=\left(\frac{k_B T}{h}\right)\frac{Q_{TS}^{vib}(ij)}{Q_i^{vib}}\exp\left(-\frac{E_a}{k_B T}\right) \tag{2.158}$$

Where h is planck's constant, k_B is the Boltzmann constant, E_a is the activation energy barrier, and T is the temperature.

2.9.2 Harmonic Transition State Theory

Harmonic transition theory (HTST) is the practically useful form of the transition state theory under the following assumptions: First, saddle points on the potential energy surface represent the higher energy points along the reaction coordinate, particularly the hyperplane surfaces perpendicular to the unstable direction of the saddle point, that separates out the reactants from the products configurations, and the second is potential energy surfaces around the reactant configuration and the saddle point are locally harmonic.

HTST – a modified version of TST – is a good approximation for many reactions on solid surfaces, and it is also referred to as Vineyard theory [92]. It is often used to calculate the rate

constants in the *ab-initio* Kinetic Monte Carlo simulations. One can approximate that the potential energy near the minimum energy basin can be well described by an Taylor expansion of the potential energy terminated at the second-order, the so-called the harmonic approximation. For a system of N atoms, there are 3N vibrational modes at the minimum energy configuration, and 3N-1 modes at the saddle point owing to the fact that one degree of freedom is restricted (along reaction coordinate). If one calculates these modes, there should be a single imaginary frequency at the saddle-point configuration. The rate of a transition for a system of N atoms is then expressed as:

$$k^{HTST} = \frac{\prod_{i}^{3N} f_i^{min}}{\prod_{i}^{3N-1} f_i^{sad}} \exp\left(-\frac{E_a}{k_B T}\right) \tag{2.159}$$

where E_a is the activation energy barrier, i.e. difference in energy between the saddle point and the minimum energy configuration of reactants), k_B is the Boltzmann constant, and T is the temperature. Here, f_i^{min} are the 3N normal mode frequencies at the minimum, and f_i^{sad} are 3N-1 non-imaginary frequencies at the saddle point.

2.9.3 Spatial and Temporal Evolution

Although molecular dynamics (MD) simulation can accurately describe the spatial and temporal evolution of a system, it encounters the time-scale problem: the accurate integration of Newton's equation of motion requires the time steps $\sim 10^{-15}$ s to resolve the atomic vibrations. Thus, MD simulation is not the efficient tool to study the long-term time evolution of the "rare event" system in which the relevant dynamics proceeds by occasional transition from one state to the other in long periods of time. Instead of generating trajectories through each vibrational period,

kinetic Monte Carlo method treats the time-evolution of the dynamical system by considering the state-to-state transitions directly. An important characteristics of kMC simulation is that it can, in principle, gives the exact dynamical evolution of a system.

2.9.4 Kinetic Monte Carlo Simulation

In solid systems, the dynamical evolution occurs through a series of rare events, where system spends a long time in one potential-energy surface (PES) minimum before escaping to another one. Since the localized motion in the PES minima is not significant, the dynamical evolution can be simulated as a series of transition between PES minima. Thus, the main idea of kMC simulation is to coarse-grain the time evolution to the discrete rare events.

To gain insights into underlying processes in heterogeneous catalysis where the kinetics play a critical role for the complex reaction mechanisms on the solid catalyst surfaces, it is fundamentally important to carry out the long-time evolution of the system. One can use *ab-initio* kMC method [34,35,93] which combines the *ab-initio* DFT with a statistical approach to accurately describe the kinetics of the reactions on solid systems. The inputs (kinetic parameters) for *ab-initio* kMC simulation are obtained from DFT calculations, and then master equation based algorithm is employed to perform the long time simulation.

A kMC simulation provides a particular solution of the master equation, which is given by

$$\frac{dP_i(t)}{dt} = -\sum_{j \neq i} k_{ij} P_i(t) + \sum_{j \neq i} k_{ji} P_j(t) \qquad (2.160)$$

where $P_i(t)$ is the probability density function to find the system in state i (PES minima), and k_{ij} are the rate constants for the transition from state i to state j.

The KMC algorithm we implement is based on the so-called "rejection free" algorithm, also known as (BKL) [94] or residence-time algorithm. The idea of this standard algorithm is to obtain the numerical solution to the master equation (2.160) by generating the ensemble of trajectories in which each trajectory propagates the system from one state to the other such that the average over the whole ensemble of trajectories gives the probability density function $P_i(t)$ for all states i that satisfy eq. (2.160). A general flow of this algorithm is shown in Figure 2.2.

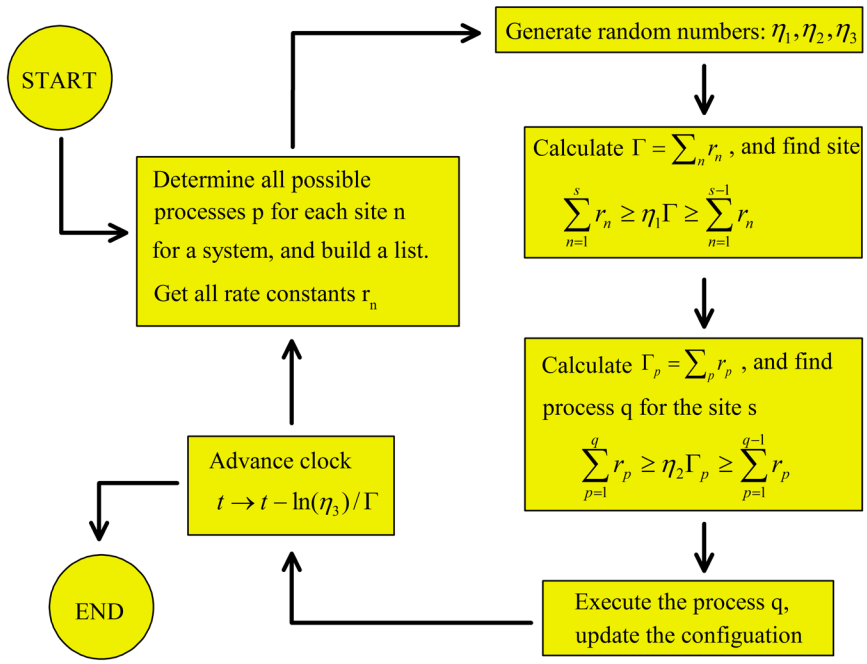

Figure 2.2 Flow chart for a standard kMC algorithm.

In kMC algorithm, the loop starts with the determination of all possible processes for which the rate constants are determined using $r = \frac{\tilde{s}P}{\Omega\sqrt{2\pi m k_B T}}$ for adsorption process (where $\tilde{s}$, P, Ω, m, k_B, and T are the sticking coefficient, partial pressure, site density, mass, Boltzmann constant, and temperature, respectively), and $r = A\exp\{-E_a/k_B T\}$ (where A and E_a are the prefactor and

activation energy barrier, respectively) for the desorption and other reactions. The total reaction rate Γ can be obtained as follows:

$$\Gamma = \sum_{n}^{total-sites} \left(\sum_{p}^{total-processes} r_n \right) \tag{2.161}$$

When r_n satisfies the condition: $\sum_{n=1}^{s} r_n \geq \eta_1 \Gamma \geq \sum_{n=1}^{s-1} r_n$ for a random number, $0 < \eta_1 < 1$, site s is selected. After choosing a site, the process is selected in the similar fashion by generating another random number $0 < \eta_2 < 1$. Local scan is then performed around the selected site to find a new process. Then, total reaction rate Γ is updated. At the end of each loop, the system clock is advanced by, $t = t - \ln(\eta_3)/\Gamma$. The above loop can be terminated for a long time span at which system reaches a steady state.

The kMC is very efficient method for carrying out the long time scale simulations. But, the drawback of the method is that it relies on the input parameters, which can be obtained either from either from experiments or MD simulations or *ab initio* calculations. Nevertheless, kMC bears the potentiality for predicting reaction kinetics at the mesoscale.

CHAPTER 3 EFFECT OF SINGLE-LAYER MoS_2 ON THE GEOMETRY, ELECTRONIC STRUCTURE, AND REACTIVITY OF TRANSITION METAL NANOPARTICLES

We present results of *ab initio* density functional theory (DFT) based calculations of the geometry, electronic structure, and reactivity of sub-nanometer-sized (29-atom) transition metal nanoparticles (NPs) (Cu_{29}, Ag_{29}, and Au_{29}) supported on single-layer MoS_2. As compared to its pristine form, defect-laden MoS_2 (with a S vacancy row) has relatively larger effect on the above properties of the NPs. The NPs bind more strongly on defect-laden than on pristine MoS_2 (in the order Cu_{29}>Ag_{29}>Au_{29}), confirming the important role of vacancies in stabilizing the NPs on the support. The presence of vacancies also leads to an increase in charge transfer from the NPs to MoS_2 (with the same elemental trend as for their binding energy), and to a shift of the d-band center of the NPs further toward the Fermi level, in turn influencing their propensity toward chemical activity. We examine the adsorption and dissociation of O_2 as the prototype reactions, and find that there is no barrier for O_2 to adsorb on top of an atom at the NP apex, where the frontier orbitals are localized, and that the dissociation channel proceeds through a chemisorbed state. The presence of the support leads to increase in the number of sites at which O_2 can adsorb with similar binding energy (<0.1 eV difference). Interestingly, energy barriers for both dissociation and recombination of O_2, when adsorbing at the NP apex, increase in the presence of the MoS_2 support. However, since the increase in the barrier for recombination is much larger than for dissociation, the latter should be more favored. In particular, for defect-laden-MoS_2 supported Au_{29} the recombination faces a barrier of 1.36 eV whereas the dissociation does 0.5 eV, implying that the defect-laden support may significantly improve the catalytic performance of Au_{29} toward oxidation.

3.1 Introduction

In heterogeneous catalysis research, the properties and applications of transition-metal (TM) nanoparticles continue to be intriguing topics because of their potential advantages over traditional catalysts. To begin with, NPs provide a much higher surface-to-bulk ratio than their single crystal surface counterparts, offering more active sites to reactants which often leads to enhanced activity [95,96] as well as high selectivity [97]. Because of their excellent performance, TM NPs have found wide catalytic applications in oxidation [98,99], water-gas shift [100], hydrogenations [101,102] and fuel cell related reactions [103,104]. These and related studies suggest that catalytic activity of the NPs depends upon factors such as the number of under-coordinated sites, electronic structure, shape, size, surface composition, stability, and interface with the support. A microscopic understanding of the exact relationship of these factors to catalytic properties is fundamentally important to enable the bottom-up approach of designing catalysts with desirable activity and product selectivity.

While catalytic properties of NPs continue to be the subject of investigations, those of single-layer molybdenum disulphide (MoS_2) are interesting in their own right [105-107]. Given that, it is natural to investigate whether their combination would result in an even better catalyst for specific reactions than the constituent parts individually. It is thus not surprising to find experimental approaches [108-111] aimed at functionalizing metal NPs with MoS_2 for specific chemical reactions, e.g. so-designed MoS_2-decorated NPs for hydrogen-evolution reaction (HER) [108,112] and oxidation reactions [109,113]. Furthermore, Cu-MoS_2 hybrid appears to have better electro-catalytic activity for oxidation of glucose than Cu nanoparticles [114]; Ag-MoS_2 catalyzes the HER, [115,116] and is also found to promote electro-catalytic activity for oxidation of

tryptophan [117]; Au-MoS_2 shows good electro-catalytic activity for oxidation of ascorbic acid, dopamine, and uric acid [16] and for oxidation of catechol [118]. In addition, Au-MoS_2 composite shows good catalytic activity in oxygen reduction reaction [119], and enhanced photo-catalytic activity in water splitting [120]. These experimental studies thus clearly suggest that these NP-MoS_2 hybrids have important catalytic applications. The electronic structural changes resulting from the charge transfer between NP and support [121], and NP-support interactions [122] could modify the active sites, influencing their activity and product selectivity. Further manipulation of these characteristics may be attained through defects such as sulfur vacancies.

Our interest herein is to examine the effect of single-layer-MoS_2 support on the geometry, electronic structure and catalytic properties of a set of small nanoparticles derived from commonly employed transition metals, and to compare their propensity for facilitating the adsorption and dissociation of O_2, a frequent subject of theoretical and experimental studies on the metal-oxide-supported TM NPs [123-131]. In the latter systems, the interfacial sites are generally found to be the catalytically active ones. Still, it is difficult to postulate a general mechanism that unravels the microscopic details of the reactivity of supported TM NPs owing to the fact that reactions such as O_2 activation may proceed through a variety of reaction channels. For instance, O_2 may directly dissociate on the support leaving oxygen atoms to diffuse to the NPs [126], or it may adsorb molecularly on the support and diffuse to the NPs-support interface [130], or it may adsorb and dissociate directly at the interfacial sites [128,131], or it may molecularly adsorb and dissociate somewhere on the NPs resulting in oxygen atoms which diffuse to the particle-support interface, and so on. The scenarios depend upon many factors such as particle shape and size, reaction conditions, support materials and their electronic effects, and eventually on the local atomic

environment. The relevant question here is: what scenario is associated with the case of NPs when supported by a metal-sulfide? To shed light on this issue, we examine the adsorption and dissociation of O_2 on 29-atom NPs, M_{29} (where M=Cu, Ag, and Au). The choice of 29 atom NPs as our model system stems from various factors. First, while they are small enough to be handled computationally, they are large enough (almost 1nm) to mimic realistic sizes in experiments. Second, their shape (boat shape – pyramidal structure with (111) and (100) faces) [100] reflects observed structures of supported NPs [132]. Third, since they have been widely studied [100,133-136] and proposed as possible catalysts (Cu_{29} and Au_{29}) for water-gas-shift reaction [137], our work here provides another perspective on their viability as sub-nanometer-sized catalysts. Moreover, MoS_2-supported Ag NPs appear to exhibit good electro-catalytic activity for oxidation [117,138], and photo-catalytic activity for hydrogen evolution reaction [115].

In what follows we first employ *ab initio* density functional theory (DFT) with the inclusion of van der Waals interactions [139,140] to examine the geometric and the electronic structures of M_{29} on MoS_2 supports – pristine and defect-laden. Next, we study the effect of these supports on the adsorption and dissociation of O_2 on the NPs as preliminary probes of the catalytic performance of the systems.

3.2 Calculation Details

We perform density functional theory (DFT) based calculations using Vienna *ab initio* Simulation Package (VASP) [141]. We use projector-augmented wave (PAW) method [72,73] for the electron-ion interactions, and the optB88-vdW functional [139,140] for the electron exchange-correlation. We have also carried out calculations using the PBE functional [43]. We set the

electron kinetic energy cut-off at 500 eV for the plane-wave expansion. We use our optimized lattice constant (a=3.18 Å) for constructing an (8x8) supercell of single-layer of MoS_2 with 15Å vacuum. The coordinates of all atoms in the systems (including adsorbed NPs and molecules) are relaxed until all components of forces acting on each atom are smaller than 0.01 eV/Å. The binding energy (BE) is calculated using $BE = -\{E_{(adsorbate/substrate)} - (E_{(adsorbate)} + E_{(substrate)})\}$, where $E_{(adsorbate)}$, $E_{(substrate)}$ and $E_{(adsorbate/substrate)}$ represent the total energies of the adsorbate, the substrate, and the adsorbate-substrate system, respectively. Positive value of the binding energy indicates the stable structure. We use Bader's approach [77,78] to calculate the charge transfer. In order to calculate the activation barrier for O_2 dissociation on unsupported and MoS_2-supported NPs, we use the climbing-image nudged-elastic-band (CI-NEB) [91] method with 7 or 9 images. Our model systems of MoS_2 both in pristine and defect-laden forms, and of M_{29} (M=Cu, Ag, Au) are shown in Figure 3.1.

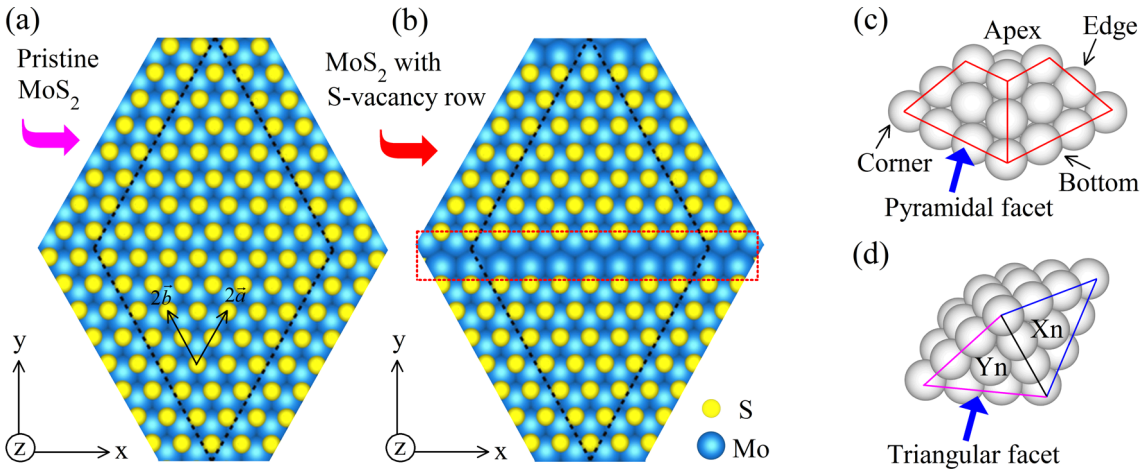

Figure 3.1 Schematic representation of model systems: single-layer MoS_2 - (a) pristine and (b) defect-laden (via a S-vacancy row); M_{29} - (c) apex and side facets and (d) triangular facets at the bottom where two facets are represented by (Xn,Yn), with n=1, 2, 3 for Cu, Ag, and Au, respectively. [T. B. Rawal, D. Le, T. S. Rahman, J. Phys. Chem. C, (2017)] (Copyright: American Chemical Society 2017).

3.3 Results and Discussion

3.3.1 Geometry and Electronic Structure of Defect-Laden MoS_2

Figure 3.2a shows the optimized structure of (1x8) supercell of defect-laden MoS_2, in which an S atom is missing from one side of the layer. The Mo atoms near the S vacancy are represented by dark blue balls, labeled as exposed Mo atoms.

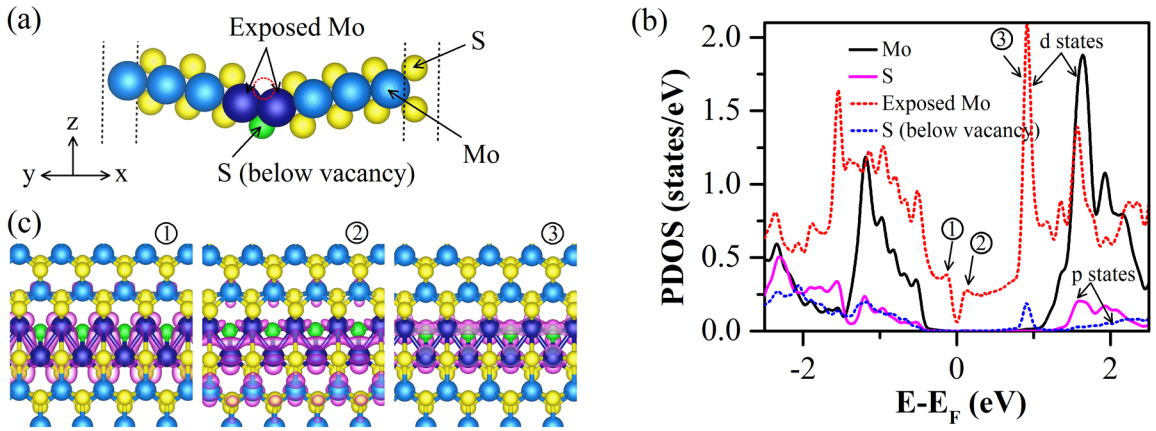

Figure 3.2 (a) Schematic representation of (1x8) unit of single-layer defect-laden MoS_2; (b) Density of states projected onto the d-orbitals and p-orbitals of selected atoms indicated by arrows in (a); and (c) Spatial distribution of orbitals corresponding to the states labeled by 1, 2, and 3 in (b), calculated at k=0. The value of iso-density is 0.005 a.u. [T. B. Rawal, D. Le, T. S. Rahman, J. Phys. Chem. C, (2017)] (Copyright: American Chemical Society 2017).

Figure 3.2b shows the density of states projected onto the d orbitals of Mo atom which is away from the vacancy (indicated by an arrow in Figure 3.2a), onto the d orbitals of exposed Mo atoms, onto the p orbitals of S atom which is away from S vacancy (indicated by an arrow in Figure 3.2a), and on the p orbitals of S atom just below the vacancy (shown by green ball in Figure 3.2a). As shown in Figure 3.2b, the midgap states are introduced inside the energy gap (~1.8 eV) of the

pristine MoS_2 by S vacancies. These midgap states are dominantly from the exposed Mo atoms. Two states appear above the Fermi level, labelled as ❷ and ❸, whereas one states appears below the Fermi level, as labelled as ❶. The calculation of partial charge density further confirms that these states are mainly derived from the exposed Mo atoms near the S vacancy. Figure 3.2(c) shows the spatial distribution of the partial density of the selected midgap states ❶, ❷ and ❸.

3.3.2 Geometric and Electronic Structure of Cu_{29}, Ag_{29} and Au_{29} on MoS_2

3.3.2.1 Adsorption of Cu_{29}, Ag_{29} and Au_{29} on Single-Layer MoS_2

Figure 3.3(a-f) show the optimized structures of Cu_{29}, Ag_{29}, and Au_{29} supported on single-layer pristine MoS_2. After ionic relaxation, these NPs retain their boat-shaped structure as in their isolated phase. NPs interact with the support through one triangular facet. On the other hand, when these NPs are supported on defect-laden MoS_2, their shapes are changed [Figure 3.3(g-l)].

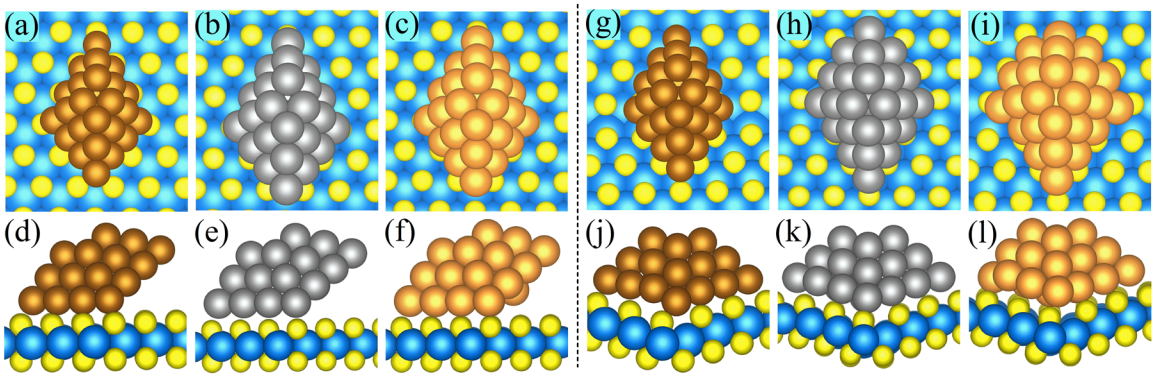

Figure 3.3 Relaxed structures of Cu_{29}, Ag_{29}, and Au_{29}, respectively, supported on (a)–(f) pristine MoS_2; (g)–(l) defect-laden MoS_2. The upper and lower panels show the top and side view, respectively. [T. B. Rawal, D. Le, T. S. Rahman, J. Phys. Chem. C, (2017)] (Copyright: American Chemical Society 2017).

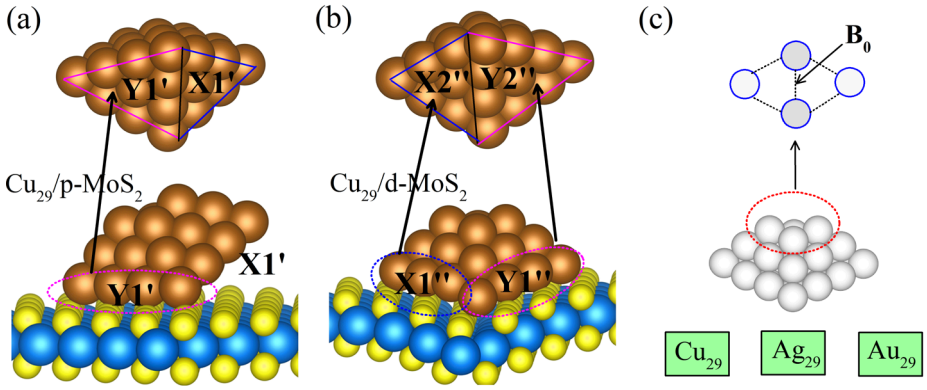

Figure 3.4 Schematic display of triangular facets of Cu_{29} nanoparticles adsorbed on: (a) pristine MoS_2 and (b) defect-laden MoS_2. The Ag_{29} and Au_{29} NPs have the identical facets as those of Cu_{29}, and adsorb on both p-MoS_2 and d-MoS_2 in the similar fashion as that of Cu_{29}; (c) Schematic representation of (M-M) bond (B_0), the values of which are tabulated in the Table 3.1 (below), at the apex of all NPs. [T. B. Rawal, D. Le, T. S. Rahman, J. Phys. Chem. C, (2017)] (Copyright: American Chemical Society 2017).

Figure 3.5 summarizes the distribution of bond length (BL) of atoms at the triangular facets, before and after the adsorption of NPs on MoS_2 supports. Clearly, p-MoS_2 and d-MoS_2 do not have the same effect on the bond lengths of Cu_{29}, partially because of the structural differences of the two MoS_2 supports: d-MoS_2 has a v-shaped surface which is more corrugated than the planar one of p-MoS_2. In Table 3.1, we present the average bond lengths of NPs atoms, expressed as the metal-metal distance (M-M) at the facets, the average metal-sulfur distance (M-S) at the interface, and the average B_0 bond between two atoms at the apex of NPs. As compared to the average bonds of atoms on the two facets of the unsupported NPs, the bonds of those of supported NPs are increased. As shown in Figure 3.5, the effect of support on the BL distribution is significantly higher in the case of Au_{29} supported by d-MoS_2. Moreover, it is evident that the p-MoS_2 has the smaller effect on relaxation of the bonds in the NPs as compared to that of d-MoS_2. The largest effect of the support is found on d-MoS_2-supported Au_{29} (10.8%), followed by that on d-MoS_2-

supported Ag_{29} (5.10 %), while the effect of either support is small on BL of atoms in Cu_{29}. Our results further show that the average B_0 is largest for d-MoS_2-supported Au_{29}, in the NPs considered here.

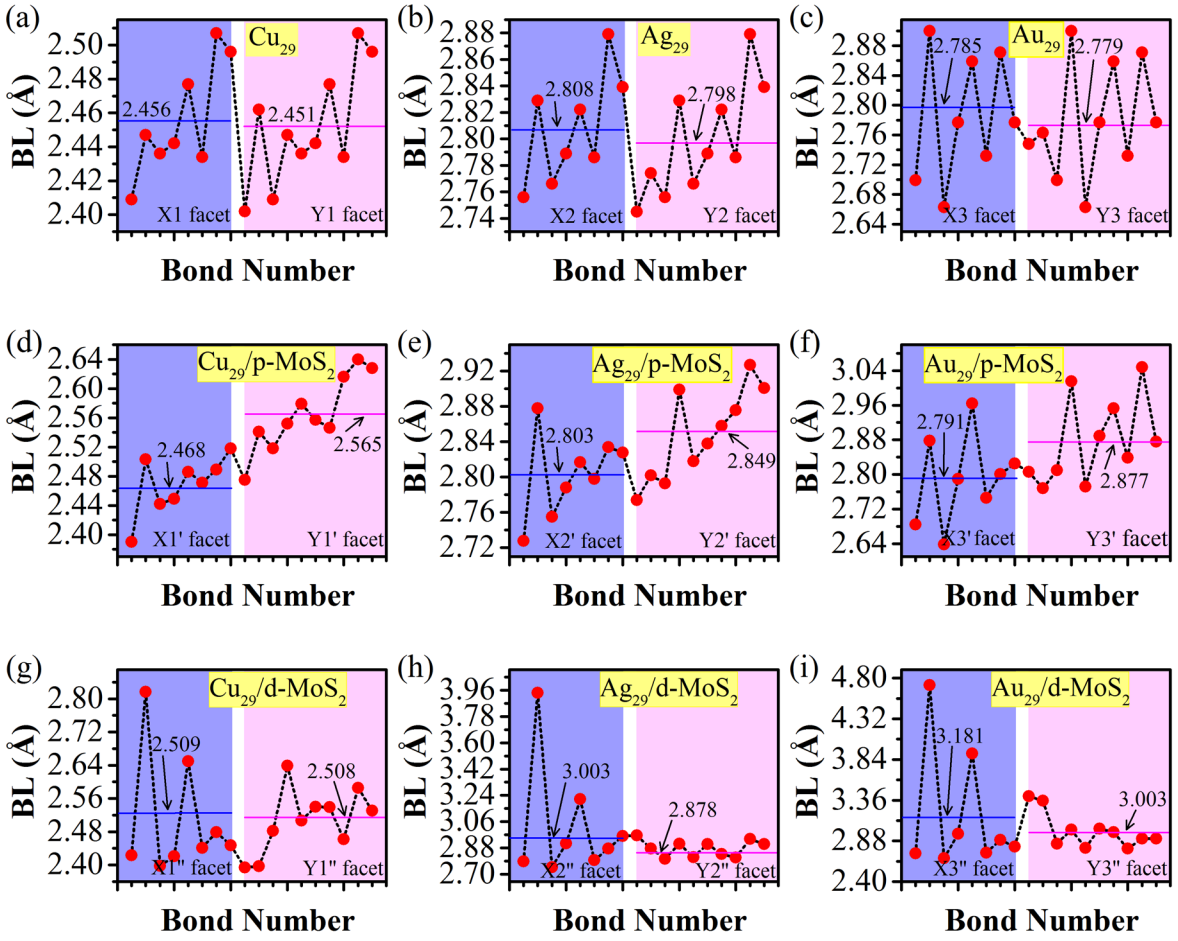

Figure 3.5 Calculated bond lengths of atoms in triangular facets of Cu_{29}, Ag_{29}, and Au_{29} nanoparticles: (a-c) unsupported; (d-f) supported by pristine MoS_2; and (g-i) supported by defect-laden MoS_2. The average bond length in each facet is noted in the figure. Note that only the unique bond lengths are plotted here (i.e., repeated bond lengths are excluded). [T. B. Rawal, D. Le, T. S. Rahman, J. Phys. Chem. C, (2017)] (Copyright: American Chemical Society 2017).

Table 3.1 Average bond lengths before and after adsorption of NPs on MoS_2. Here, both facets are triangular. The values in parenthesis represent percentage change, calculated with respect to the bond in the unsupported NPs.

Systems	**M-M (Å) at the facets**	**M-M (Å) at the interface**	**M-S (Å) at the interface**	**M-M (Å) at apex (B_0 bond)**
Cu_{29}	2.453	--	--	2.461
Cu_{29}/p-MoS_2	2.522 (2.81 %)	2.565	2.312	2.494 (1.34 %)
Cu_{29}/d-MoS_2	2.508 (2.24 %)	2.508	2.551	2.536 (3.04 %)
Ag_{29}	2.803	--	--	2.813
Ag_{29}/p-MoS_2	2.828 (0.89 %)	2.849	2.630	2.843 (1.07 %)
Ag_{29}/d-MoS_2	2.946 (5.10 %)	2.946	2.801	2.891 (2.77 %)
Au_{29}	2.782	--	--	2.834
Au_{29}/p-MoS_2	2.839 (2.05 %)	2.878	2.551	2.854 (0.70 %)
Au_{29}/d-MoS_2	3.082 (10.8%)	3.082	2.701	3.143 (10.9 %)

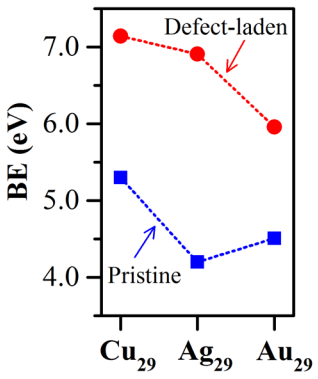

Figure 3.6 Binding energy (BE) of M_{29} on pristine MoS_2 (solid squares), and on defect-laden MoS_2 (solid circles). [T. B. Rawal, D. Le, T. S. Rahman, J. Phys. Chem. C, (2017)] (Copyright: American Chemical Society 2017).

Figure 3.6 summarizes the BEs of Cu_{29}, Ag_{29}, and Au_{29} on the p-MoS_2 and on the d-MoS_2. Comparison of the calculated BEs of Cu_{29}, Ag_{29}, and Au_{29} on pristine and defect-laden MoS_2, shows that the latter offers more binding than the former (5.30, 4.20, and 4.35 eV, respectively, to be compared to 7.14, 6.91, and 5.96 eV). These results indicate that these NPs are more stable on the d-MoS_2 than on p-MoS_2, indicating S vacancies play an important role for stabilizing these NPs. In addition, the significant difference in the BEs of NPs on the supports can be traced to the differences in the local environment (or geometry) at the interface that the NP encounters on pristine and defect-laden MoS_2 (Figures 3.4a-b). In the case of Cu_{29} supported by p-MoS_2 (Figure 3.4a), for instance, one facet containing ten Cu atoms involve in forming the interface whereas six Cu atoms on another facet are away from the interface. In contrast, in the case of Cu_{29} supported by d-MoS_2 (Figure 3.4b), both facets of Cu_{29} containing 16 atoms participate in forming the interface. The Ag_{29} and Au_{29} have the similar triangular facets as those of Cu_{29}, and their adsorption structures on pristine MoS_2 and on d-MoS_2 are qualitatively similar. Thus, in all cases, the local coordination of NPs atoms with the p-MoS_2 surface atoms are different from that with the d-MoS_2 surface atoms at the interface. The details of bond-length distribution of atoms in the triangular facets depicted in Figure 3.5, and the average M-M and Mo-S distances tabulated in Table 3.1 further elaborate the differences. There is a stronger hybridization between the NPs orbitals and Mo d orbitals of the d-MoS_2 (see Figures 3.7 and 3.8 in the case of Cu_{29} and Au_{29}, respectively, and note that we find the similar behaviors in the case of Ag_{29}), as will be discussed below. The stronger hybridization of the orbitals just below the Fermi level suggests that the exposed Mo atoms near the defect sites (refer Figure 3.2a) facilitate stronger attractive NPs-MoS_2 interaction in the defect-laden case, leading to the enhanced BE of the NPs, over those supported on p-MoS_2.

Note that it has already been suggested that the exposed Mo atoms at defect sites allow d states to participate in the formation of covalent bonds with adsorbates [13]. It is important to note that the trend in the BE of the NPs supported on pristine MoS_2 is found as Cu_{29}>Au_{29}>Ag_{29} whereas for NPs supported on d-MoS_2 it is Cu_{29}>Ag_{29}>Au_{29}.On pristine MoS_2, the BE of Au_{29} turns out to be larger than that of Ag_{29} owing to the fact that the vdW interaction for Au_{29} is larger than that for Ag_{29} (Figure 3.8b). The tendency of the metal NPs to bind at the S vacancy sites more strongly than to the basal-plane S sites of MoS_2 is analogous to the preference of the NPs to adsorb at the O vacancy sites in the metal-oxide supports [129,142,143].

3.3.2.2 Hybridization of Orbitals of NPs and MoS_2

Figure 3.7 shows the density of states projected onto the atomic orbitals of Cu_{29}/p-MoS_2 and Cu_{29}/d-MoS_2. As shown in Figure 3.7a, there is hardly any hybridization of Cu s and Cu d states with Mo d states just below the Fermi level of Cu_{29}/p-MoS_2. In contrast, there is a strong hybridization between those Cu orbitals and Mo d orbitals near the Fermi level, as shown in Figure 3.7b, in the case of d-MoS_2 due to the existence of midgap states. We found the similar trend of stronger hybridization of those orbitals in the case of Ag_{29}/d-MoS_2 and Au_{29}/d-MoS_2, as compared to that of p-MoS_2-supported systems. The density of states projected onto the Au orbitals and Mo d and s orbitals of Au_{29}/p-MoS_2 and Au_{29}/d-MoS_2.are shown in Figure 3.8. As shown in Figure 3.8b, there is there is a strong hybridization between those Au orbitals and Mo d orbitals near the Fermi level. As described just earlier, these differences in strength of hybridization play an important role for binding properties of the NPs. Our results clearly show that stronger the hybridization, the higher the binding energy of the NPs.

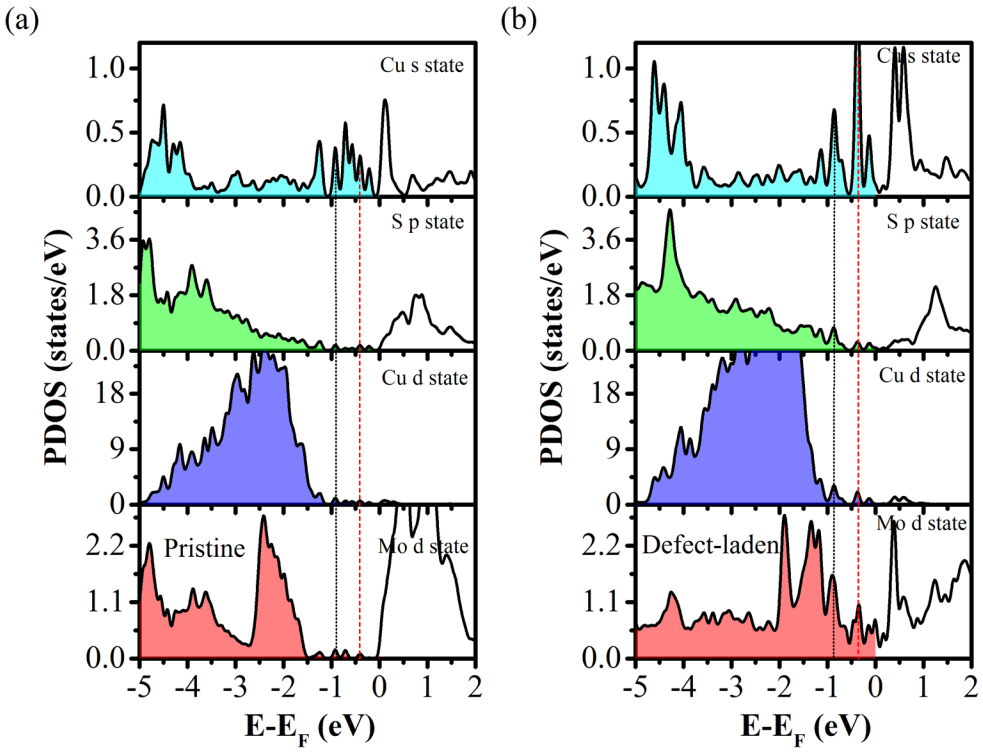

Figure 3.7 Projected density of states of Cu and S atoms at the interface formed by adsorption of Cu_{29} on: (a) pristine and (b) defect-laden MoS_2. The density of states projected onto d-orbitals of selected Mo atoms (below Cu atoms of Cu_{29}) at the defect sites of d-MoS_2, and those of p-MoS_2 are also depicted. [T. B. Rawal, D. Le, T. S. Rahman, J. Phys. Chem. C, (2017)] (Copyright: American Chemical Society 2017).

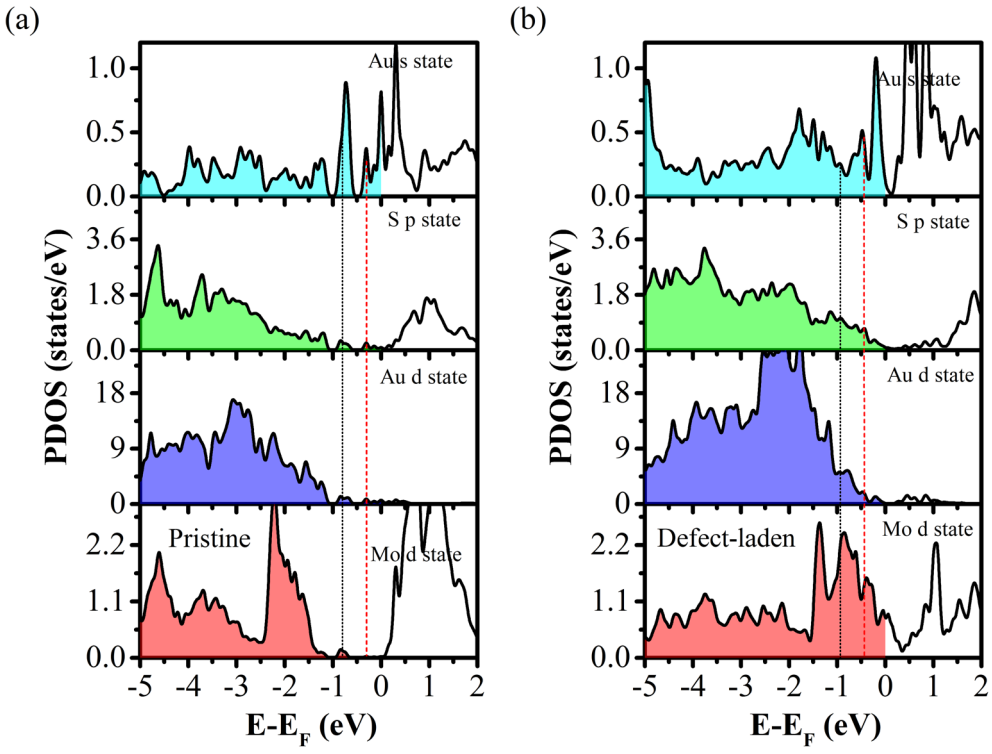

Figure 3.8 Projected density of states of Au and S atoms at the interface formed by adsorption of Au_{29} on: (a) pristine MoS_2 and (b) defect-laden MoS_2. The density of states projected onto d-orbitals of selected Mo atoms (below Au atoms of Au_{29}) at the defect sites of defect-laden MoS_2, and those of pristine MoS_2 are also depicted. [T. B. Rawal, D. Le, T. S. Rahman, J. Phys. Chem. C, (2017)] (Copyright: American Chemical Society 2017).

3.3.2.3 Assessing Interaction between NPs and MoS_2

In order to understand the nature of interaction (covalent and vdW interaction) between NPs and MoS_2, we compare the BEs of NPs on MoS_2 calculated using the PBE functional (Figure 3.9a) and optB88-vdW functional (i.e. when vdW interaction is included explicitly in our calculations. Figure 3.9b, summarizing the difference in the BE (ΔBE) of the NPs on MoS_2 as calculated using the two functionals, shows a significant increase in the binding strengths of the

NPs on MoS_2 while we include vdW interaction in our calculations. These results indicate that not only covalent but also vdW interaction are responsible for binding strengths of the NPs on MoS_2. Moreover, it is apparent from Figure 3.9b that interaction between Cu_{29} and pristine MoS_2 is dominantly covalent, but between Au_{29} and pristine MoS_2 it is dominantly vdW. Without including vdW interaction into calculations, we see from Figure 3.9a that the BE of Au_{29}, in particular, increases slightly by 0.19 eV in spite of letting NPs to interact with defect-laden MoS_2. In contrast, BE of Au_{29} on pristine MoS_2 increases significantly by 2.71 eV (even without S vacancies on MoS_2) (Figure 3.9b), when we use the optB88-vdW functional in place of the PBE functional. Overall, the trend for vdW interaction (or for covalent interaction) between NPs and p-MoS_2 can be summarized as follows: Au_{29}>Ag_{29}>Cu_{29} (or Cu_{29}>Ag_{29}>Au_{29}), suggesting that the binding characteristics of these NPs are different owing to the different magnitudes of covalent and/or vdW interaction with MoS_2.

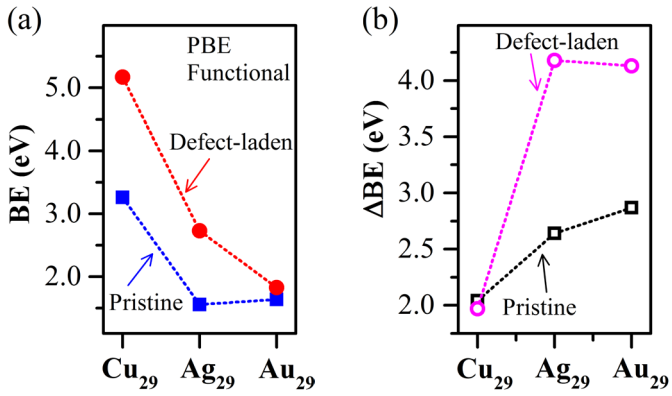

Figure 3.9 (a) Binding energy (BE) of M_{29} on pristine MoS_2 (solid squares), and on defect-laden MoS_2 (solid circles) using PBE functional; (b) the difference of binding energies (ΔBE) of NPs on pristine MoS_2 (squares), and on defect-laden MoS_2 (circles) obtained from replacing the PBE functional by the optB88-vdW. [T. B. Rawal, D. Le, T. S. Rahman, J. Phys. Chem. C, (2017)] (Copyright: American Chemical Society 2017).

3.3.2.4 Charge Transfer between NPs and MoS_2

The charge transfer between NPs and the support, as summarized in Figure 3.10, shows the expected differences for the three elements. While the charge transfer always takes place from the NP to MoS_2, there is a large difference in the magnitude. For the p-MoS_2, we find the net charge transfer from Cu_{29}, Ag_{29}, and Au_{29} to MoS_2 to be 1.18, 0.85, and 0.02e, respectively. For NPs/d-MoS_2, these increase to 2.16, 1.98, and 0.62e, respectively, indicating the presence of S vacancies leads to increase the charge transfer from NPs to MoS_2. As shown in Figure, the trend for the charge transfer from NPs to MoS_2, regardless of its form (pristine or defect-laden), is Cu_{29}>Ag_{29}>Au_{29}, with more charge transfer occurring for the defect-laden support, as is to be expected. This trend in charge transfer can be attributed to the strength of covalent interaction between NPs and the MoS_2 support. Firstly for both pristine and d-MoS_2, The larger charge transfer in the case of the d-MoS_2 support can also be traced to the presence of midgap states (Figure 3.2b-c), which are missing when the support is pristine.

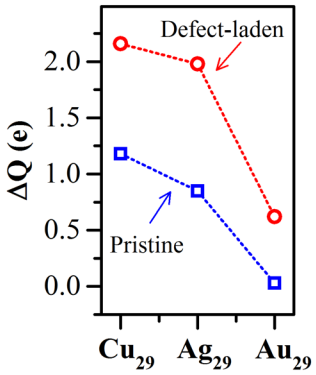

Figure 3.10 Charge transfer (ΔQ) from M_{29} to pristine MoS_2 (squares), and to defect-laden MoS_2 (circles). [T. B. Rawal, D. Le, T. S. Rahman, J. Phys. Chem. C, (2017)] (Copyright: American Chemical Society 2017).

3.3.2.5 Charge Distribution in Unsupported and Supported Nanoparticles

Figure 3.11 shows the Bader charge distributions in unsupported NPs and those supported by p-MoS_2 and d-MoS_2. These two types of supports have different effects on the charge redistribution in NPS, resulting in interesting variation in charge of atoms in different parts of the NPs. As compared to the case of unsupported NPs, atoms at the apex of the NPs receive slightly more charge when supported by MoS_2. In addition, the effect of the MoS_2 support is more pronounced for Au_{29} as compared that for Cu_{29} and Ag_{29}. Our results further reveal that the NPs atoms at the interface donate more charge to MoS_2 than those not at the interface.

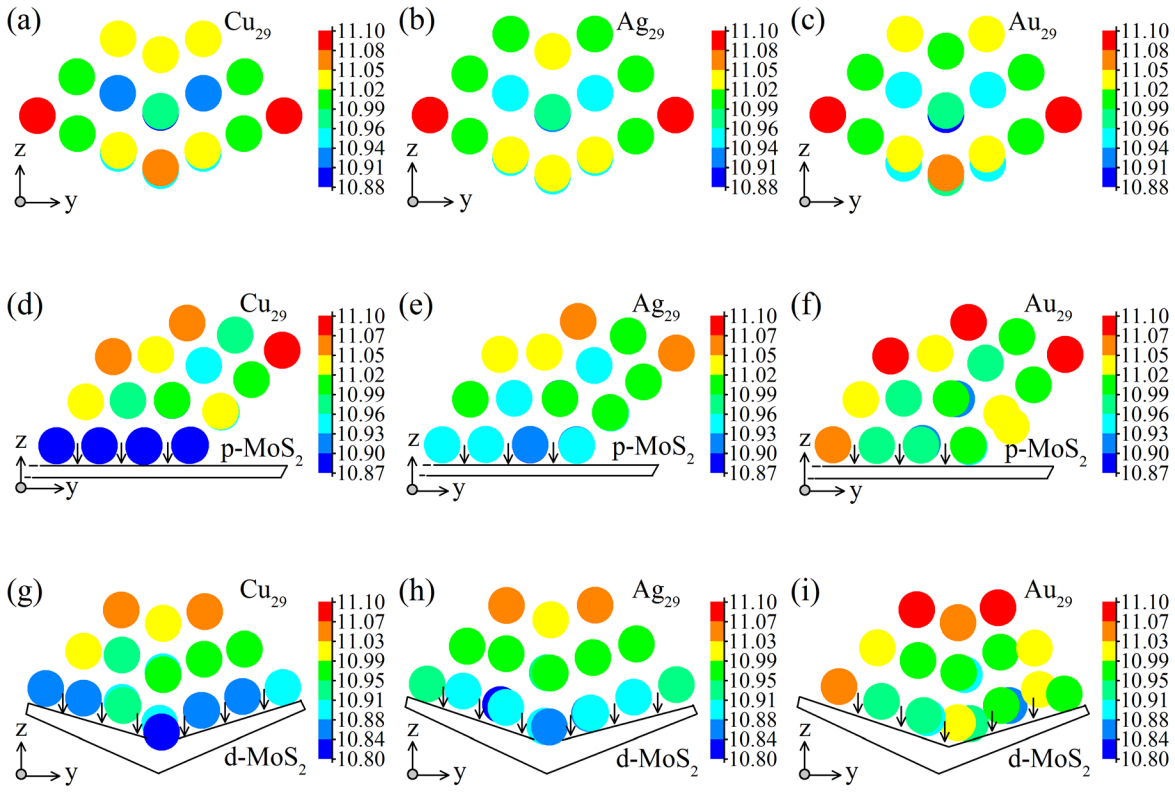

Figure 3.11 Bader charge distribution in Cu_{29}, Ag_{29}, and Au_{29}: (a-c) unsupported; (d-f) supported by p-MoS_2); and (g-i) supported by d-MoS_2 [T. B. Rawal, D. Le, T. S. Rahman, J. Phys. Chem. C, Supplement material (2017)]. (Copyright: American Chemical Society 2017).

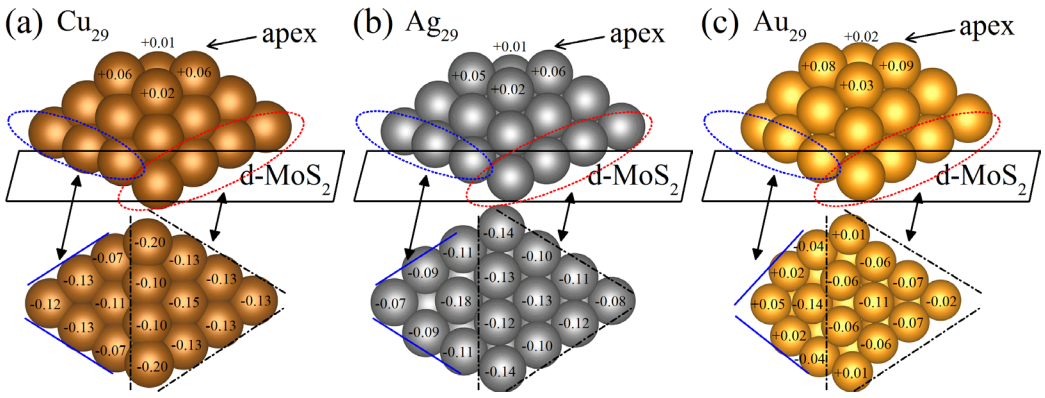

Figure 3.12 Charged states of atoms at the interface and the apex of M_{29} supported by d-MoS_2. Here, the signs (+/-) represent the charge gain or loss calculated with respect to the neutral valence charge of each atoms.

Figure 3.12 shows the charged state of atoms at the two facets and the apex of NPs after adsorption on d-MoS_2. For all NPs, the charged states of atoms on the two facets and on the apex are changed. In particular, atoms at the apex of the NPs acquire relatively more charge while supported by the supports. In addition, atoms of the facets at the interface lose more chare than the atoms which are away from the interface. This indicates that MoS_2 supports play an important role for altering the charged states of NPs. Our results further reveal that the atoms at the apex of Au_{29} accumulate relatively more charge as compared to those of Cu_{29} and Ag_{29}. In the case of p-MoS_2-supported Cu_{29}, the atoms at the facet (X1') at the interface lose more charge than those at the other facet (Y1'), which is away from the interface. But, in the case of d-MoS_2-supported Cu_{29}, the atoms on both facets (X1" and Y1") lose charges since all are in contact with the support atoms. In the case of d-MoS_2-supported Ag_{29}, atoms of the facet (X2") have the charged states in the range of -0.07e to -0.18e whereas on the facet (Y2") they are in the range -0.08e to -0.14e. On the other

hand, in the case of p-MoS_2-supported Ag_{29}, atoms on X2' have the charged states of +0.06e to -0.06e whereas on Y2' they are in the range -0.05e to -0.1e. In the case of d-MoS_2-supported Au_{29}, atoms on the facet (X3") possesses the charge states in the range +0.05e to -0.14e whereas on the atoms of the facet (Y3") they are +0.01e to -0.11e. On the other hand, in the case of p-MoS_2-supported Au_{29}, atoms on X3' possesses the charge states in the range +0.1e to 0.0e whereas on the atoms on Y3' they are +0.06e to -0.08e. These results indicate that, as compared to the p-MoS_2, the d-MoS_2 support has more effect on the charge redistribution in the NPs.

The electron withdrawal by the MoS_2 substrate are expected to affect the electronic structures of NPs, and hence their reactivity. For demonstrating the effect of the support-induced electronic structural changes on the reactivity of the NPs we present in section 3.3.3 results of our examination of adsorption and dissociation of O_2 on these model systems.

3.3.3 Adsorption and Dissociation of O_2 on MoS_2-Supported NPs

3.3.3.1 Adsorption of O_2

On the unsupported Cu_{29}, O_2 prefers to bind at the NP apex with an adsorption energy of 2.4 eV, which is about 0.4 eV more than that for the next preferred site. On supported Cu_{29}, the apex atoms are still the preferred adsorption site with an energy of 2.63 eV for pristine and 2.34 eV for d-MoS_2. Interestingly, on d-MoS_2, the there are two other sites on which O_2 can adsorb with energies of 2.31 eV and 2.26 eV. The adsorption structures of O_2 on Cu_{29} and Cu_{29}/p-MoS_2, Cu_{29}/d-MoS_2 are provided in Figures 3.13-3.15. The details of geometrical parameters and the BE of O_2 adsorbed at the various sites of Cu_{29} (unsupported and supported) are given in Table 3.2-3.5. The

adsorption site hierarchy is more or less similar on Au_{29} and Ag_{29}. To keep matters simple, we present here detailed analysis of O_2 adsorption and dissociation at the apex atoms.

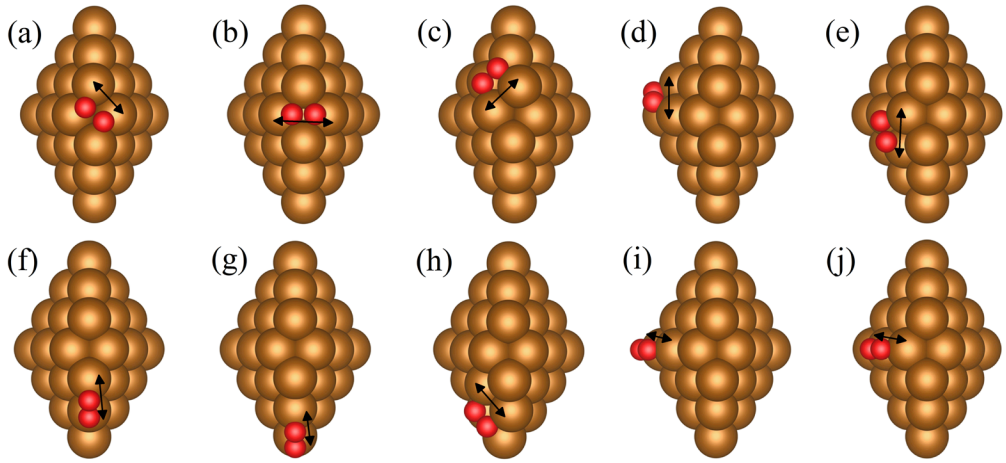

Figure 3.13 Calculated geometries of O_2 adsorbed at different sites of unsupported Cu_{29}. [T. B. Rawal, D. Le, T. S. Rahman, J. Phys. Chem. C, (2017)]. (Copyright: American Chemical Society 2017)

Table 3.2 Binding energy (BE) of O_2 adsorbed on unsupported Cu_{29}, and bond lengths. The Cu-Cu distance (as indicated by double arrow in Figure 3.13) before and after adsorption of O_2 is also depicted.

Configurations	**BE (eV)**	**O-O (Å)**	**Shortest O-Cu (Å)**	**Cu-Cu (Å) Before**	**Cu-Cu (Å) After**
Figure 3.13					
(a)	2.40	1.601	1.943	2.480	2.644
(b)	1.99	1.540	1.923	2.461	3.049
(c)	1.64	1.552	1.924	2.480	2.554
(d)	1.60	1.497	1.909	2.518	2.724
(e)	1.31	1.489	1.931	2.541	2.825
(f)	1.27	1.406	1.882	2.472	2.677
(g)	1.20	1.408	1.869	2.413	2.513
(h)	1.18	1.522	1.984	2.468	2.613
(i)	1.16	1.401	1.876	2.414	2.600
(j)	0.97	1.392	1.907	2.486	2.623

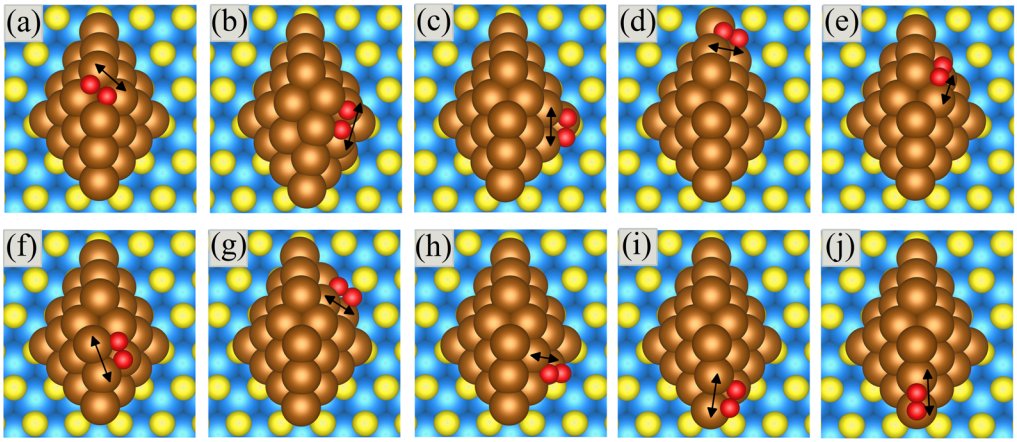

Figure 3.14 Calculated geometries of O_2 adsorbed at different sites of Cu_{29} supported by pristine MoS_2. [T. B. Rawal, D. Le, T. S. Rahman, J. Phys. Chem. C, (2017)] (Copyright: American Chemical Society 2017).

Table 3.3 Binding energy (BE) of O_2 adsorbed on Cu_{29} supported by pristine MoS_2, and bond lengths. The Cu-Cu distance (as indicated by double arrow in Figure 3.14 before and after adsorption of O_2 is also depicted.

Configurations	**BE (eV)**	**O-O (Å)**	**Shortest O-Cu (Å)**	**Cu-Cu (Å) Before**	**Cu-Cu (Å) After**
Figure 3.14					
(a)	2.63	1.577	1.939	2.477	2.599
(b)	2.29	1.556	1.940	2.516	2.545
(c)	1.84	1.525	1.895	2.475	2.643
(d)	1.72	1.550	1.905	2.447	2.585
(e)	1.68	1.511	1.937	2.479	2.637
(f)	1.58	1.528	1.930	2.483	2.525
(g)	1.43	1.470	1.919	2.485	2.667
(h)	1.39	1.477	1.882	2.502	2.703
(i)	1.32	1.467	1.850	2.457	2.785
(j)	1.31	1.407	1.963	2.457	2.588

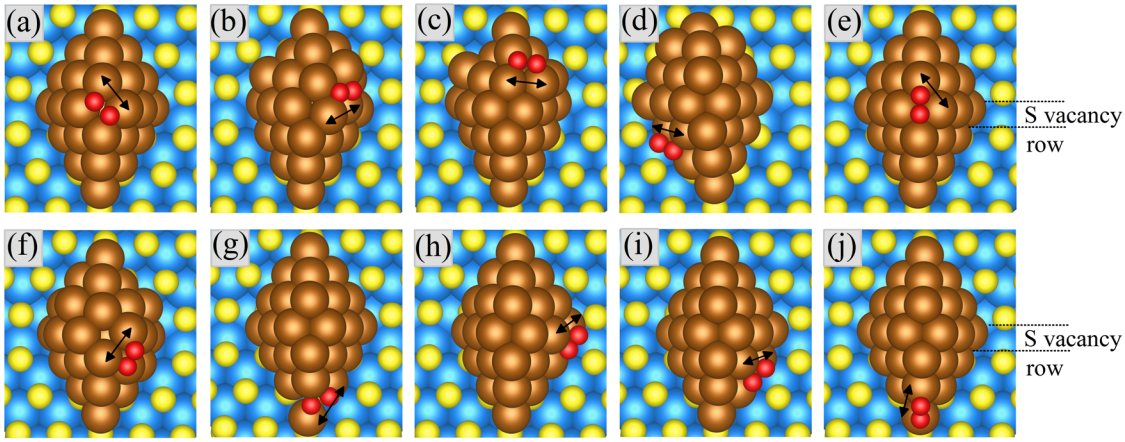

Figure 3.15 Calculated geometries of O_2 adsorbed at different sites of Cu_{29} supported by defect-laden MoS_2. [T. B. Rawal, D. Le, T. S. Rahman, J. Phys. Chem. C, (2017)] (Copyright: American Chemical Society 2017).

Table 3.4 Binding energy (BE) of O_2 adsorbed on Cu_{29} supported by defect-laden MoS_2, and bond lengths. The Cu-Cu distance (as indicated by double arrow in Figure 3.15) before and after adsorption of O_2 is also depicted.

Configurations	**BE (eV)**	**O-O (Å)**	**Shortest O-Cu (Å)**	**Cu-Cu (Å) Before**	**Cu-Cu (Å) After**
Figure 3.15					
(a)	2.34	1.569	1.956	2.557	2.612
(b)	2.31	1.551	1.921	2.521	2.720
(c)	2.26	1.500	1.883	2.409	2.589
(d)	1.99	1.474	1.922	2.530	2.593
(e)	1.87	1.571	1.870	2.528	2.659
(f)	1.75	1.482	1.862	2.528	2.812
(g)	1.61	1.549	1.828	2.550	3.263
(h)	1.51	1.493	1.835	2.635	3.244
(i)	1.09	1.521	1.918	2.479	2.778
(j)	0.95	1.404	1.849	2.550	2.905

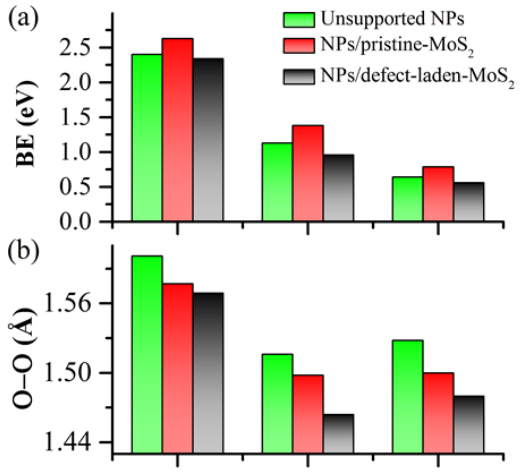

Figure 3.16 (a) Binding energy (BE) of O_2, and (b) O-O bond-length of adsorbed O_2. [T. B. Rawal, D. Le, T. S. Rahman, J. Phys. Chem. C, (2017)] (Copyright: American Chemical Society 2017).

Figure 3.16a summarizes the binding energy of O_2 on unsupported Cu_{29}, Au_{29} and Ag_{29} and those supported by p-MoS_2 and d-MoS_2. The binding energy of O_2 on Cu_{29}, Ag_{29} and Au_{29}, at the NP apex are 2.40, 1.13, and 0.64 eV, respectively. These values change slightly when these NPs are supported on MoS_2 because of the modified electronic structure of the NPs. On NPs/p-MoS_2, they increase to 2.63, 1.38, and 0.79 eV, respectively. On NPs/d-MoS_2, they slightly decrease to 2.34, 0.96, and 0.56 eV, respectively. These results indicate that the MoS_2 supports have a modest effect on the binding strength of O_2 on the NPs. In addition, we find the following trend for the BE of O_2 for all NPs: Cu_{29}>Ag_{29}>Au_{29}, regardless the type of the MoS_2 support, indicating that, among all three considered NPs, O_2 binds the most strongly on Cu_{29}.

It is interesting that when these NPs are supported on MoS_2, O_2 does not adsorb at the *interfacial sites*, but on the NP apex – a characteristic different from that on metal-oxides supports [123-129,144], which provide active interfacial sites for molecular adsorptions and reactions. It is

should also be noted that compared to the low-index surface counterparts, NPs offer enhanced O_2 binding energy.

In Figure 3.16b, we have also compared our findings for the characteristics of O-O bond length, charge transfer (to it), and dissociation barrier on unsupported and MoS_2 supported NPs. From the summary, in Figure 3.16b, of the O-O bond of an adsorbed O_2 on unsupported and MoS_2 supported NPs shows one common trend: the O-O bond is significantly elongated from that (1.232 Å) in the gas-phase. The O-O bonds on unsupported Cu_{29}, Ag_{29}, and Au_{29} are 1.601, 1.516, and 1.528 Å, respectively. When these NPs are supported on MoS_2, O-O bond decreases slightly: on pristine MoS_2, they are 1.577, 1.498, and 1.500 Å, respectively; on defect-laden MoS_2, they are 1.569, 1.464, and 1.480 Å, respectively. In addition, our results indicate that O-O bond is more elongated on Cu_{29} than when adsorbed on Ag_{29} or Au_{29}, regardless whether these NPs are supported on MoS_2 or are unsupported. The O-O bonds (>1.464 Å), depicted above, resemble to those of oxygen in peroxo-like character [145,146]. Such peroxo-like O_2 species are very active intermediates in many oxidation reactions [147,148].

3.3.3.2 Analysis of Electronic Density of States

Figure 3.17 shows the projected density of states (PDOS) onto d orbitals of the four TM atoms at the NP apex (which provides the preferred site for O_2 adsorption, as will be described below) of unsupported and MoS_2 supported Cu_{29}, Ag_{29}, and Au_{29}. The shift in the local d-states of these atoms as a result of the MoS_2 support is reflected in the Figure. Specifically, interaction of the NPs with the MoS_2 support and the charge transfer between them lead to shift of the d-states of the active sites (four apex atoms) on all NPs toward the Fermi level. Note that the shift is more

noticeable for defect-laden MoS_2 than the pristine and is correlated with the charge transfer from NPs to MoS_2, as discussed earlier. Furthermore, the shift of d-band center is largest for Au_{29} supported by d-MoS_2, about 0.62 eV, while it is 0.30 eV and of 0.37 eV, respectively, for supported Cu_{29} and Ag_{29}. It has also been reported that such energy shift towards the Fermi level leads to increase in the reactivity of the metal-oxide-supported NPs [149-151]. It will be interesting to see how the change in the electronic structure tunes the activity of NPs for O_2 dissociation, particularly that for Au_{29}.

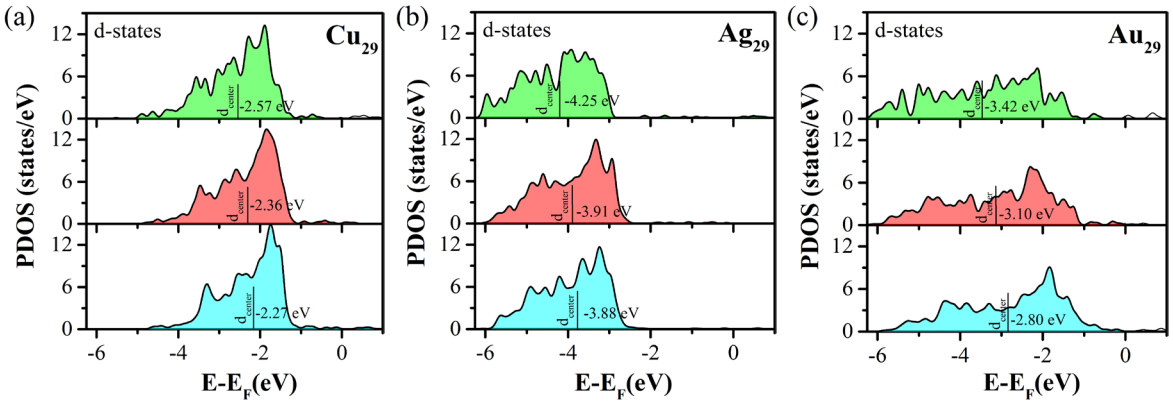

Figure 3.17 Electronic density of states projected onto d orbitals of the four TM atoms at the NP apex of (a) Cu_{29} (b) Ag_{29} and (c) Au_{29}: unsupported NP (upper panel); supported by pristine MoS_2 (middle panel) and by defect-laden MoS_2 (lower panel). Calculated d-band center of the occupied d-states is depicted in each case. [T. B. Rawal, D. Le, T. S. Rahman, J. Phys. Chem. C, (2017)] (Copyright: American Chemical Society 2017).

3.3.3.3 Charge Transfer to Adsorbed O_2

Figure 3.18 summarizes the charge transfer from Cu_{29}, Ag_{29}, and Au_{29}, both unsupported and supported, to the adsorbed O_2. It is apparent that O_2 gains relatively more charge from Cu_{29} than from Ag_{29} or Au_{29}, holding the trend Cu_{29}>Ag_{29}>Au_{29}. It decreases somewhat when the NPs

are supported on MoS_2: about 2% reduction on pristine MoS_2 and between 2.5 and 8.6% on defect-laden MoS_2. Such reduction of the charge transfer to O_2 is related to the fact that the NPs also donate charge to MoS_2. Such reductions of the charge transfer can be understood from the fact that NPs donate some charge to MoS_2.

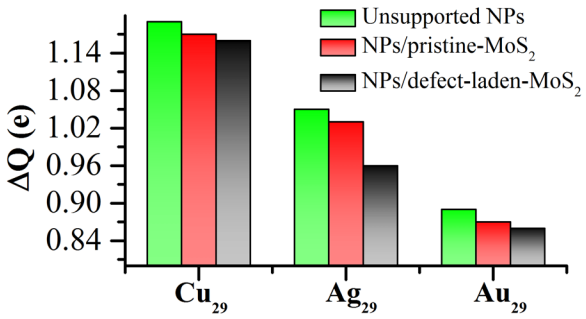

Figure 3.18 Charge transfer (ΔQ) from Cu_{29}, Ag_{29} and Au_{29} to adsorbed O_2. [T. B. Rawal, D. Le, T. S. Rahman, J. Phys. Chem. C, (2017)] (Copyright: American Chemical Society 2017).

3.3.3.4 Dissociation of O_2

Figures 3.19 and 3.20 show the minimum energy paths (MEPs) for the dissociation of O_2 on unsupported NPs, and those supported by pristine MoS_2, respectively. Clearly from these Figures, the barriers for dissociation of O_2 are lowest on Cu_{29}, attesting to the enhanced reactivity of this NP, with or without support. On unsupported Cu_{29}, Ag_{29}, and Au_{29} the energy barriers turn out to be 0.02, 0.58, and 0.25 eV, respectively. The barriers significantly increase when these NPs are supported on MoS_2: on pristine MoS_2, they are 0.09, 0.97, and 0.46 eV, respectively; on defect-laden MoS_2, they are 0.11, 1.16, and 0.50 eV, respectively. Thus, for all NPs, the MoS_2 supports significantly affect the barriers for O_2 dissociation. Activation barriers for O_2 dissociation on the supported NPs increase because of the smaller stretching of O-O bond as compared to that of

adsorbed O_2 on the unsupported NPs. In addition, we find the following trend for the barriers for O_2 dissociation on NPs: Cu_{29}<Au_{29}<Ag_{29}.

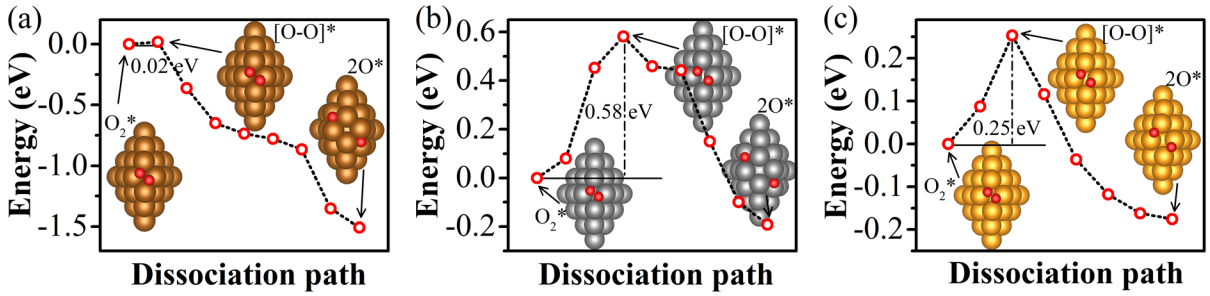

Figure 3.19 Minimum energy pathways for dissociation of O_2 on unsupported (a) Cu_{29}, (b) Ag_{29}, and (c) Au_{29}. In (a), the O-O distance in initial state, O_2*, and in transition state, [O-O]* are 1.601Å and 1.768 Å, respectively. In (b), they are 1.516 Å, and 2.112 Å, respectively. In (c), they are 1.528 Å, and 1.898 Å, respectively. [T. B. Rawal, D. Le, T. S. Rahman, J. Phys. Chem. C, (2017)] (Copyright: American Chemical Society 2017).

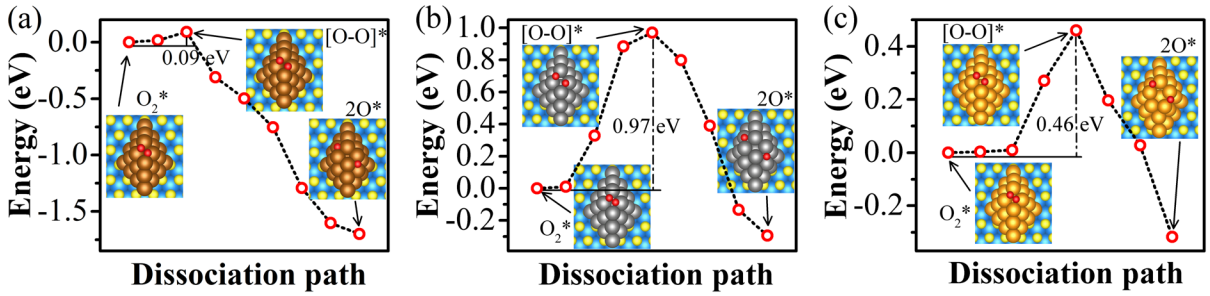

Figure 3.20 Minimum energy pathways for dissociation of O_2 pristine-MoS_2-supported (a) Cu_{29}, (b) Ag_{29}, and (c) Au_{29}. In (a), the O-O distance in initial state, O_2*, and in transition state, [O-O]* are 1.577Å and 1.931 Å, respectively. In (b), they are 1.498 Å, and 2.447 Å, respectively. In (c), they are 1.500 Å, and 2.058 Å, respectively. [T. B. Rawal, D. Le, T. S. Rahman, J. Phys. Chem. C, (2017)] (Copyright: American Chemical Society 2017).

As discussed in section 3.3.2.1, the O-O internal bond of an adsorbed O_2 on Cu_{29} is found to be longer than that on Ag_{29} and Au_{29}. The O-O internal bond of O_2 in its initial state on the NPs

holds the following trend Cu_{29}>Au_{29}>Ag_{29}, which is the exactly opposite trend (Cu_{29}<Au_{29}<Ag_{29}) for the activation barriers of O_2 dissociation on the NPs. These trends hold true for all cases – both unsupported NPs and those supported on MoS_2. These results indicate that the barriers for O_2 dissociation are directly dependent upon the O-O internal bond in adsorbed O_2, i.e. the longer (or shorter) the O-O bond, the lower (or higher) the barrier.

3.3.3.5 Catalytic Performance of NPs/MoS_2 for O_2 Activation

Figure 3.21 shows the systematic reaction paths for O_2 dissociation on the unsupported and MoS_2-supported NPs. To begin with there is no barrier for O_2 to land on these NPs, and that it is molecularly chemisorbed on them, suggesting no direct O_2 dissociation path, especially for Ag_{29} and Au_{29}, rather indirect channels which proceed from the chemisorbed state.

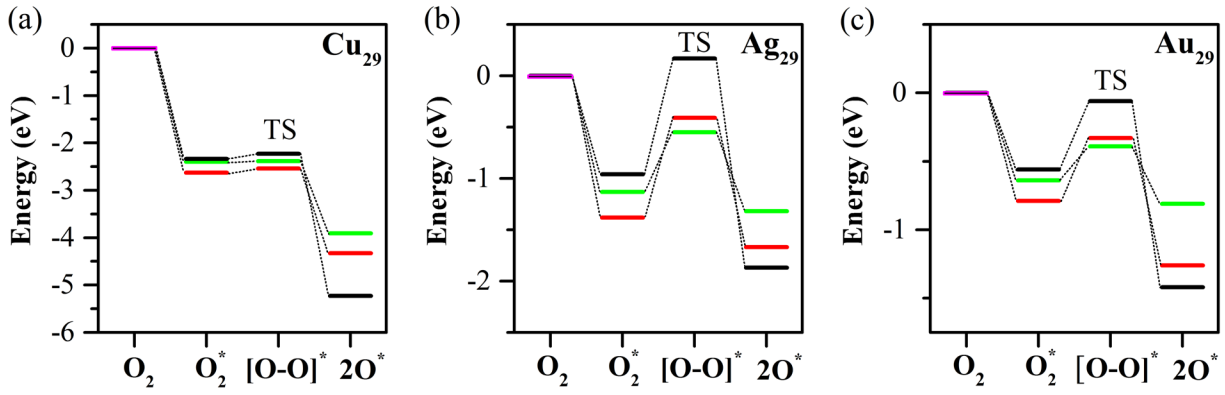

Figure 3.21 Reaction paths for O_2 dissociation on unsupported and MoS_2-supported NPs: (a) Cu_{29}, (b) Ag_{29}, and (c) Au_{29}. Energetics of the different states of O_2 on the NPs: unsupported (green bars), supported on pristine MoS_2 (red) and on defect-laden MoS_2 (black). Here (*) represents the adsorbed phases of molecular and atomic oxygen. [T. B. Rawal, D. Le, T. S. Rahman, J. Phys. Chem. C, (2017)] (Copyright: American Chemical Society 2017).

It is also evident from the Figure 3.21 that the case of Cu_{29} is very different from that of Ag_{29} and Au_{29} vis-à-vis the strong adsorption energies for both molecular and atomic oxygen. The support also does not have as much of an effect on O_2 adsorption on Cu_{29} as it does on Ag_{29} and Au_{29}. In fact, for Cu_{29} the dissociation is spontaneous. Nonetheless, it is worth mentioning that oxygen atom binds more strongly on unsupported Cu_{29}, as compared to Ag_{29} and Au_{29}, and the binding energy further increases when these NPs are supported on MoS_2, especially on defect-laden MoS_2 (Figure 10). Strong binding of atomic oxygen on Cu suggests that it would require significant energy to remove atomic oxygen from it by other molecules, e.g. CO, for further reactions. In fact the Cu NP itself would undergo oxidation, and so-oxidized particles efficiently catalyze the CO oxidation [152].

The effect of the MoS_2 support on the O_2 dissociation process is subtle, especially on Ag_{29} and Au_{29} (Figure 3.21b-c). At first glance, there is an increase in the dissociation barrier in Figure 3.21b-c. But then the overall activity is also influenced by the O-O recombination process. The support leads to substantial increase in the recombination barriers, as shown in Figures 3.21(b-c). The barriers increase to 1.26 eV and 0.93 eV from 0.77 eV and 0.42 eV, respectively, when Ag_{29} and Au_{29} are supported on pristine MoS_2. The barriers increase further to 2.07 eV and 1.36 eV when supported by defect-laden MoS_2. These results suggest that O-O recombination rate for MoS_2-supported NPs will be higher than that for unsupported NPs. This conclusion is especially noticeable for defect-laden-MoS_2-supported Au_{29} on which the recombination barrier of 1.36 eV to be compared to the dissociation barrier of 0.5 eV, suggesting that defect-laden MoS_2 may improve the catalytic activity of Au_{29} towards oxidation.

3.4 Summary

Employing *ab initio* density functional theory with the inclusion of van der Waals (optB88-vdW) functional, we have studied the geometry, electronic structure, and the propensity for O_2 adsorption and dissociation on Cu_{29}, Ag_{29}, and Au_{29} supported by single-layer MoS_2 – pristine and defect-laden. As compared to the pristine, the defect-laden MoS_2 has relatively larger effect on the above properties of these NPs as depicted below:

(i) TM NPs bind more strongly on defect-laden than on pristine MoS_2 – in the order of Cu_{29}>Ag_{29}>Au_{29} for defect-laden and of Cu_{29}>Au_{29}>Ag_{29} for pristine. Strong electronic interaction between NPs and defect-laden MoS_2 is facilitated by mid-gap states introduced by S vacancies, which also transform the planar MoS_2 structure into the corrugated one with v-shaped structure that nicely couples with the boat-shaped NP via two triangular facets. These results suggest that S vacancies not only serve as the anchoring sites for NPs to cluster but also play a role in stabilizing the NPs on MoS_2. Defect-laden MoS_2 is, therefore, a good support material for dispersing the NPs.

(ii) Both pristine and defect-laden MoS_2 help shift the d-band center of the NPs further towards the Fermi level. This effect is most noticeable for defect-laden-MoS_2-supported Au_{29}, followed by Ag_{29}. In addition, more charge transfer takes place from NPs to the defect-laden than to pristine MoS_2 with the trend as Cu_{29}>Ag_{29}>Au_{29}.

(iii) Defect-laden MoS_2 is responsible for increasing the number of active sites at which O_2 adsorb with similar binding energy (<0.1 eV difference). We find that there is no barrier for O_2 to adsorb on top of an atom at the NP apex, where the frontier orbitals are localized, and that the dissociation channel proceeds through a chemisorbed state. In addition, the significant increase in the barriers

for O-O recombination, as compared to those for O_2 dissociation, on the defect-laden-MoS_2-supported NPs, the latter process is favored. Thus, the MoS_2 support plays an important role for optimizing the O_2 dissociation activity on the NPs, in particular for Au_{29}.

Our DFT-based results thus provide a general strategy for controlling the atomic and the electronic structure of the TM NPs using the MoS_2 support, thereby tuning the reactivity of the NPs, and for designing novel functional NPs-MoS_2 catalysts for specific reactions. Our studies open the door for scrutinizing the detailed mechanism for O-O bond scission and other relevant reactions in the complex local environment of MoS_2-supported NPs, taking into account the local coordination, local electronic structure, charge transfer, and competing reaction pathways. While reliable predictions about reaction rates can only be made after a multitude of factors, importantly, reaction kinetics, are taken into account, our finding here of MoS_2-induced enhancement of adsorption (reaction) sites for O_2 on the nanoparticles is indicative of enhanced oxidation reactions when nanoparticles are supported on MoS_2.

CHAPTER 4 MoS_2-SUPPORTED GOLD NANOPARTICLE FOR CO HYDROGENATION

Employing dispersion-corrected density functional theory, we examine the geometry, electronic structure, and reactivity of 13-atom Au nanoparticle supported on defect-laden single-layer MoS_2. The planar structure of Au_{13} favored in isolated phase, transforms into the three-dimensional structure when supported on MoS_2. We find that charge is transferred from MoS_2 to Au_{13}, and that the electron density is also distributed away from the Au_{13}/MoS_2 interfacial region – making Au sites away from the interface catalytically active. Owing to effect of the support, the Au d states become narrower, and the frontier states appear close to the Fermi level. Consequently, in contrast to the reactivity of Au_{13}/TiO_2 toward methanol decomposition, Au_{13}/MoS_2 offers excellent activity toward methanol synthesis, as demonstrated here, *via* CO hydrogenation.

4.1 Introduction

Gold (Au) nanoparticles (NPs) have received considerable attention in the field of heterogeneous catalysis since the pioneering work by Haruta and co-workers [153,154]. Quite differently from the bulk counterpart (chemically inert), Au NPs exhibit a catalytic activity for several chemical reactions. Au NPs (<10 nm), for instance, efficiently catalyze CO oxidation at low-temperature [97,155]. However, the catalytic activity of the Au NPs is also affected by several factors: size of NPs [156-158] (~0.5-5nm), low-coordinated Au sites [26,159-161], charge transfer to or from the support [131,142,162-164] thereby making Au either electron-rich (cationic) or electron-deficient (anionic), Au-support interaction [165,166] (the presence of defects, via anion vacancies in the support may induce strong interaction), modification of the electronic structure of Au NPs by the

support [167,168], and the quantum-size effect [169]. Each of these factors influence the catalytic activity of the Au NPs in a dramatic manner.

Traditionally metal *oxides* have been widely employed as the support for dispersing Au NPs in heterogeneous catalysis. These oxide-supported Au catalysts have shown excellent activity in many chemical reactions: in propylene epoxidation [170,171], in hydrogenation of unsaturated hydrocarbons [172,173], of ketones [174], of aldehydes [175,176], of syngas [177,178], and in water gas shift [133,179] reactions. The experimental studies of these catalysts can evaluate the different degrees of activity for the reactions they foster, however cannot elucidate the mechanistic details of the origin of the activity. Theoretical calculations based on DFT, for example, can provide this kind of insight. Often such studies agree that the catalytic sites offered by oxide-supported Au catalysts are the interface between them. For example, at low temperature it is the interface that provides highly active sites for CO oxidation on MgO [128], on Fe_2O_3 [180], on CeO_2,[129,181] and on TiO_2 [124,182-185]. Similarly, the decomposition of methanol intermediates (CH_3O, CH_2O) is highly activated at the Au-TiO_2 interface [142].

Experimental and theoretical studies have now extended from metal-oxides to transition metal-dichalcogennides. Two-dimensional (2D) molybdenum disulfide (MoS_2), as emerging material, has become a special subject of interest for researchers in the field of heterogeneous catalysis. The 2D nature of MoS_2 makes it particularly attractive as a support material for decorating metal nanoparticles [119,120,186,187], and exploiting them for catalytic applications. Recently, several groups have synthesized Au-MoS_2 composite using various experimental techniques [120,186,188-190]. Experiments have also shown that stand-alone MoS_2 catalyzes hydrogen evolution reaction (HER) [191,192] and hydrodesulphurization [193], and that the Au-

MoS_2 composite shows enhanced activity for Plasmon-enhanced photocatalytic water splitting [120] and for the electrocatalytic HER [106,191,192]. Meanwhile, theoretical study has demonstrated the catalytic activity of MoS_2 by itself for methanol synthesis from syngas [13]. It now made reasonable to theoretically explore the reactivity of Au-MoS_2 composite toward the methanol synthesis – the more so because the nature of the active sites as well as the energetics of the reactions on Au-MoS_2 catalysts are still open questions.

To address these questions, we choose single layer MoS_2 with single S vacancy as the support material. We introduced an S vacancy to immobilize the NP, since prior studies [187,188] have shown that Au NPs tend to nucleate at defect sites on MoS_2. The other studies [187,194-196] have shown that an S vacancy produces midgap states that strongly hybridize with Au states, thus binding the NP to the surface. In this study, we have chosen as our NP 13-atom Au, (~0.55 nm in diameter) in order to compare the reactivity of Au_{13}/MoS_2 with that of Au_{13}/TiO_2 [142]. Unexpectedly, Au_{13}/MoS_2 – far from alternatively catalyzing methanol decomposition into CO and H_2 – turns out to catalyze hydrogenation of CO into methanol, i.e., to *synthesize* methanol from syn gas (CO and H_2, the products of full methanol decomposition which was observed in experiments [196,197]).

Herein, we provide fundamental insights into the geometrical and electronic structures, and the reactivity of Au_{13}/MoS_2 towards the methanol synthesis from syngas ($CO+H_2$) by carrying out dispersion-corrected density functional theory (DFT-D3) calculations. We show that a defect-laden MoS_2 not only acts as a support to provide a platform for dispersing Au particles over a large surface area but also serves as an electron donor, thereby modifying the electronic structures of Au_{13}. We propose a mechanism for methanol synthesis via CO hydrogenation that takes place at

the active Au sites (away from interface) and does not directly involve the Au_{13}/MoS_2 interface, in contrast to the generally accepted mechanism [128,129,142,198] for reactions activated by oxide-supported Au catalysts, in which the interfacial region serves as the active site and the support itself is involved directly in activating reactant molecules.

4.2 Calculation Methods

We carry out periodic density functional theory (DFT) calculations using the Vienna *Ab initio* Simulation Package (VASP) [141]. These calculations are based on the plane-wave basis set and the pseudopotential method. We use the generalized-gradient approximation in the form of the PBE functional [43] to take into account the electron-electron interaction. To account for weak van der Waals interactions, we utilize the semi-local DFT-D3 method of Grimme [65]. For the treatment of interaction between electrons and nuclei, we use the approach of projector-augmented waves of Bloch [72] in the implementation of Kresse and Joubert [73]. For the truncation of plane-waves expansion, we use cutoff of 500 eV. For relaxation of atoms, we used the one k-point in performing integration over the Brillouin zone. We relax all atoms in the systems using the standard minimization algorithm [88] until the residual forces on each atoms reach below 0.01 eV/Å and the total energy converges below 10^{-5} eV. For calculating the electronic density of states, we use dense k-mesh (5x5x1).

We constructed a periodic (6x6) system of single layer MoS_2 using an optimized lattice constant of 3.16 Å, and setting a vacuum of ~25 Å. To mimic the defect-laden MoS_2 surface (with 1.5 % defects), we remove one S atom from one side of (6x6) MoS_2. Our model system for the defect-laden single layer MoS_2 is shown in Figure 4.1. We then relax the structure of defect-laden

MoS_2, and use the optimized structure for the subsequent calculations for adsorption of Au_{13} of different shapes. We have also carried out finite-temperature *ab-initio* molecular dynamics (MD) simulations for selected Au_{13}/MoS_2 structures. The atomic motion is described by using the Nose-Hoover thermostat dynamics [199,200] for a canonical ensemble. The time step of 1fs is used for integrating the equations of motion.

We use the lowest-energy structure of Au_{13}/MoS_2 for the relaxations of the various geometries of initial states (IS) and final states (FS) involved in methanol synthesis reactions. The adsorption energy (E_{ads}) is calculated using $E_{ads} = E_{(adsorbate/slab)} - \{E_{(adsorbate)} + E_{(slab)}\}$, where $E_{(adsorbate/slab)}$, $E_{(adsorbate)}$ and $E_{(slab)}$ represent the total energies of adsorbates/slab system, adsorbates, and slab, respectively. Here, the slab represents either defect-laden MoS_2 or Au_{13}/MoS_2 composite system. To estimate the charge transfer, we use the Bader's method [77] as numerically implemented by Henklemann's group [78].

For the understanding of the charge distribution after adsorption of Au_{13} on defect-laden MoS_2, we calculate the charge density difference by subtracting the sum of densities of two individual systems: Au_{13} and MoS_2 from the density of Au_{13}/MoS_2. The electron density difference ($\Delta\rho$) is calculated using the following relation: $\Delta\rho = \rho_{(Au13/MoS2)} - \rho_{(Au13)} - \rho_{(MoS2)}$, where $\rho_{(Au_{13}/MoS_2)}$, $\rho_{Au_{13}}$, and $\rho_{(MoS_2)}$ are, respectively, the electron densities of Au_{13}/MoS_2, Au_{13}, and MoS_2. The electron densities of the latter two systems – Au_{13} and MoS_2 – are calculated by utilizing the same positions of atoms as those in Au_{13}/MoS_2. The iso-density of 0.0015 a.u. is used to depict accumulation and depletion of the electron density.

We calculate the activation barriers for the elementary reactions involved in methanol synthesis reaction via CO hydrogenation using the climbing-image nudged elastic band (CI-NEB) method [91] with 5, 7 or 9 images (depending upon the physical distance between the initial and final states) including both initial and final states. We calculate the vibrational frequencies of all modes of the system consisting of reactants/intermediates and the supported Au_{13} (the MoS_2 support atoms are frozen) at the saddle point for each reaction path, using the finite difference method as implemented in the VASP code. We identify the transition state for each reaction path as the saddle point at which the frequency of one vibrational mode is imaginary.

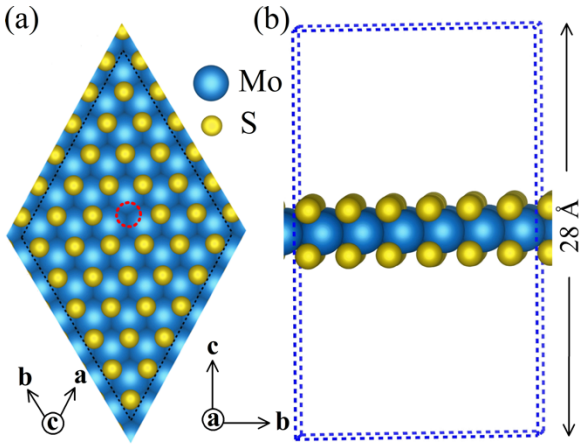

Figure 4.1 A model system of defect-laden single layer MoS_2: (a) top, and (b) side views. Single S vacancy is indicated by a dotted circle.

4.3 Results and Discussion

4.3.1 Geometry of Au_{13} Nanoparticle

In Figure 4.2, we summarize the relative energies of five different geometries of Au_{13} NPs – planar (type I and II), cuboctahedron, decahedron, and icosahedron – which have also been

studied by several groups [201-204]. Our DFT-D3 calculations indicate that the high-symmetry 3D structures are not favored since all 3D structures have the higher energies than the planar (type I) structure, in agreement with previous theoretical calculations [202,205]. As follows from Figure 4.2, there is a slight difference in the total energies of planar (type II) and planar (type I) configurations by 50 meV. The latter structure is also lower in energy than that of high-symmetry cuboctahedron, decahedron, and icosahedron by 1.09, 1.86, and 2.59 eV, respectively. These results indicate that low-symmetry planar (type I) structure is the most favorable in the isolated phase.

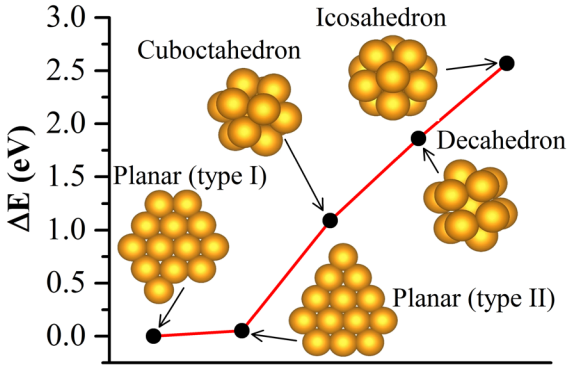

Figure 4.2 The relative energy of unsupported Au_{13} nanoparticles. Here, ΔE represents the difference in energy of all Au_{13} with respect to the energy of the lowest-energy planar (type I) configuration.

4.3.2 Au_{13} on Defect-Laden MoS_2

To determine the stable structure of Au_{13} on defect-laden MoS_2, we calculate the energy for different geometries of Au_{13} (Figure 4.2) on MoS_2. Our DFT-optimized geometries are displayed in Figure 4.3. Their relative energies with respect to the energy of the lowest-energy structure (Figure 4.3a) are also summarized. As similar to the cases of Au_{13}/CeO_2 [129] and of

Au_{13}/TiO_2 [142], Au_{13} preferentially binds to the defect (S-vacancy) site on MoS_2. As depicted in Figure 4.3, the planar (type I) Au_{13} structure (favored structure in isolated phase) is not favorable when supported. The total energy of planar (type I) Au_{13} (which is the lowest-energy structure in isolated phase, see Figure 4.2) is higher in energy by 0.93 eV than 3D distorted structure. Similarly, other high-symmetry structures: cuboctahedron, icosahedron, and decahedron as well as 2D planar (type II) of Au_{13} are also found to be higher in energy than the 3D distorted structure. These results indicate that the favorable planar (type I) structure of Au_{13} in isolated phase transforms into the 3D distorted structure when supported on MoS_2 – as qualitatively similar to what happens in the cases of Au_{13}/CeO_2 [129] and Au_{13}/TiO_2 [142]. In addition, we find that all 3D configurations of Au_{13} adsorb at the S vacancy site on MoS_2, indicating that S vacancy acts as the adsorption center. The adsorption energy of Au_{13} on defect-laden MoS_2 (c.f. Figure 4.3a for geometry) is -6.77 eV whereas for other configurations (c.f. Figures 4.3(b, c, and f)) they are -5.84 eV, -5.80 eV and -5.14 eV, respectively. Therefore, among the 3D configurations of adsorbed Au_{13}, it is the one depicted in Figure 4.3a that the Au atom at the defect site most strongly interacts with the nearest-neighbor exposed Mo atoms via covalent interaction, which comes into play to stabilize the NP on defect-laden MoS_2. The 3D distorted structure (Figure 4.3a) is thus the most stable one among all 3D configurations as well as 2D configurations. In this configuration, seven Au atoms are in direct contact with the MoS_2 support. In the case of other 3D configurations, shown in Figures 4.3b and 4.3(c, f), five and six Au atoms are in direct contact with MoS_2, respectively. Importantly, our results suggest that it could be the unbalanced s-d hybridization, in planar Au_{13} when electronically interact with defect-laden MoS_2 that can provide the driving force for the structural evolution of Au_{13} from planar to the 3D structure.

In order to gain insight into the structural evolution of a planar structure (type I) of Au_{13} (see Figure 4.2) on defect-laden MoS_2 and the finite-temperature stability of the 3D distorted structure on defect-laden MoS_2, we performed *ab initio* MD simulations for which average temperatures were considered in the range 315 K-625 K. Firstly, we find that the planar structure evolves to the non-planar (3D) structure within 9 picoseconds. The so-developed 3D structure ultimately binds at the S vacancy site, indicating that Au nanoparticles prefer to nucleate at the defect sites – in agreement with our prior study [187] on Au_{29} on MoS_2 and the experimental observation [206]. Secondly, we find that the 3D distorted structure, energetically the most favorable, maintains its shape up to ~385 K, indicating that this structure is stable even above a room temperature.

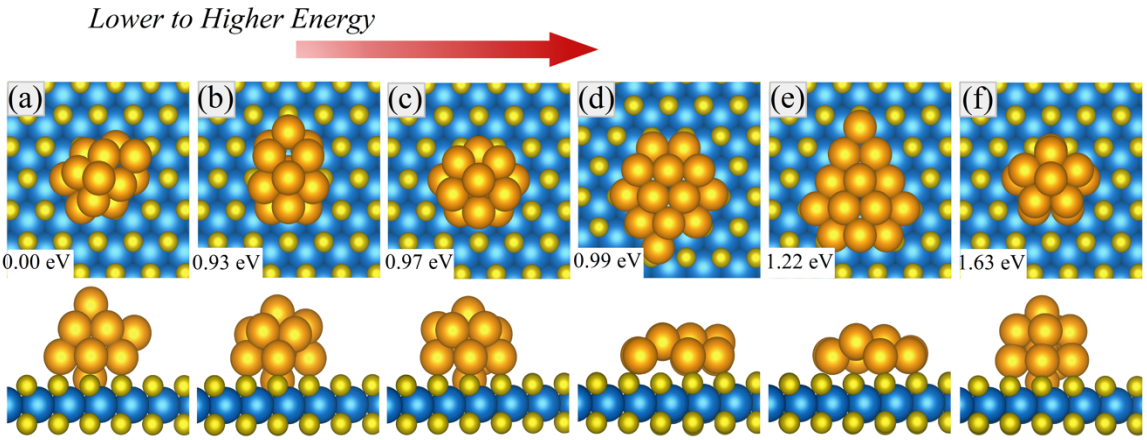

Figure 4.3 The DFT-optimized configurations of Au_{13} nanoparticles on defect-laden MoS_2: (a) 3D distorted, (b) cuboctahedron, (c) icosahedron, (d) planar (type I), (e) planar (type II), and (f) decahedron. Here, the displayed numbers represent the difference (ΔE) in energy of each supported Au_{13} configuration with respect to the energy of the lowest energy configuration shown in (a).The top and bottom panels, respectively, show the top and side views. The blue, yellow and golden balls represent the Mo, S and Au atoms respectively. Hereinafter, we use the same color representation for the atoms.

Herein, we use the lowest-energy structure of Au_{13} supported on defect-laden MoS_2 for calculating the electronic structure and the energetic involved in methanol synthesis reaction via CO hydrogenation.

4.3.3 Electronic Structure of Au_{13} on Defect-Laden MoS_2

Figure 4.4a shows the isosurface plot of $\Delta\rho$ between Au_{13}/MoS_2 and the non-interacting fragments, providing a qualitative insight into the nature of the Au_{13}–MoS_2 interaction. As shown in Figure 4.4a, some part of the electron density accumulates in the chemical bonding region of Au_{13}/MoS_2, which essentially indicates that there is covalent interaction between Au_{13} and MoS_2. The density accumulation is pronounced in the interaction region, in particular, in the bonding region of the Au atom and the exposed Mo atoms near the S vacancy. However, we note that electron accumulation is also found all over the nanoparticle, including around Au atoms away from the bonding region of Au_{13}/MoS_2 system. Some density depletion zone is visible in the bonding region of Mo and S atoms in MoS_2. These results indicate that some charge is transferred from MoS_2 to Au_{13}. Below we present further analysis of the charge transfer in the system.

Figure 4.4b shows the quantified charge distribution in Au_{13} after its adsorption on MoS_2. Overall, the Au_{13} receives a net charge of 0.3e from MoS_2 (it is also p-type doping of MoS_2), acquiring electron-rich features. Note that the direction of the charge transfer depends on the vacancy concentration as found in the Au_{13}/TiO_2 system [142] in which charge transfer takes place from TiO_2 to Au_{13} when there is 30% concentration of O vacancies and from Au_{13} to TiO_2 when the vacancy concentration decreases to 10%.

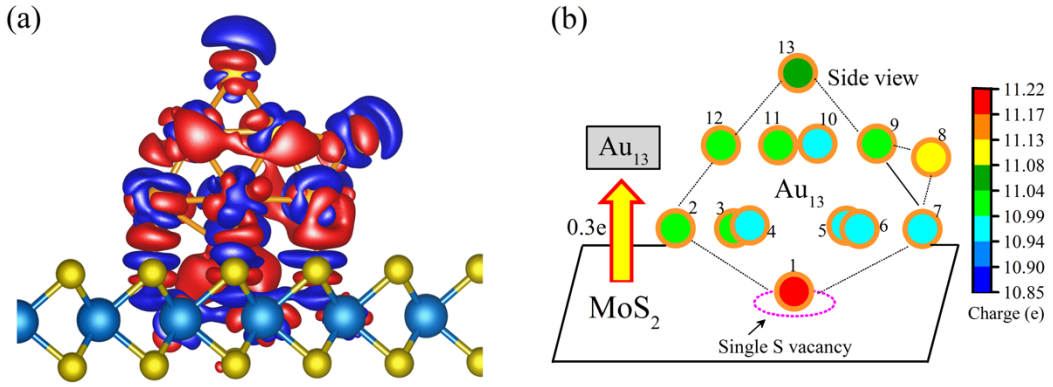

Figure 4.4 (a) Electron density difference ($\Delta\rho$) upon adsorption of Au_{13} on defect-laden MoS_2. Red and blue isosurfaces indicate charge accumulation and depletion regions, respectively. The isodensity used for the plot is as 0.0015 a.u.; (b) Bader charge on individual Au atoms of the adsorbed Au_{13} on MoS_2 according to the provided color scale. The Au atoms are numbered for convenience in the discussion in the text.

Figure 4.5a shows the density of states projected onto the s and d orbitals of an adsorbed Au_{13}. The hybridized state formed by overlapping of s and d orbitals is aligned just below the Fermi energy. As shown in Figure 4.5b, this hybridized state, the so-called the frontier state, is spatially distributed around Au atoms #2, #3, #6, #7, and #8-12 (as labeled in Figure 4.4b). As we shall see, this state participates in chemical bonding with adsorbates. The total density of states of the Au_{13}/MoS_2 (see Figure 4.6) exhibits no energy gap, indicating that the Au_{13}/MoS_2 shows metallic behavior. Owing to the support effect, the Au d states become narrower but smoothen (Figure 4.6). In addition, the availability of electronic states near the Fermi energy, attributing to the Au hybridized states, could make Au sites catalytically active for methanol synthesis. Thus, the electronic interaction between Au and MoS_2 support alters the electronic structure of Au_{13}, as shown in Figure 4.6, in a way that may be expected to promote the catalytic activity. We next proceed to examination of the adsorption characteristics of some molecules of interest on the Au_{13}/MoS_2 model system.

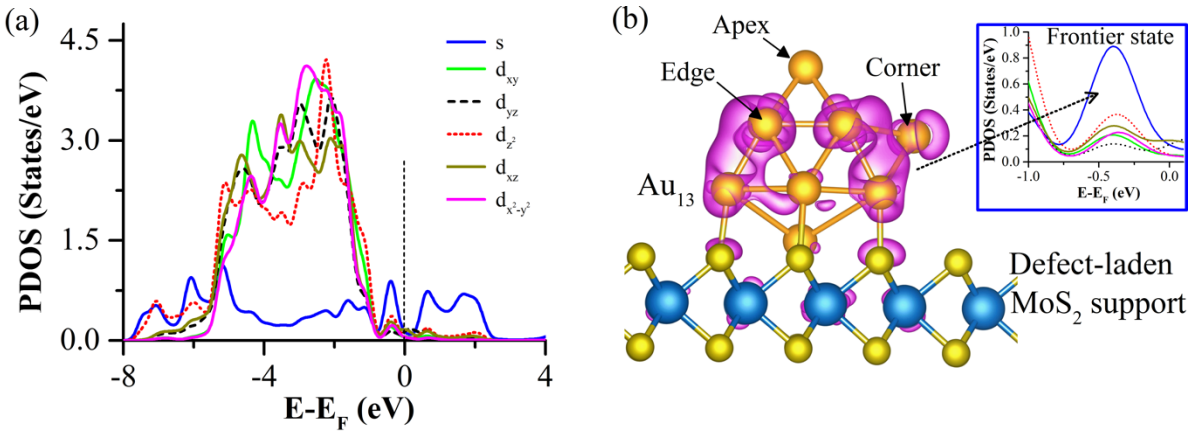

Figure 4.5 (a) Electron density of states projected onto the s and d orbitals of the adsorbed Au_{13} on defect-laden MoS_2. (Vertical line at 0 eV represents the Fermi level); (b) Spatial distribution of the frontier state located just below the Fermi-level (inset) of Au_{13}/MoS_2. The apex, corner and edge sites of the adsorbed Au_{13} are also shown in (b).

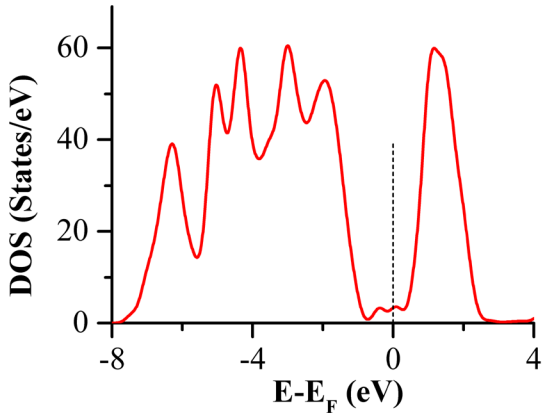

Figure 4.6 Total density of states of Au_{13}/MoS_2 system. The vertical line at 0 eV represents the Fermi level.

4.3.4 Adsorption and Dissociation of H_2

Figure 4.7 shows the optimized configurations of molecular hydrogen (H_2) adsorbed on Au_{13} supported on defect-laden MoS_2. H_2 molecularly adsorbs at the Au site (Figure 4.7a) with an adsorption energy of -0.11 eV. The molecular axis of adsorbed H_2 is parallel to the Au atom. At

the same site, H_2 can adsorb in vertical orientation as shown in Figure 4.6d. But, in this configuration the adsorption energy is slightly higher by 0.05 eV. In the former adsorbed H_2, (Figure 4.7a), the H-H distance is 0.807 Å, which is 0.057 Å longer than the bond length (0.750 Å) in the gas phase. The average Au-H distance is 1.937 Å. In the latter adsorbed H_2 (Figure 4.7d), the H-H distance is 0.764 Å, and the Au-H distance is 2.276 Å. Similarly, in other considered configurations (Figure 4.7(b,c,e)), the adsorption of H_2 at other Au sites is relatively weaker. The adsorption energy and geometrical parameters of all considered configurations are provided in Table 4.1. Overall, our results suggest that the most active site for H_2 activation on Au_{13}/MoS_2 is at the corner atom, followed by other Au atoms that are negatively charged, but not at those Au atoms (positively charged) that are in contact with the support. Note that the latter Au atoms (in contact with MoS_2), labeled as #4-7 in Figure 4.4b, have charged states of +0.03e, +0.03e, +0.05e, and +0.05e, respectively.

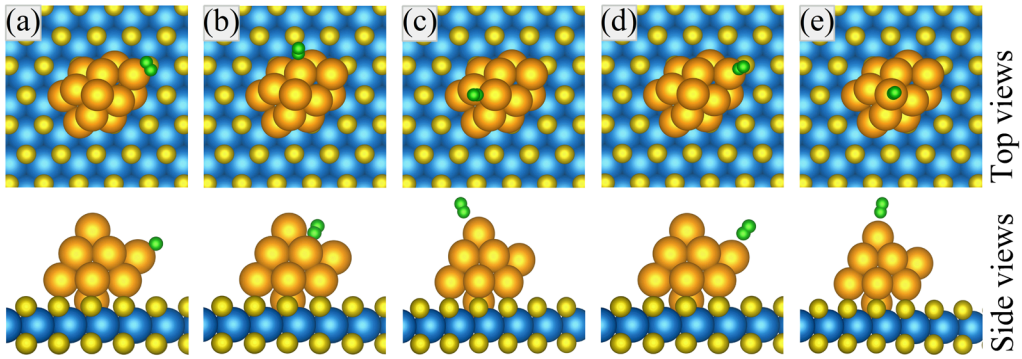

Figure 4.7 Adsorption geometries of H_2 on Au_{13} supported on defect-laden MoS_2. The green ball represents the H atom.

Table 4.1 Adsorption energy and geometrical parameters of H_2 adsorbed at different sites of Au_{13} supported on defect-laden MoS_2.

Configurations	**E_{ads} (eV)**	**$d_{(H-H)}$ (Å)**	**$d_{(H-Au)}$ (Å)**	**$A_{(H-H-Au)}$ (°)**
Fig.4.7a	-0.11	0.807	1.938	78
Fig.4.7b	-0.08	0.764	2.276	168
Fig.4.7c	-0.07	0.757	2.542	170
Fig.4.7d	-0.06	0.758	2.534	165
Fig.4.7e	-0.07	0.763	2.310	173

On Au_{13}/MoS_2, the dissociation of H_2 can occur from its adsorbed phase. Our CI-NEB calculation (the minimum energy path is shown in Figure 4.8) indicates that there is a barrier of 0.83 eV for the dissociation of adsorbed H_2 at the corner site (see Figure 4.7a), whereas the barrier is little higher for the dissociative adsorption of H_2 at the apex Au site. The resultant hydrogen atoms (H) adsorb at the bridge site of two Au atoms (apex and edge atoms). The adsorption energy of dissociated H_2 is -0.4 eV, indicating that the dissociation is exothermic. These results, therefore, suggest that the dissociation of H_2 on Au_{13}/MoS_2 is energetically feasible and that the active site for H_2 dissociation is the corner (or edge) Au site.

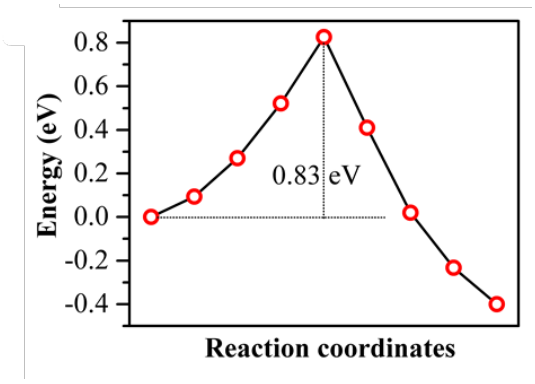

Figure 4.8 Minimum energy paths for H_2 dissociation, on Au_{13} supported on defect-laden MoS_2.

4.3.5 Adsorption of CO

Figure 4.9 shows the optimized configurations of CO adsorbed on Au_{13} supported on defect-laden MoS_2. In the two most preferred configurations, CO adsorbs at the corner Au atom – away from the interfacial region (c.f. Figure 4.9 for adsorption geometry), or at an edge Au site – also located away from the interface (c.f. Figure 4.9b). The common feature between two configurations is that CO adsorbs at Au atom via Au-C bonding. The CO adsorption energy in both configurations (Figure 4.9a-b) is almost similar i.e. ~-1.1 eV, which is comparable to that of CO adsorbed on Au_{13}/CeO_2, which binds CO with an adsorption energy of -1.13 eV [129], indicating that both Au_{13}/CeO_2 and Au_{13}/MoS_2 offer similar affinity of binding to CO. Moreover, we find there is no barrier for CO adsorption, indicating that CO adsorption is spontaneous process on Au_{13}/MoS_2. The adsorption energy and geometrical parameters for all configurations are given in Table 4.2. Note that our calculations show that H_2, CO and CH_3OH do not bind chemically to the MoS_2 basal plane in the presence of Au_{13}.

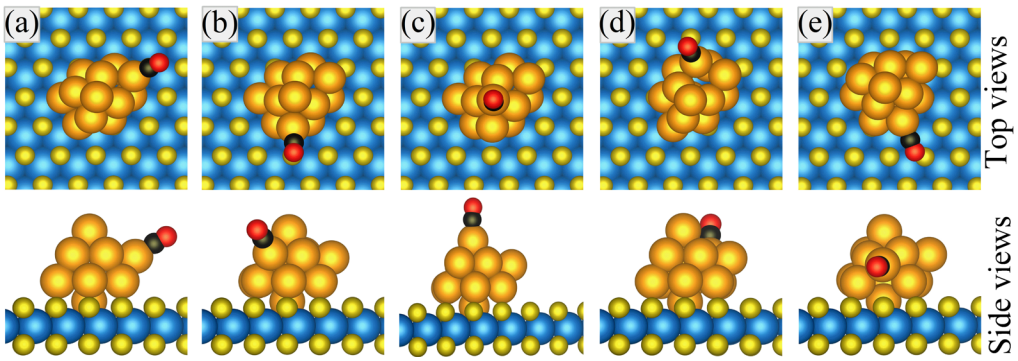

Figure 4.9 Adsorption geometries of CO on Au_{13} supported on defect-laden MoS_2. The black and red balls represent the C and O atoms, respectively.

Table 4.2 Adsorption energy and geometrical parameters of CO adsorbed at different sites of Au_{13} supported on defect-laden MoS_2.

Configurations	E_{ads} (eV)	$d_{(O-C)}$ (Å)	$d_{(C-Au)}$ (Å)	$A_{(O-C-Au)}$ (^{o})
Fig.4.9a	-1.10	1.155	1.938	174
Fig.4.9b	-1.11	1.155	1.931	175
Fig.4.9c	-0.82	1.154	1.964	164
Fig.4.9d	-1.07	1.154	1.935	174
Fig.4.9e	-0.79	1.155	1.925	178

4.3.6 Energetics for Reactions Involved in CO Hydrogenation

Before we discuss the potential energy for methanol synthesis reaction on Au_{13} supported on defect-laden MoS_2, we show the schematic representation of the reaction pathways for methanol synthesis in Figure 4.10. We first assumed that CO first adsorbs on the supported Au_{13} and then the atomic hydrogen enters into the cycle for the hydrogenation process to begin. The other adsorbed and co-adsorbed reaction intermediates are depicted as the following: c) CO*+H*, d) CHO*, e) CHO*+H*, f) CH_2O*, g) CH_2O*+H*, h) CH_3O*, and i) CH_3O*+H*. Starting from the reaction between CO* and H* to form CHO*, in each reaction step, the newly-formed intermediate undergoes hydrogenation until methanol (CH_3OH) is formed. Here, the subscript (g), superscript (*), and symbol * represent a gas species, an adsorbed species, and a surface site, respectively. The overall reaction is $CO_{(g)}+2H_{2(g)} \rightarrow CH_3OH_{(g)}$.

In Figure 4.13, we now show the calculated potential energies of the reactants, intermediates, and products involved in the CH_3OH synthesis reaction. The potential energies for each state involved in the synthesis reaction are calculated with reference to the total energy of the initial state of CO, two H_2 in gas phase, and the bare Au_{13}/MoS_2 system (i.e., the total energy of

$CO(g)+2H_2(g)+Au_{13}/MoS_2$ is set to zero). The details of the adsorption of these reactant molecules have been discussed earlier. As explained earlier, H_2 adsorbs at the corner site with an adsorption energy of -0.11 eV. It can thus be expected that adsorption and dissociation of H_2 are feasible at hydrogen-rich condition. The H_2 molecule then undergoes dissociation when it receives an energy of 0.83 eV (barrier for dissociation of H_2).

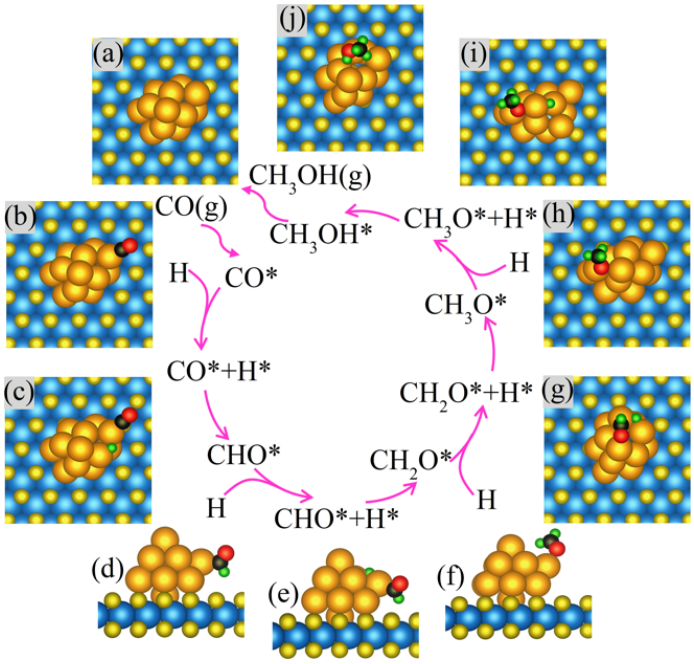

Figure 4.10 Schematic reaction mechanism (showing each reaction step) for methanol synthesis reaction on Au_{13} supported on defect-laden MoS_2. Starting from the adsorption of gas-phase CO, in each step, as indicated by arrow, intermediates react with atomic hydrogen to complete the formation of CH_3OH.

To find the minimum energy structure when two adsorbed reactants such as CO* and H* combine to form CHO* (Figure 4.10d), we apply the same procedure of relaxing several configurations in which CHO is placed at different Au sites, and subsequently use the most energetically-favorable structure as the final state (CHO*). After knowing initial states (CO*+H*) and the final state (CHO*), we perform the CI-NEB calculation for five artificial images in

between the initial and final states. This calculation yields a barrier of 1.14 eV (MEP is shown in Figure 4.11) for the formation of adsorbed formyl (CHO*) from the reaction between CO* and H* (i.e. CO*+H*→CHO*). The geometry at TS is illustrated in Figure 4.12a.

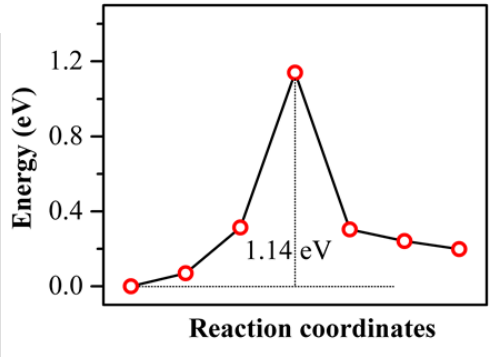

Figure 4.11 Minimum energy path for the reaction between CO* and H* to form CHO* on Au_{13} supported on defect-laden MoS_2.

After formation of CHO*, another available hydrogen (H*) reacts with CHO* to form an adsorbed formaldehyde (CH_2O*). The geometry at TS of this reaction is shown in Figure 4.12b. As depicted in Figure 4.13, the barrier for this reaction is 0.23 eV. The CH_2O* then either combines with H* (produced from H_2 dissociation) to form an adsorbed methoxy (CH_3O*) via reaction CH_2O*+H*→CH_3O* (geometry at TS is shown in Figure 4.12c) or desorbs from the supported Au_{13} to form the gas-phase formaldehyde. The barrier for CH_2O* desorption is 0.99 eV, which is larger than the barrier (0.15 eV) for the reaction between CH_2O* and H* to form CH_3O*. Thus, it is most likely to form CH_3O* from CH_2O* and H*. Next, the reaction between CH_3O* and H* leads to the formation of CH_3OH*. The barrier for the reaction, CH_3O*+H*→CH_3OH*, is 1.22 eV. The geometry at TS of this reaction is shown in Figure 4.12d. Finally, CH_3OH* needs to overcome a barrier of 0.42 eV for desorption.

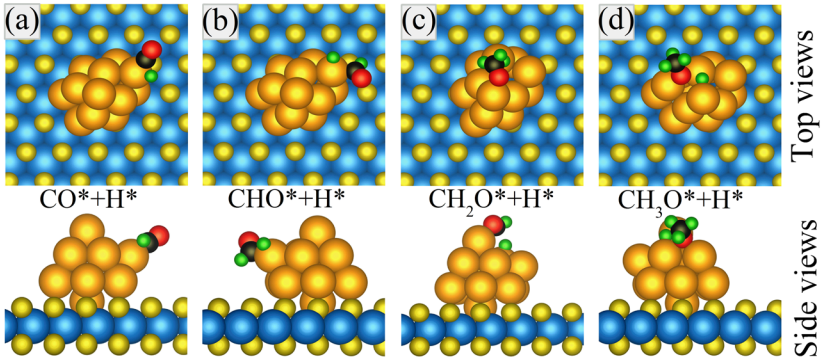

Figure 4.12 Geometries of reaction intermediates involved in CH_3OH synthesis via CO hydrogenation on Au_{13} supported on defect-laden MoS_2, at their transition states.

In the complete reaction pathway (Figure 4.13) for the formation of CH_3OH via CO hydrogenation on Au_{13}/MoS_2, the highest barriers turn out to be those for H_2 dissociation (0.83 eV) and for the reaction between CH_3O^* and H^* to form CH_3OH^* (1.22 eV). The reaction pathway for formation of $CH_2O(g)$ faces a higher potential energy than that for formation of $CH_3OH(g)$. Our results therefore suggest that Au-MoS_2 catalysts can catalyze the methanol synthesis reaction.

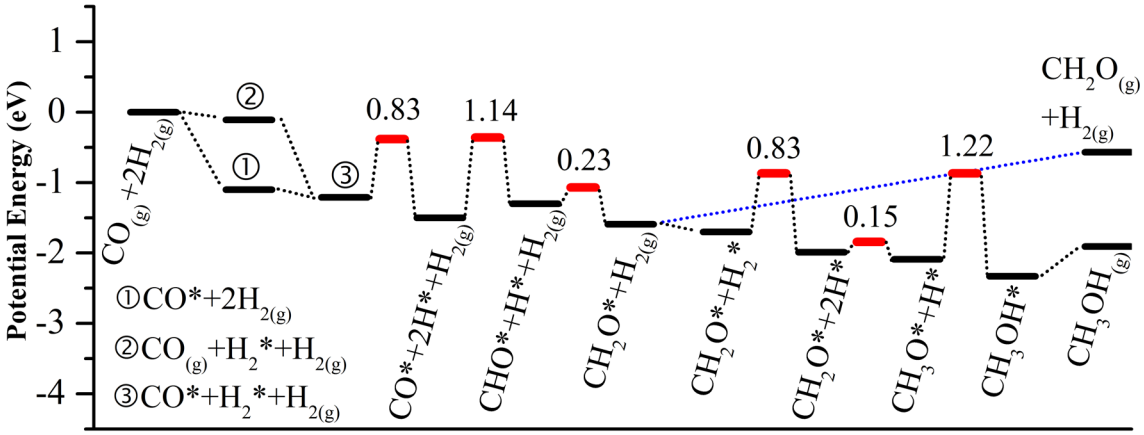

Figure 4.13 Potential energies along the reaction pathway of CH_3OH formation on Au_{13}/MoS_2. The horizontal small bars represent the intermediates states involved in the reaction while filled circles (red) represent the transition states. The activation energy barriers (in eV) is noted for each transition state. As before, superscript (*) denotes an adsorbed species whereas subscript (g) indicates a gas phase.

The catalytic performance of Au NPs significantly depends upon the nature of the support materials. The 13-atom Au NPs supported by the reduced TiO_2(110) (30% O vacancy), for example, catalyzes the CH_3OH decomposition reaction [142]. In this case, the higher activity for CH_3OH decomposition is offered by the interfacial sites, and is related to the charge-transfer (from TiO_2 to Au_{13}) that induces electrostatic interaction between reactants, gold, and the reduced TiO_2 support. Similarly, CH_3OH decomposition occurs on other oxide-supported Au catalysts (Au/CeO_2, Au/MgO, Au/Al_2O_3) with different activity and selectivity for the products [196]. On Au/CeO_2 and Au/MgO catalysts, the major products are H_2 and CO (with higher selectivity of H_2), but on Au/Al_2O_3 catalyst the dominant product is dimethyl ether (DME) [196]. The sulfide-supported Au NP used in our study (Au_{13}/MoS_2), exhibits a quite different catalytic performance from that of the oxide-supported Au catalysts just mentioned: on Au_{13}/MoS_2, we find that formation of CH_3OH via CO hydrogenation is favorable rather than CH_3OH decomposition, as manifested by the potential energy profile shown in Figure 4.13. Such different reactivity (and selectivity) of MoS_2-supported Au NP from that of metal-oxide-supported Au catalysts originates from the different nature of their catalytically active sites, which results in turn from the degree and kind of electronic interaction between Au NPs and the support.

4.4 Summary

Employing dispersion-corrected density functional theory (DFT-D3), we have examined the geometry, electronic structure, and catalytic properties of 13-atom gold nanoparticle on defect-laden single-layer MoS_2. The planar structure of Au_{13}, favored in isolated phase, transforms into the three-dimensional structure when Au_{13} is supported on MoS_2 – as confirmed by *ab-initio* MD

simulation. Charge is transferred from MoS_2 to Au_{13}: the electron density is also redistributed around Au atoms located away from the Au-MoS_2 interface thereby increasing the concentration of electrons in those Au atoms, enhancing those atoms' catalytic activity. Analysis of projected density of states indicates that Au d states become narrower and the *frontier states* appear close to the Fermi level. The modified electronic structure strikingly affects the catalytic activity of the Au_{13}/MoS_2, offering selectivity toward methanol synthesis via the CO hydrogenation route, in stark contrast to the catalytic activity of Au_{13}/TiO_2 [142] which promotes methanol decomposition.

Our results open up a new avenue for utilizing the 2D transition-metal dichalcogenides (TMDs), in general, as the support materials for Au nanoparticles that can catalyze a number of technologically relevant reactions, and therefore call for, in the longer run, both theoretical and experimental investigations on whether for synthesis of higher alcohols or other potential catalytic reactions, Au or other transition metal NPs (of various sizes) functionalized with 2D TMDs that may offer different activity and selectivity depending on whether the support is "active" with respect to the reactants or "inert". Of course, it would be important to accompany the thermodynamical analysis presented here with those resulting from reaction kinetics. The reaction energetics presented here are self-contained and we hope that they provide sufficient motivation for experimental work on this interesting composite catalyst. We await an experimental verification of our findings.

CHAPTER 5 Cu(111)-SUPPORTED SINGLE-LAYER MoS_2 FOR ALCOHOL SYNTHESIS FROM SYNGAS: FIRST PRINCIPLES STUDY

Rational designing of cheap and efficient catalyst material for alcohol synthesis from syngas is in great demand because of diminishing supply of the current state-of-the-art catalysts. One material of interest is single-layer MoS_2 owing to its low cost, abundancy, and catalytic applications. Because of the inertness of its basal plane, however, it is essential to find ways that make it catalytically active. Herein, by means of DFT-based calculations of reaction pathways and activation energy barriers, we show that a general strategy to make MoS_2 active is by the creation of S vacancies. However, the S vacancy row structures – energetically stable and naturally present in samples – are found to be less reactive compared to vacancy patches for methanol synthesis reactions. Enhancement of chemical activity and selectivity can be achieved by interfacing the MoS_2 layer with a metallic support. When defect-laden MoS_2 is grown on Cu(111) there is an increase in the active region (surface area of active sites) of MoS_2. Moreover, charge transfer from Cu to MoS_2 and strong electronic interaction between them results in shift the Fermi energy such that the frontier states (d orbitals of the exposed Mo atoms) appear close to the Fermi level, making it more amenable for catalytic activity. Based on our calculations, we conclude that the Cu(111) substrate promotes alcohol (methanol, ethanol) synthesis from syngas.

5.1 Introduction

Synthesis of higher alcohol from syngas (synthetic gases) has been of great research interest owing to the increasing petroleum price, environmental concerns, and the need for gasoline additives that increase gasoline's octane rating. It is therefore essential to develop the efficient catalytic process

of producing alcohols which is only possible by using good catalysts. One of the possible routes is via CO hydrogenation, which normally occurs at higher temperature and pressure in presence of solid catalysts [207-215]. The process of synthesizing higher alcohols from mixtures of CO and H_2 (syngas), leads to yield methanol as the primary product and higher alcohols [216,217]. However, there are still challenges associated with CO hydrogenation since the catalysts generate many undesired by-products such as water and hydrocarbons [210,218-221]. In addition, large-scale production of higher alcohols from syngas has been hindered by poor selectivity toward higher alcohols and low yields [222].

Alcohols are very important chemicals – for instance, methanol is useful for hydrogen storage [223], and has been considered as an excellent alternative energy carrier in the future energy infrastructure, called 'methanol economy' [224,225] because of its high energy density. Ethanol has even higher energy density and at the present it is blended with gasoline for maximizing the engine efficiency and for reducing the harmful gas emissions [226,227]. To produce these alcohols, Cu or Cu based catalysts have been tested and utilized [222,228,229]. One major downside of Cu catalysts, however, is their low tolerance toward sulfur (a catalyst poison) [230]. Because biomass (source of syngas) contains significant amount of sulfur [231], it is critical to design catalysts which bear sulfur tolerance. Unlike to Cu catalysts, MoS_2 shows high resistance to sulfur poisoning [232]. This motivates us to choose MoS_2, which has already shown a good catalytic activity for alcohol synthesis from CO or CO_2 hydrogenation [13,232-234]. Moreover, alkali-promoted MoS_2 offers a high selectivity toward higher alcohols [216,233,235,236]. Other possible ways to achieve the higher activity and selectivity toward alcohol synthesis could be the

creation of vacancies on MoS_2 of which catalytic properties can be altered using metallic substrate materials such that high activity and selectivity can be achieved.

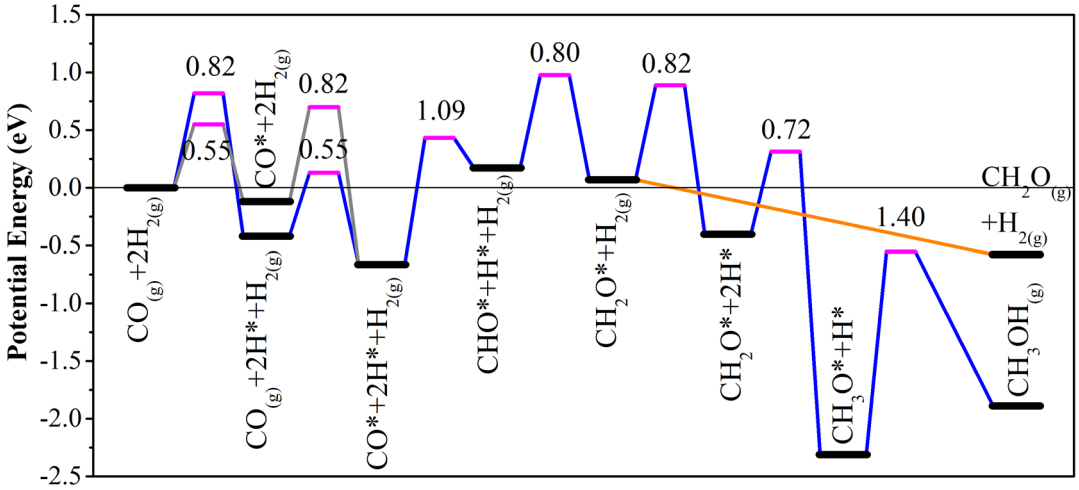

Figure 5.1 Potential energies along the reaction pathway of the formation of CH_3OH via the CO hydrogenation on defect-laden MoS_2. Thicker-longer bars represent the intermediate states while thinner-shorter bars represent transition states. Numbers (in eV) are energetic barriers. Superscript * indicates adsorbed specie. Subscript (g) indicates gas phase. [D. Le, T. B. Rawal, T. S. Rahman, J. Phys. Chem. C, (2014)] (Copyright: American Chemical Society 2014).

To optimize the activity and selectivity of single-layer MoS_2, one may engineer the geometric and electronic structures of MoS_2 by introducing a line defect (S vacancies row). It was already reported that MoS_2 with S vacancies row can be utilized as catalyst for methanol synthesis from syngas [13]. Figure 5.1 shows the potential energy profile for methanol synthesis reaction from synthetic gas ($CO+H_2$) via CO hydrogenation on single-layer MoS_2 with S vacancy row. As shown in the Figure, the intermediate reactions have higher potential energies with respect to the reference energy, indicating only S vacancies row structure may not facilitate this reaction. Thus, there is a need to functionalize it. One way of functionalizing it is through the use of metallic

support. Using the metallic support such as copper, we may enhance the activity for the reaction. Nevertheless, some important and relevant questions arise: i) what is the role of Cu(111)?; ii) can Cu(111) substrate be responsible for modifying the geometry and electronic structure of MoS_2?; iii) will the modified structures of MoS_2 help achieve high activity and selectivity for alcohols? In this study, we show indeed that one can tune the geometrical and electronic structures of MoS_2 using the Cu(111) substrate, thereby making the supported MoS_2 amenable for alcohol synthesis. Thus, this study puts one step forward on the development of atomistic level understanding of how we control the geometric and electronic structures in order to optimize the catalytic activity of defect-laden single-layer MoS_2 toward alcohol synthesis from syngas (CO and H_2).

Herein, using DFT together with the semi-empirical DFT-D3 approximation to account for van der Waals interaction, we first present the results of our calculated geometric and electronic structures of defect-laden MoS_2 supported on Cu(111). Based on our calculated potential energy with activation energy barriers for several reaction steps associated with alcohol synthesis, we show that the formation of ethanol (desired product) is energetically favorable than the formation of methane (an undesired product). We trace the superior activity of Cu-supported MoS_2 over the MoS_2 alone on the modified geometric and electronic structures of defect-laden MoS_2 by the substrate.

5.2 Theoretical Methods

Plane-wave DFT calculations were carried out using the VASP code [141]. For the exchange-correlation of electrons, PBE functional [43] within the form of the generalized-gradient approximation was used. The van der Waals interaction was taken into account using DFT-D3

[65] approximation . The wavefunctions were constructed by expanding a series of plane waves within a cutoff energy of 500 eV, where the interactions between the core and valence electrons were described using PAW pseudopotentials [72]. The total energy was converged to 10^{-5} eV, and the force on each atom was optimized to less than 0.01 eV $Å^{-1}$.

The Cu(111) surface was constructed using a (5x5) unit cell with five Cu layers and a 20 Å vacuum region between each slab. The top three layers were allowed to relax, and the bottom two layers were maintained at the DFT-optimized bulk lattice constant of 3.566 Å, in reasonable agreement with experiment (3.615 Å) [237]. Similarly, we constructed the defect-laden (DL) single layer MoS_2 by removing S atoms in a line from one side of MoS_2, which is mimicked by (4x4) unit using the bulk lattice constant of 3.16 Å. For the relaxation of these structures including the various gas adsorbates or intermediates involved in CO hydrogenation, (3x3x1) k point mesh was used to sample the first Brillouin zone (BZ). A dense (9x9x1) k-mesh was used to sample the first BZ for the calculation of electronic structure of DL-MoS_2 on Cu(111). Bader analysis [77,78] was used to estimate the charge transfer between DL-MoS_2 and Cu(111).

All calculated adsorption energies and reaction energies are reported as negative values for exothermic adsorption processes and positive values for endothermic processes. The reaction energies are expressed as the energy difference between initial state (IS) and the final state (FS). The transition states (TS) were determined using the nudged-elastic band (NEB) and the climbing-image (CI-) NEB methods of Henkelman and co-workers [86,91]. The prefactors were calculated using the Vineyard formula [92].

5.3 Results and Discussion

5.3.1 Effect of Cu(111) Substrate on the Electronic Structure of DL-MoS_2

Figure 5.2a show the DFT-optimized structure of DL-MoS_2/Cu(111). After structural relaxation, it turns out that DL-MoS_2 maintains the planar structure as in the pristine form due to interaction with the substrate. The Cu(111) substrate helps reduce the corrugation of DL-MoS_2. In other words, Cu(111) helps flatten the MoS_2 vacancy row structure, which is a v-shaped structure ((with narrow region of active sites) in the isolated phase, thereby making the active sites easily accessible to reactants (gas) or reaction intermediate adsorbates.

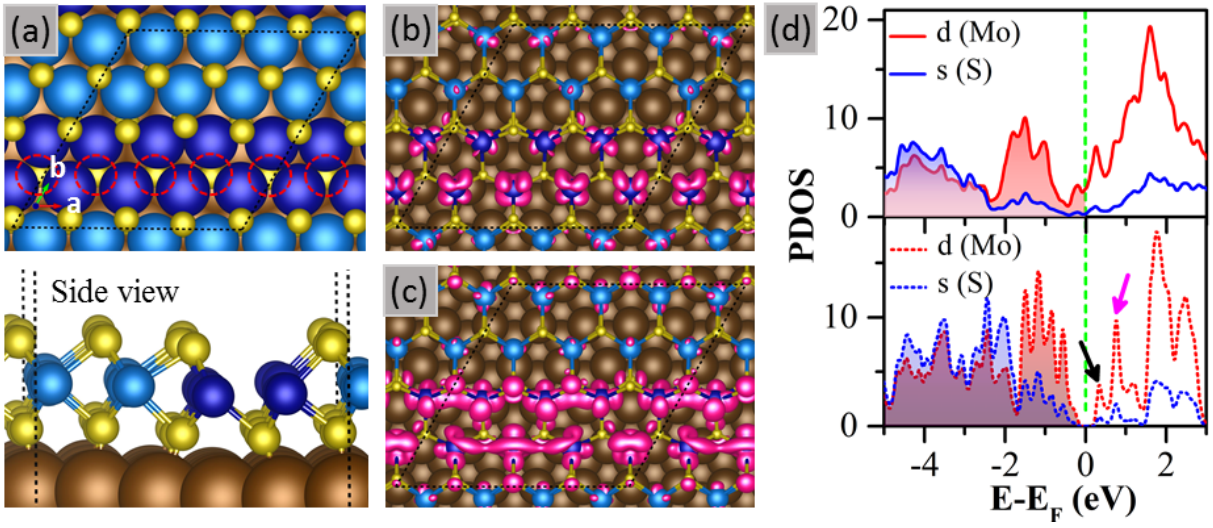

Figure 5.2 (a) DFT-optimized structure of DL-MoS_2 on Cu(111): top view (Upper panel) and side view (Lower panel); (b, c) The partial charge density corresponding to b) the highest occupied state and c) the lowest unoccupied state (The iso-value for the plot is taken as 0.005 a.u.); (d) The projected density of states (PDOS) onto Mo d orbitals and S p orbitals of unsupported/supported DL-MoS_2: Supported (Upper panel) and unsupported (Lower panel). (The vertical line at zero (in eV) refers to the Fermi energy which is different for each systems).

Figure 5.2(b-c) show the partial charge density of the selected states, which are very close the Fermi level, namely highest occupied (HO) state and the lowest unoccupied (LU) state. These states are dominantly d states of exposed Mo atoms (represented by dark blue balls), as shown in Figure 5.2d (upper panel).

Figure 5.2d shows the density of states of adsorbed DL-MoS_2. As seen from the figure that the presence of S vacancies, and the interaction between DL-MoS_2 and Cu(111) leads to introduce the midgap states, very close the Fermi level, the so-called the frontier orbitals. These orbitals are strongly localized in the vacancy region of adsorbed DL-MoS_2 (Figure 5.2b-c). In the absence of Cu(111), these states are unoccupied (marked by black and pink arrow, Figure 5.2d (lower panel)), and originated from exposed Mo atoms near S vacancies. When Cu(111) substrate interacts with DL-MoS_2, there is a charge transfer of 0.3e from Cu to MoS_2, leading to shift the Fermi level of MoS_2 toward the higher energy. As a result, both the lowest and second-lowest unoccupied orbitals of unsupported DL-MoS_2 appear very close to the Fermi level. This means the substrate helps shift the frontier orbitals close to the Fermi level. It is, therefore, expected that DL-MoS_2 supported on Cu(111) would be more catalytically active than the unsupported one.

5.3.2 Adsorption of Reactants, Intermediates and Products

Figure 5.3 shows the adsorption geometries of CO and dissociated H_2 which are the reactants for alcohol synthesis. CO adsorbs at an exposed Mo atom (near S vacancy) with an adsorption energy of -1.46 eV – slightly in tilted configuration (see Figure 5.3a) with bond lengths of C-O=1.17 Å, and C-Mo=2.01 Å. The adsorption of CO on the supported DL-MoS_2 is not spontaneous since there is a barrier of 0.04 eV, which is ~14 times lower than that (0.55eV) [13]

for the same process on unsupported one. Similarly, we find the non-spontaneous H_2 adsorption which is dissociative. Figure 5.3b shows the optimized adsorption geometry of dissociated H_2 on the supported DL-MoS_2. After dissociation, the atomic hydrogen adsorbs at the S vacancy site. The Mo-H distance is 1.98Å. The adsorption energy of dissociated H_2 is -0.77 eV. Our CI-NEB calculation indicates that the energy barrier for dissociative adsorption of H_2 is 0.20 eV, which is ~4 times smaller than that (0.82 eV [13]) for the same process on unsupported DL-MoS_2. These results clearly indicate that Cu substrate plays an important role for enhancing the adsorption energy of CO and H_2 as well as for reducing the barrier for adsorption of CO and H_2. These effects of Cu(111) substrate on the adsorption characteristics of reactant molecules would have direct impact on the on catalytic activity of DL-MoS_2 toward alcohol synthesis, as will be discerned below.

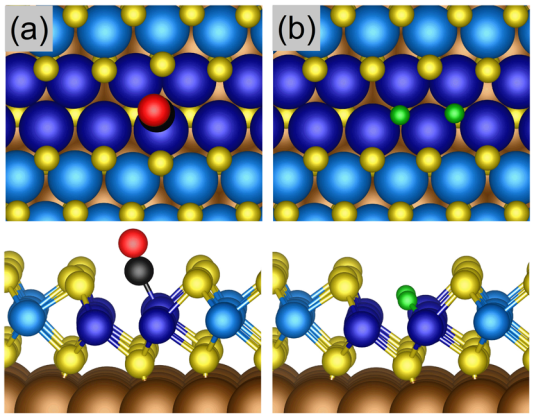

Figure 5.3 Optimized structures of reactants for alcohol synthesis on DL-MoS_2 supported on Cu(111): (a) adsorbed CO, and (b) dissociative H_2 (Top and side views: Upper & lower panels, respectively).

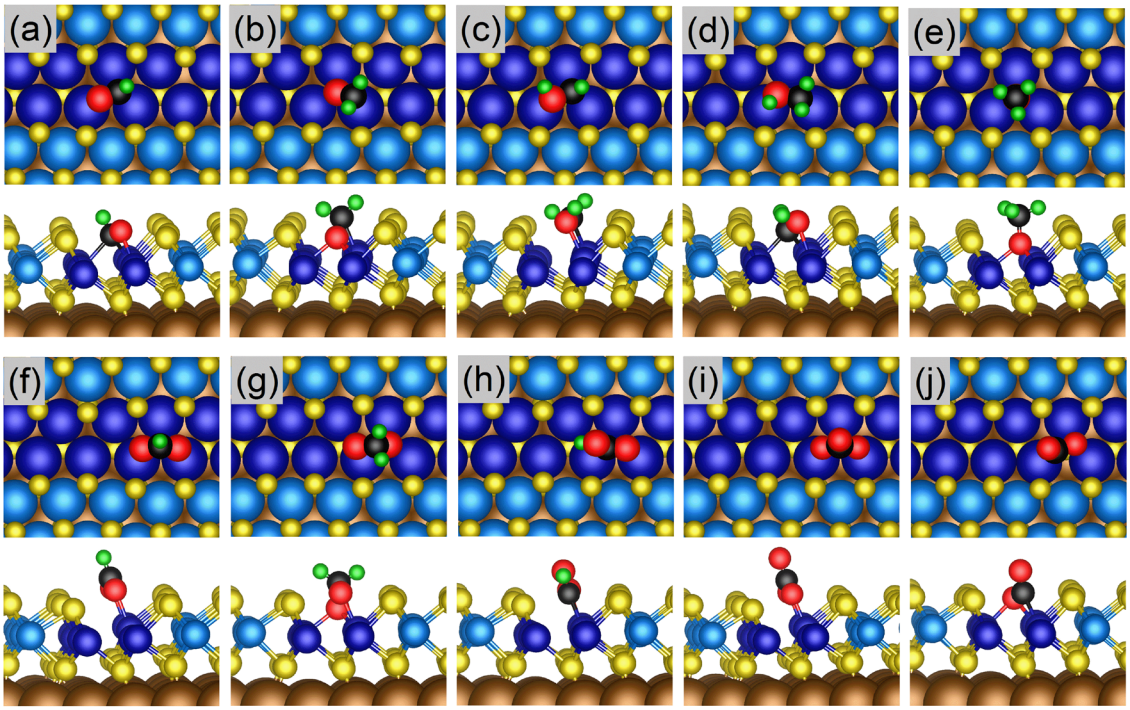

Figure 5.4 Optimized structures of the most stable geometries of intermediates: (a) CHO*, (b) CH_2O*, (c) CHOH*, (d) CH_2OH*, (e) CH_3O*, (f) HCOO*, (g) H_2COO*, (h) COOH*, (i) CO_3* and (j) CO_2*. For each structure, the side views are also displayed in lower panels.

Figure 5.4 and 5.5 show the DFT-optimized structures of the intermediates involved in CO hydrogenation. The calculated adsorption energy and the frequencies of some representative intermediates are provided in Table 5.1. The first intermediate in CO hydrogenation could be formyl (CHO*), of which adsorption geometry on the supported DL-MoS_2 is shown in Figure 5.4a. Here, (*) represents the adsorbed surface chemical species. The surface CHO* can undergo either further hydrogenation to form formaldehyde (CH_2O*) or hydroxymethylene (CHOH*) or dissociation to form CH* and O*. If CH_2O* is formed, then it binds to the surface such that O sits at the S vacancy (S_v) site and C attaches to Mo1 (see Figure 5.4b). If CHOH* is formed, then it binds such that both O and C attach to the Mo1 (see Figure 5.4c). Our calculations show that the

adsorption of CHOH* is relatively stronger than CH_2O*. However, note that the adsorption energy here is calculated with respect to the reference energy of the corresponding species in isolated system. The formation of these two competent species depends upon the overall potential energy. Similarly, the hydrogenation of CH_2O* leads to the formation either hydroxymethyl (CH_2OH*) or methoxy (CH_3O*) depending upon their potential energy surface. In our calculations, we find that the final intermediate before formation of CH_3OH* is methoxy (CH_3O*) which binds to surface through O atom which sits at the S vacancy site (see Figure 5.4e). The adsorption energy of CH_3O* turns out to -3.80 eV, indicating the binding of CH_3O* is relatively stronger. Note also that, along this process of hydrogenation, other several intermediates can be formed on the catalyst surface. One of the intermediates is formate (HCOO*) which binds at the exposed Mo atoms through O atoms (Figure 5.4f). This species may undergo further hydrogenation to form H_2COO* which binds such that O sits at the S vacancy site and another O attaches to Mo1. Another intermediate species could be carboxyl (COOH*), favorably adsorbing at Mo1 atoms through C and O atoms (Figure 5.4h), which may lead to the formation of CO_2* species. Note that the adsorption of CO_2 (see Figure 5.4j) is endothermic since the adsorption energy turns out to +0.04 eV.

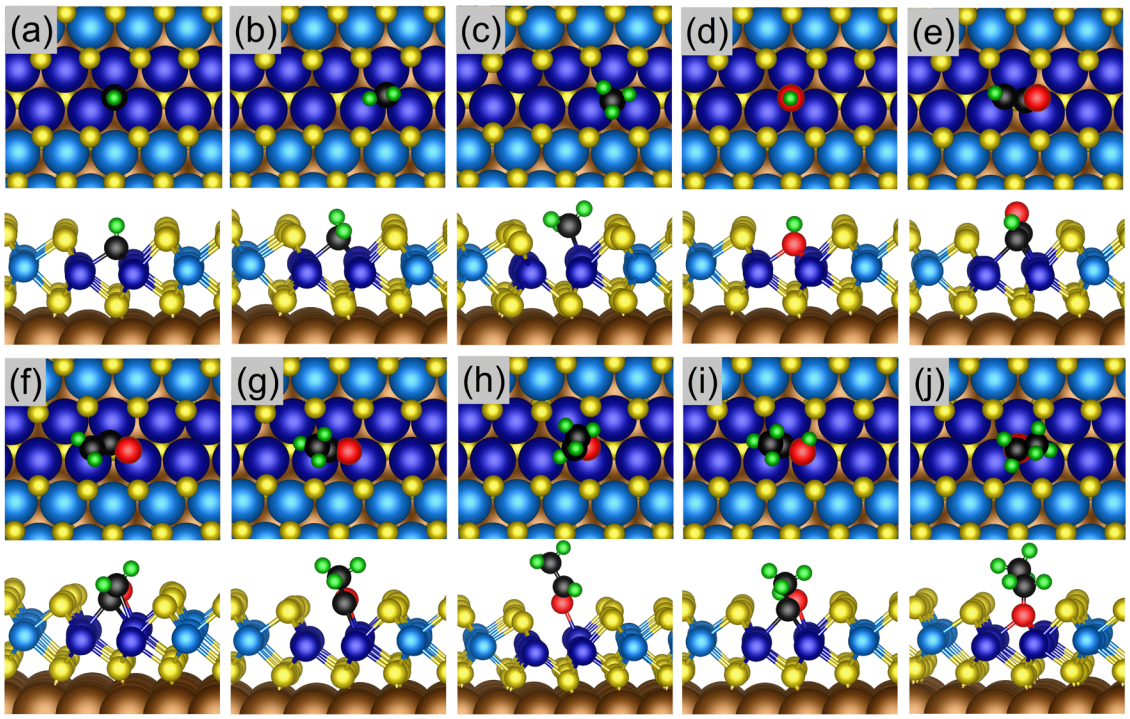

Figure 5.5 Optimized structures of most stable geometries of intermediates: (a) CH*, (b) CH_2*, (c) CH_3*, (d) OH*, (e) CHCO*, (f) CH_2CO*, (g) CH_3CO*, (h) CH_3CHO*, (i) CH_3COH*, and (j) CH_3CH_2OH. For each structure, the side views are also displayed in lower panels.

As mentioned before, the formation of CHO* can undergo dissociation to form CH* and O*. On the supported DL-MoS_2, the CH* intermediate binds at the S_v site (see Figure 5.5a) through C atom. This species may undergo hydrogenation to form CH_2*, which also adsorbs at the S_v site (Figure 5.5b). On the other hand, CH_3* species preferentially binds at the bridge site of two Mo1 atoms (Figure 5.5 c) with adsorption energy of -1.53 eV. The formation of these intermediates species are important for the formation of both methane (CH_4) and ethanol (CH_3CH_2OH) products. Note, however, that the formation of these products depend upon the overall potential energy as well as the reaction conditions. Next, intermediate species could be hydroxyl (OH*), which energetically favors the S_v site (see Figure 5.5d). Since the adsorption energy of OH* is -4.11 eV,

it is quite stable and therefore may induce the hydrolysis of CHO* or CH_3* species. We also calculate the adsorption energy of other intermediates which, in particular involve in ethanol synthesis. The CH_3* species can combine with CO* to form CH_3CO*, which adsorbs at the Mo1 atoms through C and O atoms (Figure 5.5g). The adsorption energy turns out to -2.34 eV. Once it gets hydrogenated, a transient intermediate species (CH_3CHO*) may form. The binding of this species is relatively weak since the adsorption energy is only -0.53 eV. The successive hydrogenation leads to the ethoxy (CH_3CH_2O*) that binds to S_v site (Figure 5.5i), and to the ethanol which attach to the Mo1 through O. Thus, the energy must be sufficient enough (>0.6 eV) to break Mo-O bond for releasing the final product as ethanol.

Table 5.1 Adsorption energy and frequencies of reactants, intermediates and products for alcohol synthesis.

	Sites	**Adsorption energy (eV)**	**Frequency (cm^{-1})**
CO*	Mo1	-1.46	2118, 86, 65, 42, 23, 22
H_2O*	Mo1	-0.33	3673, 3573, 1524, 588, 459, 279, 206, 197, 108
OH*	S_v	-4.11	3621, 735, 695, 434, 384, 343
H*	S_v	-2.65 (-0.38)	1062, 894, 692
CHO*	Mo1-Mo2 (via C and O)	-2.49	2917, 1242, 1196, 812, 495, 404, 293, 271, 220
CH_2O*	Mo1 & S_v (via C and O)	-0.70	3126, 3022, 1424, 1120, 1081, 892, 707, 446, 402, 386, 349, 157
CH_3O*	S_v (via O)	-3.80	3090, 3084, 2987, 1423, 1419, 1400, 1124, 1119, 914, 441, 377, 313, 250, 226, 106
CH_3OH*	Mo1 (via O)	-0.44	3499, 3089, 3057, 2960, 1443, 1438, 1411, 1284, 1131, 1037, 948, 543, 303, 223, 169, 157, 136, 49
CH_2OH*	Mo1(via C and O)	-1.84	3615, 3038, 2977, 1411, 1268, 1173, 1116, 845, 655, 523, 408, 318, 287, 223, 181
CHOH*	Mo1-Mo2 (via C and O)	-2.99	3381, 2950, 1277, 1156, 919, 813, 654, 480, 428, 327, 301, 198
HCOO*	Mo1-Mo2 (via O)	-3.19	3004, 1509, 1334, 1308, 960, 720, 374, 316, 269, 253, 215, 112
CH_3*	Bridge Mo1 (via C)	-1.53	3058, 2985, 2542, 1408, 1283, 1262, 754, 602, 436, 376, 326, 275
CH_2*	S_v	-5.36	2996, 2156, 1497, 873, 646, 606, 543, 490, 357
CH_3CO*	Mo1, Mo2 (via C and O)	-2.34	3099, 3050, 2967, 1417, 1411, 1373, 1316, 1050, 968, 920, 587, 452, 307, 270, 240, 218, 181, 167
CH_3CHO*	Mo1 (via O)	-0.53	3113, 3019, 2964, 2935, 1625, 1405, 1403, 1364, 1321, 1121, 1054, 901, 769, 527, 270, 162, 150, 132, 102, 57, 22
CH_3CH_2O*	Mo1	-3.24	3089, 3051, 3042, 2992, 2959, 1443, 1431, 1422, 1364, 1339, 1262, 1114, 1056, 984, 794, 755, 489, 419, 307, 236, 208, 173, 153, 83
CH_3CH_2OH*	Mo1	-0.63	3495, 3066, 3054, 3037, 2985, 2958, 1457, 1445, 1437, 1366, 1349, 1296, 1224, 1101, 1036, 996, 840, 792, 541, 455, 301, 230, 170, 148, 127, 46, 45

5.3.3 Reaction Pathways Involved in CO Hydrogenation to Alcohol

Now, we turn to discuss the various reaction pathways involved in CO hydrogenation to form alcohols. The calculated reaction energies (ΔE), activation barriers and prefators for the elementary reactions are provided in Table 5.2. Below details of the energetics associated with some of the intermediates are summarized.

5.3.3.1 Formyl (CHO)

It is the first intermediate that can be formed in CO hydrogenation. Our DFT results indicate that the reaction between CO* and H* (R3) is endothermic (ΔE=0.79 eV), and that the barrier for the reaction is 0.98 eV. This means the backward process (CHO*→CO*+H*) is energetically favorable. Alternatively, it can undergo dissociation to form CH* and O*. The dissociation of CHO* (R9) is highly exothermic (ΔE=-3.01 eV), and needs to overcome the barrier of 1.06 eV.

5.3.3.2 Formaldehyde (CH_2O) vs Hydroxymethylene (CHOH)

Formaldehyde is another intermediate that forms in alcohol synthesis from hydrogenation of syngas. The formation of this intermediate was proposed as one of the key in thesynthesis of CH_3OH on various catalyst surfaces [238-241] via hydrogenation of CHO*. Our DFT results indicate that the reaction between H* and CHO* (R4) is endothermic (ΔE=0.18 eV), and that the barrier for the reaction is 0.97 eV (see Table 5.2). Note that the reaction between CHO* and H* can also lead to CHOH* (R10) for which there is the reaction energy (ΔE) is 0.36 eV, twice larger than that for the reaction R4. In addition, the barrier for the reaction R10 is 1.29 eV, which is

higher than that (0.97 eV) for the reaction R4 (see Table 5.2). These differences are also clearly depicted in Figure 5.6. Moreover, the total energy of CH_2O* turns out to 0.19 eV lower than that of CHOH*, indicating the former species is relatively more stable than the latter. These results indicate that the formation of CH_2O* is both energetically and kinetically favored over the formation of CHOH* via the hydrogenation of CHO*.

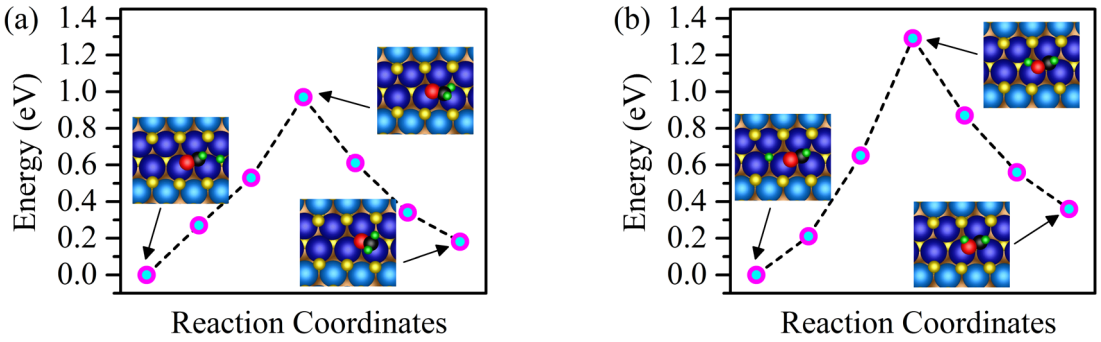

Figure 5.6 Minimum energy pathways for the formation of intermediates: a) CH_2O* and b) CHOH*.

These intermediates can undergo dissociation to form hydrocarbon intermediates. The decomposition reactions of CHOH* (R11) and CH_2O* (R12) are both highly exothermic: the reaction energy for the former is -2.56 eV whereas that for the latter is -2.16 eV. The activation barriers for the former is 0.05 eV, which is much smaller than the barrier of 0.64 eV for the latter. Thus, once CH_2OH* is formed, it is kinetically favored for dissociation into CH* and OH*.

5.3.3.3 Methoxy (CH_3O) vs Hydroxymethyl (CH_2OH)

Depending upon the energetics and kinetics, the successive hydrogenation of CH_2O* leads to either CH_3O* or CH_2OH*. In the former pathway, the C-H bond needs to be formed whereas in the latter it is O-H bond. The formation of CH_3O* via the reaction R5 (see Table 5.2) is exothermic

(ΔE=-1.31 eV) with activation barrier of 0.68 eV. In contrast, the formation of CH_2OH^* via the reaction R13 (see Table 5.2) is endothermic (ΔE=0.29 eV) with the relatively higher activation barrier of 1.39 eV. These differences are also clearly traced in Figure 5.7. Note that there is also the difference in total energy of these two intermediate species. The total energy of CH_3O^* is 1.59 eV lower than that of CH_2OH^*, indicating the much higher stability of CH_3O^* as compared with CH_2OH^* on the supported DL-MoS_2. The higher stability of CH_3O^* leads to a higher surface coverage compared with CH_2OH^*, and the abundance of CH_3O^* species on the surface counteracts the high activation barrier for its last hydrogenation step. Overall, our DFT calculations reveal that that the reaction pathway of CH_3O^* is both energetically and kinetically favorable over the pathway of CH_2OH^*, and hence the formation of former species is dominant over the latter.

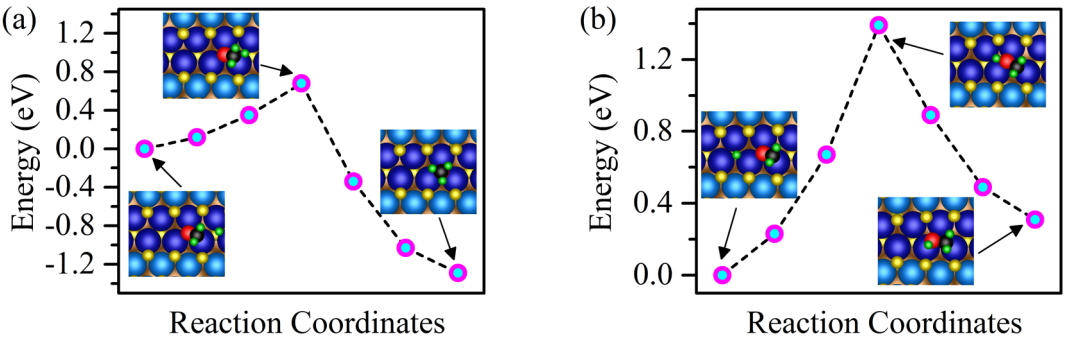

Figure 5.7 Minimum energy pathways for the formation of intermediates: a) CH_3O^* and b) CH_2OH^*.

The CH_3O^* and CH_2OH^* can undergo dissociation to form hydrocarbon intermediates. The decomposition reactions of CH_2OH^* (R14) and CH_3O^* (R15) are both exothermic: the reaction energy for the former is -1.66 eV whereas that for the latter is -0.47 eV. The activation barriers for the former is 0.08 eV, which is much smaller than the barrier of 0.92 eV for the latter.

5.3.3.4 Hydrocarbons

The hydrocarbon intermediate species such as CH*, CH_2* and CH_3* can also be formed in alcohol synthesis. As shown in Table 5.2, these species can be formed via reactions: R9, R11, R12, R14 and R15. These species may then react with CO*, or O* or OH* intermediates to form other intermediates which involve in the formation of higher alcohols, as shall be discussed below. Note also that CH* and CH_2* species can react with H* to form CH_2* and CH_3*. The barrier for the reaction CH*+H*→CH_2* (R16) is 0.60 eV, and that for the reaction CH_2*+H*→CH_3* (R17) is 0.88 eV (see Table 5.2). The CH_3* can undergo hydrolysis to form CH_2* and H_2O* (R31). Finally, CH_3* can undergo further hydrogenation to form methane (CH_4) – reaction R18 which is exothermic (ΔE=-0.80 eV) with activation barrier of 0.98 eV – which is undesired product in alcohol synthesis reactions. Once CH_4 is formed, it does not attach to the active Mo atoms of the supported DL-MoS_2 and desorbs immediately without experiencing any barrier. Note, however, that the CH_4 formation path competes with the reaction between CH_3* and CO*. As shall be discerned from Table 5.2, the formation of CH_4 needs to cost higher barrier than that for the reaction between CH_3* and CO*.

5.3.3.5 H_2COO

H_2COO is an intermediate which can be formed either the reaction between CH_2O* and O* (R19) or the hydrogenation of HCOO* (R20, reverse process). The latter reaction was also reported in previous studies [238,239] of methanol synthesis on metal oxide surfaces. Our DFT calculations show that the reaction HCOO*+H*→H_2COO* is endothermic by 1.15 eV. The barrier for this process turns out to 2.10 eV. These results indicate that the formation of H_2COO* via

hydrogenation of HCOO* is both thermodynamically and kinetically not favored. Similarly, the formation of H_2COO* via R19 is also endothermic (ΔE=1.44 eV). The barrier for this reaction is 1.55 eV (see Table 5.2). Thus, the formation of H_2COO* on the supported DL-MoS_2 is not energetically favorable.

5.3.3.6 Formate (HCOO)

The formate intermediate is one of the key intermediates in alcohol synthesis from syngas. The HCOO* species can be formed in different ways: (i) decomposition of H_2COO*, (ii) combination of CO_2 and H*, and (iii) decomposition of HCOOH*. Our DFT calculation shows that the decomposition of H_2COO* (R20) is exothermic (ΔE=-1.15 eV) with activation barrier of 0.95 eV. The combination reaction between CO_2(g) and H* (the backward process of R21, see Table 5.2) is also exothermic by -0.32 eV. The barrier for this backward reaction is 1.78 eV. Since the barrier for the latter reaction is higher than the former process of H_2COO* dissociation, it is most likely to form HCOO* via reaction R20. Thus, the lowest-energy path for the formation of HCOO*on the supported DL-MoS_2 is through the C-H bond breaking of H_2COO*.

5.3.3.7 Ethoxy (CH_3CH_2O)

The ethoxy is the final intermediate for the reaction pathways toward the formation of ethanol (CH_3CH_2OH). The several intermediates may involve before the formation of ethoxy. Here, we first discuss the reaction pathway for the formation of CH_3CO* from the reaction between CH_3* and CO* (R32). The barrier for the formation of CH_3CO* is 0.67 eV. The MEPs is shown in Figure 5.8a. Once it is formed, then it can undergo hydrogenation to form CH_3CHO* via C-H

bond making. The reaction $CH_3CO^*+H^* \rightarrow CH_3CHO^*$ (R33, see in Table 5.2) needs to overcome a barrier of 0.77 eV. On the other hand, the reaction of CH_3CHO^* and H* (R34) faces relatively smaller barrier for the overall process toward the formation of ethoxy. The MEPs for this reaction step is shown in Figure 5.8b. As shown in Figure, the reaction is exothermic by -1.11 eV, indicating the formation of ethoxy from CH_3CHO^* is both thermodynamically and kinetically favorable.

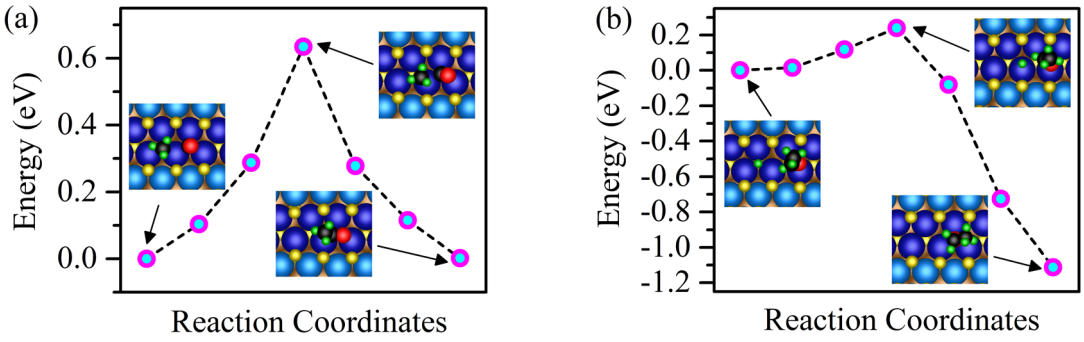

Figure 5.8 Minimum energy pathways for the reactions: a) $CH_3^*+CO^* \rightarrow CH_3CO^*$ and b) $CH_3CHO^*+H^* \rightarrow CH_3CH_2O^*$.

5.3.3.8 Ethanol (CH_3CH_2OH)

Ethanol is a desired product in alcohol synthesis reaction from syngas. Since the overall reaction is highly exothermic [$\Delta H^o(298\ K) = -2.63$ eV], the direct synthesis of CH_3CH_2OH is thermodynamically favorable. On the catalyst surface, the potential energy for the synthesis of CH_3CH_2OH is even lower than that for the direct synthesis. As shall be shown below, the formation of ethanol is, indeed, energetically much favored than the formation of methane and methanol. The hydrogenation of $CH_3CH_2O^*$ (R35, Table 5.2) leads to ethanol. The reaction is endothermic and the barrier for this reaction is 0.91 eV. Finally, it desorbs when it overcomes the barrier of 0.63 eV.

Table 5.2 Reaction energy (ΔE), activation barriers and the prefactors for the several elementary reactions associated with alcohol synthesis.

	Reactions	**ΔE (eV)**	**Activation barrier (eV)**	**Prefactor (s^{-1})**
R1	$CO(g)+*\rightarrow CO*$	-1.46	0.04	$2.634x10^{11}$
R2	$H_2(g)+2*\rightarrow 2H*$	-0.77	0.20	$9.385x10^{10}$
R3	$CO*+H*\rightarrow CHO*+*$	0.79	0.98	$2.742x10^{11}$
R4	$CHO*+H*\rightarrow CH_2O*+*$	0.18	0.97	$4.0x10^{12}$
R5	$CH_2O*+H*\rightarrow CH_3O*+*$	-1.31	0.68	$1.526x10^{13}$
R6	$CH_3O*+H*\rightarrow CH_3OH*+*$	0.96	1.33	$1.158x10^{13}$
R7	$CH_3OH*\rightarrow CH_3OH(g)+*$	0.43	--	$1.0x10^{13}$
R8	$CH_2O*\rightarrow CH_2O(g)+*$	0.70	--	$1.0x10^{13}$
R9	$CHO*+*\rightarrow CH*+O*$	-3.01	1.06	$7.772x10^{12}$
R10	$CHO*+H*\rightarrow CHOH*+*$	0.36	1.29	$1.834x10^{13}$
R11	$CHOH*+*\rightarrow CH*+OH*$	-2.56	0.05	$1.282x10^{13}$
R12	$CH_2O*+*\rightarrow CH_2*+O*$	-2.16	0.64	$3.591x10^{13}$
R13	$CH_2O*+H*\rightarrow CH_2OH*$	0.29	1.39	$1.560x10^{13}$
R14	$CH_2OH*+*\rightarrow CH_2*+OH*$	-1.66	0.08	$1.112x10^{13}$
R15	$CH_3O*+*\rightarrow CH_3*+O*$	-0.47	0.92	$6.585x10^{14}$
R16	$CH*+H*\rightarrow CH_2*+*$	0.45	0.60	$2.152x10^{13}$
R17	$CH_2*+H*\rightarrow CH_3*+*$	-0.70	0.88	$1.660x10^{13}$
R18	$CH_3*+H*\rightarrow CH_4(g)+*$	-0.80	0.98	$1.0x10^{13}$
R19	$CH_2O*+O*\rightarrow H_2COO*+*$	1.44	1.55	$9.453x10^{13}$
R20	$H_2COO*\rightarrow HCOO*+H*$	-1.15	0.95	$1.026x10^{14}$
R21	$HCOO*+*\rightarrow CO_2(g)+H*$	0.32	2.10	$4.967x10^{13}$
R22	$CHO*+O*\rightarrow OH*+CO*$	-1.25	0.25	$1.031x10^{15}$
R23	$CHO*+OH*\rightarrow CO*+H_2O*$	-0.99	0.30	$1.052x10^{14}$
R24	$H_2O*\rightarrow H_2O(g)+*$	0.33	--	$1.0x10^{13}$
R25	$H_2O*+*\rightarrow OH*+H*$	-0.89	1.27	$7.668x10^{12}$
R26	$OH*+*\rightarrow O*+H*$	-0.77	0.91	$3.888x10^{13}$
R27	$CO*+O*\rightarrow CO_2(g)+*$	1.66	2.63	$1.0x10^{13}$
R28	$CO*+OH*\rightarrow COOH*+*$	+1.47	3.04	$2.201x10^{15}$
R29	$COOH*\rightarrow H*+CO_2(g)$	-0.24	1.14	$4.967x10^{13}$
R30	$CHO*+O*\rightarrow HCOO*+*$	-1.59	0.57	$1.113x10^{13}$
R31	$CH_3*+OH*\rightarrow CH_2*+H_2O*$	-1.63	0.51	$1.021x10^{13}$
R32	$CH_3*+CO*\rightarrow CH_3CO*+*$	0.01	0.67	$1.199\ x10^{13}$
R33	$CH_3CO*+H*\rightarrow CH_3CHO*+*$	-0.12	0.77	$5.657\ x10^{13}$
R34	$CH_3CHO*+H*\rightarrow CH_3CH_2O*+*$	-1.11	0.12	$4.229x10^{14}$
R35	$CH_3CH_2O*+H*\rightarrow CH_3CH_2OH*+*$	0.63	0.91	$1.322x10^{13}$
R36	$CH_3CH_2OH*\rightarrow CH_3CH_2OH(g)$	0.63	--	$1.0x10^{13}$

5.3.4 Comparison of Potential Energy Profile

As compared to the methanol formation from CO hydrogenation on DL-MoS_2 (see Figure 5.1) [13] without the Cu substrate, the same process is more favorable on Cu-supported DL-MoS_2. On DL-MoS_2, some intermediate states have positive potential energy (i.e. above the reference energy, as indicated by zero, see Figure 5.1). In contrast, for the case of Cu-supported DL-MoS_2, we find that there are no intermediate states with positive potential energy. In addition, the energy barriers for the intermediate reactions are comparatively smaller than those for the same reactions on unsupported DL-MoS_2. We find the barrier of 0.98 eV for the reaction CO*+H*→CHO*. The highest barrier for the successive hydrogenation toward the formation of CH_3OH is for the reaction between H* and CH_3O*, i.e. CH_3O*+H*→CH_3OH*. The barrier for this reaction is 1.33 eV. Then, it needs to overcome a barrier of 0.44 eV for desorption.

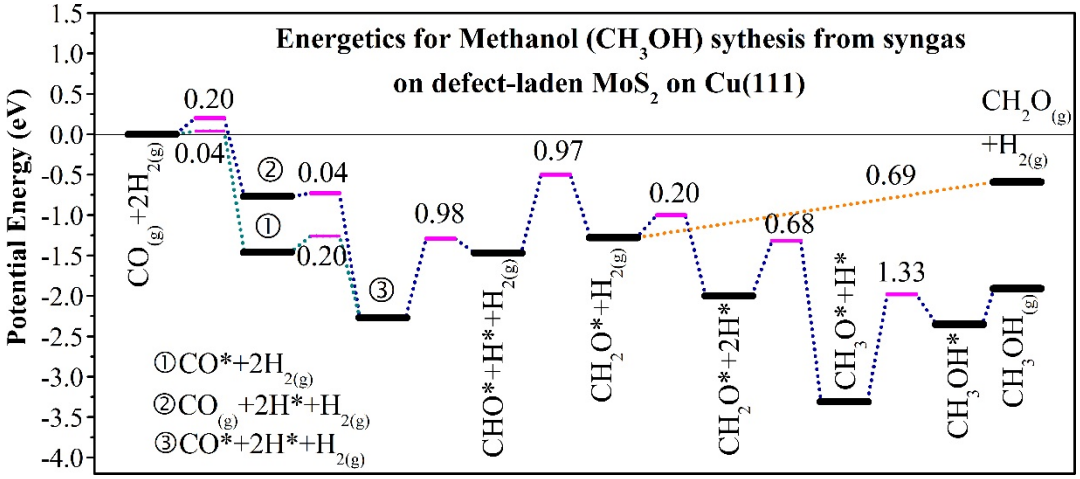

Figure 5.9 Potential energies along the reaction pathways for the formation of methanol via the CO hydrogenation on DL-MoS_2 supported on Cu(111).

Figure 5.9 shows the potential energy along the reaction pathway for methanol synthesis reaction via CO hydrogenation on DL-MoS_2 supported on Cu(111). As seen from the figure, there

are smaller barriers for both adsorption of CO and the dissociative adsorption of H_2, leading to the facile adsorption of CO and dissociative adsorption of H_2. These barriers turn out to be relatively smaller than those for the same processes on unsupported DL-MoS_2 [13]. Importantly, the overall energetics, both the reaction energies and the barriers, for each reaction step turn out to be lower than those in the case of unsupported DL-MoS_2. Thus, these results clearly indicate that the Cu substrate facilitates the methanol synthesis reaction on DL-MoS_2. However, we notice that the potential energy for the formation of CH_3OH is relatively at higher energy than the formation of CH_4 and CH_3CH_2OH.

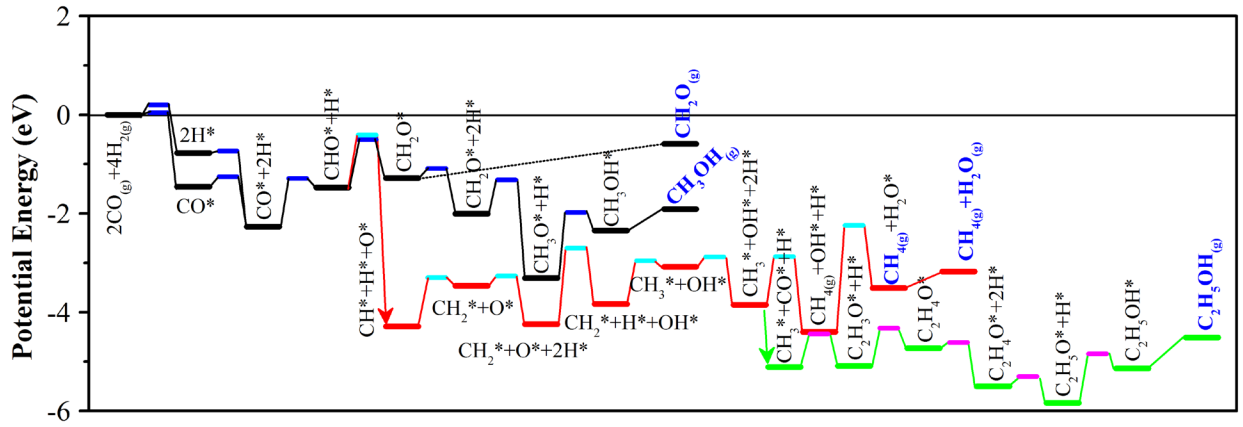

Figure 5.10 Comparison of the potential energies for various reaction pathways for the formation of different products involved in alcohol synthesis via the CO hydrogenation on DL-MoS_2 supported on Cu(111). For the easy readability, the main intermediates are depicted. The H_2 and CO or H_2O can be added for balancing the chemical equations.

Figure 5.10 shows the potential energy toward the formation of various products involved in CO hydrogenation. As clearly demonstrated in the Figure, the formation of CH_2O product is at the most higher energy. The formation of CH_4 is quite lower than the formation of CH_3OH. Strikingly, it turns out that the formation of CH_3CH_2OH is much favorable in terms of energetics

over the other two products: CH_4 and CH_3OH. Thus, these results clearly indicate that the Cu substrate strikingly facilitates the methanol synthesis reaction on DL-MoS_2. The enhanced chemical activity of the supported DL-MoS_2 can be traced to the modified electronic structure of DL-MoS_2 owing to the interaction with Cu substrate and the charge transfer between them.

5.4 Summary

Employing density functional theory with semi-local approximation (DFT-D3), we have studied alcohol synthesis from syngas on DL-MoS_2 supported on Cu(111). Significant charge transfer from Cu to MoS_2 and strong interaction between them leads to shift the Fermi energy toward the higher energy, thereby the position of the frontier orbitals toward the Fermi level, thereby making DL-MoS_2/Cu(111) more active than unsupported one. The Cu substrate leads to increase the adsorption energy of CO and H_2 on DL-MoS_2. Activation energy barriers for each individual intermediate reactions involved in methanol synthesis reaction reduce significantly as compared to those in the case of MoS_2 alone. On the basis of our DFT-calculated energetics, we conclude that the Cu(111) substrate strikingly promotes alcohol synthesis on DL-MoS_2.

We have provided a general strategy to make single-layer MoS_2 chemically active by the creation of S vacancies and the functionalizing it with Cu(111) substrate. Our DFT-calculated potential energy profile taken together with activation barriers, indeed, shows that the substrate strikingly promotes the ethanol synthesis from syngas on DL-MoS_2. The formation of ethanol is thermodynamically favored over the formation of CH_4. Thus, these results will be applicable to rational design of MoS_2-based catalysts for higher alcohol synthesis from syngas.

CHAPTER 6 STRUCTURE, REACTIVITY, AND SURFACE RECONSTRUCTION OF Ag(110) UPON INTERACTION WITH OXYGEN

6.1 Part I. Adsorption, Diffusion and Vibration of Oxygen on Ag(110)

We have employed *ab initio* density functional theory (DFT) to study the adsorption, dissociation, diffusion, and vibration of oxygen on Ag(110). We find that the fourfold-hollow site is the preferred site for O_2 adsorption and that the O_2 molecular axis marginally prefers to align along the $[1\bar{1}0]$ direction (for which the adsorption energy is −0.41eV) rather than along the [001] (for which it is −0.37eV). By weakening the O-O bond, the net charge transfer of ~0.9e from Ag to the antibonding orbital ($2\pi*$) of O_2 facilitates dissociation of O_2 on Ag(110). Contrary to a previous theoretical suggestion, our DFT calculations for adsorption energies and dissociation energy barriers, taken together with findings concerning vibrational frequencies and charge transfer, indicate that, when adsorbing, O_2 prefers to align along the $[1\bar{1}0]$ direction, and when dissociating, does align along the [001] direction with the dissociated O atoms adsorbing onto threefold-hollow sites rather than short-bridge sites. Importantly, our calculations clearly show that dissociation of O_2 on Ag(110) is coupled with the surface Rayleigh mode (~4meV) and O_2 dissociation along the [001] direction is more strongly coupled with the substrate motion than O_2 dissociation along the $[1\bar{1}0]$ direction indicating that O_2 dissociation (particularly, O_2[001]) can be activated by surface phonon even at quite low temperature. Once thus dissociated, the O atoms can more easily diffuse in the $[1\bar{1}0]$ direction, from one fourfold-hollow site to the next owing to a smaller diffusion barrier in the latter.

6.1.1 Introduction

Silver is an important catalyst for oxidation reactions in industry. It is used as a catalyst for the oxidative dehydrogenation of methanol [242], the photolysis of molecular oxygen (O_2) at high coverage [243], and the epoxidation of ethylene [244,245]. Accordingly, Ag surfaces have been extensively investigated over the last decades. As the most corrugated surface among the low-Miller-index surfaces of Ag, the (110) surface's interaction with gas molecules such as oxygen proceeds via such fundamental physical processes as adsorption and dissociation. For accurate manipulation of such gas-surface interactions [246-248], and of the oxidation reactions of CO [249,250] and hydrocarbons [251] on Ag(110), it is essential to understand the surface structures of various phases of oxygen moieties formed on Ag(110) upon the adsorption and dissociation of O_2. The microscopic characterization of such adsorbed species is of general interest for understanding the catalytic activity of Ag(110). Such understanding may provide insights into the mechanisms that enable enhancement of the catalytic oxidation reaction at the large scale.

Extensive and various experimental investigation of the O_2/Ag(110) system over the last few decades has led to substantial understanding of the gas-surface dynamics and oxidation reactions. Scanning Tunneling microscopy (STM) studies [252,253], for example, have shown that some adsorption modes of O_2 on Ag(110) are closely connected to the activity of the surface in CO oxidation – specifically, that CO oxidation occurs at $T > 90$ K, and that dissociated O atoms act as the reaction intermediates on the surface [253]. Another earlier STM study [254] has shown that on Ag(110) O_2 serves as a chemisorbed, but transient, highly mobile hot precursors which can be trapped by some other stabilized adsorbates, the phenomena of which is of the catalytic significance for the complex surface reactions associated with heterogeneous catalysis. High-

energy [255] and medium-energy [256] ion-scattering experiments have shown that at room temperature the spacing between the first and second layers contracts but that between the second and third layers expands, that this multilayer relaxation is oscillatory, and that the first-two layers exhibit anisotropy in vibrational amplitude. Reflection-anisotropy spectroscopy (RAS) experiment [257] has shown that transitions between occupied and unoccupied surface states near Y-point in the Brillouin zone (BZ) are responsible for resonance in reflection anisotropy from the Ag(110) surface and, in particular, that this anisotropy stems from dipole transitions among the surface states at the Y-point in the BZ. An angle-resolved photoemission study [258] has shown that oxygen adsorbs on Ag(110) in three distinct modes: a molecular physisorbed (weakly bound) mode at T < 40 K, a molecular chemisorbed mode between 60 K and 180 K, and a dissociated chemisorbed (i.e. atomic) mode at T >180 K. Electron-energy-loss spectroscopy (EELS) and thermal-desorption spectroscopy (TDS) studies [259] have observed two chemisorbed species of O_2 on Ag(110) [259]: (1) α-O_2, which was oriented along the [001] direction with a vibrational frequency of 79.5 meV and formed as a result of the conversion of the physisorbed precursor at 100 K, and (2) β-O_2, which was oriented along the $[1\bar{1}0]$ direction with a vibrational frequency of 85 meV and formed upon O_2 dosing at higher temperature ~110 K. An earlier HREELS study [260] have observed a similar trend for Ag(001) – in this instance three distinct chemisorbed O_2 species, the vibrational signatures of two of which are quite close to those just described. In addition, it found that, though O_2 molecules are stable below 130 K, when temperature rises above 150 K atomic oxygen (O) moieties form on the substrate, followed by a substantial change in the morphology of Ag(110) [261]. A yet earlier low-energy electron diffraction (LEED) study [262] have shown that the adsorption of O leads at 300 K to the formation of ordered (nx1) adlayer

chains on Ag(110). A subsequent STM study has strongly suggested that, upon adsorption of O, Ag(110) undergoes added-row reconstruction on the step edges along the [001] direction [263]. Similarly, LEED and Helium-diffraction measurements together with phonon-dispersion calculations [264] and low-energy ion-scattering measurements complemented by Monte Carlo simulation of the ion trajectories [265] have clearly demonstrated that the adsorption of O on Ag(110) results in an O(2x1)-Ag(110) structure, which induces a missing-row reconstruction (from the complementary point of view an added-row reconstruction) along the [001] direction, as has been shown in the analogous case of O(2x1)-Cu(110) [266-270].

In spite of this extensive history of investigation, there still remain unresolved issues. While O_2 preferentially adsorbs in a FFH site on Ag(110), where it lies flat on the surface, its orientation (the alignment of its molecular axis with respect to the Ag rows aligned along the $[1\bar{1}0]$ direction) has been controversial. For instance, an STM study [271] concluded that tunneling electrons cause the rotation of O_2 from the [001] direction to the $[1\bar{1}0]$, so that O_2 along the $[1\bar{1}0]$ is more stable than O_2 along the [001]. Nevertheless, conclusions drawn from theoretical studies conflict with this picture as well as with each other. For example, a DFT study by Gravil *et al.* [272] shows that O_2[001] is more favorable than $O_2[1\bar{1}0]$ by 40 meV. Another DFT study by Olsson *et al.* [273] claims that O_2[001] and $O_2[1\bar{1}0]$ have the same adsorption energy with no preference of their two orientations. In contrast, a theoretical study [274] of the energetics and dissociation of O_2 on an Ag(110) surface of an Ag_{24} cluster shows that the chemisorbed O_2 lay along the $[1\bar{1}0]$ direction. And a recent DFT study [275] also finds that the adsorption of O_2 with the orientation along the $[1\bar{1}0]$ is slightly more stable than that of O_2 along the [001] (The chemisorption energy of $O_2[1\bar{1}0]$ and O_2[001] are found to be 0.449 eV and 0.439 eV, respectively) and Thus, the energetic

preference for the orientation of adsorbed O_2 is yet to be conclusively established, probably because energy difference between the two orientations is so small (~ 40 meV).

An STM study [271] claims that negative-voltage-biasing induced dissociation of O_2 forms an O-O complex consisting of one O atom in the four–fold-hollow (FFH) site and another in a short-bridge (SB) site, resulting in two dissociated O atoms (one remains in original FFH site while the other moves away along [001] direction) separated by more than 10 Å (~11.7 Å, the average atomic separation of dissociated O atoms [276]). The former is stable whereas the latter is highly mobile. It also claims that O in an SB site always diffuses to another SB site, either along the [001] or $[1\bar{1}0]$ direction. The plausibility of such SB-to-SB diffusion, however, will depend on the relative stability of O in an SB with respect to that of O in other sites on Ag(110). This question, however, remains to be investigated. Moreover, theoretical investigations so far fall short of elucidating the O diffusion pathway. Lastly, no detailed study of O_2 vibrational modes that could induce O_2 dissociation on Ag(110) has yet been performed.

To address these gaps in our understanding – the orientation of an adsorbed O_2, the source and effect of the energy that promotes dissociation of O_2, and the nature of the diffusion path of atomic O after dissociation – we have carried out DFT calculations to systematically examine the relaxed geometrical structures, associated electronic properties, and energetics involved in the adsorption, dissociation, diffusion, and vibration of oxygen on Ag(110).

Employing DFT, we have systematically studied the geometrical and electronic structures, and energetics involved in the adsorption, dissociation, diffusion, and vibration of oxygen on Ag(110).

6.1.2 Theoretical Methods

Our model system of Ag(110) is shown in Figure 6.1. There are five key adsorption sites on the (110) surface – namely, four-fold hollow (FFH), three-fold hollow (TFH), on-top (TP), short-bridge (SB), and long-bridge (LB) sites. Molecular oxygen (O_2) adsorbs with two possible orientations with their molecular axis aligned along either the [1$\bar{1}$0] or the [001] direction.

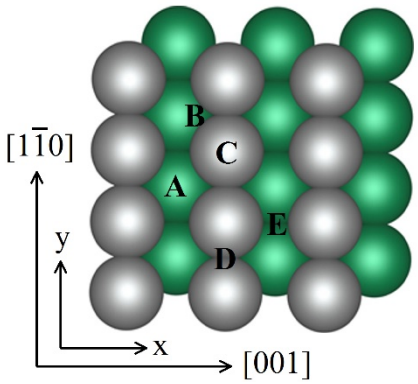

Figure 6.1 A schematic representation of Ag(110) with (3x4) surface unit cell. Light gray spheres represent Ag atoms on the top layer and light green spheres represent Ag atoms in the second layer. The possible adsorption sites for oxygen on Ag(110) are labelled as follows: A: four-fold hollow (FFH), B: three-fold hollow (TFH), C: on-top (TP), D: short-bridge (SB) and, E: long-bridge (LB). [T. B. Rawal et al., Phys. Rev. B, (2015)] (Copyright: American Physical Society 2015).

We have carried out spin-polarized DFT calculations using the VASP code [141]. We use the generalized-gradient approximation in the form of the PBE funtional [43] for the exchange-correlation of electrons. We use the PAW method [72] for ion-electron interaction. Our calculated lattice constant 4.147 Å, for the bulk Ag, is in good agreement with experimental value 4.086 Å (within 1.5%) [277]. We use the kinetic energy cutoff of 500 eV for the plane-wave expansion and sample the Brillouin zone with 9 irreducible k-points generated according to the Monkhorst-Pack scheme [74], using the Methfessel and Paxton smearing technique [76] with a smearing width of

0.1 eV. We mimic the Ag(110) using a (3x4) supercell of 5 layers with the periodic boundary condition and with 10 Å vacuum. We relax all atoms with all degrees of freedom including the adsorbates (O_2 and its dissociated O atoms) on Ag(110) until the force and the total energy reach to 0.01 eV/Å and 10^{-4} eV, respectively.

The adsorption energy (E_{ad}) is calculated as follows: $E_{ad} = E_{(slab/adsorbate)} - \left(E_{(slab)} + E_{(adsorbate)}\right)$ where $E_{(slab)}$, $E_{(adsorbate)}$ and $E_{(slab/adsorbate)}$ represent the total energies of the slab, the gas-phase adsorbates and the slab-adsorbates complex, respectively. To calculate the barriers for the dissociation of O_2 and diffusion of O species on Ag(110), we use the climbing-image nudged-elastic-band (CI-NEB) method [91] with 5 images (or 7 images for some cases) including the initial states and final states.

For calculation of vibrational frequencies of both atomic (O) and molecular (O_2) oxygen on Ag(110), we use the finite-difference method as implemented in VASP. In this work, Hessian matrix is constructed from the forces calculated after the displacement of each ion by 0.01 Å in the direction of each Cartesian coordinate. We adopt Bader analysis [77,78] for calculating the charge transfer between adsorbates and the Ag(110) substrate.

6.1.3 Results and Discussion

6.1.3.1 Adsorption and Dissociation of O_2 on Ag(110)

In Table 6.1, we present the calculated geometrical parameters and energetics per site and orientation, charge transfer. We denote these orientations of adsorbed O_2 as $O_2[1\bar{1}0]$ and $O_2[001]$, respectively. Our DFT calculations show that the most preferred adsorption site is FFH, regardless of orientation. The adsorption energy of $O_2[1\bar{1}0]$ is -0.41 eV and that of $O_2[001]$ is -0.37 eV. The

former orientation is slightly favored over the later by 40 meV. STM measurements [271] showed a ratio of the population of $O_2[1\bar{1}0]$ to that of $O_2[001]$ is 1.41 at 45 K and 1.35 at 75 K. This analysis supports our conclusion about preferred adsorption orientation by O_2. At the LB site, we find O_2 adsorption is either weak (E_{ad}= -0.07 eV) or unstable, depending on the axis of orientation. At a SB site, $O_2[1\bar{1}0]$ is considerably more favorable than for $O_2[001]$. On the other hand, O_2 adsorption at the TP site, aligned along [001] or [110], is not stable.

Table 6.1 The adsorption energy, zero-point energy, bond length, charge gained, and magnetization of O_2 on the adsorption sites at different orientations on Ag(110). do-o indicates distance between the constituent O atoms; shortest do-Ag indicates a distance between an O atom and the Ag closest to it. [T. B. Rawal et al., Phys. Rev. B, (2015)] (Copyright: American Physical Society 2015).

Adsorption site	**O_2 orientation**	**Adsorption energy (eV)**	**Zero-point energy (eV)**	**d_{O-O} (Å)**	**shortest d_{O-Ag} (Å)**	**Charge gained by O_2 (electron)**	**Magnetization (μ_B)**
FFH	[001]	– 0.37	0.101	1.428	2.331	0.90	0.08
	$[1\bar{1}0]$	– 0.41	0.106	1.465	2.348	0.95	0.00
TP	[001]	0.45	0.072	1.328	2.337	0.54	0.48
	$[1\bar{1}0]$	0.42	-0.016	1.329	2.372	0.55	1.41
SB	[001]	0.12	0.068	1.412	2.345	0.81	0.04
	$[1\bar{1}0]$	– 0.07	0.113	1.341	2.211	0.71	0.21
LB	[001]	– 0.07	0.085	1.334	2.231	0.64	0.00
	$[1\bar{1}0]$	0.07	0.070	1.470	2.458	0.98	0.00

Figure 6.2(a-b) show the minimum energy paths (MEPs) for O_2 dissociation at FFH site. The calculated energy barriers for dissociation of $O_2[1\bar{1}0]$ and $O_2[001]$ are 0.50 eV and 0.42 eV, respectively. Our calculated values are found to be smaller than those (0.62 eV and 0.76 eV, respectively) calculated by Gravil [272] by more than 0.1 eV. Interstingly, in the final state of O

atoms dissociated along [001] (Figure 6.1.2b), O atoms cause a slight a local disorder on Ag(110), i.e, a Ag atom in the second layer buckled up by dissociated O atoms by ~0.5Å.

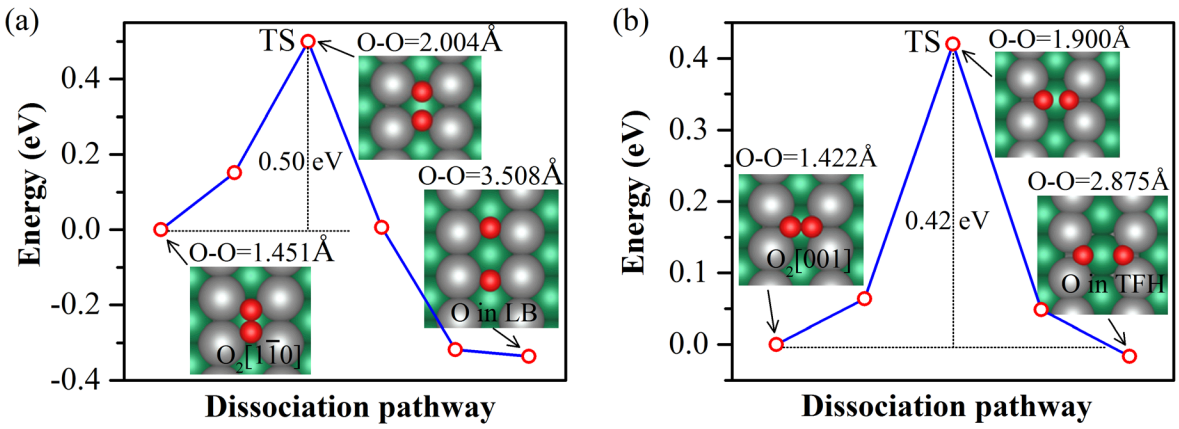

Figure 6.2 Minimum energy pathways (MEPs) for the dissociation of O_2 adsorbed in an FFH site with its orientation along the (a) $[1\bar{1}0]$ and (b) [001] directions, respectively. The structures for initial states, transition states and final states (local minima) are shown above. Color code: Ag atoms on top layer (light gray), Ag atoms on second-from-top layer (light green, O atoms (red). [T. B. Rawal et al., Phys. Rev. B, (2015)] (Copyright: American Physical Society 2015).

On Ag(110), O_2 dissociation can be induced by injecting electrons to O_2 from the STM tip [271,276]. Under the application of bias voltage, the tunneling of electrons takes place from the STM tip to the anti-bonding orbital ($2\pi^*$) of the adsorbed O_2. This is so-called the injecting of electrons to O_2 which leads to the elongation of O-O bond, thereby making O_2 dissociation easier. Therefore, to gain insights into the charging effects in O_2/Ag(110) systems, we do the calculations of the electronic structure and the energetics of the systems by adding or removing an electron.

The most noticeable effect of the charged systems is the difference in energetic and the geometry of $O_2[001]$ and $O_2[1\bar{1}0]$. Recall that, in the case of neutral system, $O_2[1\bar{1}0]$ adsorbed at FFH site in parallel to the surface is the preferred one. On the other hand, when an electron is

added to the neutral O_2/Ag(110) sytem, then the prefereed orientation of O_2 is altered from [$1\bar{1}0$] to [001] since O_2[001] has lower energy of 0.08 eV than O_2[$1\bar{1}0$] does. Thus, we expect that O_2 aligned along [$1\bar{1}0$] can rotate to the [001] direction upon the tunneling of electrons from STM tip to the molecule, as observed in the experiment. Furthermore, the O-Ag and O-O bonds are found to be affected differently for O_2[001] and O_2[$1\bar{1}0$] molecules. Figure 6.3 summarizes these bonds as a function of these O_2 species under different conditions: neutral, charged by adding or removing electron. Upon charging the O_2/Ag(110) by removal or addition of an electron, it turns out that there is an trivial affect in the geometry of O_2[$1\bar{1}0$]. In contrast, the geometry of O_2[001] is significantly affected when an electron is added to the system. Our calculations reveal that O-Ag bond is shortened by 0.28 Å whereas O-O bond is increased by 1.45 Å.

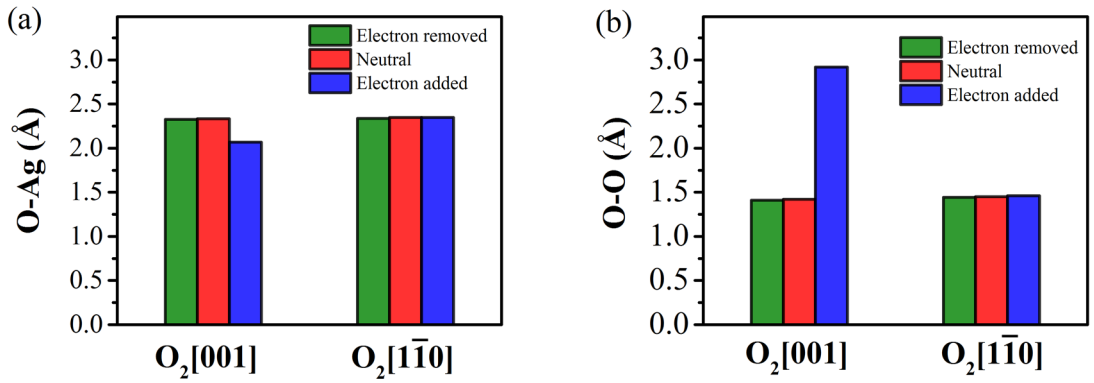

Figure 6.3 Bond lengths: (a) O-Ag and (b) O-O of O_2 on Ag(110) aligned in two orientations, namely [001] and [$1\bar{1}0$].

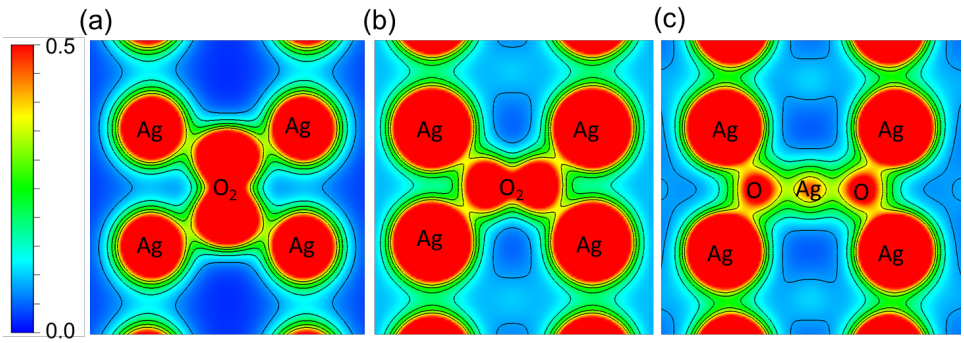

Figure 6.4 Valence charge density of the charged O_2/Ag(110) systems (+1 electron) with O_2: (a) aligned along $[1\bar{1}0]$; (b) aligned along [001] at the FFH (For this structure only electronic relaxation is performed); and (c) dissociated along [001]. The charge density is plotted by selecting three atoms for the (001) plane with the saturation level ranging from 0.0 to 0.5 e/Å^3. The contour values range from 0.08 to 0.43 with the interval 0.07 e/Å^3.

In order to understand the bonding characteristic of the charged O_2/Ag(110) upon addition of an electron, we have calculated the valence charge density, shown in Figure 6.5. As clearly seen in the Figure, $O_2[1\bar{1}0]$ has molecular bonding with the individual atoms covalently bonded with two Ag atoms at the top layer. On the other hand, O_2[001] dissociates upon the addition of electron, and dissociated molecule, i.e. two atomic oxygen forms covalent bonding with two Ag atoms at the top layer and with one Ag atoms at the second layer.

Figure 6.5 shows the electronic denisty of states projected onto the O p orbtials of the charged system. As shown in the figure, the anti-bonding state (red trace) is filled up by electron, leading to this state becomes occupied (green trace). The analysis of electronic density of states thus allows us to conclude that the O_2[001] dissociation on Ag(110) occurs when an electron is added to O_2/Ag(110) system owing to the fact that the anti-bonding orbital is filled up by electron.

Threrefore, we can say that the injected electron to O_2 occupies the σ_{2p_x} antibonding state of O_2, thus inducing the O_2 dissociation.

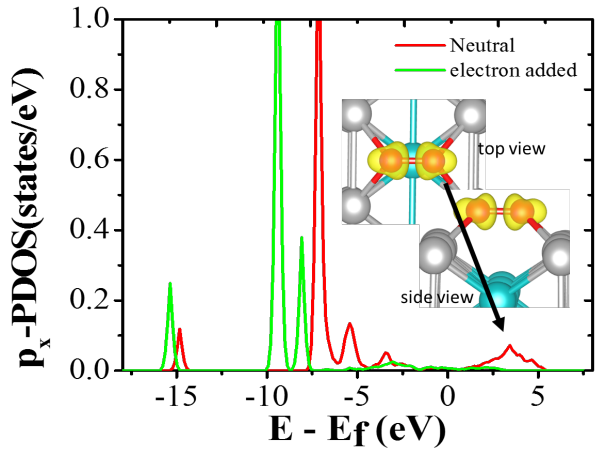

Figure 6.5 Projected density of states (PDOS) for p_x orbitals of O_2 aligned along [001] on Ag(110). The red curve is for the neutral O_2/Ag(110) system with full relaxation but the green curve for the charged system with addition of an electron. Here, the PDOS of the latter was obtained after only the electronic relaxation. The partial charge density related to anti-bonding (unoccupied) states are given in inset.

Important scenario could be associated with the charged O_2/Ag(110) systems: (i) initially O_2 adsorbs at the FFH site aligning along $[1\bar{1}0]$; (ii) when electron is injected (e.g. by a STM tip), this electron excites O_2 and then occupies the σ_{2p_x} anti-bonding state. This could lead to the rotation of O_2 from $[1\bar{1}0]$ to [001] direction by 90^0; (iii) finally the excited O_2 dissociates. iv) After O_2 dissociation each O atom prefers three-fold coordinated, and an Ag atom (right below adsorbed O_2) is pulled up by O atoms. The peak above the Fermi-level indicated by an arrow is σ_{2p_x} anti-bonding state, and these state is filled upon injection of an electron.

6.1.3.2 Adsorption and Diffusion of Atomic Oxygen

Atomic oxygen prefers to adsorb at FFH, with an adsorption energy of -3.88 eV. The next-preferred adsorption site is TFH, where O adsorbs with an adsorption energy of -3.87 eV. Inclusion of zero-point energy slightly decreases the adsorption energy by 10-20 meV. Based on Bader analysis, we find that the charge transfer takes place from Ag to O species. In each case, increasing the O-Ag distance (distance between O and first-neighboring Ag atoms in the first layer) is proportional to the magnitude of the charge transfer. Overall, these results show the trend, FFH> LB>TFH>SB, for both the charge transfer and O-Ag bond length of O species adsorbed in sites.

Our DFT results show that there is no barrier for the diffusion of O from SB to TFH or FFH along [001]. On the other hand, O atom has to overcome a barrier of 0.39 eV in order to diffuse from TFH to SB. Moreover, we find that there is a barrier of 0.42 eV for the diffusion of O from SB to another SB along [001] (Figure 6.6a). And, the energy barrier for the diffusion of O from FFH to the next nearest FFH along $[1\bar{1}0]$ is 0.072 eV (Figure 6.6b). On the other hand, the barrier for the diffusion of O from one FFH to the next FFH along [001] is 0.42 eV, suggesting that O diffusion from FFH to the next along [001] is not favorable. In addition, we find that there is a barrier of 0.045 eV for diffusion of O from LB to FFH. Overall, our results show that an O atom can easily diffuse from an FFH site to another FFH site along $[1\bar{1}0]$.

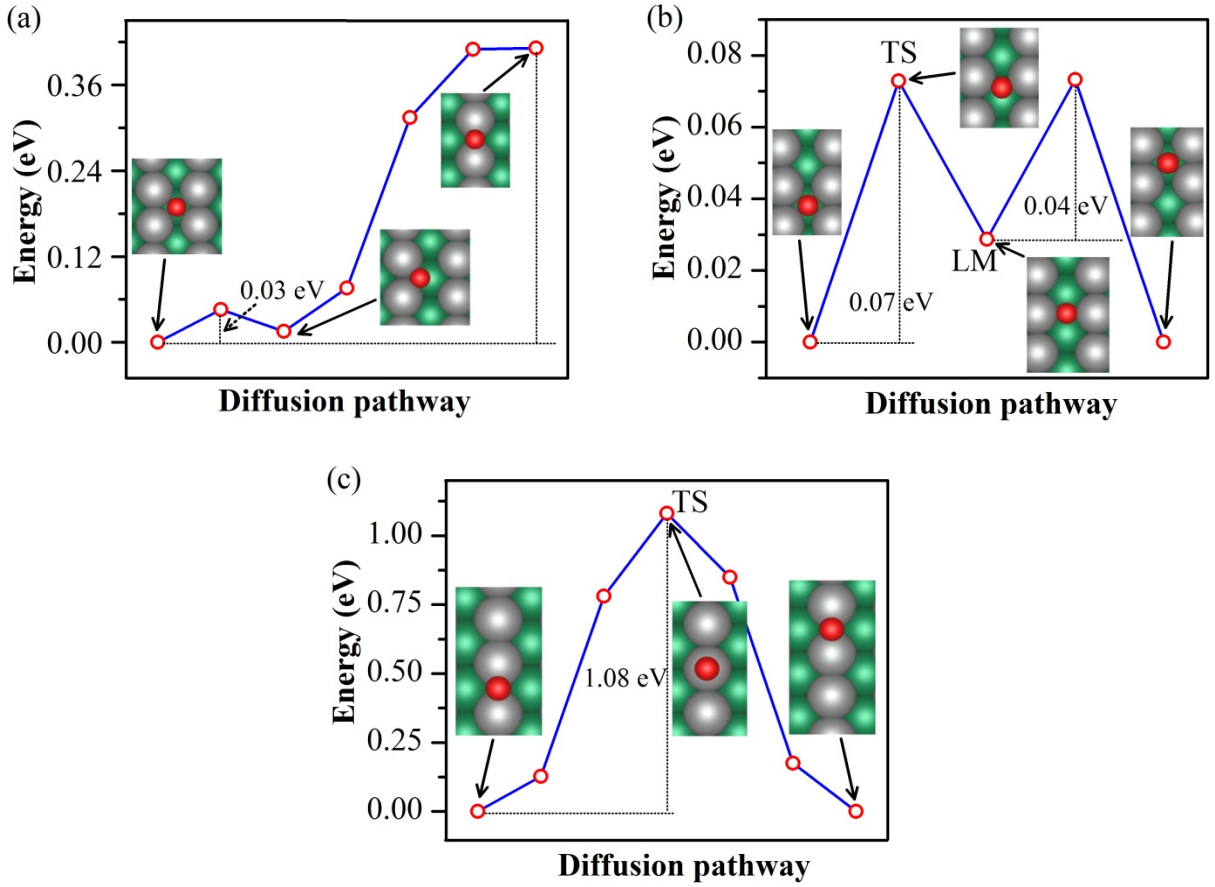

Figure 6.6 Diffusion of atomic oxygen: (a) from FFH to SB along [001] direction, (b) from FFH to FFH along [1$\bar{1}$0] direction, and (c) from SB to SB along the [1$\bar{1}$0] direction. The initial states, transition states and final states are also shown. [T. B. Rawal et al., Phys. Rev. B (2015)] (Copyright: American Physical Society 2015).

Furthermore, our results show that O needs to overcome an energy barrier of 1.08 eV in order to diffuse from one SB site to another SB along [1$\bar{1}$0]. This barrier is higher than the barrier of 0.42 eV along the [001], indicating that O can easily diffuse along [001]. However, Hahn and Ho [271] suggest that O diffusion from a SB to another SB is easier than O diffusion from a SB to FFH. Our calculated PES profile (Figure 6.6a), however, shows that O species can easily diffuse

from an SB to an FFH site without experiencing a barrier. Therefore, our DFT calculations suggest that O atoms cannot exist at the SB site as residual stable species.

6.1.3.3 Simulated STM Image for O on Ag(110)

Figure 6.7(a) shows the optimized geometry of O adsorbed in four-fold hollow (FFH) site of Ag(110). As discussed earlier, O at FFH site is the preferred geometry at 0K temperature. In this configuration, O covalently bonds with four Ag atoms on the top layer. The O1-Ag1, and Ag1-Ag3 distances are calculated to be 2.396Å and 3.688 Å, respectively.

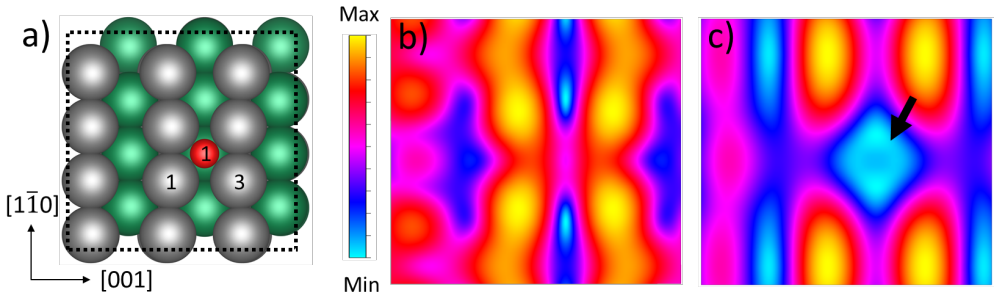

Figure 6.7 (a) DFT-optimized structure of O in FFH site of Ag(110); (b-c) the corresponding simulated STM image for the bias of (b) -0.07 V and (c) 0.3 V.

Figure 6.7(b-c) shows the simulated STM image of O in FFH site which indicates that the topological STM images of O relates to the depression feature either at or near the vicinity of O atom. As compared to the simulated STM image at -0.07V, the STM image simulated at 0.3V has clear depression. This depression feature is related to the depletion of metal-free electron like charge density in the vicinity of O atom. Thus, these atomic features on the simulated images can be understood from the electronic structures. The contribution to the electronic states near the Fermi level from O p states must be smaller than the Ag states. Therefore, the contribution to local

density of states integrated from -0.3 V to Fermi energy from the tunneling through Ag states is electronically favorable over the contribution from tunneling through O p states.

Figure 6.8(a) shows the optimized geometry of O adsorbed in three-fold hollow (TFH) site of Ag(110). As discussed earlier, O at TFH site is the second preferred geometry at 0K temperature. In this configuration, O covalently bonds with two Ag atoms on the top layer. The O1-Ag1, and Ag1-Ag2 distances are calculated to be 2.147Å and 3.159 Å, respectively.

Figure 6.8(b-c) shows the simulated STM image of O in TFH site which indicates that the topological STM images of O relates to the depression feature either at or near the vicinity of O atom. The results indicate that STM image for both bias -0.07 V and 0.3 V, there is asymmetric type of depressions around the vicinity of O in TFH site.

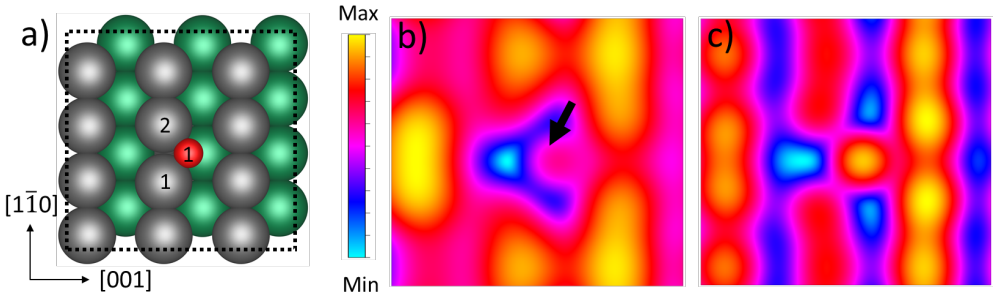

Figure 6.8 (a) DFT-optimized structure of O in TFH site of Ag(110); (b-c) the corresponding simulated STM image for the bias of (b) -0.07 V and (c) 0.3 V.

6.1.3.4 Vibration of Oxygen on Ag(110)

Calculated vibrational frequencies of atomic oxygen on Ag(110) are provided in Table 6.2. The stretching mode of an O atom at FFH against the substrate has a frequency of 38 meV, in agreement with the experiment (39.1 meV) [278]. The vibrational frequency of O at LB with the

same stretching mode (stretching of O against the substrate) is found as 43 meV, closer to the experiment (40 meV [279]; 40.5 meV [259]). Our calculated vibrational frequencies for the same stretching mode of O at TFH and SB are 44 and 54 meV, respectively. Since O atom at SB has one negative mode, i.e., the frustrated translation mode with frequency -10 meV, implying O at SB is unstable.

Table 6.2 Vibrational frequencies of an O atom adsorbed at four possible sites on Ag(110), after relaxation of both adsorbate and substrate. For each site of O on Ag(110), we give in parentheses the frequencies calculated with only O allowed to vibrate, and the Ag substrate is frozen. [T. B. Rawal, Phys. Rev. B (2015)] (Copyright: American Physical Society 2015).

Vibrational modes	**FFH (meV)**	**TFH (meV)**	**SB (meV)**	**LB (meV)**	**Exp. (meV)**
O-Ag stretching	38(35)	44(39)	54(51)	43(33)	40.5, 39.1, 40.0
Frustrated translation along the $[1\bar{1}0]$ direction	21(19)	41(38)	51(47)	35(30)	
Frustrated translation along the [001] direction	20(13)	33(23)	-10(-7)	22(19)	

The O-O intra-molecular vibrational frequency of gas-phase O_2 is found as 194 meV, in good agreement with the experiment (196 meV). Upon adsorption on Ag(110), its vibrational frequency is affected by the O_2-Ag interaction. Figure 6.9 summarizes the O-O stretching frequencies of O_2 adsorbed at various sites of Ag(110). Our calculated O-O stretching frequency of $O_2[1\bar{1}0]$ on Ag(110) is 92 meV, slightly higher than experiment [47,20]. On the other hand, the stretching frequency of O_2[001] is 84 meV (in the frozen configuration) and 96 meV (in the unfrozen configuration). Previous theoretical study [280] reports that, at FFH, the frequency of O_2[001] and $O_2[1\bar{1}0]$ are 100 and 95 meV, respectively. Another study [281] reports that the

vibrational frequencies of $O_2[001]$ and $O_2[1\bar{1}0]$ at FFH are 103 and 101 meV, respectively. Thus, our calculated frequencies are in reasonable agreement with calculated values reported by previous theoretical studies [280,281].

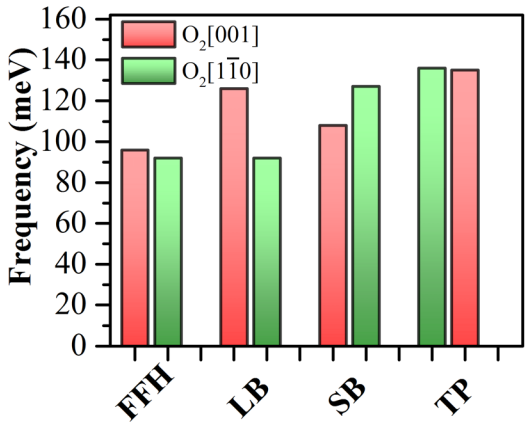

Figure 6.9 O-O stretching frequency of adsorbed O_2 at FFH, LB, SB, and TP sites of Ag(110).

Our DFT results reveal that, although the O-O stretching frequency of $O_2[1\bar{1}0]$ is not affected even by letting the Ag substrate to vibrate in our calculations, that of $O_2[001]$ is significantly affected by the substrate – upto 10-12 meV. This indicates that the stretching frequency of $O_2[001]$ is strongly coupled with the substrate vibration, and that the dissociation of $O_2[001]$ is more strongly affected by substrate vibrations than that of $O_2[1\bar{1}0]$. Our results is consistent with the previous reports that the $2\pi^*$ orbital resonance, located at the Fermi level of $O_2[001]$ [273] involves vibrations [282] like the O-O stretching frequency as well as the stretching frequency of O_2 againest the Ag substrate.

6.1.4 Summary

Employing DFT, we have studied adsorption, dissociation, diffusion, and vibration of oxygen on Ag(110). Our results show that O_2 at the favored FFH site oriented along $[1\bar{1}0]$ is slightly more favorable than O_2 along [001]. In addition, dissociation of O_2 along [001] is more favorable than that of O_2 along $[1\bar{1}0]$. In contrast to $O_2[1\bar{1}0]$, O_2[001] species gains vibrational energy from the substrate, so the dissociation of O_2[001] is relatively more favorable than that of $O_2[1\bar{1}0]$.

Our DFT calculations reveal that O will not follow a diffusion path from one SB site to another. Since O species at the SB site has imaginary frequency which can induce the oscillation of this species toward the minimum potential energy site – either TFH or FFH. The barrier for diffusing O from an FFH site to the next nearest FFH site along $[1\bar{1}0]$ is ~0.07 eV, which is far smaller (5.7 times smaller) than the barrier for diffusing from an SB to another SB, regardless of the direction. Therefore, most likely diffusion path of O can be from a SB site is to the TFH site because of the downhill potential along the diffusion path.

6.2 Part II. CO Oxidation on Disordered Ag(110): Insights from First Principles Study

Using density functional theory (DFT)-based simulations, we examine the CO oxidation on Ag(110). We find that free Ag atoms at the top surface layer and those involved in the O-Ag-O chain have distinct local chemical activity since they provide different binding affinity to CO. Additionally, we find that there are two chemically-distinct O species on Ag(110) – strongly bound O species that forms O-Ag-O chains, and weakly-bound O species that exists as single species. The former species spontaneously reacts with CO whereas the latter species needs a barrier for the

reaction. The chemical activity of disordered Ag(110) can, therefore, be quite different from that of pristine surface.

6.2.1 Introduction

Oxidation of carbon monoxide (CO) has long been a model catalytic reaction in heterogeneous catalysis [283-286]. Since CO is a toxic gas and a poisoning gas in many industrial catalytic processes, its oxidation is of great importance in gas purification and in efficiently catalytic conversion of the reactant gases. Silver (Ag) can be a potential candidate for catalyzing CO oxidation at low temperature. Indeed, there are some earlier studies [250,287,288] on the exploration of Ag-based materials for CO oxidation.

Identification of reactive O species on Ag(110) is essential for understanding the catalytic oxidation of CO since various O species can lead to different reaction channels. Note that the dissociative adsorption of O_2 above 150-200 K [258,261,272] can lead to a variety of O species. Indeed, two chemically distinct O species, denoted as O_A and O_B, are reported [289]. The former was identified as O species adsorbed at the four fold hollow site whereas the latter was speculated to be the O species involved in the formation of O-Ag-O chains. Two O species with their different reactive nature were also observed on Cu(110) [290]. However, none of these studies has provided a rationale for why these two species are chemically distinct.

Herein, we examine the catalytic CO oxidation on Ag(110) by means of DFT. We provide insights in the formation of O-Ag-O chain, leading to the locally disordered surface which have quite different chemical activity from that of pristine surface.

6.2.2 Computational Details

We perform density functional theory (DFT) calculations using VASP code[141]. We use PBE functional [43] for the exchange-correlation of electrons, and used the projector-augmented wave (PAW) method [72] for the ion-electron interaction. We use the kinetic energy cutoff of 500 eV for plane-wave expansion and sample the Brillouin zone with (4x5x1) and (8x10x1) k-points mesh (for 4x4 and 2x2 supercells, respectively), which are generated according to the Monkhorst-Pack scheme [74]. We use the Methfessel and Paxton smearing technique [76] with a smearing width of 0.1 eV for integration over the Brillouin zone. We use (4x4) and (2x2) supercells of 5 Ag layers with periodic boundary conditions with 15 Å vacuum. We relax the atoms in the considered systems until the accuracy for the force and energy convergence are reached to 0.01 eV/Å and 10^{-4} eV, respectively.

We calculate the minimum energy paths for diffusion and oxidation of CO using the climbing-image nudged elastic band (CI-NEB) method [86,91] with 7 or 9 images including the initial states and final states.

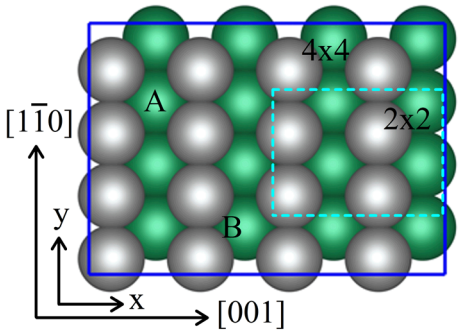

Figure 6.10 A schematic diagram of (4x4) of Ag(110); Inset: (2x2) unit cell. Color code: Ag atoms at the top layer (gray) and Ag atoms at the second layer (green). We use the similar representation for Ag atoms hereinafter. Adsorption sites: A- four-fold hollow (FFH) and, B- three-fold hollow (TFH) are also shown.

6.2.3 Results and Discussion

Before we present our results for the reaction between CO and O reaction on Ag(110), we show that at high coverage O atoms prefer to form O-Ag-O chain on the surface. As we shall show that the formation of the O-Ag-O chain, resulting in the significant rumpling of the surface.

6.2.3.1 Formation of O-Ag-O Chain and Disordering on Ag(110)

Prior to the formation of O-Ag-O chain on Ag(110), O_2 molecules are imposed to undergo dissociation either along $[1\bar{1}0]$ or [001] depending upon the orientation of O_2. Depending upon their coverage, the dissociation may lead to various O species on the surface. Here, we will depict two kinds based on our DFT calculations. At very low O coverage, we find that the most favored species are O atoms adsorbed at four-fold hollow (FFH) site, denoted as O_{FFH}. The next favored are O atoms adsorbed in three-fold hollow (TFH) site, denoted as O_{TFH}. The binding energies of these O species differ only by 10 meV.

In Figure 6.11, we present optimized structures for the different configurations of four O atoms adsorbed at various sites on Ag(110), corresponding to 1/4 monolayer (ML) coverage, in the energetic order from the lowest to the highest. The two lowest-energy O/Ag(110) configurations (Figures 6.11a-b) exhibit the formation of O-Ag-O chains. It is thus clear that the formation of O-Ag-O chains is more favorable than the scattered distributions of single O atoms on Ag(110) (Figures 6.11c-h). In fact, the O-Ag-O chains, shown in Figures 6.11(a-b), are infinitely long (because of the periodic boundary condition used in our calculations). While the formation of such an infinite long chain is not practical in reality, our results are quite enough to prove the formation of short O-Ag-O chains on Ag(110). Note that O species in the O-Ag-O chains

are either the combination of O_{FFH} and O_{TFH} or the combination of only O_{TFH}. Although both configurations in Figures 6.11(a-b) show significant surface structural changes, the O-Ag-O chain in Figure 6.11(a) exhibits a more pronounced lateral displacement by the chain than that in Figure 6.11(b), as a result of additional bonding of the O atoms with a nearby Ag rows along [$1\bar{1}0$]. In addition, in this chain half of the O species are in FFH, i.e. O_{FFH} and the other half in TFH. But, in the geometric structure as displayed in Figure 6.11(b) Ag atoms in the O-Ag-O chain undergo only vertical displacement, i.e. buckling by 0.56 Å.

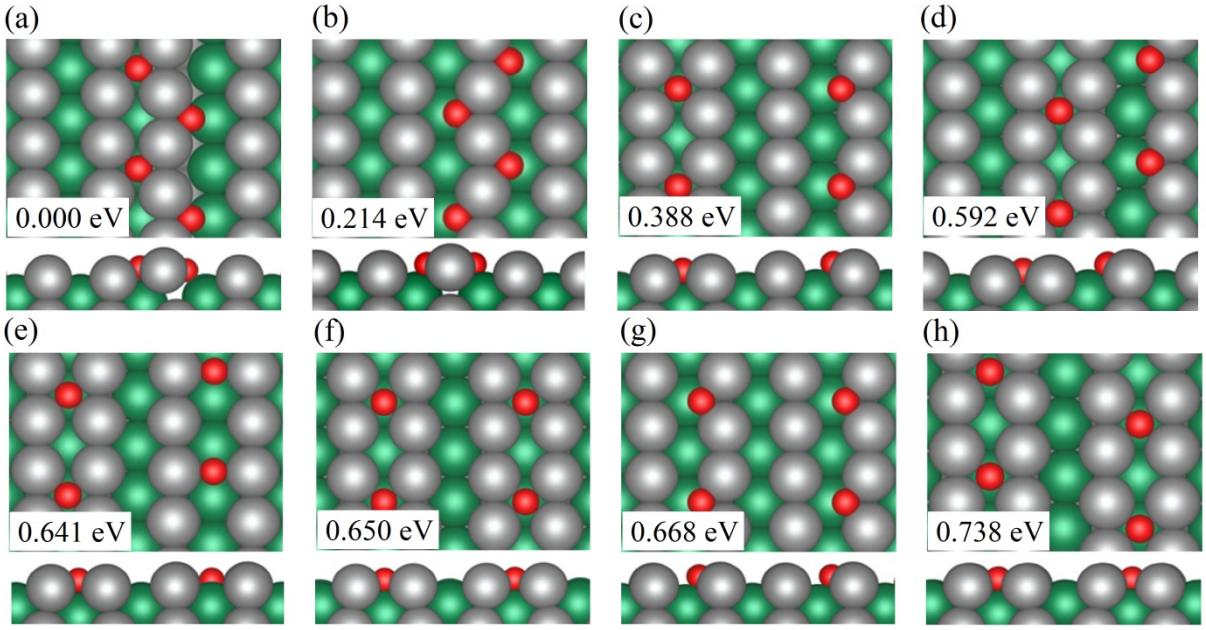

Figure 6.11 Configurations of four O atoms adsorbed on Ag(110), corresponding to 0.25 ML coverage on Ag(110): (a) formation of O-Ag-O chains where two O atoms are four-fold coordinated and two O atoms are three-fold coordinated; (b) same as (a) but all O atoms are three-fold coordinated; (c-h) various other O/Ag(110) configurations. Here, ΔE is the energy difference with respect to the lowest energy configuration. In each figures from (a) to (h), top panel shows the top views of the relaxed structures, and the bottom panel shows the side views. Color code: O atoms (red).

Figure 6.12 shows the optimized structure of O-Ag-O chain on Ag(110), as mimicked by (2x2) unit cell. The Ag atoms forming the O-Ag-O chain undergo vertical and lateral displacements of 0.564 Å and 0.774 Å, respectively (see Figure 6.12b). Such a large Ag displacement does not, however, occur in the other configurations of single, scattered O species adsorbed on Ag(110) as shown in Figure 6.11(f), in which there is only minor displacement of the Ag atoms surrounding the adsorbed O atoms. Therefore, we designate the Ag(110) surface with the formation of the O-Ag-O chains as the disordered Ag(110) phase and the Ag(110) surface with single O species to be the ordered one. The energy difference between the ordered and disordered Ag(110), namely, between the configurations shown in Figure 6.11(f) and Figure 6.11(b) is 0.44 eV. We estimate that the binding energy of the O_{TFH} species (per atom) forming the O-Ag-O chain (Figure 6.11b) is ~0.1 eV larger than that of the single O_{FFH} species (Figure 6.11(f)). Thus, O species embedded in the disordered Ag(110) phase is more tightly bound to Ag atoms than the species on the ordered surface.

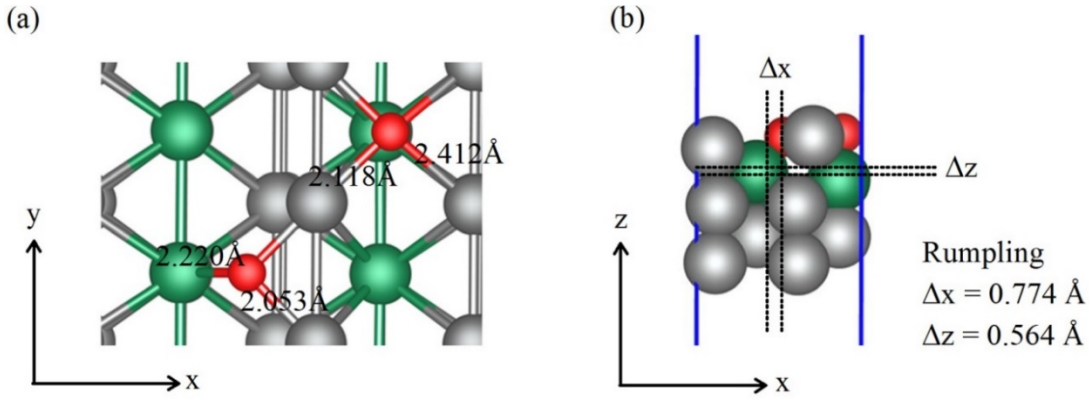

Figure 6.12 Optimized structure of O/Ag(110) system: (a) top and (b) side views.

6.2.3.2 Adsorption of CO on Ag(110)

In Table 6.3, we summarize the adsorption energies of CO at various sites (LB, SB, TP) for the coverage of 1ML,1/2ML,1/4ML,1/8ML, and 1/12 ML. These results indicate that at half monolayer (ML) coverage and below, the adsorption energy of CO is almost constant, ~ -0.33 eV but at full coverage (1 ML) it reaches to -0.25 eV due to the steric repulsion. Our results show that the favorable adsorption site is at TP of Ag atom (Figure 6.15a).

Table 6.3 Adsorption energies and optimized geometrical parameters of CO on ordered Ag(110).

Coverage	**Unit Cell**	**Sites**	**E_{ads} (eV)**	**$d_{(C-O)}$ (Å)**	**$d_{(C-Ag)}$ (Å)**	**$A_{(O-C-Ag)}$ (°)**
1 ML	1x1	TP	-0.25	1.153	2.111	180
1/2 ML	1x2	LB	-0.02	1.161	2.539	125
		SB	-0.28	1.162	2.248	138
		TP	-0.33	1.152	2.108	180
1/4 ML	2x2	LB	-0.05	1.165	2.401	127
		SB	-0.29	1.163	2.253	138
		TP	-0.33	1.151	2.113	180
1/6 ML	2x3	LB	-0.02	1.166	2.392	126
		SB	-0.29	1.163	2.247	138
		TP	-0.33	1.150	2.110	180
1/8 ML	2x4	LB	-0.06	1.166	2.380	126
		SB	-0.27	1.164	2.242	138
		TP	-0.33	1.150	2.115	180
1/12 ML	3x4	LB	-0.05	1.165	2.395	126
		SB	-0.30	1.163	2.245	138
		TP	-0.35	1.150	2.116	180
			(in gas phase)	1.143		

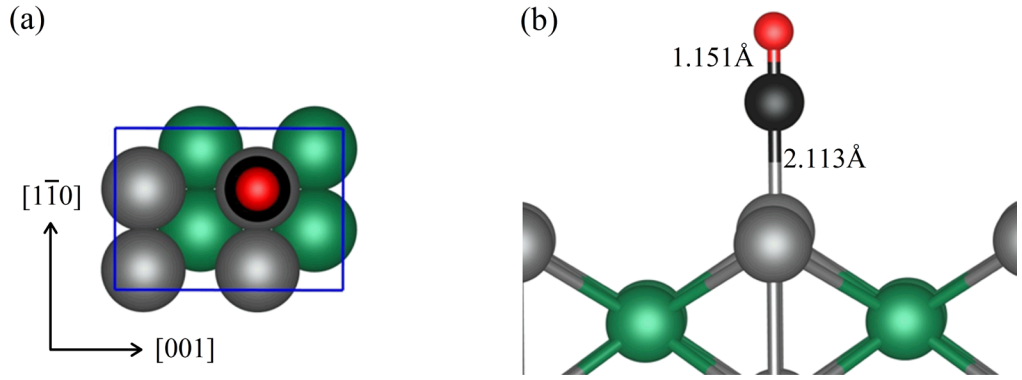

Figure 6.13 Optimized structure of CO/Ag(110) system: (a) top view, and (b) side view. Here, the angle O-C-Ag is 180º. Color code: C atom (black) and O atom (red).

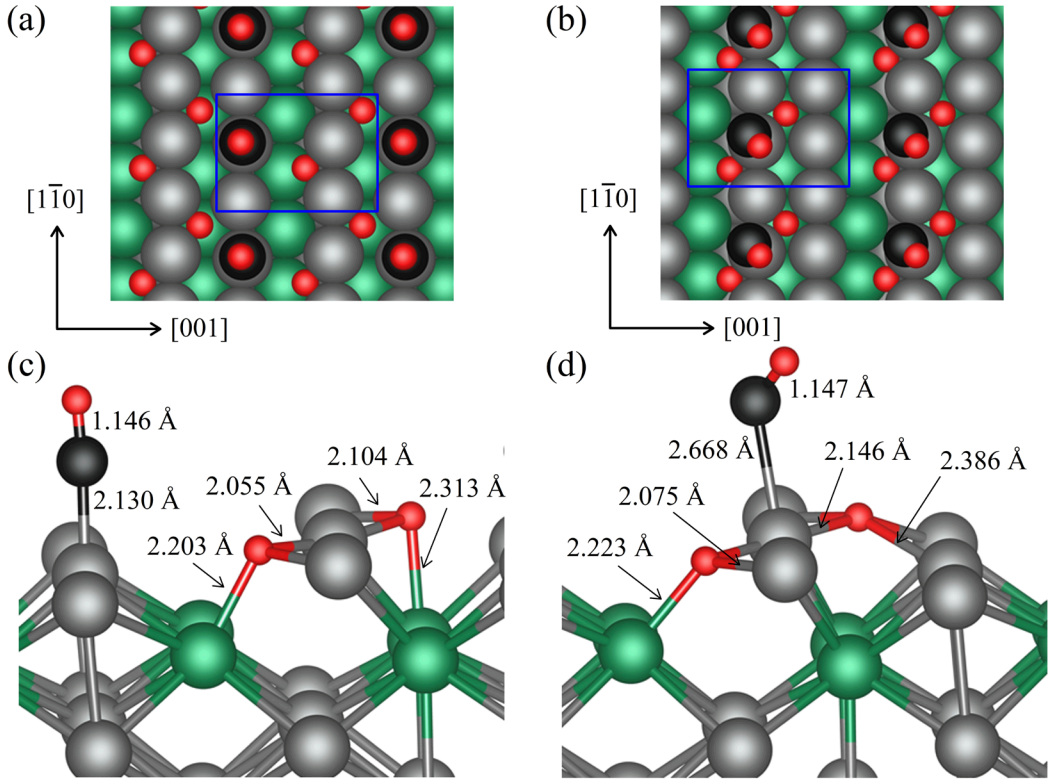

Figure 6.14 CO adsorption on the disordered Ag(110) with pre-adsorbed O atoms: (a, c) Top and side views of CO adsorbed at Ag site, which does not participate in the O-Ag-O chain; (b, d) Top and side views of CO adsorbed at Ag site, which participate in the O-Ag-O chain. The blue solid line represents the (2x2) surface unit cell.

Figure 6.14 shows the adsorption of CO at the two inequivalent TP sites on the disordered Ag(110). The two inequivalent Ag sites are: i) Ag atoms that are not involved in the formation of O-Ag-O chain (Figure 6.14a), and ii) Ag atoms that are involved in the formation of the O-Ag-O chain (Figure 6.14b). Interestingly, CO adsorption for the configuration (Figure 6.14a), with adsorption energy of -0.36 eV is more stable by ~0.3 eV than that for the configuration (Figure 6.14b) with -0.06 eV only. The C-Ag distance of the former (Figure 6.14c) is significantly shorter by 0.5 Å than that of the latter (Figure 6.14d).

6.2.3.3 CO Oxidation

Figure 6.15 depicts the minimum energy paths for CO oxidation on the disordered Ag(110). We find that the barrier for the reaction between CO and O embedded in the chain is ~0.01-0.13 eV. Thus, CO oxidation on the disordered Ag(110) needs to overcome at least energy barrier. In contrast, CO oxidation on the ordered surface, in which no O-Ag-O chain forms and singly dispersed O species are mostly monomeric, is spontaneous. Thus, the chemical activity of disordered Ag(110) is different from that of ordered surface.

We now calculate the CO diffusion from TP to TP site along the [$1\bar{1}0$] direction. Note that CO diffusion along [001] is less likely owing to its larger diffusion barrier by more than ~0.3 eV than the one from TP to TP. To discern the CO diffusion on Ag(110) in the absence/presence of O atoms, we show in Figure 6.16 the minimum energy paths for the diffusion of CO from a TP site to another TP. Note that in order to obtain the final state for the ordered Ag(110), we fixed the x,y coordinates of C atom of CO; otherwise it would spontaneously react with surface O to form CO_2.

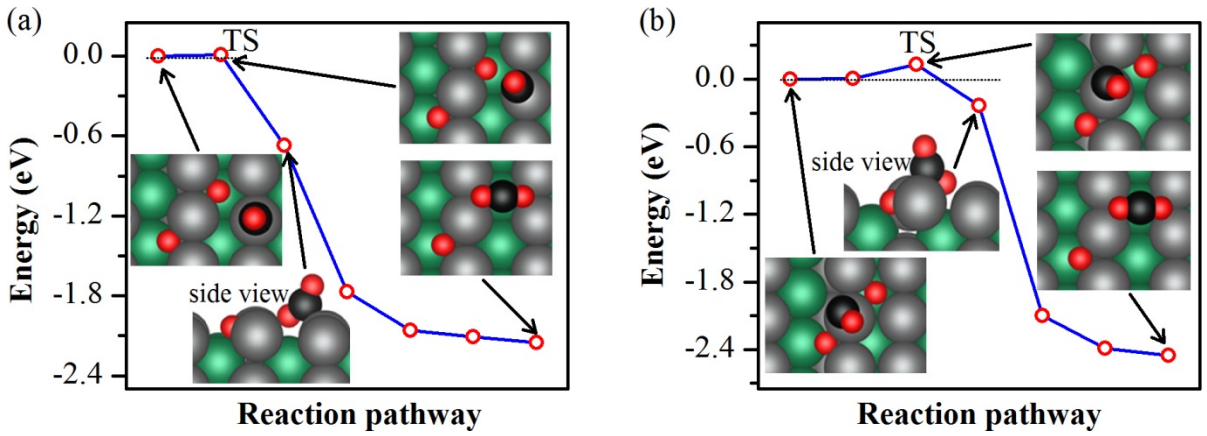

Figure 6.15 DFT-calculated minimum energy paths for CO oxidation with O species embedded in the O-Ag-O chain: (a) CO adsorbs at Ag site that has no bond with O species, and (b) CO adsorbs at the Ag site which participates in the O-Ag-O chain.

The barriers for CO diffusion on ordered Ag(110) are similar as the order of ~0.06 eV whereas the barrier on the disordered surface is relatively higher, i.e. ~0.11 eV. The highest-energy point in the potential energy profile for the CO diffusion on the disordered surface occurs when a diffused CO sits at the SB site (Figure 6.16b) whereas on the ordered surfaces the same point occurs just before the CO sits in the SB sites (Figures 6.16a,c). This suggests that CO adsorption at the SB site on the disordered Ag(110) has higher energy.

On both ordered and disordered Ag(110), the calculated CO diffusion barrier (~60-100 meV) turns out to be significantly larger than the barrier (10 meV) for reaction between O and CO, implying that overall CO oxidation on both surfaces may be governed by CO diffusion rather than activation for reaction between O and CO. Thus, difference in reactivity of ordered and disordered Ag(110) thus may arise from CO kinetics, rather than CO reaction energetic.

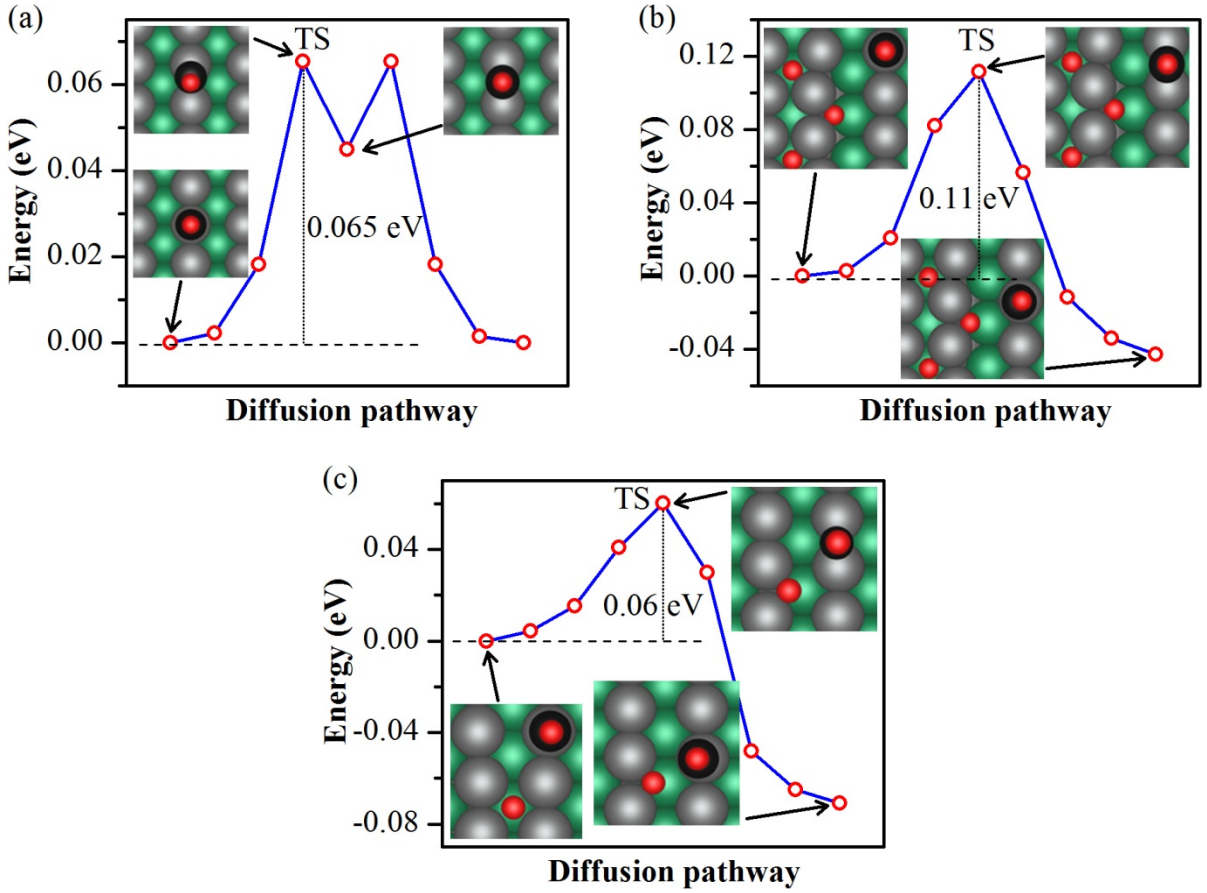

Figure 6.16 Diffusion of CO on: (a) the ordered, and (b) disordered Ag(110), making O-Ag-O short chain; and (c) the ordered Ag(110) with singly dispersed O species.

As discussed earlier, we have found that the catalytic activity of ordered and disordered Ag(110) is distinct such that i) the energy barrier for reaction between O and CO is zero on the ordered surface whereas it is in the range of 10-130 meV on the disordered Ag(110), and ii) the diffusion barrier is 60 meV on the ordered Ag(110) whereas it is 110 meV on the disordered surface. Furthermore, CO adsorption and activation energy, even on the same disordered surface, are different for the Ag atoms that forms the O-Ag-O chains from those for the Ag atoms that do not form the chain. The CO adsorption energy and diffusion barrier on the latter (-0.36 and 0.01

eV, respectively) are stronger and smaller, respectively, than those on the former (-0.06 and 0.13 eV, respectively). Considering that the former are bonded both to O_{TFH} and O_{FFH} but the latter are bonded only to single O_{FFH} species, all these findings point to the clear distinction in catalytic activity such that the Ag atoms bonded to O_{TFH} (in O-Ag-O chain) are catalytically less active than those bonded only to single O_{FFH}.

6.2.3.4 Bader Analysis and Density of States

Bader analysis indicates that there is a difference in charge redistribution between the Ag atoms that form O-Ag-O chain and those that do not. The latter lose ~0.18e whereas the former lose ~0.47e. Since less electron is less available on the former, CO adsorbs less strongly on the former than on the latter.

Figure 6.17 shows the projected density of states of O/Ag(110) in the absence/presence of CO. As seen in Figure 6.17a, the hybridized states between p orbital of O_{TFH}/O_{FFH} and d orbital of Ag, extending from the Fermi level to -8.0 eV below, must involve the electrons which are transferred from Ag to O atoms. When CO adsorbs at the Ag atom which does not form the O-Ag-O chain, weak but appreciable hybridization between CO p and Ag d orbitals occurs (Figure 6.17b) below the Fermi level. Even smaller change in the d states of the Ag atoms occurs in case in which CO adsorbs at the Ag atom which forms the chain, and thus no significant hybridization of CO p-orbital and Ag d-orbital occurs (Figure 6.17c). These changes in the electronic structure indicate that the electrons transferred from Ag to O_{TFH} forming the chain, hardly participate in the Ag-CO bond formation. Therefore, the transferred electrons are passivated as a consequence of the Ag-

O_{TFH} bond formation. This finding is in good accord with the fact that the oxidation states of these Ag atoms change by trivial amount, before and after CO adsorption.

The formation of O-Ag-O chain involves the conversion of the rather-loosely-bound O_{FFH} species into the tightly-bound O_{TFH} species. In this conversion process, the donated electrons by Ag atoms to the O_{TFH} species become trapped and cannot participate in further bond formation (passivated), consequently their reactivity reduces. In other words, the availability of electrons reduce on Ag atoms which are embedded in the chain. Therefore, it indicates that the O_{TFH}-Ag bond in O-Ag-O chain is stronger than the O_{FFH}-Ag bond. Indeed, adsorption of CO at top of Ag atoms bonded to O_{TFH} species is much weaker (0.06 eV) than that at the Ag atoms bonded to O_{FFH} (0.36 eV).

Our calculations suggest that strong Ag-O bond in the chain is relatively harder to activate and that these Ag atoms are not able to provide active sites for molecular adsorption strong enough required for chemical reaction because of low electron availability in there. Nevertheless, some metal oxides have been reported to be active for CO oxidation on RuO_2(110) [291-293]. However, note that these active oxide surfaces have the so-called “under-coordinated” surface metal atoms and O species as active centers, which have unpaired electrons. Similarly, the presence of Ag vacancies also could affect the catalytic activity of Ag(110).

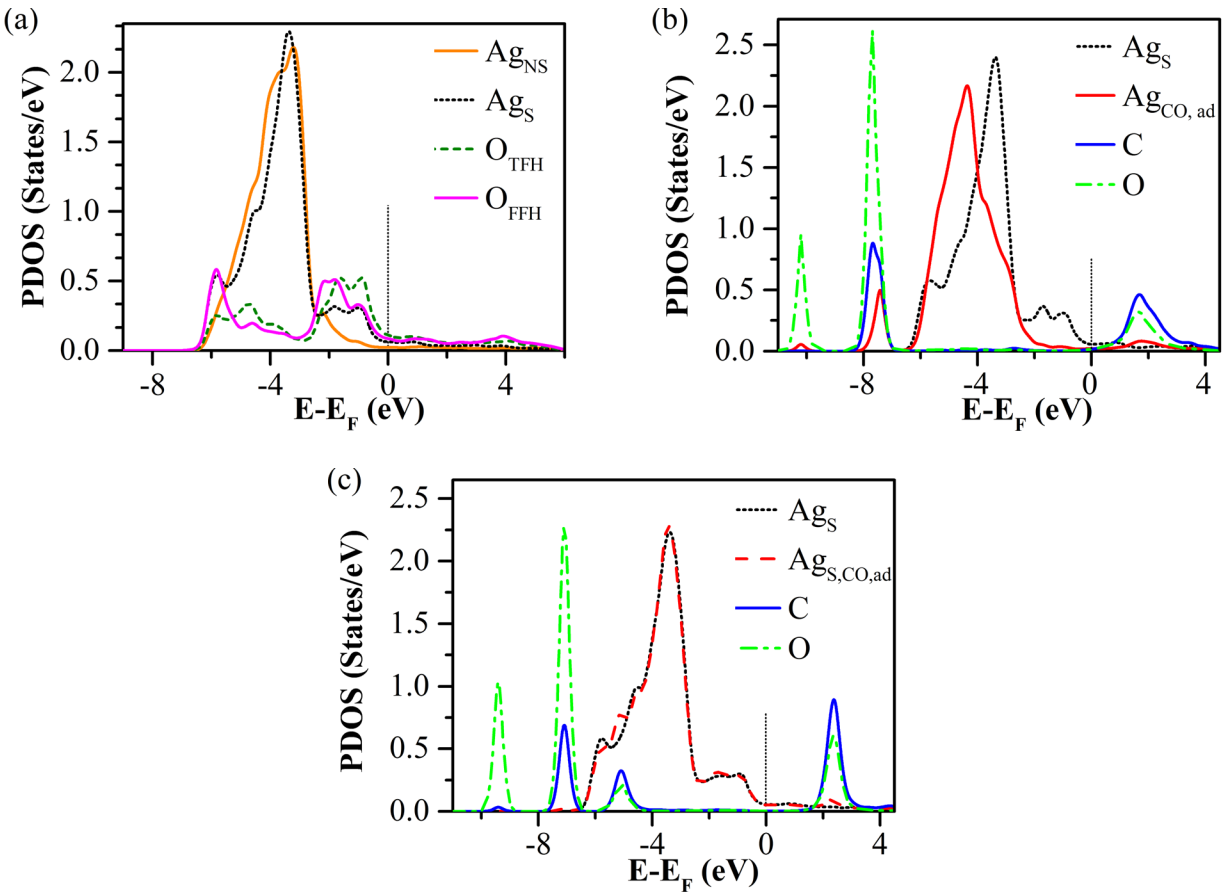

Figure 6.17 Electronic density of states projected onto the d-orbitals of the selected Ag atoms in the first layer and p-orbitals of adsorbed O atoms on the disordered Ag(110) (a) in the absence of CO, (b) in the presence of CO which adsorbs at Ag atom that is not shared by O species, and (c) in the presence of CO which adsorbs at Ag atom that is shared by O species. Ag_{NS} (not shared Ag) refers to the Ag atom that does not form the O-Ag-O chain, Ag_S (shared Ag) refer to the Ag atom that forms the O-Ag-O chain. Single O atoms represented by O_{TFH} and O_{FFH}, are adsorbed in TFH and FFH sites respectively.

6.2.3.5 Catalytic Activity of Disordered Ag(110)

The binding energy of the O_{TFH} species on the disordered Ag(110) is larger by ~0.2 eV than that of the singly distributed O_{FFH}. The difference in binding strengths has an impact on the reactive nature of O species. The reaction of the O_{FFH} species with CO is spontaneous whereas the

reaction of tightly bound O_{TFH} species (embedded in O-Ag-O chains) needs an activation energy (although not large). Indeed, our calculations show that the O_{TFH} species breaks from the O-Ag-O chain and become the O_{FFH} species just before recombination with CO. We assign the chemically distinct O_A and O_B species to the weakly-bound singly dispersed O_{FFH} and tightly-bound O_{TFH} species, respectively, confirming experiment [288]. The same kind of O species were also found for Cu(110) [290].

The diffusion of CO near the area of two O species (O_{FFH} and O_{TFH}) differs such that the diffusion barrier around O_{TFH} is twice larger than that around singly dispersed O_{FFH}. These differences in CO diffusion can, therefore, cause the reaction slow for the former species. Thus, our calculations predict that the reaction between CO and singly dispersed O_{FFH} species (O_A species) is faster than that of CO and embedded O_{TFH} species (O_B species) due to CO kinetics, in accord with an experiment [289].

Our DFT calculations show that strong Ag-O bond is hard to activate and that these Ag atoms are not able to provide active sites for CO adsorption strong enough required for CO oxidation because of low availability of electrons in there. Nevertheless, some metal oxides have been reported to be active for CO oxidation on RuO_2(110) [291-293]. However, note that these active oxide surfaces have the so-called under-coordinated metal sites and O sites as active centers, which have unpaired electrons.

6.2.4 Summary

Based on DFT-based simulations, we found that free Ag atoms at the top surface layer and those involved in the O-Ag-O complex have distinct local chemical activity since they provide

different binding affinity to CO. Furthermore, we found that the tightly-bound O_{TFH} species on disordered Ag(110) is less reactive than the weakly-bound singly dispersed O_{FFH} on the ordered surface. Therefore, the chemical activity of disordered Ag(110) can be quite different from that of ordered one. We trace these differences to the significant electron transfer from Ag to O atoms and passivation of those transferred electrons in the strongly hybridized Ag d and O p states upon the formation of O-Ag-O chains.

6.3 Part III. Oxygen-Induced Vacancy Formation on Ag(110)

We have studied the geometric structures and energetics of O/Ag(110) systems by means of DFT calculations. We propose a new mechanism involved in the process of Ag vacancy formation on Ag(110), and reveal that Ag atoms are only possible to extract from pristine (110) terraces in the presence of oxygen atoms, and the process gets easier for the higher oxygen coverage, leading to the formation of complex structures.

6.3.1 Introduction

Surface reconstructions are common phenomena in surface physics, and have the fundamental importance in understanding the surface chemistry of the metal surfaces. Many metallic surfaces undergo reconstruction upon dissociative O_2 adsorption, which is usually accompanied by the breaking of several nearest-neighbour bonds within the metal substrate lattice, yielding a reconstructed surface. Such rearrangements of the surface consisting of chains of alternatingly oxygen and metal atoms along the [001], forming the added-row structures. Both

oxygen and metal atoms diffuse across the substrate terraces, where they condense into the added rows.

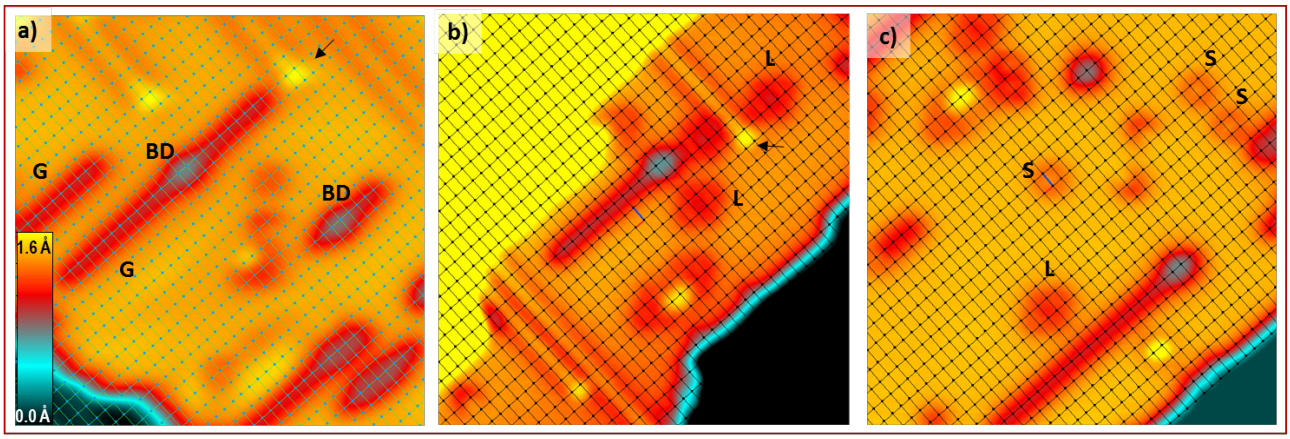

Figure 6.18 a) STM image of an area of Ag(110) in which BD and G structures co-exist with the added O-Ag rows extending in the <001> direction. The yellow spots (black arrow) correspond to the terminal Ag atoms of added rows, which are known to sit in fourfold hollow sites. Taking these features as reference, a grid corresponding to the position of the Ag atoms of the surface is superimposed to the image. Both BD and G structures are located on top of the Ag rows. The same procedure allows to locate the centre of the lozenges in fourfold hollow sites (b) and the sombrero structures in long bridge sites (c). For all images, size: 100 x 100 $Å^2$, V=31 mV in a) and 70 mV in (b-c). Bottom-left inset: colour scale. [J. Pal, T. B. Rawal et al., Phys. Rev. Lett., (2017)] (Copyright: American Physical Society).

Dissociative adsorption of oxygen on Ag(110) can lead to the vacancy formation which is plays an important role for added-row reconstruction. The currently accepted mechanism is that Ag atoms are released from pre-existing step edges and diffuse eventually out to the terraces. The extraction of Ag atoms from the top layer of the substrate to generate adatoms, which can participate in added-row reconstruction was thereby suggested to dominate when the supply from steps is inhibited [10]. However, the driving forces and mechanisms for formation are not well understood. The microscopic mechanism for the oxygen-induced vacancy formation is thus calls for atomistic examination.

Exposure of O_2 leads to cause the dissociative adsorption on Ag(110) for T>150 K. Dissociative O_2 adsorption induces the substantial change in the surface morphology of Ag(110), resulting the formation of added rows for T>190 K [246,258,264,265]. At 300 K, ordered (nx1) oxygen adlayer chains are formed on Ag(110) [262]. Not only temperature but also high O coverage was also reported to induce an added-row reconstruction on Ag(110) along [001] [264,265,294]. The increased O coverage, at T>150K, creates a substantial modification of the surface morphology of Ag(110). Such disorder on Ag(110) was confirmed by a remarkable drop in elastic reflectivity of more than 80% with respect to the bare surface reflectivity [261].

Figure 6.18 shows the experimental STM observation of the O-related features on the Ag(110). The experimental observation, indeed, show that Ag atom excavation occurs on Ag(110) at the temperature at which O_2 dissociative adsorption takes place.

In this work, we investigate the geometric structures and energetics of O/Ag(110) systems by employing DFT. We observe oxygen-induced formation of isolated Ag vacancies on the Ag(110) surface, and unravel the mechanism involved in the extraction of Ag atoms induced by O adatoms. Our results reveal that the vacancy formation is possible only in presence of O adatoms and the process gets easier for the higher O coverage, leading to the formation of complex structures.

6.3.2 Computational Details

We have performed *ab initio* spin-polarized DFT calculations using VASP [141] code. To describe the exchange-correlation of electrons, we use generalized-gradient approximation in the form of the PBE functional [43]. We adopt the PAW method [72] to take into account the ion-

electron interaction. We use the kinetic energy cutoff of 500 eV for the plane-wave expansion. We use (3x4), (4x4), and (6x8) supercells of 5 Ag layers with periodic boundary conditions with 15 Å vacuum. For sampling of Brillouin zone (BZ), we have used 12, 9, and 4 irreducible k-points which are generated according to the Monkhorst-Pack scheme [74], using the Methfessel and Paxton smearing technique [76]. We relax all atoms in the considered systems until the force convergence and the total energy convergence reached to 0.01 eV/Å and 10^{-4} eV, respectively.

We apply the Tersoff and Hamann (TH) model [80,81] to simulate the STM image at low bias voltage, At higher bias voltage V, the simulated STM images were approximated by the DFT-calculated iso-surface (with iso-value of 10^{-5} e/Å^3) of the local density of states (DOS) integrated over the sample states from –V (in eV) to the Fermi level.

The formation energy of an n-Ag vacancy is calculated using the relation:

$$E_v^{ad,vac} = -\{(n+1)E_N - (nE_{N+1} + nE_{N-n})\}$$

where E_N, E_{N+1}, and E_{N-n} represent the total energies of the pristine Ag(110) system with N Ag atoms, the system with single Ag adatom, and the defect system with n-Ag vacancies.

To calculate energy barriers for the formation and diffusion of an Ag vacancy on Ag(110), we use the climbing-image nudged-elastic-band (CI-NEB) method [91] with seven configurations (images) including the initial states and final states.

6.3.3 Results and Discussion

6.3.3.1 Formation of Single Vacancy on Ag(110)

The formation energy of an Ag vacancy plus Ag adatom on pristine Ag(110) turns out to be 0.42 eV. However, this energy does not account for the energy needed for breaking the bonds. The latter energy, the so-called the barrier for formation of Ag vacancy, is estimated using CI-NEB method. Figure 6.19 shows the minimum energy paths for the formation of Ag vacancy on Ag(110) with or without the presence of oxygen atoms. The energy barrier for the formation of Ag vacancy on the pristine surface is 0.69 eV, whereas the barrier to fill the just created vacancy is 0.27 eV. Moreover, the latter value is lower than the barrier of 0.47 eV for the diffusion of the Ag vacancy along $[1\bar{1}0]$, and even much lower than the barrier of 0.80 eV for the vacancy diffusion along [001]. Vacancy migration along $[1\bar{1}0]$ is possible at T=175 K, leading to the formation of the complex structures. Since the barrier for the refilling the vacancy is lower than the barrier for the formation of vacancy as well as the barrier (0.47 eV) for the diffusion of the vacancy along [001], extracted Ag atoms are most likely to refill the just created vacancy implying that, in absence of oxygen, vacancy formation is not feasible at the low temperature.

The Ag vacancy formation on Ag(110) becomes possible in the presence of oxygen atoms since the formation energy $E_v^{ad,O-Ag-O}$ is reduced to 0.055 eV. The reduction in formation energy (from 0.42 eV to 55 meV) of Ag vacancy on Ag(110) in the presence of O atoms, already provide an indication that oxygen facilitates the vacancy formation [295]. In fact, this process occurs on Ag(110) in the presence of O atoms even though the formation of an Ag vacancy in the presence

of an oxygen-decorated Ag adatom is slightly endothermic. The endothermic energy is compensated by the entropy contribution to the free energy.

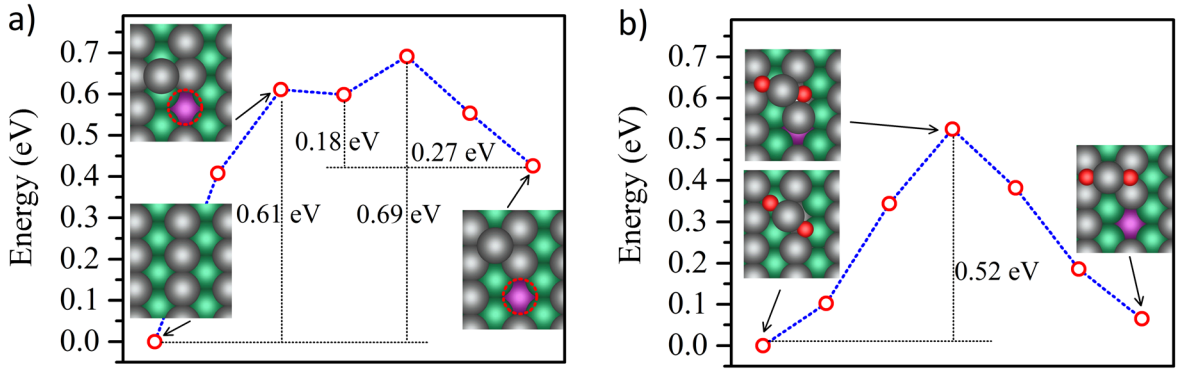

Figure 6.19 Minimum energy pathway for the formation of single Ag vacancy on: a) pristine Ag(110), and b) Ag(110) in the presence of dissociated oxygen atoms with a coverage of 0.16 ML. The gray, green, pink and red balls represent the Ag atoms at the top layer, Ag atoms the second layer, Ag atoms at the third layer, and O atoms, respectively. [J. Pal, T. B. Rawal et al., Phys. Rev. Lett., (2017)] (Copyright: American Physical Society 2017).

Now the question is how much energy needs to cost for vacancy formation on Ag(110) in the presence of O atoms. To address this question, we again calculated the minimum energy path (MEP) for O-assisted Ag vacancy formation on Ag(110). We find that the barrier for the formation of Ag vacancy plus added O-Ag-O unit reduces to 0.52 eV for the concerted motion in which the O-Ag-O complex diffuses to the nearest neighbouring FFH site dragging also the Ag atom along [1$\bar{1}$0]. The MEP for the diffusion of Ag vacancy in concerted motion with O-Ag-O complex is depicted in Figure 6.19b. From the comparison of the diffusion process of Ag vacancies with or without O-assisted cases (Figures 6.19a-b), it is apparent that the Ag vacancy formation process is relatively easier while assisted by dissociated oxygen atoms.

The formation of a Ag vacancy and an added O-Ag-O complex is facilitated by the concerted motion in which the movement of O-Ag-O complex is simultaneously followed by an Ag atom along [$1\bar{1}0$]. At the O coverage of 0.25 ML (three O adatoms per (3x4) unit cell), we find a barrier of 0.46 eV. This barrier is 0.06 eV lower than the barrier of 0.52 eV for the vacancy formation on Ag(110) with an O coverage of 0.16 ML (two O adatoms per (3x4) unit cell). With increasing O coverage the barrier is reduced to 0.46 eV, indicating the O-coverage dependency of the vacancy formation barrier for vacancy formation on Ag(110). The reverse barrier increases substantially, thus inhibiting the vacancy-destruction process. Once formed the vacancy diffuses away from the O decorated Ag adatom avoiding recombination, this leads to the isolated vacancy and the O-decorated Ag adatom.

6.3.3.2 Simulation of STM Images

Figure 6.20a shows the DFT-optimized structure of O-Ag-O complex on Ag(110) which is the precursor for the initial phase of surface reconstruction. In this configuration, two O atoms (labelled as #1 and #2) prefer to share an Ag atom (labelled as #1). The competition of these two O atoms to pull Ag atom result in both the lateral and vertical displacements (i.e. 0.745Å and 0.587 Å) of the shared Ag atom (Ag1). The O2-Ag1, O1-Ag1, O1-Ag2, O2-Ag3 distances are calculated to be 2.113, 2.047, 2.153, 2.241 Å, respectively.

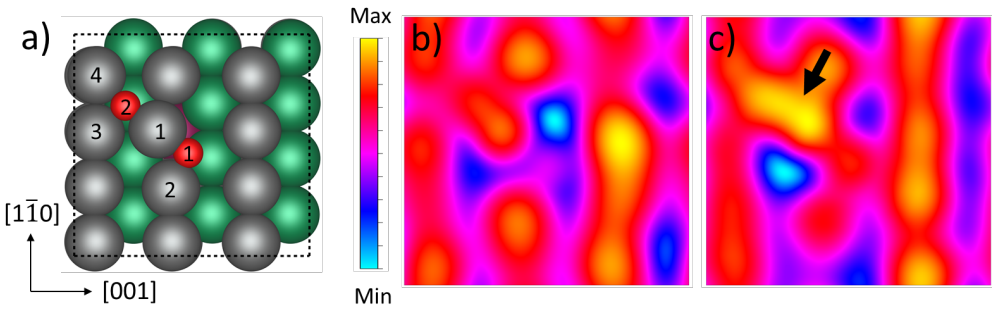

Figure 6.20 (a) DFT-optimized structure of O-Ag-O complex on Ag(110); (b-c) the corresponding simulated STM image for the bias of (b) -0.07 V and (c) 0.3 V.

Figure 6.20(b-c) show the simulated STM image of O-Ag-O complex on Ag(110) for bias -0.07 V and 0.3 V, respectively. They consist of one displaced Ag atom and two O at non-equivalent sites. The Ag atom protrudes thereby by 0.56 Å from the surface plane. In addition, the results clearly show that the protrusion of the displaced Ag atom is greatly enhanced for the higher bias voltage (0.3 V).

Figure 6.21a shows the DFT-optimized structure of an isolated Ag vacancy on Ag(110). Due to the formation of Ag vacancy, it is expected to see the change in electronic structure at the vicinity of the Ag vacancy.

Figure 6.21(b-c) show the simulated STM image of an isolated single Ag vacancy for the bias -0.07 V and 0.3 V, respectively. In both cases, we see the depression in the vicinity of Ag vacancy. The depression at the region of Ag vacancy can be understood in terms of the local density of states, which are relatively much lower than Ag atoms on the top layer.

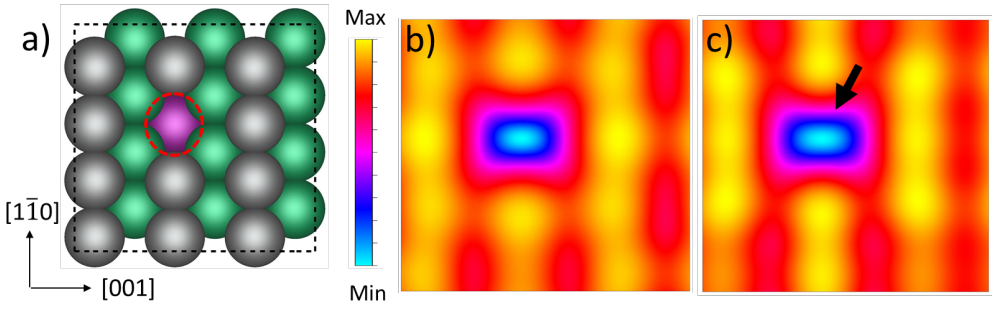

Figure 6.21 (a) DFT-optimized structure of Ag vacancy with the presence of O atom on Ag(110); (b-c) the corresponding simulated STM image for the bias of (b) -0.07 V and (c) 0.3 V.

Figure 6.22a shows the DFT-optimized structure of oxygen-decorated Ag adatom at the position of LB site on Ag(110). The covalent interaction of Ag ad-atom with oxygen atoms leads to stabilize the Ag ad-atom. In the absence of oxygen atoms, Ag adatom may not be stable, rather mobile on the surface. The Ag1-Ag2, O4-Ag2 and O1-Ag3 distances are calculated to be 3.052, 2.031 and 2.147 Å, respectively.

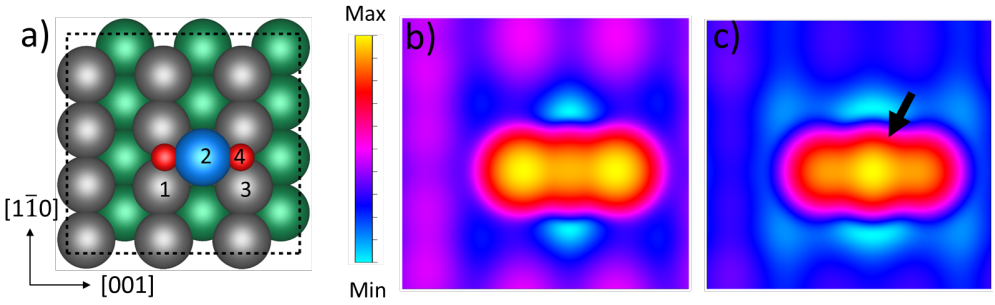

Figure 6.22 (a) DFT-optimized structure of Ag vacancy with the presence of O atom on Ag(110); (b-c) the corresponding simulated STM image for the bias of (b) -0.07 V and (c) 0.3 V. The blue ball represents the Ag atom of the added O-Ag-O complex.

Figure 6.22(b-c) shows the simulated STM image of oxygen-decorated Ag adatom on Ag(110). The high protrusion at the region of Ag adatom can be understood in terms of the local

density of states, which is relatively much higher at the position of Ag adatom. At the higher voltage (0.3 V), the high protrusion feature of Ag ad-atom is clearly evident (Figure 6.22c).

Figure 6.23a shows the DFT-optimized structure of two O-Ag-O complex on Ag(110) in the presence of double Ag vacancies. In the O-Ag-O geometry, after optimization, one O atom of the complex sits in the LB site, and bonded to two Ag atoms on the top layer, whereas another O atom of the complex sits slightly off from FFH site, i.e., this O atom is bonded with three O atoms in the top layer. These O-Ag-O complex structures are quite stable than the singly dispersed O atoms on Ag(110). More importantly, the formation of these complex structures help to form another Ag vacancy on the surface, thereby leading to large vacancy structures. Therefore, we predict that Ag vacancy formation with the aid of oxygen atoms is facile way than on the pristine (without O atoms). The O1-Ag2 and O1-Ag3 distances are calculated to be 2.094, and 2.130 Å, respectively.

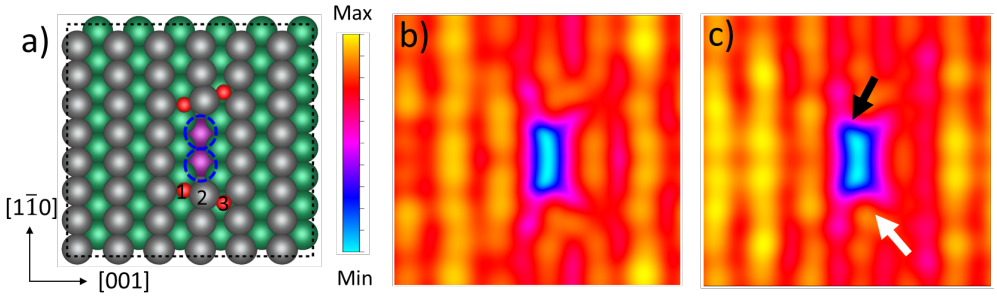

Figure 6.23 (a) DFT-optimized structure of double Ag vacancies (represented by dotted circles) with the presence of O atoms on Ag(110); (b-c) the corresponding simulated STM image for the bias of (b) -0.07 V and (c) 0.3 V.

Figure 6.23(b-c) show the simulated STM image of two O-Ag-O complex on Ag(110) in the presence of double Ag vacancies calculated at -0.07 V and 0.3 V. The depression feature

(marked by black arrow) on the STM images are associated with Ag vacancies. On the other hand, the slightly protrusion feature (marked by white arrow) is related with the displaced Ag atom, which is shared by two O atoms. At the higher voltage (0.3 V), the width of the depression is slightly increased. Meanwhile the protrusion feature of the displaced Ag atom is also slightly enhanced (Figure 6.23c).

The simulated STM image of a pair of O-Ag-O complex in the presence of double Ag vacancies on Ag(110) (see Figure 6.23a for the geometry) at 0.07 V nicely agrees with the butterfly STM feature observed in the experiment [295].

6.3.3.3 Kinetic Monte Carlo Simulations

As our DFT results clearly indicate that there exists Ag vacancies on Ag(110), we need to understand that what is the driving force for vacancy formation. At the low temperature at which the O_2 dissociation takes, the surface undergoes initial phase of disorder in the presence of oxygen atoms. This implies that O-Ag-O complex is formed because the O/Ag(110) system having the complex significantly gains energy as compared to that of the system having single scattered O atoms. At that temperature, the formation of isolated Ag vacancies become a specific property of the O/Ag(110) system. Unlike to the case of pristine Ag(110), there is no kinetic limitation for the formation of Ag vacancies on Ag(110) in the presence of O atoms. Therefore, the formation of vacancies must be favored thermodynamically and kinetically.

In order to understand the kinetics of the O_2 dissociation and subsequently the vacancy formation on Ag(110), we perform the Kinetic Monte Carlo (kMC) simulations (Figure 6.28). For the O_2 dissociation which needs to overcome the barrier of 0.42 eV, the maximum number events

occurs at 157 K (green curve). Consequently, dissociated O atoms lead to induce the formation of O-Ag-O complex. Actually, the dissociation process of O_2 yielding two O atoms is exothermic with a barrier of 0.42 eV. On the other hand, the O/Ag(110) system needs to overcome the a barrier of 0.52 eV for the vacancy formation. KMC simulation shows that this process is peaked at 185-190 K in the presence of oxygen atoms at 0.16 ML O coverage (red curve). As mentioned earlier, the barrier for vacancy formation decreases with increasing O coverage. This implies, for the process to occur, the peak temperature will also decrease with the increasing of O coverage. Therefore, the relative populations of O-Ag-O complexes and Ag vacancies will depend on the temperature and oxygen coverage.

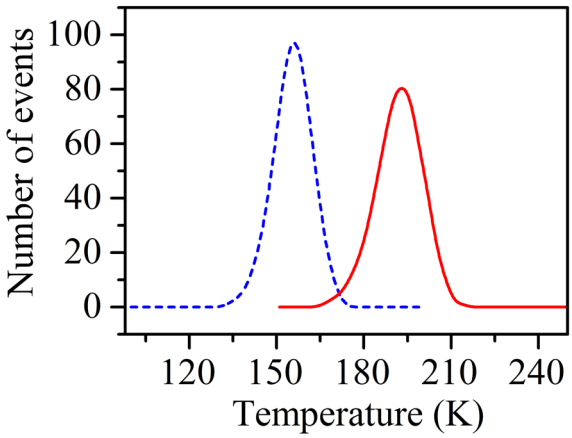

Figure 6.24 Kinetic Monte Carlo simulation of O_2 dissociation (green trace) and Ag vacancy formation (red trace) on Ag(110) at O coverage of 0.16 ML as a function of temperature. [J. Pal, T. B. Rawal et al., Phys. Rev. Lett., (2017)] (Copyright: American Physical Society 2017).

6.3.3.4 Formation of Multiple Vacancies on Ag(110)

Figure 6.24 shows the formation energies per vacancy for multiple vacancy structures on Ag(110). Here, ΔE represents the difference between formation energies per Ag vacancy (squares,

dashed line). The calculated values of ΔE_1, ΔE_2, and ΔE_3 are 0.1 eV, 0.03 eV, and 0.02 eV, respectively. Except for single Ag vacancy, shown in inset (i), the lowest energy structure consists of Ag vacancies along $[1\bar{1}0]$ next to each other (squares connected by a dashed line). These vacancies prefer next to each other because of the attractive interaction between them. The squares (not connected by the dashed line) represent the calculated values for other vacancy structures shown in the inset. Here, we have considered those configurations in which Ag atoms are only missing from the top layer. Then, the calculated configurations are described below in the order going from the lowest to highest formation energy.

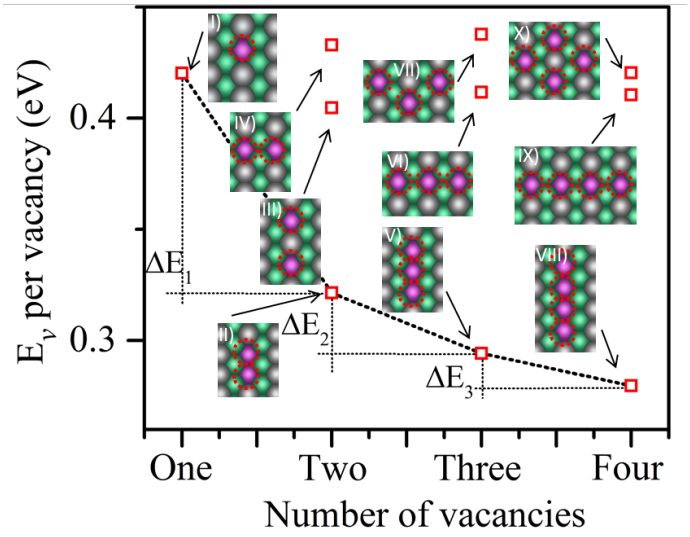

Figure 6.25 Formation energy per Ag vacancy for several vacancy structures. The preference for forming multi-vacancy structures along $[1\bar{1}0]$ appears evident. The locations of Ag vacancies are indicated by dotted circles. [J. Pal, T. B. Rawal et al., Phys. Rev. Lett., (2017)] (Copyright: American Physical Society 2017).

For the case of two Ag vacancies, we optimize the geometries for three different structures with vacancies separated, respectively by: II) one lattice spacing ($a/\sqrt{2}$) along $[1\bar{1}0]$, III) two lattice spacing along $[1\bar{1}0]$, IV) one lattice spacing (a) along [001]. For three vacancies, we select

three optimized structures corresponding, respectively, to Ag vacancies separated by: V) one lattice spacing along [$1\bar{1}0$], VI) one lattice spacing along [001]; VII) two lattice spacings along [001] and the third one at one lattice spacing along [$1\bar{1}0$] (arranged in a nearly equilateral triangle). For four vacancies, we select three optimized structures corresponding, respectively, to: VIII); each vacancy at one lattice spacing away from each other along [$1\bar{1}0$]; IX) each vacancy separated by one lattice spacing along [001]; X) two vacancies separated by two lattice spacing along [001] and the other two separated by two lattice spacing along [$1\bar{1}0$], forming a diamond-shaped vacancy structure.

Our DFT results reveal that the formation energy per Ag vacancy decreases as the number of Ag vacancies increases until the vacancy formation saturates (Figure 6.24). The formation of multiple Ag vacancies occur due to the tendency of forming a new vacancy next to the existing vacancy costs less energy than creating the new vacancy. Ultimately, the process saturates above three Ag vacancies, which can be compared nicely with the observed lengths of the body of the experimentally observed 'butterfly' structure.

6.3.4 Summary

On the basis of DFT–based calculations, we propose a new mechanism involved in the process of Ag vacancy formation on Ag(110). We show that the vacancy formation is possible only in presence of O adatoms and the process gets easier for the higher O coverage, leading to the formation of complex structures. In particular, the formation of Ag vacancy and O-Ag-O structures act as the building blocks for the added-row reconstruction on Ag(110). This explains added-rows formation in the middle of the terraces, as observed in the experiment. Insights into these properties

are potentially helpful for comprehending the catalytic properties of Ag(110) since vacancies, being of under-coordinated, can provide the reactive sites.

CHAPTER 7 Pd_1/ZNO CATALYST FOR METHANOL PARTIAL OXIDATION

We present results of density functional theory (DFT) in combination with kinetic Monte Carlo simulation (kMC) for methanol partial oxidation (MPO) reaction on $Pd_1/ZnO(10\bar{1}0)$. We discuss the adsorption characteristics of reactant molecules (CH_3OH, O_2) and the products (CO, CO_2, H_2O, H_2), and the potential energy with activation barriers for the elementary reactions associated with MPO. Single dispersion of Pd on ZnO surface surprisingly offers high activity and selectivity for MPO. Our DFT+kMC simulation, indeed, indicates the high selectivity for H_2 and CO_2 over H_2O and CO. The high activity of Pd_1/ZnO for MPO can be credited to the local environment (or geometry) and electronic structure of the active Zn sites modified by single Pd sites. Our DFT calculations also rationalize that single Pd loading not only plays a decisive role for providing higher affinity to CH_3OH but also induces the spontaneous CO_2 formation, the nearly spontaneous dissociation of H_2O, and the stabilization of H_2 right at or near the sites. These factors help increase the selectivity for H_2 and CO_2.

7.1 Introduction

Methanol partial oxidation is an industrially important reaction for production of H_2, a excellent source of clean energy in fuel cell technology. The overall reaction is $CH_3OH+½\ O_2 \rightarrow CO_2 + 2H_2$, proceeding through several intermediate steps ultimately leading to the production of H_2 and CO_2 as desirable products, which compete with undesirable counterparts H_2O and CO, respectively. Prior experimental studies [296-298] have already shown that ZnO-supported Pd catalysts exhibit high activity and selectivity for H_2, indicating ZnO-supported Pd is a promising catalyst for MPO.

Yet, there is a lack of atomistic understanding of the catalytic activity and selectivity of supported Pd catalyst at limit of single atom.

On the other hand, Pd [299,300] surface exhibits good catalytic performance for dehydrogenation of methanol (intermediate reaction path for MPO). However, its cost hinders effective utilization of the catalyst for MPO. It is therefore essential for searching an alternative way to maximize the efficiency of Pd metal atoms by downsizing particles to single atom. Thus, there is a need for atomistic understanding of the local geometry (or environment) of dispersed Pd on the support. The local environment strongly depends upon the anchoring sites for single atoms. Prior studies have shown that surface defects of the oxide supports could serve as anchoring sites for single atoms [301,302]. In this work, the surface oxygen vacancy is considered as an anchoring site.

Herein, we employ a combination DFT and kMC methods to study the MPO reaction on $Pd_1/ZnO(10\bar{1}0)$. We begin with the study of adsorption of single Pd atom on ZnO with O vacancy. Secondly, we utilize the stable Pd_1/ZnO system to explore the adsorption properties of reactants (CH_3OH, O_2) and products (CO, CO_2, H_2O, H_2) associated with MPO. We then calculate the energetics for competing reaction pathways – successive hydrogen abstraction from CH_3OH, oxidation and hydrolysis of intermediates – involved in MPO. Finally, we perform kMC simulation for kinetics of the reactions using input parameters derived from DFT. We provide insights into the higher selectivity for the formation of H_2 and CO_2 over H_2O and CO.

7.2 Model Systems

Pristine ZnO($10\bar{1}0$) and ZnO($10\bar{1}0$) with an O vacancy are shown in Figure 7.1. Among four low-index surfaces – (0001), ($000\bar{1}$), (1120), and ($10\bar{1}0$) of the hexagonal wurtzite ZnO crystals, the non-polar ($10\bar{1}0$) surface is the most stable surface with the lowest surface energy (the surface energy is ~1/2 that of the other polar surfaces, (0001) and ($000\bar{1}$)) [303]. The non-polar ZnO($10\bar{1}0$) surface is formed by the cleavage of the same number of Zn and O-bonds at the surface, reducing the coordination of Zn and O atoms from four-fold to three-fold. These atoms form the characteristic rows of ZnO dimers separated by trenches running along ($1\bar{2}10$) direction [304].

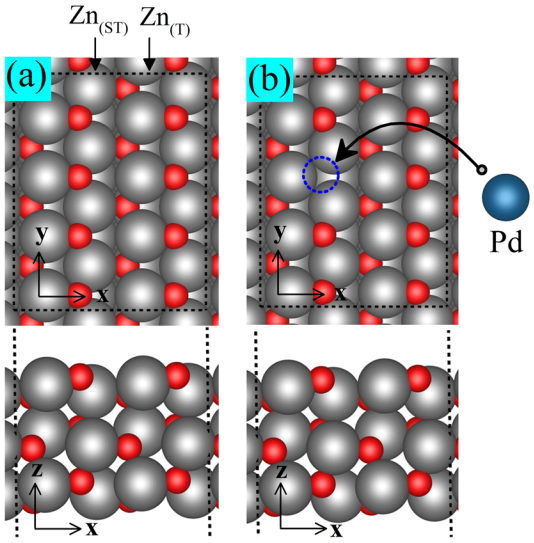

Figure 7.1 Model systems: a) Pristine ZnO($10\bar{1}0$) and b) ZnO($10\bar{1}0$) with an O vacancy (indicated by dotted circle). Gray, and red balls represent Zn and O atoms, respectively.

Our model for the stoichiometric, non-polar ZnO($10\bar{1}0$) surface is constructed from the hexagonal wurtzite crystal structure, with space group C_{6v}. Our calculated equilibrium lattice constants are a=3.282Å and c=5.308Å in agreement with the experiment (a=3.25Å and c=5.206Å

[305,306]) within 1% and 2%, respectively. Our supercell consists of a (4x4x6) unit cell to model ZnO($10\bar{1}0$) and a 16 Å vacuum along z-direction between ZnO slabs to avoid spurious electrostatic interaction between their periodic images. We then remove an O atom to construct the defective (4x4) ZnO($10\bar{1}0$) with 13% O vacancy. We then introduce a single Pd atom at different sites in order to obtain the lowest-energy Pd_1/ZnO model system. The energetics for adsorption of single Pd atom at different sites will be described in Section 7.4.1.

7.3 Theoretical Methods

We perform *ab-initio* calculations based on DFT implemented in VASP code [307]. The total energies are obtained by solving Kohn-Sham [32] equation self-consistently. Interactions between ionic cores and valence electrons are treated using the projector-augmented wave (PAW) method [72]. For electron-electron interaction, we adopt the generalized-gradient approximation in the form of PBE functional [43]. We use a cutoff energy of 400 eV for the plane wave expansion.

The non-polar ZnO($10\bar{1}0$) surface is constructed from the hexagonal wurtzite crystal structure, with space group C_{6v}, for which our calculated equilibrium lattice constants are a=3.282Å and c=5.308Å in agreement with the experiment (a=3.25Å and c=5.206Å [305,306]) within 1% and 2%, respectively. To mimic ZnO($10\bar{1}0$), we use (4x4x6) unit cell (shown in Figure 7.1a-b) and 16 Å vacuum along z-direction to avoid spurious electrostatic interaction between periodic images. The model systems are shown in Figure 7.1. In all calculations, we relax all atoms in the supercell until the force on each atom reduces below 0.01 eV/Å. For integration over the Brillouin zone, we employ the (3x4x1) k-point mesh generated using the Monkhorst-Pack scheme [74].

The adsorption energy (E_{ad}) is calculated using $E_{ad} = E_{(Adsorbate/Slab)} - E_{(Adsorbate)} - E_{(Slab)}$, where $E_{(Adsorbate/Slab)}$, $E_{(Adsorbate)}$ and $E_{(Slab)}$ represent the total energies of adsorbate/slab, adsorbate and slab systems, respectively. Here, slab represents either ZnO with single O vacancy or $Pd_1/ZnO(10\bar{1}0)$. The reaction energy (ΔE) are calculated using the difference in energy between initial state (IS) and the final state (FS). We use the Nudged Elastic Band (NEB) method [86] to calculate the minimum energy pathways (MEPs) and then refine them using Climbing-Image NEB (CI-NEB) method [91].

We use the standard *ab-initio* kMC approach [34,35,308,309] to perform the kMC simulation for which the kinetic parameters are derived from DFT calculations. The rate constants (R) for reaction, desorption and diffusion are calculated using the following relation:

$$R = A \exp\left(-E_a/k_B T\right),$$

where A, E_a, k_B, and T are the pre-exponential factor, activation barrier, Boltzmann constant, and reaction temperature, respectively.

The rate constants (R') for adsorption of reactant species are calculated using the following relation:

$$R' = \frac{\tilde{s}\, P}{\sigma\sqrt{2\pi M k_B T}} \exp\left(-E_a/k_B T\right),$$

where $\tilde{s}$, σ, P, and M are the sticking coefficient, site density, pressure and mass of the reactant species, respectively. We have chosen the sticking coefficients for each reactant species to be unity. Further details on the algorithms of our KMC code can be found elsewhere [308].

7.4 Results and Discussion

7.4.1 Adsorption of Single Pd Atom on Defective ZnO(10$\bar{1}$0)

In Figure 7.2, we show the various configurations of single Pd atom adsorbed on the partially reduced ZnO(10$\bar{1}$0) (single oxygen vacancy per 4x4 unit cell). Singly dispersed Pd atom strongly prefers to adsorb in the O vacancy site, with the adsorption energy of -3.0 eV. Strong preference of single Pd atom in the O vacancy site for adsorption may be attributed to two factors: i) strong hybridization between Pd and O-vacancy states, leading to enhanced s-d hybridization of Pd's outer orbitals, and ii) decrease in Pauli repulsion. The adsorption of Pd atoms at the other sites (shown in Figure 7.2b-d) of defective ZnO are significantly weaker with adsorption energies of -1.74, -1.71, and -1.54 eV, respectively. As compared with that adsorbed on the pristine ZnO, Pd atom on the reduced ZnO is thus found to be quite stable similarly as similar to that on TiO_2(110)[310] and on MgO(100) [311]. Similarly, reduced FeO_x stabilizes single Ir atoms [312]. Thus, the reduced metal-oxide surfaces can stabilize singly-dispersed Pd atoms.

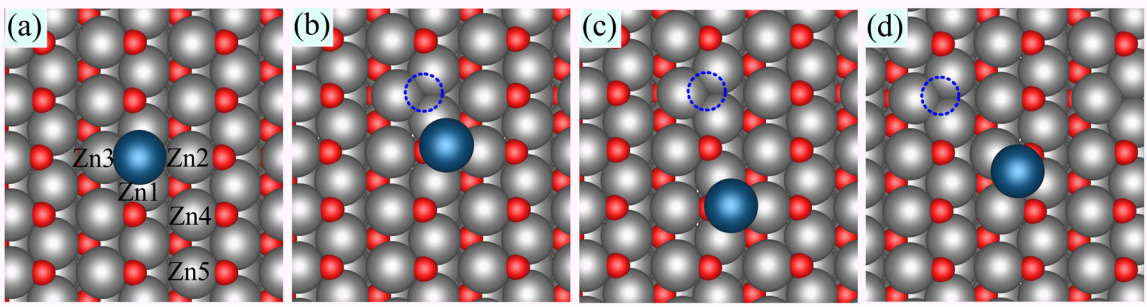

Figure 7.2 Adsorption of Pd atoms in fou different sites on defective ZnO(10$\bar{1}$0). Gray, red, and light blue balls represent Zn, O and Pd atoms, respectively. The positions of O vacancy sites are indicated by dotted circles)

7.4.2 Adsorption of Reactants, Intermediates, and Products of MPO

We first present the results of adsorption of reactants (CH_3OH and O_2) and products (CO, CO_2, H_2 and H_2O) associated with MPO reaction for understanding their geometry and energetic in Pd_1/ZnO. The DFT-optimized structures of the molecules at the key sites of this model catalyst system are shown in Figure 7.3. In Table 7.1, we present our DFT-calculated adsorption energetics of the molecules at various sites.

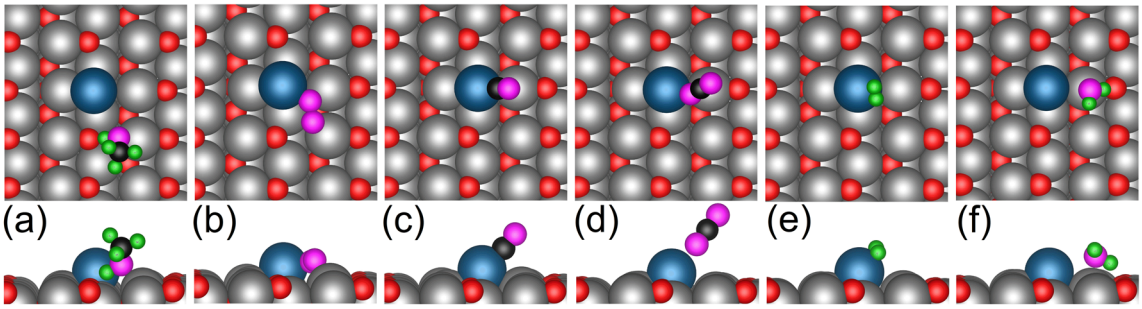

Figure 7.3 DFT-optimized structures of adsorbed reactants and products on Pd_1/ZnO: a) CH_3OH, b) O_2, c) CO, d) CO_2, e) H_2 and e) H_2O molecules. Top and bottom panel shows the top and side views, respectively. Black, pink, and green balls represent the C, O (of adsorbed molecules), and H atoms, respectively.

Table 7.1 Adsorption energies of reactants and products of MPO, adsorbed at various sites of Pd_1/ZnO. For clarity, specific adsorption sites are provided for each system (the sites are depicted in Figure 7.2a). The energies are expressed in eV.

Sites	**Reactants**		**Products**			
	CH_3OH	**O_2**	**CO**	**CO_2**	**H_2**	**H_2O**
Zn	-1.02 (Zn4)	--	-0.30 (Zn5)		-0.12 (Zn4)	-0.64 (Zn2)
Pd	-0.58	--	-1.43	-0.18	-0.53	-0.57
Pd-Zn	-0.63 (Pd-Zn2)	-0.83 (Pd-Zn2-Zn4)	--	-0.12 (Pd-Zn2)	--	--
Zn-Zn	--	+0.13 (Zn4-Zn5)	--	--	--	--

Table 7.2 Adsorption energies and vibrational frequencies of adsorbed species (reactants, intermediates and products) at the energetically favorable sites.

	Favorable sites	**Adsorption energy (eV)**	**Co-adsorption energy (eV)**	**Frequency (cm^{-1})**
O*	Pd-Zn2-Zn4	-4.06	-5.63 (with H*)	445, 295, 293
H*	O_{surf}	-2.68	-3.95 (with O*)	3562, 753, 662
OH*	Pd-Zn2	-2.80	-4.08 (with H*)	3735, 763, 442, 384, 319, 115
H_2O*	Zn2	-0.64		3727, 2872, 1577, 883, 524, 422, 215, 152, 63
O_2*	Pd-Zn2	-0.83		1013, 411, 357, 263, 212, 121
CO*	Pd	-1.43	-1.45 (with H*)	2036, 378, 275, 239, 58, 40
CO_2*	Pd	-0.18 (weakly adsorbed)		2363, 1316, 611, 610, 89, 50, 35, 28, 3
H_2*	Pd	-0.53		3304, 1196, 837, 279, 231, 157
CH_3OH*	Zn4	-1.02	-0.86 (with O*) -1.14 (with OH*) -1.08 (with H_2O*)	3074, 3029, 2973, 2440, 1487, 1453, 1451, 1426, 1145, 1143, 1047, 1008, 308, 222, 149, 145, 116, 79
CH_3O*	Pd-Zn2	-2.37	-3.03 (with O*) -3.69 (with OH*) -2.67 (with H_2O*)	3001, 2969, 1917, 1442, 1432, 1421, 1136, 1106, 1042, 408, 276, 140, 99, 71, 40
CH_2O*	Pd-Zn2	-1.00	-1.27 (with O*) -1.14 (with OH*) -1.26 (with H_2O*)	3000, 2902, 1493, 1299, 1149, 1022, 639, 415, 292, 226, 197, 106
CHO*	Zn2-O_{surf}	-2.84	-3.21 (with O*) -3.88 (with OH*) -2.85 (with H_2O*)	2990, 1528, 1342, 1026, 989, 533, 286, 239, 118
HCOO*	Pd-Zn2-Zn4	-2.92	-3.25 (with H*)	2954, 1558, 1356, 1289, 997, 716, 305, 274, 253, 130, 104, 98
H_2COO*	Pd-Zn2-Zn4	--		2951, 2925, 1456, 1325, 1186, 1088, 1055, 852, 615, 409, 344, 288, 239, 165, 140

7.4.2.1 Methanol

Adsorption of methanol (CH_3OH) is one of the initial elementary steps for MPO reaction. We have calculated the different adsorption geometries (Figure 7.4) by placing CH_3OH at different sites of Pd_1/ZnO. We find that on Pd_1/ZnO methanol preferentially adsorbs at a Zn4 site (Figure 7.2a), with an adsorption energy of -1.02 eV (see Table 7.1), close to that (~-1.1 eV) [313,314]. The molecular axis of CH_3OH tilts such that a H atom points to the (lattice) O atom in the top layer. This hydrogen and the lattice O nearby forms a H-bond with the bond length of 1.530 Å. On the other hand, CH_3OH adsorbs relatively weakly at the single bimetallic Zn2-Pd site (Figure 7.2a), with an energy of -0.63 eV, and at the Pd site with an energy of -0.58 eV.

7.4.2.2 Oxygen

The adsorption of molecular oxygen (O_2) is another important step for MPO. Our calculations show that the single bimetallic site Zn2-Pd offers stable site for O_2 binding. In Figure 7.3b, we show the optimized structure of O_2 adsorbed in the preferred site on the Pd_1/ZnO. The O-O bond of adsorbed O_2 is 1.356 Å, i.e. slightly elongated as compared to 1.232 Å in gas-phase. In this geometry, O_2 preferentially adsorbs at Pd-Zn2 site, with an adsorption energy of -0.83 eV, with its axis parallel to the surface with one O atom sitting at a Pd-Zn2 site and the other bonded to Zn atom in the top layer. At Zn4-Zn5 site (see Figure 7.2a), O_2 does not bind because the adsorption energy is positive (+0.13 eV).

Our calculations indicate that there is an activation energy barrier of 1.10 eV for O_2 dissociation. One O atom adsorbs at the single bimetallic site and the other in the hollow site. For the lowest-energy configuration, the adsorption energy of dissociated oxygen turns out to be -0.12

eV. While defect-free Zn is completely inactive for O_2 adsorption and dissociation, Zn surfaces with increasing Pd becomes more favorable for O_2 adsorption and dissociation. Note that the affinity for binding O species by catalytic sites directly affects the propensity of oxidation of intermediates and the selectivity for final products in MPO.

7.4.2.3 Carbon Monoxide

Carbon Monoxide (CO), being an undesired product in MPO, must be converted either into CO_2 or other less toxic carbonates. It is thus important to find the adsorption site and energy. Our calculations show that CO preferentially adsorbs at the Pd site (Figure 7.3c), with an adsorption energy of -1.43 eV, indicating CO desorption not possible at low temperature. In this configuration, the Pd-C and C-O distances are 1.914 Å and 1.156Å, respectively. On the other hand, CO weakly adsorbs at a Zn5 site with energy of -0.30 eV. We also find that CO does not adsorb at a single bimetallic Pd-Zn2 site (energetically unfavorable). We also find that there is a spontaneous migration of CO from Pd-Zn2 site to single Pd site. Similarly, CO also migrates spontaneously from Zn2-Zn4 bridge (near Pd) site (see Figure 7.2a), indicating CO is stabilized by an dispersed Pd atom.

7.4.2.4 Carbon Dioxide

Carbon dioxide (CO_2) can be formed *via* the reactions such as CO oxidation, or abstraction of H* from HCOO* intermediate. In our study, we have considered the reaction between CO and O, as will be discussed later. Since we already know the favorable sites for CO and O on Pd_1/ZnO,

it makes easier to determine the adsorption site for CO_2. Indeed, we find that CO_2 weakly adsorbs at the singly-dispersed Pd site (Figure 7.3d), with an adsorption energy of -0.18 eV.

7.4.2.5 Hydrogen

In Figure 7.3e, we show the energetically favorable adsorption geometry of H_2 on Pd_1/ZnO. The favorable site for H_2 adsorption is at the Pd site, with an adsorption energy of -0.53 eV. It can adsorb at the same site with different orientations which have slightly higher energy. On the other hand, it weakly adsorbs at Zn with an adsorption energy of -0.12 eV.

7.4.2.6 Water

In Figure 7.3f, we show the energetically favorable adsorption geometry of H_2O in which H_2O preferentially adsorbs at the Zn2 site (near the Pd atom, see Figure 7.2a) with an adsorption energy of -0.63 eV. In this geometry, H atom of an adsorbed H_2O forms a hydrogen bond (1.718 Å) with the surface O in the topmost layer.

7.4.2.7 Some Reaction Intermediates

The embedded Pd atom in O vacancy of ZnO($10\bar{1}0$) can dramatically alter the adsorption sites, adsorption energies of molecules and the intermediates. In Table 7.2, we summarize our results of the adsorption energies of intermediates either in isolated or in co-adsorbed with other intermediates at the energetically favorable sites, and the vibrational frequencies. Upon co-adsorption with other intermediates, the adsorption energies of these intermediate species may

significantly vary. Our results show that the CH_3OH does not gain energy when co-adsorbed with O*, but gains energy by 0.1 eV when co-adsorbed with OH*. On the other hand, CH_3O* significantly gains energy by 0.75 eV and 1.41 eV when co-adsorbed with O* and OH*, respectively. Similarly, the CH_2O* also gains energy by 0.27 eV and 0.14 eV, when co-adsorbed with O* and OH*, respectively. Adsorption of formyl (CHO) is also found to be stronger when it is co-adsorbed with O* and OH* (see Table 7.2). Thus, these results indicate that co-adsorption effect leads to increase the binding affinity of the intermediates on Pd_1/ZnO.

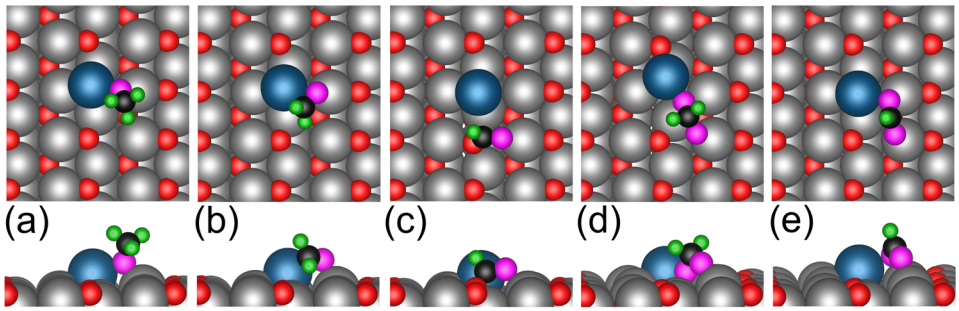

Figure 7.4 DFT-optimized geometries of most stable intermediates on Pd_1/ZnO: a) CH_3O*, b) CH_2O*, c) CHO*, d) H_2COO*, and e) HCOO* species. Top and bottom panels show the top and side views, respectively.

7.4.3 Dehydrogenation of Methanol

There is a general agreement [315-319] that, on solid catalyst surfaces, the dehydrogenation of CH_3OH to CO and H occurs via methoxy (CH_3O) as the first intermediate, and then followed by the stepwise hydrogen abstraction to formaldehyde (CH_2O), formyl (CHO) and CO.

On Pd_1/ZnO, the dissociation of CH_3OH^* into CH_3O^* and H^* via O-H bond breaking is slightly endothermic (ΔE=+0.07 eV and E_a=0.14 eV). On the other hand, C-H bond breaking of the resulting CH_3O^* is energetically favorable (ΔE=-0.13 eV, E_a=0.56 eV). The minimum energy pathways for the reactions $CH_3OH^* \rightarrow CH_3O^* + H^*$ and $CH_3O^* \rightarrow CH_3O^* + H^*$ are shown in Figure 7.5(a-b). The further decomposition of CH_2O^* into CHO^* and H^* is again slightly endothermic (ΔE=0.11 eV, E_a=0.79 eV). Finally the activation of C-H bond breaking is energetically favorable ($CHO^* \rightarrow CO^* + H^*$; ΔE=-0.23 eV, E_a=0.13 eV).

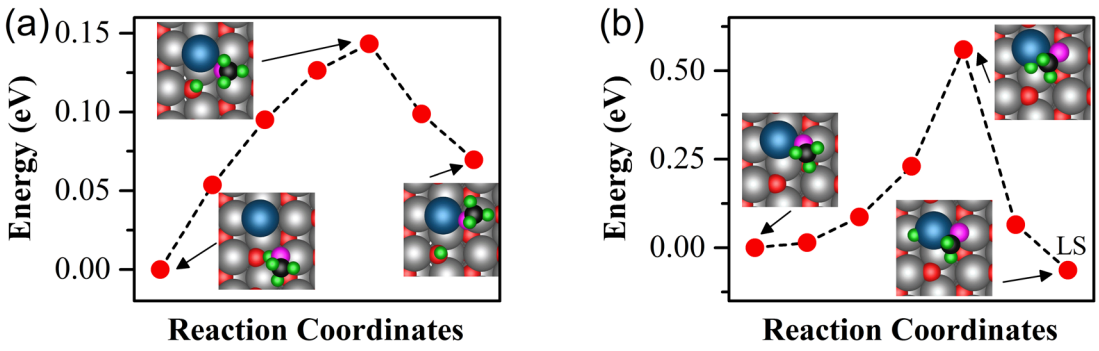

Figure 7.5 Minimum energy pathways for decomposition of a) MeOH* and b) CH_3O^* on Pd_1/ZnO. In b) LS represents the local minimum state.

Figure 7.6 shows the potential energy profile for the subsequent dehydrogenation of CH_3OH on Pd_1/ZnO. These results provide insights into the catalytic activity of Pd_1/ZnO model catalyst toward dehydrogenation of CH_3OH to produce atomic hydrogen. Indeed, Cubeiro et al. [297,320] shows that 1% Pd/ZnO greatly facilitates the dehydrogenation of CH_3OH, producing CO as the intermediate species. Moreover, Chin et al. [321] shows that with the increase of Pd content the formation of CO decreases due to the formation PdZn alloy. This could be related to the reduction of the binding affinity of CH_3OH when Pd content increases.

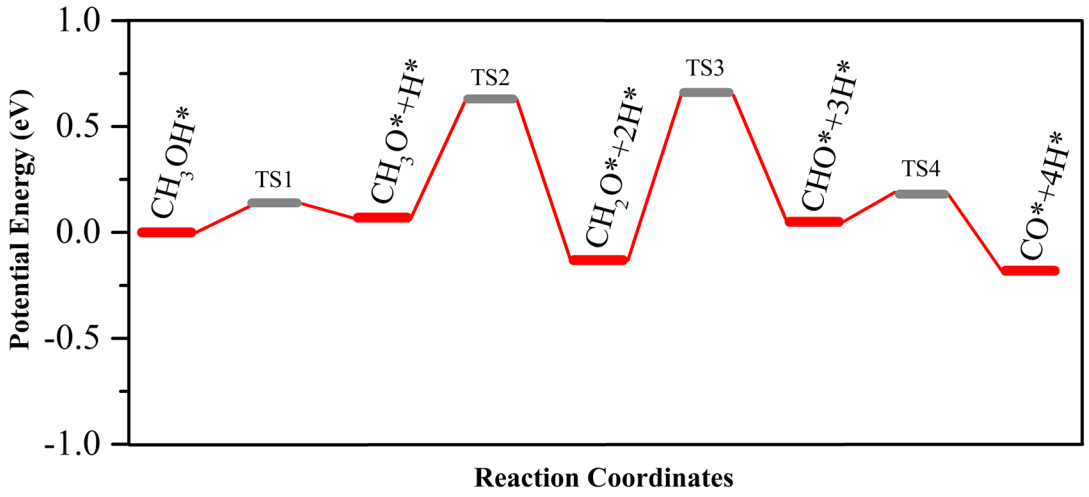

Figure 7.6 Potential energy for successive dehydrogenation of CH_3OH to produce atomic hydrogens on Pd_1/ZnO model systems. The gray bars represent the corresponding transition states.

7.4.4 Reaction with Oxygen and Hydroxyl

Figure 7.7 shows the reaction steps for oxidation of CH_3OH and its intermediate species with oxygen, with barriers (E_f) and (E_r), respectively, for both forward and backward reactions steps. Since the barriers for forward process are smaller than the barriers for the backward reactions, oxidation of the species are thermodynamically favorable. The highest barrier turns out to be higher for the reaction, $CH_3O^*+O^* \rightarrow CH_2O^*+OH^*$. The other reaction steps can easily occur at room temperature. However, we note that the oxidation of the intermediate species can be controlled by the partial pressure of oxygen. Moreover, the adsorption and dissociation, and desorption of oxygen also control the overall process of oxidation.

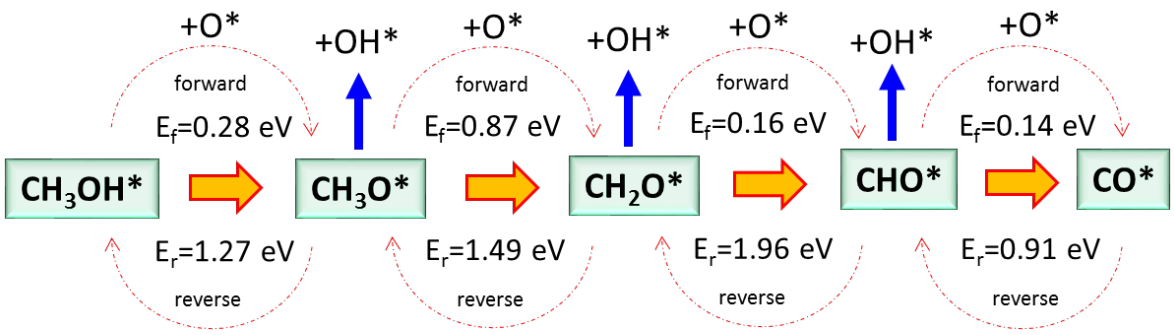

Figure 7.7 Reaction of chemical species with atomic oxygen (O*) to form carbon contained species plus hydroxyl (OH*). Here, (*) represent the adsorbed phases of the chemical species.

Figure 7.8 shows the reaction steps for reaction of CH_3OH and its intermediate species with hydroxyl, with barriers (E_f) and (E_r), respectively, for both forward and backward reactions steps. Since the barriers for forward process are smaller than the barriers for the backward reactions, oxidation of the species are thermodynamically favorable. The highest barrier turns out to be higher for the reaction, CHO*+OH*→CO*+H_2O*. The other reaction steps can easily occur at room temperature. We note, however, that the oxidation of the intermediate species can be controlled by the partial pressure of oxygen.

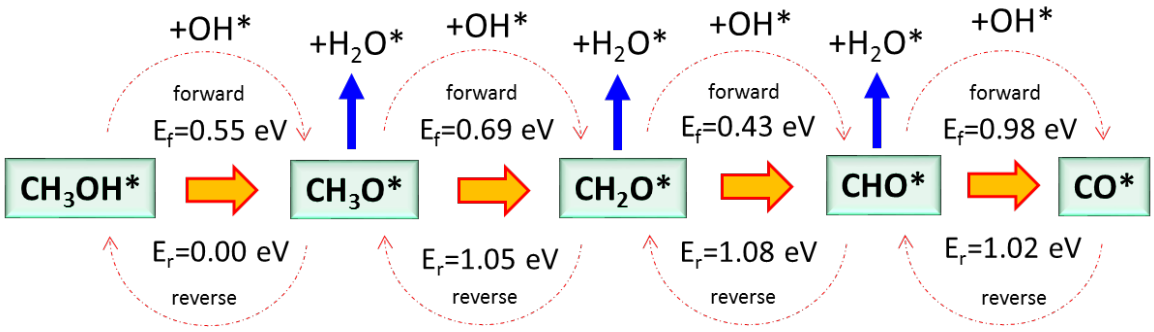

Figure 7.8 Reaction of chemical species with hydroxyl (OH*) to form carbon contained species plus water (H_2O*). Here, (*) represent the adsorbed phases of the chemical species.

7.4.5 Formation of CO versus CO_2

In Figure 7.9, we show the potential energy profile for the formation of CO(g) and CO_2(g) on Pd_1/ZnO. Here, superscript (*) indicates the adsorbed phase of CO. The formation of CO* occurs via abstraction of H from CHO* intermediate species (formed in dehydrogenation of CH_3OH reaction) by C-H scission. The activation barrier for such process on is 0.14 eV. Thus, the CH scission of CHO* to form CO* and H* is activated quite easier. These results indicate that the activity for the formation of CO* is higher (thus facile). However, CO desorption needs to overcome a large barrier of 1.43 eV. The barrier for CO desorption is quite higher than the formation of CO_2(g) *via* the combination reaction of CO* and O*. Here, the reaction between CO* and O* is strongly exothermic, spontaneous reaction followed by a small desorption barrier of 0.18 eV (which is 7.9 times smaller than the desorption barrier of CO). Thus, these results clearly indicate that the activity for the formation of CO_2 gas is higher in the case of Pd_1/ZnO. These results indicate that the formation of CO_2(g) via CO oxidation is facile on Pd_1/ZnO, suggesting formation of CO_2 is thermodynamically and kinetically preferred.

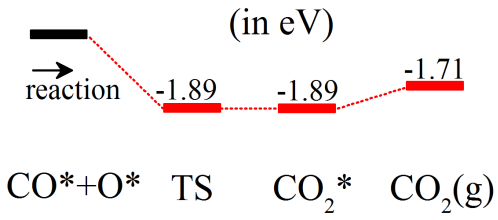

Figure 7.9 DFT-calculated energetics for formation of CO_2(g) on Pd_1/ZnO.

7.4.6 Formation of H_2 versus H_2O

In Figure 7.10, we show the potential energy profiles for the formation of H_2(g) and H_2O(g)

on $Pd_1/ZnO(10\bar{1}0)$. As shown in Figure 7.15, on Pd_1/ZnO, the barrier for the reaction between H* and H* is 0.91 eV. The desorption barrier for the conversion of H_2* to free H_2(g) is 0.87 eV. Thus, H_2 has equal probability of dissociation and desorption. As shown in Figure 7.15, the reaction between H* and OH* to form H_2O* is not energetically favorable over H_2O dissociation. Since the barrier (0.63 eV) for the formation of H_2O* is quite larger than the barrier (0.08 eV) for the reverse process $H_2O^* \rightarrow H^*+OH^*$, indicating that H_2O dissociation is highly activated on $Pd_1/ZnO(10\bar{1}0)$. For H_2O to be desorbed, it must overcome a barrier of 0.54 eV. Thus, the adsorbed H_2O on Pd_1/ZnO prefers to dissociate into OH* and H* instead of desorption to H_2O(g). That is, H_2O is unstable whereas H_2 is stable, suggesting high H_2 selectivity.

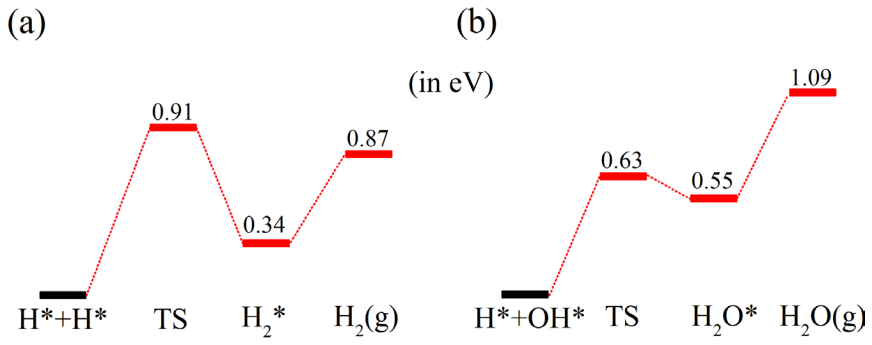

Figure 7.10 DFT calculated energetics for formation of: a) H_2(g), and b) H_2O(g) on Pd_1/ZnO.

7.4.7 Electronic Density of States and Charge Transfer

We now analyze the density of states to understand the followings: i) how single Zn atoms near Pd are electronically modified from those of pristine ZnO; ii) why single Pd atom or Pd-Zn are active sites than only Zn atoms of pristine ZnO. Firstly, Figure 7.11a exhibits a narrow distribution with only three peaks for bonding with Zn below, the major DOS distributed between -2 eV and -0.5 eV, closer to the Fermi level than that of Pd atom in $Pd_{16}Zn_{16}$. There is a signature

of the frontier state, below the Fermi energy (~0.5 eV), mainly made of d_{x2-y2} (Figure 7.11a). The most pronounced peak at -1 eV below the Fermi level is dominantly of d_{xy} character, and is mixed with d_{x2-y2}. These results indicate that the singly dispersed Pd atom bears unique electron-rich features near the Fermi energy, which thus improve the catalytic activity. Secondly, Zn atoms near single Pd are electronically modified: the density of states of a Zn atom (inset Figure 7.11b) is different from that of Zn atom pristine ZnO. This difference is clearly visible for the energy range from -2 eV to 0 eV (with respect to Fermi energy), as indicated by dotted rectangle (see Figure 7.3b). Since the local electronic structure of neighboring Zn atoms is modified by singly dispersed Pd atom, monoatomic dispersion of Pd on ZnO plays an important role for the optimal activity

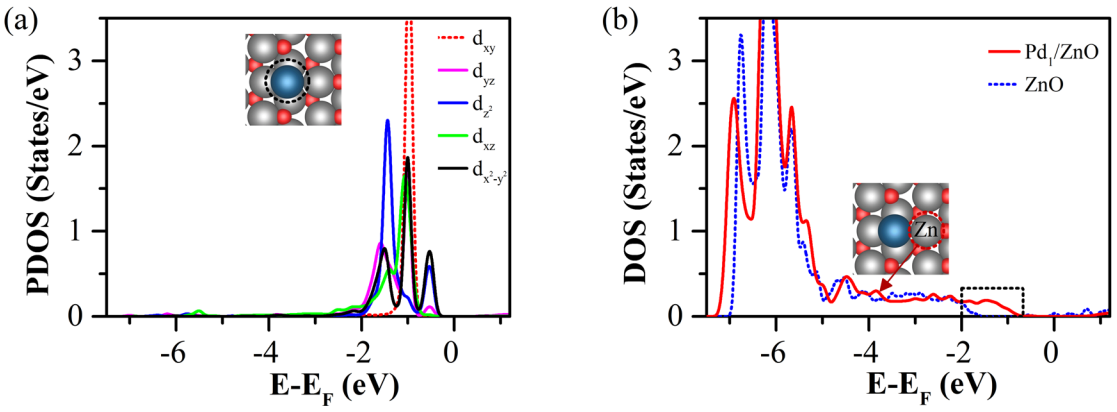

Figure 7.11 (a) Density of states projected onto d orbitals of single Pd atom on ZnO($10\bar{1}0$); (b) Atom-resolved density of states of Zn atom (indicated in inset) of Pd_1/ZnO system and surface Zn atom of pristine ZnO. The zero (in eV) represents the reference level with respect to the Fermi energy which is different for these two systems.

On the basis of Bader analysis, we find that single Pd on ZnO is charged -0.36e thus gaining electrons from surrounding Zn atoms. The Zn atom bonded to the Pd atom is charged +0.85e or

+1.0e while others bonded to O atoms are charged about +1.3e. Thus, Zn bonded to Pd is less cationic than those bonded to O.

7.4.8 Catalytic Reactions and Energetics of MPO on Pd_1/ZnO

In Figure 7.12, we show the geometric structures and energetics of the intermediates involved in the catalytic cycle I for MPO, in which methanol undergoes dehydrogenation *via* abstraction of H until surface formaldehyde (CH_2O*) is formed. The cycle first starts from the adsorption of CH_3OH at the most favorable adsorption site (Zn next to single Pd site). Then one half of O_2 is consumed by the cycle I. This means CH_2O* undergoes oxidation to form H_2COO*, which decompose into two intermediate species: HCOO* and H*. Finally, CO_2 is formed by the decomposition of formate (HCOO*). As the starting point of the cycle I, methanol adsorbs with an adsorption energy of -1.02 eV. The decomposition of CH_3OH* into CH_3O* and H*, as the first intermediates, is slightly endothermic ($\Delta E = 0.07$ eV). Then, further abstraction of hydrogen takes place leading to CH_2O* Then, the co-adsorption of two hydrogen (2H*) on the ZnO($10\bar{1}0$) reduce the energy of the system. The energy difference (ΔE) or reaction energy (ΔE) for CH_3O*+H* and CH_2O*+2H* turns out to be -0.06 eV, slightly exothermic. Including the co-adsorption effect, we find that the energy barrier for the abstraction of H* from CH_3O* is 0.56 eV. Then, the reaction between O* and CH_2O* yield H_2COO*. The formation of H_2COO* from oxidation of CH_2O* is exothermic ($\Delta E = -0.31$eV), and needs to cost an energy barrier of 0.71 eV. So, formed H_2COO* undergoes dehydrogenation to form two intermediates: HCOO* and H*. This process is highly exothermic (ΔE=-2.89 eV), however, needs to overcome the high barrier of 1.62 eV. Then,

HCOO* undergoes further dehydrogenation to form COO* and H*, for which system needs extra energy of 1.04 eV (which is the difference in energy between HCOO*+H* and COO*+2H*). So produced H* and H* combine to form H_2* (for which the barrier turns out to be 0.91 eV). Finally, desorption of H_2 and CO_2 occur at single-dispersed Pd site.

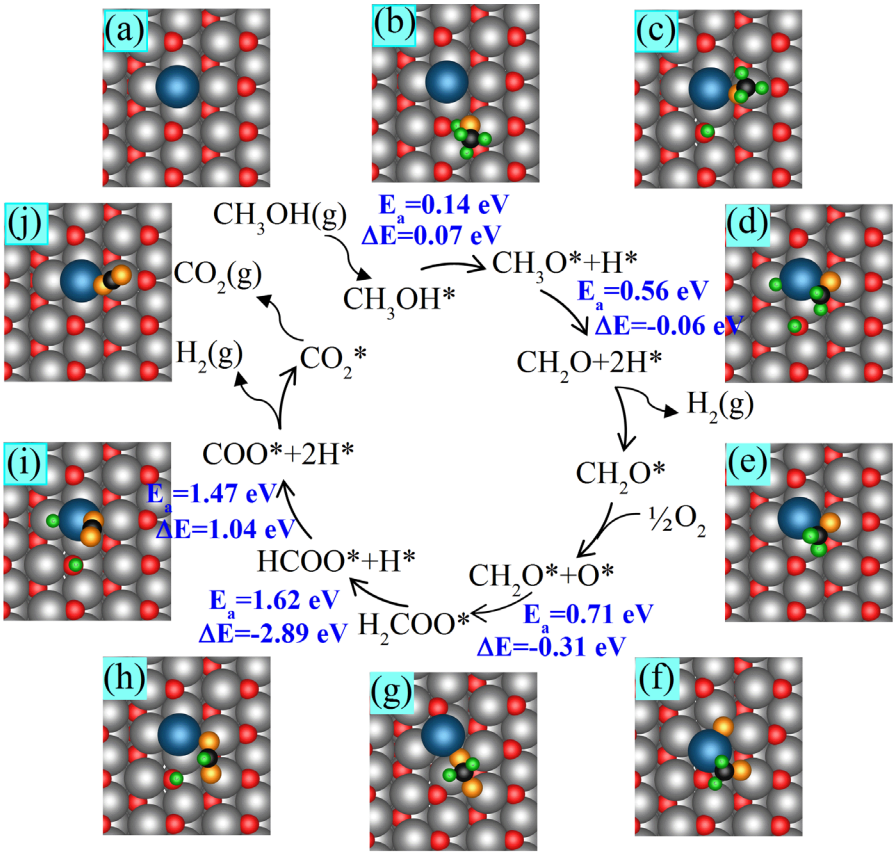

Figure 7.12 Catalytic cycle I for MPO reaction on $Pd_1/ZnO(10\bar{1}0)$. In this cycle, CH_3OH undergoes dehydrogenation until the formation of surface formaldehyde (CH_2O*), which then oxidizes to form H_2COO*.

In Figure 7.13, we show the geometric structures and energetics of the intermediates involved in the catalytic cycle II for MPO, in which CHO* is formed from the successive dehydrogenation of CH_3OH*. In cycle II, atomic oxygen then reacts with CHO*. There will be

two reactions scenarios: i) either the formation of HCOO* from the oxidation of CHO* or ii) formation of CO* via abstraction of H from CHO*. Based on the activation barrier for these two reactions, one of the reactions is dominant and kinetically favorable. Thus, the kinetics plays an important role for the selection of the process. As depicted above for the cycle I (Figure 7.12), the process of dehydrogenation of methanol in the cycle II is similar upto the formation of surface formaldehyde (CH_2O*). From this step, CH_2O* now undergoes dehydrogenation rather than oxidation (CH_2O*+O*, in cycle I) to form CHO*+H*. This process is exothermic (ΔE=-0.25 eV), and is activated by an energy of 0.79 eV. Then, surface formyl (CHO*) either gets oxidized to form HCOO* or undergo further dehydrogenation to form CO*+H*. Formation of HCOO* (via. CHO*+O*+H*→HCOO*+H*) is exothermic (ΔE=-1.77 eV), and needs to overcome an activation barrier of 1.04 eV. On the other hand, the formation of CO* (via. CHO*+O*+H*→CO*+O*+2H*) is less exothermic (ΔE=-1.02 eV), considering the co-adsorption effect, and needs to cost a smaller barrier of 0.11 eV. Importantly, the small barrier for the formation of CO* via the abstraction of H* from CHO* is far kinetically favorable than the formation of HCOO* from oxidation of CHO*. Similarly, the formation of COO* from CO oxidation is exothermic (ΔE=-1.71 eV) whereas the formation of COO* from dehydrogenation of HCOO* is highly endothermic (ΔE =+1.04 eV). In addition, the formation of CO_2* from oxidation of CO is spontaneous whereas from the dehydrogenation of HCOO* it costs a huge barrier of 1.47 eV. These results indicate that formation of CO_2 is both thermodynamically and kinetically favorable via O*+CO* →CO_2* path as compared to HCOO*→H*+CO_2*.

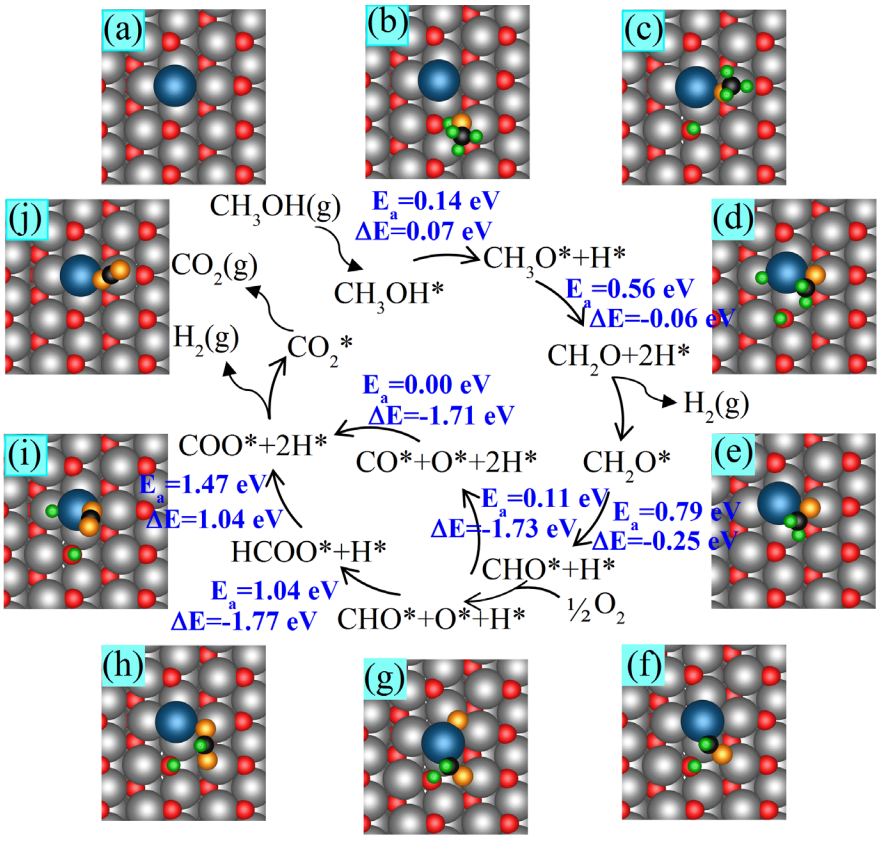

Figure 7.13 Catalytic cycle II for MPO reaction on $Pd_1/ZnO(10\bar{1}0)$. In this cycle, CH_3OH undergoes dehydrogenation until surface formyl (HCO*) is formed. Then, HCO* gets oxidized to form HCOO*.

7.4.9 Kinetic Monte Carlo Simulations

In Figure 7.14(a-b), we present our kMC results for steady-state surface coverage of H and CO species as a function of time and temperature, respectively. For our simulation of a total $1.7x10^9$ kMC steps for a total simulation time of 832 s, we have sampled steady-state statistics for every 10^5 KMC steps on average. As shown in Figure 7.14, the coverage of H and CO is equal at 292^0C. As the temperature increases, the CO coverage decreases. There is no trace of H_2O on the surface.

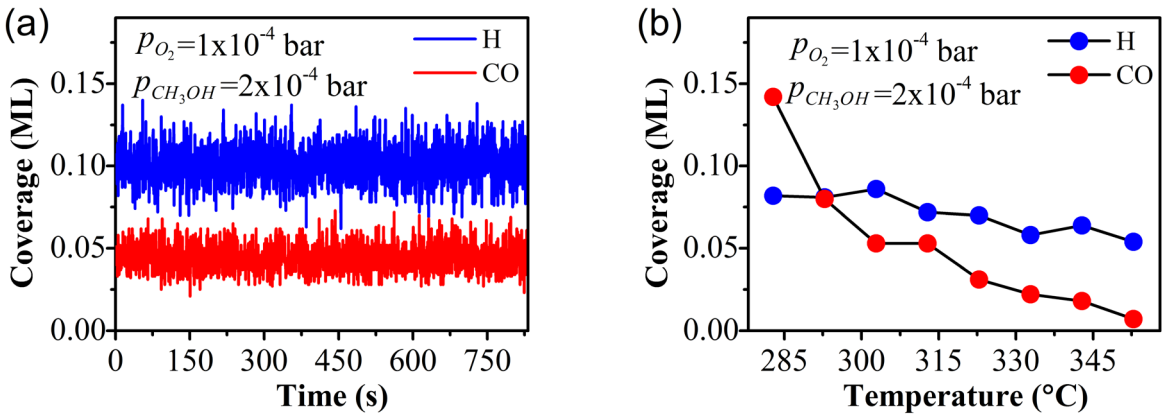

Figure 7.14 (a) Evolution of coverage vs reaction time; and (b) Steady-state coverage of H and CO. For simulation, O_2 and CH_3OH pressures are maintained as 1x10^{-4} bar and 2x10^{-4} bar, respectively.

Now the selectivity for the products (H_2, H_2O; CO, CO_2) is defined as

$$S_{H_2} = \frac{r_{H_2}}{r_{H_2} + r_{H_2O}} \qquad S_{H_2O} = \frac{r_{H_2O}}{r_{H_2} + r_{H_2O}}$$

$$S_{CO} = \frac{r_{CO}}{r_{CO} + r_{CO_2}} \qquad S_{CO_2} = \frac{r_{CO_2}}{r_{CO} + r_{CO_2}}$$

Figure 7.15 shows the product selectivity for H_2 versus H_2O, and for CO_2 versus CO formed in MPO on Pd_1/ZnO. The ratio of the partial pressures for O_2/CH_3OH is kept as 1:2. For our simulation, the partial pressures of O_2 and CH_3OH are chosen as 1x10^{-4} bar and 2x10^{-4} bar, respectively. The selectivity towards the formation of H_2 at 290°C 97%, in good agreement with experiment (~90%) [322]. At the same temperature, we find the selectivity for H_2O product is only 3%, a quite lower than the selectivity for H_2. Similarly, the selectivity for CO_2 at 290°C is 87%, in very good agreement with experiment (~85%) [322]. At the same temperature, we find the selectivity for CO is 13%, which is lower than the selectivity for CO_2. Thus, these results clearly indicate that Pd_1/ZnO offer high selectivity for H_2 and CO_2 products.

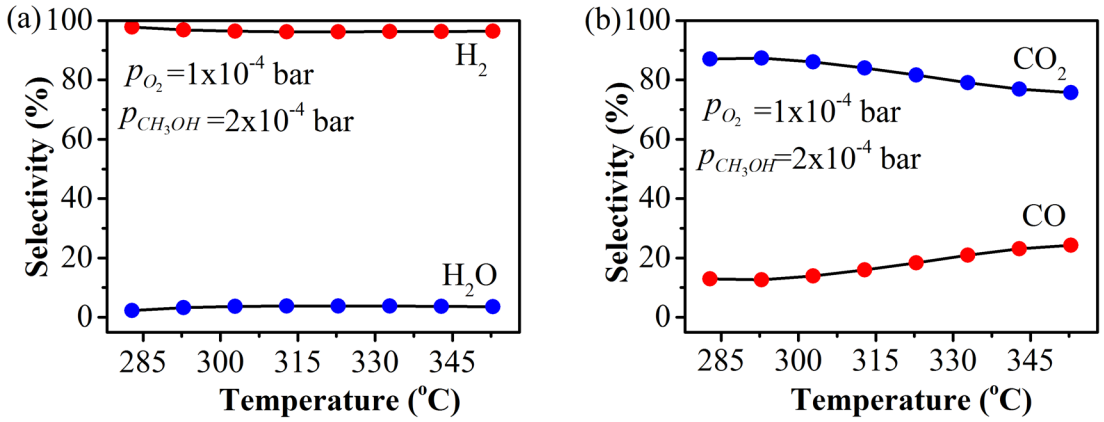

Figure 7.15 Selectivity for (a) H_2 vs H_2O, and (b) CO_2 vs CO calculated for various temperatures.

The catalytic activity and selectivity of Pd/ZnO have been explored experimentally by other groups. Cubeiro et al. [320] reported that the 1% Pd/ZnO catalyst, with O_2/CH_3OH feed ratio of 1/2, efficiently catalyzes the CH_3OH conversion and results in mainly four products. At 270 ^{0}C, the O_2 was completely consumed and the methanol conversion reached to 80%. At 350^{0}C, the highly selective products during partial oxidation of MPO on 1% Pd/ZnO catalyst were found to be CO_2 and H_2 with selectivity of 80% and 78%, respectively.

Usami et al. [323] showed that the catalytic activity of 15wt% Pd/ZrO_2 increased with increase in time, and methanol conversion reached 18% at 200^{0}C. The 15 wt% of Pd/ZrO_2 catalyst can produce high catalytic activity in the selective decomposition of CH_3OH to CO and H_2 T<=200^{0}C. The selectivity for CO is ~98% at 200^{0}C and 250^{0}C on Pd/ZrO_2 [323]. Also, 2 wt% of Pd/ZrO_2 are very active in CH_3OH decomposition [324]. On the other hand, on 1% Pd/ZrO_2, the methanol conversion is reached to 82% at 250 ^{0}C. The increase in the CH_3OH conversion is thus dependent upon the composition of catalyst and the reaction temperature. The selectivity for CO on 1% Pd/ZrO_2 is ~80%. These results suggest that with the decrease of Pd content, the selectivity

for CO decreases. In addition, it has been found that the effect of metal-oxide support also affects the catalytic activity and the selectivity for the products. Cubeeiro et al. [320] shows that, for the O_2/CH_3OH feed ratio of 1/2 and temperature of 255^0C, the selectivity for H_2 on 1% Pd/ZnO is ~80% whereas it is only ~40% on 1% Pd/ZrO_2.

7.5 Summary

Employing DFT+kMC simulations, we have studied the methanol partial oxidation on Pd_1/ZnO. The high catalytic activity of Pd_1/ZnO can be credited to the decisive influence of the local environment (or geometry) and electronic structure of the active Zn sites modified by single Pd, and those of the active single Pd and Pd-Zn sites. Singly-distributed Pd sites embedded in ZnO support moderately modify both geometric and electronic structures of the cationic Zn sites for the optimal activity. Indeed, there are spontaneous CO_2 formation, nearly spontaneous dissociation of H_2O, and stabilization of O_2 and H_2 right at or near the singly-dispersed Pd sites. These processes can control the selectivity for the products.

Through our DFT examination, we have identified the optimal pathway for formation of the desired products. The alternative paths for production of CO_2: $H_2COO \rightarrow HCOO^* + H^*$ and $HCOO^* \rightarrow COO^* + H^*$ are slow since these processes need to overcome activation barriers of 1.62 eV, and 1.47 eV, respectively. Thus, the rate-limiting steps of the overall production of CO_2 are dissociation of H_2COO^*, followed by decomposition of HCOO* into CO_2^* and H*. The strong affinity of binding of HCOO* at the Pd-Zn site, owing to the strong attractive interaction between HCOO* and the substrate, is a hindrance to CO_2 formation *via* HCOO* path. On the other hand, the CO_2 formation via CO* path is very fast since there is no barrier for the reaction between O*

and CO*, which is produced *via* $CH_3OH^* \rightarrow CH_3O^* \rightarrow CH_2O^* \rightarrow CHO^* \rightarrow CO^*$. The successive dehydrogenation of MeOH, with the moderate barriers, is also the key for producing atomic hydrogen, thereby leading to the H_2 formation.

Our *ab-initio* DFT+kMC simulation, for which input parameters are derived from DFT calculations, clearly reveals that there are mainly four products, namely H_2, H_2O, CO_2 and CO – in accordance with earlier experiments on Pd/ZnO catalysts [297]. For conditions relevant to experiments, we have obtained high selectivity for H_2 and CO_2 over that of H_2O and CO as reaction products.

CHAPTER 8 COMPLEMENTARY ROLES OF BENZYLPIPERAZINE AND IODINE IN STRONG ENHANCEMENT OF ORANGE PHOTOLUMINESCENCE FROM CuI(111) THIN FILM

In this work, we employ density functional theory (DFT) with the inclusion of onsite Coulomb (U) term to explain the mechanism for the enhanced orange photoluminescence (PL) of a coupled system of benzylpiperazine (BZP) molecule with a CuI(111) thin film in the presence of an iodine 'vapor' atom. Our results show that the adsorbed BZP and the iodine atom play complimentary roles in producing the PL in the visible range. The iodine 'vapor' atom on Cu(111) creates an impurity state, located ~0.25 eV above the valence band-edge of the film – in good agreement with experiment (~0.2 eV). Upon photo-excitation of the BZP/CuI(111) system with iodine 'vapor' atoms, excited electrons are transferred into the conduction band (CB) of CuI, and holes are trapped by the atoms. These holes then relax into the BZP HOMO state. The relaxation of holes is facilitated by the realignment of the electronic states of BZP, which adsorbs on Cu(111) in the immediate vicinity of iodine 'vapor' atom. Relaxed holes subsequently recombine with excited electrons in the CB of the CuI film, thereby producing a luminescence peak at ~2.1 eV.

8.1 Introduction

Cuprous iodide (CuI) has received considerable attention in materials research owing to its interesting physical properties and potential applications. It has a wide band gap of 3.1 eV (visible range). At low-temperature, bulk CuI in its "zinc blende" (γ-phase) behaves as a fast-ion conductor [325] with low electrical conductivity. Under X-ray excitation, CuI powder exhibits a narrow blue photoluminescence (PL), whereas CuI crystals, under the same condition, show a strong red

luminescence. The later phenomena is associated with the optical transition, which is facilitated by surface iodine vacancy states [326]. On the other hand, upon exposure to low ultraviolet (UV) radiation, pure CuI crystals produce blue PL with pronounceable excitonic features in the spectrum [327]. γ-CuI nanoparticles fluoresce with a strong emission peak at 2.97 eV [328]. On the other hand, CuI thin films have unique physical properties. Experimental investigation of PL properties in CuI thin films grown on different substrate materials has laid the possible ground for controlling the exciton-relaxation process mediated by the longitudinal optical (LO)-phonon scattering in CuI films for which the intensity of PL oscillates with the period of variation in LO-phonon energy [329]. In CuI thin films grown on a NaCl substrate, it was shown that two PL bands originate under photo-excitation: one with a peak at 3.05 eV (attributed to the heavy-hole exciton), the other with a peak at 3.0 eV (attributed to biexcitons resulting from the exciton-exciton scattering) [330]. Highly-oriented γ-phase CuI(110) thin films grown on a copper substrate produce a single sharp exciton band at 3.02 eV, whereas CuI(111) films grown on the same substrate yields fluorescence emission at 2.95 eV [331]. Highly-oriented electro-deposited γ-phase CuI(111) thin films grown on a indium doped tin oxide (ITO) glass substrate exhibit the large exciton band luminescence at room temperature with an intense emission peak at 3.1 eV and a weak emission peak at 2.94 eV [332]. Thus, CuI films possessing these beautiful properties can be used in dye-sensitized solid-state solar cells (as the hole-collecting and/or -transporting agent) [333-337]. Moreover, these films can be potentially applicable in the fabrication of organic light-emitting devices [338], in light/chemical sensors, and in field-emission and vacuum fluorescent display products [339].

The PL characteristics of CuI films can be affected by several factors such as substrate materials or foreign atoms or molecules or so on. For example, a CuI film grown on a glass

substrate shows a strongly enhanced PL peak at 2.98 eV when exposed to iodine atoms [336]. Affinity of adsorbing of organic molecules by the film can also impact the PL properties of CuI film: a hybrid composite CuI(111)/beta-cyclodextrin thin film exhibits PL with peaks at 3.02 eV and 2.94 eV, owing to the passivation of iodine-related defect sites by beta-cyclodextrin matrix [340]. A recent experimental study [341] of complexes formed between CuI and benzylpiperazine (BZP) molecules in the solution suggests that the CuI(111) film, upon adsorption of BZP, can emit light of wavelength equivalent to orange light in the visible range. Indeed, this turns out to be the case only when the BZP/CuI(111) system is supplemented by iodine 'vapor' atoms. Moreover, the electronic structures and optical properties of CuI films with various adsorbates (atoms and/or molecules) have not been theoretically studied.

Herein, we present DFT+U results with detailed analysis of geometry and electronic structures, and optical properties of coupled BZP/CuI(111) systems both without and in the presence of iodine ad-atoms in order to explain the mechanism behind the enhanced orange photoluminescence (PL) of a coupled BZP/CuI(111) system in the presence of an iodine ad-atom.

8.2 Computational Details

We carry out first-principle density functional theory (DFT) and DFT+U calculations using the Quantum Espresso code [342]. To describe the electron-electron interaction, we use the generalized-gradient approximation in form of PBE functional [43]. We use the PAW method [72,73] to account for the interaction between ion and electron. For the plane wave expansion, we set the kinetic energy cutoff to 476 eV. We set the criterion for the force convergence for the

relaxation of various structures and the threshold for the total energy in the self-consistent calculations to 0.01 eV/Å and 10^{-4} eV respectively.

To model isolated pristine CuI films – i.e. films with no iodine 'vapor' atom as well as BZP, we construct (1x1) supercell of 5, 7, 9 and 11-layers (total atoms = 10, 14, 18 or 22, respectively), and sample the Brillouin zone with a 7x7x1 k-mesh for simplifying the relaxation procedure and with a 15x15x1 k-mesh for calculating density of states. We confined our further calculations to 5-layer system because the results did not vary significantly for films of different thicknesses. To model films with an iodine ad-atom or adsorbed BZP or both, we construct (4x4) supercell of CuI(111) film with an iodine 'vapor' atom, with an adsorbed BZP and with an adsorbed BZP in the immediate vicinity of an adsorbed iodine (total atoms = 161, 189 or 190, respectively). In all cases, we sample the Brillouin zone using the Gamma point for simplifying the relaxation procedure, and a 3x3x1 k-mesh for calculating the density of states. To generate the k-points, we adopt the Monkhorst-Pack scheme [74], using the Methfessel and Paxton smearing technique [76] with a smearing width of 0.01 Ry.

8.3 Results and Discussion

8.3.1 Benzylpiperazine Molecule

Figure 8.1 shows the partial charge density for the selected molecular orbitals of benzylpiperazine (BPZ) molecule. In particular, there are strong charge redistributions in the excited states of BZP, as shown in Figure 8.1d-e. The excited electronic charges are confined mostly to the top part of BZP, while the highest occupied orbital charges (HOMO and HOMO-1)

are distributed mostly to the bottom part of BZP. These highest orbitals of the adsorbed BZP are located mostly close to the surface (energies -0.83 eV and -1.42 eV for HOMO and HOMO-1, respectively). As will be described below, such charge distribution is important for the PL mechanism, which involves the fast hole-drift from a CuI(111) thin film to BZP when the BZP/CuI(111) system is incorporated with an iodine ad-atom. The total energy difference between HOMO-1 and HOMO is 0.16 eV, and that between HOMO-1 and HOMO-2 is 1.0 eV. The isolated BZP molecule has a large HOMO-LUMO gap (3.6 eV), which makes it optically inactive in the visible range.

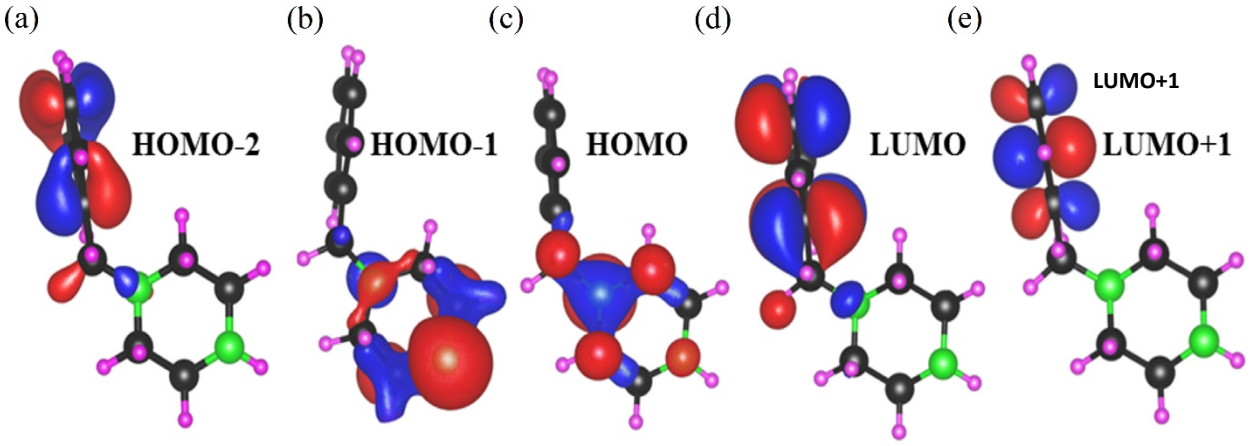

Figure 8.1 (a) HOMO-2 (b) HOMO-1 (c) HOMO (d) LUMO and (e) LUMO+1 molecular orbitals of the BZP molecule. The iso-surface value for the plot is taken as 0.02 eV/Å^3. Red lobes represent negative Iso-density and blue lobes represent positive Iso-density. Green, black, and magenta balls represent N, C, and H atoms, respectively [T. B. Rawal, V. Turkowski, T. S. Rahman, J. Phys.: Condens. Matt., (2014)] (Copyright: IOP publishing 2014).

8.3.2 Cuprous Iodide (CuI)

We perform DFT+U calculations to study the electronic structures of the γ-phase crystalline CuI. The crystal structure is depicted in Figure 8.2. To obtain the band gap of 3.1 eV, we incorporate different values of U's in DFT+U calculations (see Figure 8.3). The values of U that produce this band gap turn out to be U(Cu)=8 eV and U(I)=5 eV respectively. The lattice parameters obtained using DFT and DFT+U approaches are 6.118Å and 6.194 Å, respectively. These calculated values agree with experimental value (6.054 Å) [34], within 1% and 2.3%, respectively. To study the U-dependence of the energy gap, we use the experimental value of the lattice parameter. However, to compute the band structure and the DOS we use the optimized lattice parameter (6.194 Å), which corresponds to a slightly reduced gap of 3.08 eV. The difference (0.03 eV) is tiny enough to justify our choice of the value of U for calculating the electronic structure and optical spectrum of CuI.

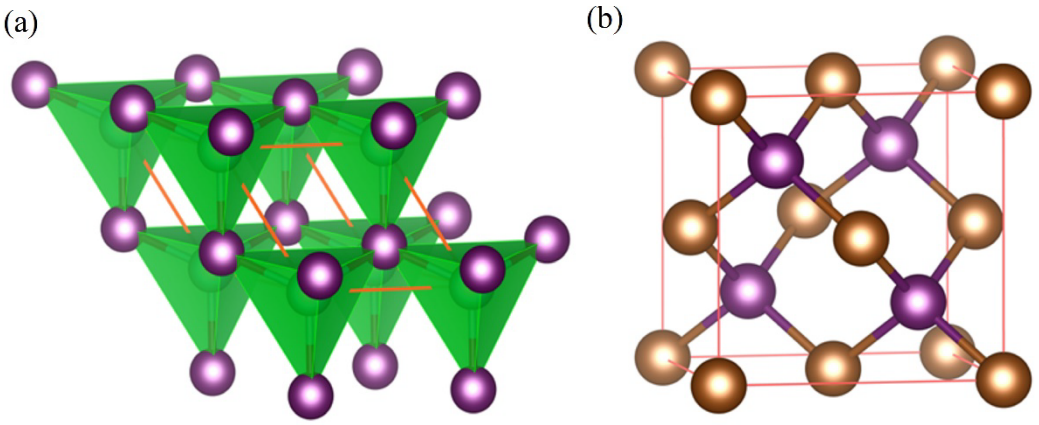

Figure 8.2 (a) Unit-cell of γ-phase crystal structure of CuI. Each I atom is coordinated to four Cu atoms, forming a tetrahedron. The stacking of these tetrahedra within the crystal is also displayed. (b) The face-centered cubic crystal structure of CuI. Brown and purple balls represent the Cu and I atoms, respectively [T. B. Rawal, V. Turkowski, T. S. Rahman, J. Phys.: Condens. Matt. (2014)] (Copyright: IOP publishing 2014).

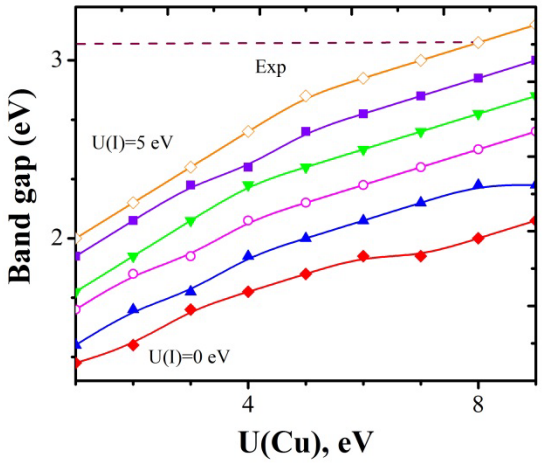

Figure 8.3 Band gap as a function of Coulomb repulsion U(Cu) at U(I)=5eV. The experimental gap corresponds to U(Cu)=8 eV and U(I)=5eV. [T. B. Rawal, V. Turkowski, T. S. Rahman, J. Phys.: Condens. Matt. (2014)] (Copyright: IOP publishing 2014).

Figure 8.4(a-b) show the electronic band structures of bulk CuI calculated within DFT and DFT+U. The results obtained for both approaches are similar in terms of band dispersion and orbital symmetry, but the orbital energy calculated using DFT is different from that calculated using DFT+U. In both cases, the top valence band consists of hybridized I 5p and Cu 3d states. The lowest-energy conduction states are formed mainly by Cu 4s-electrons, with some contribution of the Cu 4p, I 5s and I 5p orbitals. Indeed, in a crude approximation, the 4s electron of the Cu atom contributes to the complete filling of I 5p orbitals, making the Cu 4s orbital empty. Our calculated DFT band gap is ~1.1 eV, which is in good agreement with other DFT calculations (see, e.g., Ref. [343]), however, much smaller than the experimental value of ~3.1 eV [344]. This experimental band gap is well reproduced, however, by DFT+U, which takes the electron correlation effects into account. The localized Cu 3d electrons play a major role in the correlation effects within the system. Owing to correlation effects, an electron which occupies Cu 4s orbital

gains an additional energy ~U due to the strong Coulomb repulsion from the occupied electron in Cu 3d state. This energy shift is a cause for the band gap increase in our DFT+U results.

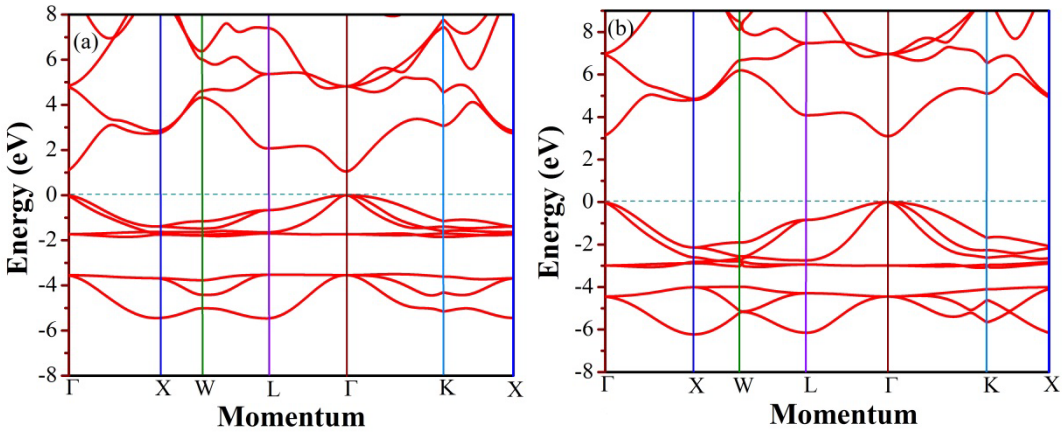

Figure 8.4 Band structure of bulk CuI obtained from: (a) DFT and (b) DFT+U (Here and hereinafter, the values of Coulomb repulsion are taken as U(Cu)=8 eV and U(I)=5 eV). [T. B. Rawal, V. Turkowski, T. S. Rahman, J. Phys.: Condens. Matt., (2014)] (Copyright: IOP publishing 2014).

We have studied (1×1) supercell systems with 5, 7, 9 and 11 molecular-layers of CuI(111) (the thickness ranging from approximately 1.5 nm to 3.3 nm). Because there is no inversion symmetry in the γ-phase of CuI, the two free surfaces are non-equivalent, with Cu atoms on the higher top surface and I atoms on the lower bottom surface. The top layer, consisting of Cu and I atomic sub-layers, acquires nearly planner structure after full ionic relaxation. As will be explained later that the role played by such iodine 'vapor' atoms in producing the PL when a BZP molecule adsorb on a CuI(111) thin film is far more attenuated than that played by 'vapor' atoms introduced into the identical molecular-conjugated system.

8.3.3 Effects of Iodine Atom on CuI(111)

CuI samples always contain a stoichiometric excess of surface iodine that naturally rises from the bulk [335]. The adsorption of iodine 'vapor' atoms on the surface leads to additional surface states, which can play an important role for tuning the PL of the system. Here, we consider the case in which the coverage of the iodine 'vapor' atoms is equal to 1/16 ML, i.e., one atom per (4×4) surface unit cell. Figure 8.5b-c show the DFT+U optimized structure of the 5-layer CuI(111) with an iodine atom adsorbed on the top of a Cu atom, whose coordination is thus changed from three-fold (3f) to 4f. The distance between the 'vapor' atom and the nearest neighbor Cu atom is 2.45Å (compared with the bulk Cu-I distance 2.68Å). The 'vapor' atom causes also a slight distortion on the surface: the surface Cu atom bonded to ad-atom is buckled by 1.13 Å out of the virtually planer surface.

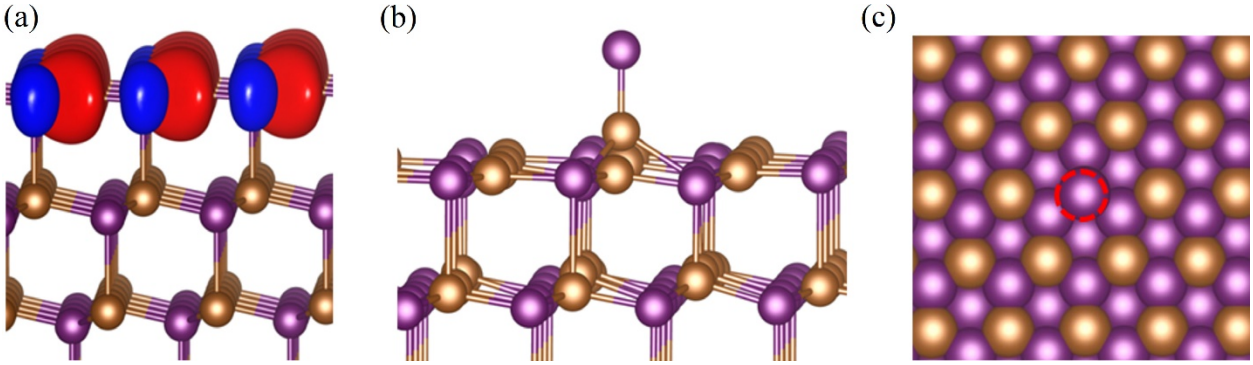

Figure 8.5 (a) Partial electron density calculated for the topmost valence band composed of orbitals that are strongly localized on the pristine CuI(111) (calculated for Γ-point at the zone center). The iso-surface value for the plot is set to 0.02 eV/Å^3. The localization of the p-d hybridized orbitals on the topmost layer indicates that the surface-layer is optically very active in comparison to the bulk-layers. Relaxed structures of I/CuI(111) 5-layer film: (b) ball-and-stick model (side view) and (c) ball model (top view). In the top-view, the iodine ad-atom is encircled by red-dotted circle. Brown and purple balls represent by Cu and I atoms, respectively. [T. B. Rawal, V. Turkowski, T. S. Rahman, J. Phys.: Condens. Matt. (2014)] (Copyright: IOP publishing 2014).

As shown in Figure 8.5a, the p-d hybridized orbitals of CuI film states are strongly localized on the surface layer. The localized character of these surface orbitals makes them electronically different from the bulk-like orbitals of layers below. Before analyzing the mechanism of PL of the coupled BZP/CuI(111) system in the presence of an ad-atom, we present the DFT+U results for the PDOS of the top layer of I/CuI(111) system (Figure 8.6b). As shown in Figure 8.6(b), the occupied iodine 'vapor' state, so-called trapping state, lies at ~0.25 eV above the valence band-edge of the system – in good agreement with experiment [336]. One can see from Figure 8.6b (inset) that this state is formed predominantly by I p-orbital, which correspond in character to dangling I p-bonds.

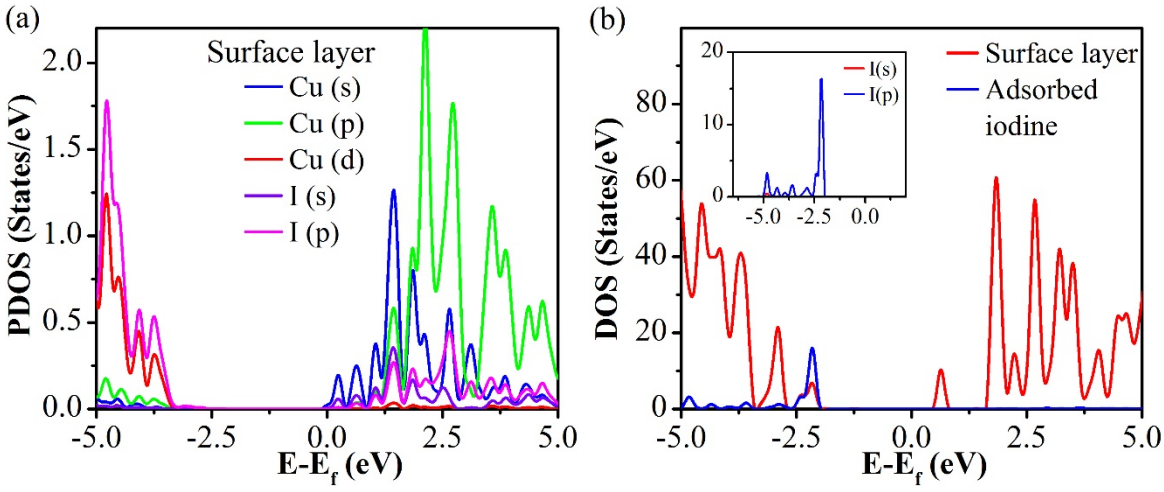

Figure 8.6 DFT+U (a) PDOS of the surface layer atoms of a pristine CuI(111) film, (1x1) unit cell, and (b) DOS of the surface layer atoms (red curve) of CuI(111) film, (4x4) unit cell, and of an iodine 'vapor' atom (blue curve). Here, the surface layer consists of both Cu and I atoms on the (111) surface. The inset shows the PDOS of the 'vapor' atom. The values of Coulomb repulsions for Cu and I are 8.0 eV and 5.0 eV respectively.

The results suggest that neither a pristine CuI film nor a CuI film with the 'vapor' atom can produce an orange PL, owing to lack of the corresponding interband transitions. Therefore, one needs to

study the optical properties of the coupled BZP/CuI(111) system both in absence and in presence of an iodine ‘vapor’ atom, in order to explain at the quantum level the striking PL produced in the latter case.

8.3.4 BZP/CuI System

Figure 8.7 clearly indicates that there is a striking difference in charge distributions in the states #3 and #5 below the Fermi level and in the excited states #6 and #7 above the Fermi level: in the former, the charges are more distributed among the iodine ‘vapor’ atom, the BZP and the CuI(111). But in the excited state the charges are confined quite closely to the surface of the film. This suggests that charges are mostly localized on the CuI surface, on the adsorbed BZP and on the iodine ‘vapor’ atom in the immediate vicinity to the BZP. Such charge redistribution facilities both the hole-drift and optical transitions.

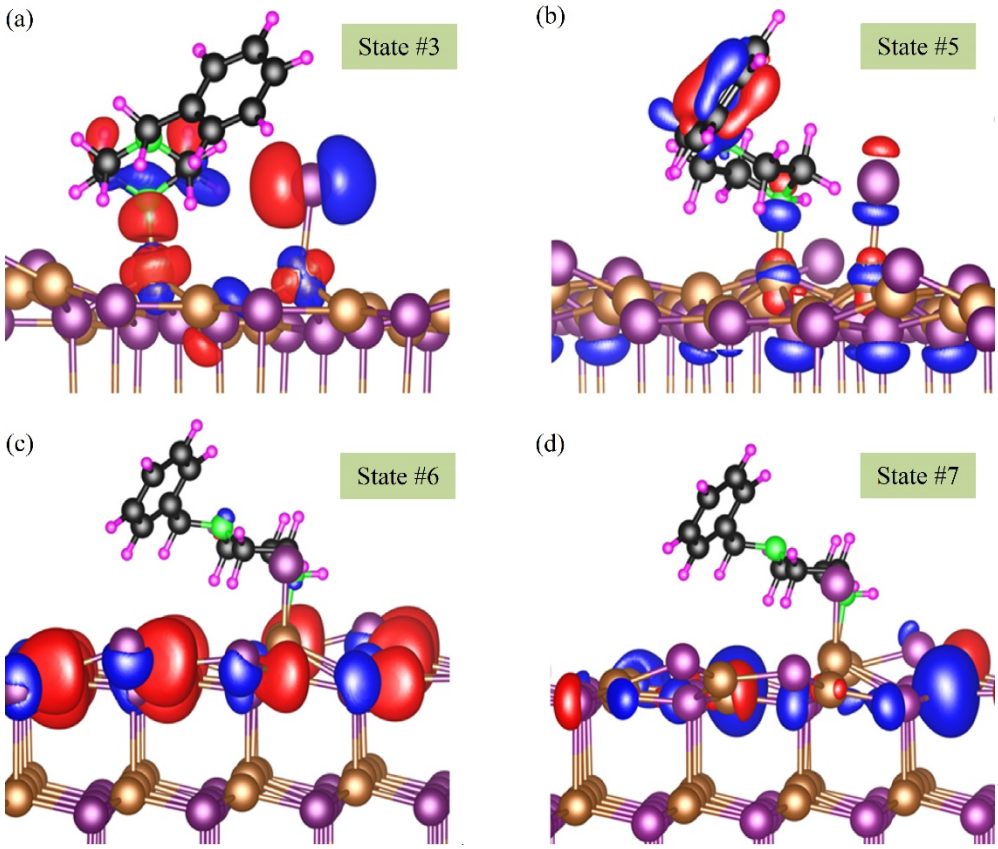

Figure 8.7 Partial charge density of selected molecular orbitals of the coupled BZP/CuI(111) system with an iodine 'vapor' atom, localized in optically active states, with state index numbers (#s) (see Fig. 8(b)): (a) the state #3', composed of strongly hybridized orbitals of the CuI surface atoms, orbitals of the 'vapor' atom and the HOMO-2 orbitals of the adsorbed BZP molecule; (b) state #5' (adsorbed BZP HOMO state dominant); (c) state #6', the CuI conduction band; (d) state #7', the CuI conduction band. These states mainly contribute to the optical transitions. For clarity, state index numbers (#s), which are labeled in Fig. 8(*b*), are also given for each plots. The iso-surface value for the plot is set to 0.005 eV/Å^3. Brown, purple, green, black and magenta balls represent the Cu, I, N, C and H atoms, respectively. [T. B. Rawal, V. Turkowski, T. S. Rahman, J. Phys.: Condens. Matt. (2014)] (Copyright: IOP publishing 2014).

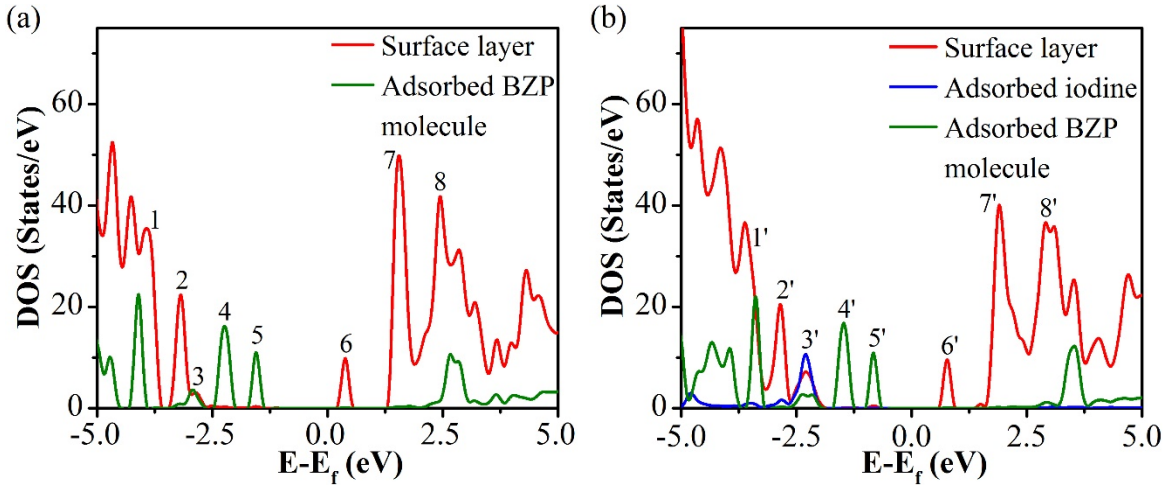

Figure 8.8 DFT+U projected density of states of (a) the BZP/CuI(111) system and (b) the conjugated BZP/CuI(111) system with an iodine 'vapor' atom. [T. B. Rawal, V. Turkowski, T. S. Rahman, J. Phys.: Condens. Matt., 26, 18 (2014)] (Copyright: IOP publishing 2014).

Figure 8.8(a-b) show the projected DOS of both the BZP/CuI(111) system and that with an adsorbed iodine. As shown in Figures, an BZP HOMO and HOMO-1 states are located inside the gap, thus reducing the band gap of CuI film. In order to explain the emission mechanism and the role of electronic states of an iodine 'vapor' and of BZP, we analyze in detail the projected DOS of the optically most active parts of the coupled BZP/CuI(111) system with the iodine 'vapor'. As shown in Figure 8.8(b), the iodine 'vapor' atom creates a trapping state (state #3), which is located at ~ 0.25 eV above the valence-band edge of the CuI film. This state is strongly hybridized with both surface state orbitals of the CuI film and the HOMO-2 orbital of the BZP. This strong hybridization plays the key role in inducing the PL. Although the iodine state is located below both the HOMO-1 (state #4) and HOMO (state #5) states of BZP, it has the largest dipole moment with respect to the lowest CuI conduction bands (states #6 and #7) (see Table 8.1). This suggests that light absorption will lead to creation of a hole which occupies the hybridized state of 'vapor' atom

orbital and the surface orbitals of the CuI film. Since the corresponding hybridized states are formed as a consequence of the hybridization of 'vapor' I-p orbital, surface Cu-d and I-p orbitals and molecular orbitals, a fast drift of the hole to the molecular HOMO (state #5) will take place upon absorption of light. When relaxed to the BZP HOMO state, the hole will recombine with excited electron from states #6 and #7, producing an enhanced orange PL.

The schematic representation of PL mechanisms for both conjugated BZP/CuI(111) systems – without and in the presence of the 'vapor' atom – are shown in Figure 8.9(a-b), respectively. In the absence of the adsorbed iodine, the probability of hole transfer from the CuI surface state to the BZP HOMO state is lower than that of hole transfer from the hybridized ad-atom state to the BZP HOMO state, owing to the fact that the transition dipole moment in the case of BZP/CuI(111) system is less than that in the case of the coupled system with the iodine 'vapor' atom in the vicinity to the BZP.

Table 8.1 Dipole moments of the BZP/CuI(111) system with an iodine 'vapor' atom for interband optical transitions.

Interband Transitions	**Dipole moments (a.u.)**	**Interband Transitions**	**Dipole moments (a.u.)**
2' → 6'	4.408×10^{-3}	**2' → 7'**	9.935×10^{-2}
3' → 6'	5.722×10^{-2}	**3' → 7'**	2.641×10^{-1}
4' → 6'	4.718×10^{-3}	**4' → 7'**	4.528×10^{-3}
5' → 6'	2.063×10^{-3}	**5' → 7'**	9.516×10^{-4}

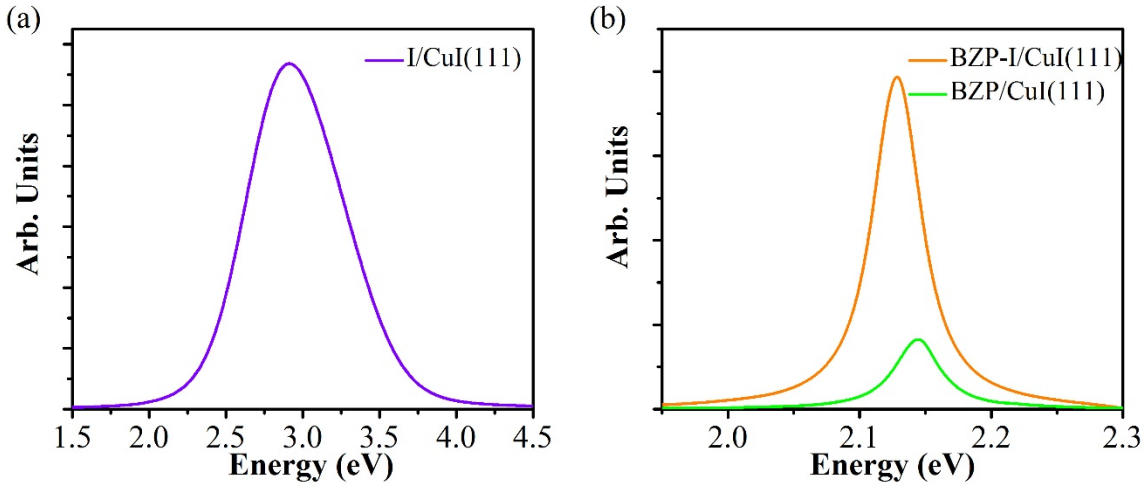

Figure 8.9 Optical emission spectra of (a) the CuI(111) thin film with only an iodine 'vapor' atom and of (b) the coupled BZP/CuI(111) system with and without the iodine. [T. B. Rawal, V. Turkowski, T. S. Rahman, J. Phys.: Condens. Matt. (2014)] (Copyright: IOP publishing 2014).

Adsorption of BZP on CuI(111) leads to a shift in the emission spectrum of the I/CuI(111) film from the violet-blue (~2.9 eV) range to the orange (~2.1 eV) range (see Figure 8.9a-b), in good agreement with the so-far available experimental measurements on the optical spectra of analogous systems of complexes formed between BZP and CuI in acetonitrile solution [341]. Nonetheless, the strong enhancement of orange PL is achieved when ad-atom adsorbs on CuI(111) in the vicinity of adsorbed BZP. The difference in the intensity of the optical emission spectra of the BZP/CuI system and BZP-I/CuI system is possibly originated from the difference in the rates of hole-migration from iodine 'vapor' atoms and from the other surface iodine 'vapor' atoms to the BZP HOMO state. Our results, therefore, suggest that the 'vapor' atoms serve as light absorbers, and consequently as deliverer of the excited holes to the molecular HOMO state (in virtue of the vicinity of the adatom to BZP). The hole-trapping states created by 'vapor' atoms and the alignment of these states with those of the conjugated BZP are responsible for the dramatic

enhancement of orange PL. In particular, both BZP and a iodine 'vapor' atom play the complementary roles for the strong orange PL. In the absence of adsorbed iodine, the light is absorbed by the CuI film surface, which also leads to hole creation on the surface, but the drift of the hole to the BZP HOMO is not rapid enough to produce the strong orange PL. The reason for this is misalignment between the corresponding CuI and molecular energy levels: the magnitude of the dipole moment for the transition from the CuI surface state #2 to the BZP HOMO state #5 is about one-fourth times smaller than that for the transition from the hybridized iodine state #3 to the state #5.

8.4 Summary

We have studied the electronic structure and optical properties of a coupled BZP/CuI(111) system using DFT+U. Electronic coupling between the BZP molecule and CuI(111) in the presence of an iodine 'vapor' atom results in a strong orange PL. Our results show that an important role for producing this luminescence is played by the BZP HOMO state and a hole-trapping state which is generated near the film surface by the iodine 'vapor' atom. The trapping state hybridizes strongly with one of the occupied (HOMO-2) molecular states. In particular, when the system absorbs a photon, excited holes are mostly created on the hybridized iodine-molecule-surface states. These excited holes rapidly drift to the molecular HOMO state, where they subsequently recombine with the excited electrons as these relax from the CuI conduction band. The iodine states can act as the trapping sites (residing ~0.25 eV above the valence band-edge, in good agreement with experiment) for photo-generated holes. In addition, we have found that the main PL peak is located at ~2.1 eV, which corresponds to an orange emission. Our results show that this

peak shifts to the higher energy, when there is no iodine adsorbed on the CuI(111) in the vicinity of BZP. In this case, we find the weak emission peak at ~2.15 eV. Our results for both types of systems are in rather good qualitative agreement with experiment [341] – a shift of the PL peak in the emission spectrum of the systems under adsorption of BZP with respect to that of pristine CuI. This result would be useful for potential forensic applications.

Our results suggest that the PL of CuI(111) can be altered in the visible range by the choice of different molecules inside the energy gap of the coupled system. Designing of such systems with tunable optical properties would have technological importance in solar-cells, photo-sensors and drug-detectors. The PL spectra of such systems are affected by various excitation under variation of density of iodine 'vapor' atoms. Analogous effects can be expected either from substitution of other halide dopants for iodine or from other Cu-halide films, opening more possibilities for tuning the optical properties of Cu-halide-based materials.

CHAPTER 9 CONCLUSIONS

In this dissertation, I have explored the structural, catalytic and optical properties of functional materials using modern-quantum-mechanical approach, density functional theory (DFT). I have also studied the kinetics of the reactions on the catalyst surface using *ab initio* kinetic Monte Carlo method. The results presented here should not only help gain fundamental understanding of those properties of the materials at the nanoscale but may also provide guidelines to design novel functional materials for catalytic and sensor applications. The majority of my focus was on finding ways to activate single-layer transition metal dichalcogenide, MoS_2, by a variety of strategies: creation of vacancies, interface with nanoparticles, and a metallic support. Below is a chapter-wise summary of specific conclusions.

In chapter 3, we focused on the effect of single-layer MoS_2 on the geometry, electronic structure, and reactivity of 29-atom Cu_{29}, Ag_{29}, and Au_{29} nanoparticles. The calculations showed that the nanoparticles bind more strongly on defect-laden than pristine MoS_2 – in the order of Cu_{29}>Ag_{29}>Au_{29} for defect-laden and of Cu_{29}>Au_{29}>Ag_{29} for pristine. The d-band center of the NPs is shifted further toward the Fermi level when the support is defect-laden. Importantly, the relatively larger shift of d band center was found for Au_{29}. Indeed, we found that defect-laden MoS_2 helps increase the number of active sites on the Au nanoparticle at which can O_2 adsorb with similar binding energy (<0.1 eV difference). Our findings of MoS_2-induced enhancement of adsorption (reaction) sites for O_2 on the nanoparticles is indicative of enhanced oxidation reactions when they are supported on MoS_2.

In chapter 4, we showed that the modified electronic structure of Au_{13}/MoS_2 composite strikingly affects the catalytic activity of the Au_{13}/MoS_2, offering selectivity toward methanol

synthesis via the CO hydrogenation route, in contrast to the catalytic activity of Au_{13}/TiO_2 [142] which promotes the decomposition of methanol. Thus, our results open up a new avenue for utilizing the 2D TMDs, in general, as the support materials for Au nanoparticles that may catalyze a number of technologically relevant reactions.

In chapter 5, we found that significant charge transfer from Cu to MoS_2 and strong interaction between them leads to shift the Fermi energy toward the higher energy, thereby the position of the frontier orbitals toward the Fermi level, making defect-laden MoS_2 supported on Cu(111) more active than unsupported one. Based on the DFT-calculated energetics, we found that the substrate promotes the ethanol synthesis from syngas on defect ladenMoS_2. The formation of ethanol is thermodynamically favored over the formation of methane. Thus, these results would be applicable to rational design of MoS_2-based catalysts for higher alcohol synthesis from syngas.

In chapter 6, I turned to examination of the adsorption, dissociation, diffusion, and vibration characteristics of oxygen on Ag(110). Since O_2[001] adsorbed at four-fold hollow (FFH) site gains vibrational energy, the dissociation of this species faces lower energy barrier than does $O_2[1\bar{1}0]$. The O atoms then diffuse from FFH to another FFH site. Since the O at short-bridge site has an imaginary frequency, the most likely diffusion path of O is from a short-bridge to the three-fold hollow site because of the downhill potential along the path. We find that free Ag atoms at the top surface layer and those involved in the O-Ag-O complex have distinct local chemical activity since they provide different binding affinity to CO. Furthermore, we find that the tightly-bound O species on disordered Ag(110) is less reactive than the weakly-bound singly dispersed O on the ordered surface, indicating the chemical activity of disordered Ag(110) would be quite different from that of ordered one. Finally, we proposed a new mechanism involved in the process

of Ag vacancy formation on Ag(110) which reveals that Ag atoms can be extracted from pristine Ag(110) only in the presence of oxygen atoms. This process becomes facile for higher oxygen coverage, resulting in the formation of complex structures. The formation of Ag vacancy and O-Ag-O structures act as the precursor processes for the added-row reconstruction on Ag(110).

The chapter 7 described the results of DFT in combination with kinetic Monte Carlo simulation for methanol partial oxidation on $Pd_1/ZnO(10\bar{1}0)$. The high catalytic activity of Pd_1/ZnO can be credited to the decisive influence of the local environment (or geometry) and electronic structure of the active Zn sites modified by single Pd, and those of the active single Pd and Pd-Zn sites. Our calculations, indeed, reveal that single Pd site plays a critical role inmodifying the geometrical and electronic structures of cationic Zn sites for optimal activity. Single Pd loading not only plays an important role for providing higher affinity to CH_3OH but also induces spontaneous CO_2 formation, the nearly spontaneous dissociation of H_2O, and the stabilization of H_2 right at or near the sites. The DFT+kMC simulations indicate high selectivity for H_2 and CO_2 formation over that of H_2O and CO.

Finally in chapter 8, we proposed a mechanism for enhanced orange photoluminescence from a coupled system of benzylpiperazine (BZP) molecule with a CuI(111) thin film in the presence of an iodine ‘vapor’ atom. Our results showed that the adsorbed BZP and the iodine ‘vapor’ atom play complimentary roles in producing the PL in the visible range. The recombination of relaxed holes in BZP HOMO with excited electrons in the CB of the CuI film, produce a luminescence peak at ~2.1 eV.

APPENDIX A: COPYRIGHT AND PERMISSIONS

Title: Adatom Extraction from Pristine Metal Terraces by Dissociative Oxygen Adsorption: Combined STM and Density Functional Theory Investigation of $\mathrm{O}/\mathrm{Ag}(110)$

Author: Jagriti Pal et al.

Publication: Physical Review Letters

Publisher: American Physical Society

Date: Jun 1, 2017

Order Completed

Thank you for your order.

This Agreement between Takat B Rawal ("You") and American Physical Society ("American Physical Society") consists of your license details and the terms and conditions provided by American Physical Society and Copyright Clearance Center.

Your confirmation email will contain your order number for future reference.

Printable details.

License Number	4143791328796
License date	Jul 07, 2017
Licensed Content Publisher	American Physical Society
Licensed Content Publication	Physical Review Letters
Licensed Content Title	Adatom Extraction from Pristine Metal Terraces by Dissociative Oxygen Adsorption: Combined STM and Density Functional Theory Investigation of $\mathrm{O}/\mathrm{Ag}(110)$
Licensed Content Author	Jagriti Pal et al.
Licensed Content Date	Jun 1, 2017
Licensed Content Volume	118
Type of use	Thesis/Dissertation
Requestor type	Student
Format	Electronic
Portion	chapter/article
Rights for	Main product
Duration of use	Life of Current Edition
Creation of copies for the disabled	no
With minor editing privileges	no
For distribution to	United States
In the following language(s)	Original language of publication
With incidental promotional use	no
Lifetime unit quantity of new product	0 to 499
The requesting person/organization	Takat B. Rawal
Order reference number	
Title of your thesis / dissertation	Predictive modeling of functional materials for catalytic and sensor applications
Expected completion date	Aug 2017
Expected size (number of pages)	275
Requestor Location	Takat B Rawal 4111 Libra Drive, PSB 412 ORLANDO, FL 32816 United States Attn: Takat B Rawal
Billing Type	Invoice
Billing address	Takat B Rawal

Title: Adsorption, diffusion, and vibration of oxygen on $\mathrm{Ag}(110)$
Author: Takat B. Rawal et al.
Publication: Physical Review B
Publisher: American Physical Society
Date: Jul 31, 2015

Order Completed

Thank you for your order.

This Agreement between Takat B Rawal ("You") and American Physical Society ("American Physical Society") consists of your license details and the terms and conditions provided by American Physical Society and Copyright Clearance Center.

Your confirmation email will contain your order number for future reference.

Printable details.

License Number	4143800339308
License date	Jul 07, 2017
Licensed Content Publisher	American Physical Society
Licensed Content Publication	Physical Review B
Licensed Content Title	Adsorption, diffusion, and vibration of oxygen on $\mathrm{Ag}(110)$
Licensed Content Author	Takat B. Rawal et al.
Licensed Content Date	Jul 31, 2015
Licensed Content Volume	92
Type of use	Thesis/Dissertation
Requestor type	Student
Format	Electronic
Portion	chapter/article
Rights for	Main product
Duration of use	Life of Current Edition
Creation of copies for the disabled	no
With minor editing privileges	no
For distribution to	United States
In the following language(s)	Original language of publication
With incidental promotional use	no
Lifetime unit quantity of new product	0 to 499
The requesting person/organization	Takat B. Rawal
Order reference number	
Title of your thesis / dissertation	Predictive modeling of functional materials for catalytic and sensor applications
Expected completion date	Aug 2017
Expected size (number of pages)	275
Requestor Location	Takat B Rawal 4111 Libra Drive, PSB 412 ORLANDO, FL 32816 United States Attn: Takat B Rawal
Billing Type	Invoice
Billing address	Takat B Rawal 4111 Libra Drive, PSB 412 ORLANDO, FL 32816 United States Attn: Takat B Rawal

Case #00281899 - Regarding permission to reuse my publised article in Journal of physics: Condensed Matter [ref:_00D30oeGz._500a01JCaMU:ref]

T

takat

Tue 3/21, 10:42 AM

info@copyright.com

Reply all

Dear Alex,

Thank you for information and sending the link.

Takat

...

N

noreply@salesforce.com on behalf of info@copyright.com

Tue 3/21, 4:46 AM

Dear Takat Rawal,
Your order for the reuse of the article in your thesis/dissertation has been approved by the publisher. Please follow this link https://s100.copyright.com/CustomerAdmin/FC.jsp?ref=ad779322-cd42-4c10-8c26-cd2b4633dc98&pName=repub? to view the order and choose to accept or decline the offer.
If you have any further questions please don't hesitate to contact a Customer Account Specialist at 855-239-3415 Monday-Friday, 24 hours/day.
Best regards,
Alex Pechera
Customer Account Specialist
Copyright Clearance Center
222 Rosewood Drive
Danvers, MA 01923
www.copyright.com
+1.855.239.3415

Facebook - Twitter - LinkedIn

APPENDIX B: LIST OF PUBLICATIONS

1. **T. B. Rawal**, D. Le, and T. S. Rahman, *Effect of single-layer MoS_2 on the geometry, electronic structure and reactivity of transition metal nanoparticles*, Journal of Physical Chemistry C, **121**, 7282 (2017).

2. J. Pal, **T. B. Rawal**, M. Smerieri, S. Hong, M. Alatalo, L. Savio, L. Vattuone, T. S. Rahman, and M. Rocca, *Adatom extraction off pristine terraces by dissociative oxygen adsorption at metal surfaces: combined STM and DFT investigation of O/Ag(110)*, Physical Review Letter, **118**, 226101, (2017).

3. A. Gupta, **T. B. Rawal**, C. Neal, S. Das, T. S. Rahman, and S. Seal, *Molybdenum disulfide for ultra-low detection of free radicals: electrochemical response and molecular modeling*, 2D Materials, **4**, 2 (2017).

4. I. Tanabe, T. Komesu, D. Le, **T. B. Rawal**, E. F. Schwier, M. Zheng, Y. Kojima, H. Iwasawa, K. Shimada, T. S. Rahman, and P. A. Dowben, *The symmetry-resolved electronic structure of 2H-WSe_2(0001)*, Journal of Physics: Condensed Matter **28**, 345503 (2016).

5. **T. B. Rawal**, S. Hong, A. Pulkkinen, M. Alatalo, and T. S. Rahman, *Adsorption, vibration, and diffusion of oxygen on Ag(110)*, Physical Review B, **92**, 035444, (2015).

6. D. Le., **T. B. Rawal**, and T. S. Rahman, *Single-layer MoS_2 with sulfur vacancies: structure and catalytic application*, Journal of Physical Chemistry C, **118**, 5346 (2014).

7. **T. B. Rawal**, V. Turkowski, and T. S. Rahman, *Complementary roles of benzylpiperazine and iodine 'vapor' in the strong enhancement of orange photoluminescence from CuI(111) thin film*, Journal of Physics: Condensed Matter, **26**, 185005 (2014).

8. **T. B. Rawal,** D. Le, and T. S. Rahman, *MoS_2–supported gold nanoparticle for CO hydrogenation* (under review Journal of Physics: Condensed Matter).

9. C. Merida, D. Le, E. Echeverria, A. Nguyen, and **T. B. Rawal** *et al.*, *Gold dispersion and Activation on the Basal Plane of Single-Layer MoS_2,* (submitted to ACS Catalysis, 2017).

In preparation

10. D. Le, **T. B. Rawal**, Ludwig Bartels, Peter A. Dowben, and T. S. Rahman, *First principles study of MoS_2/Cu(111) catalyst for alcohol synthesis from syngas.*

11. **T. B. Rawal**, S. Acharya, S. Hong, and T. S. Rahman, *High catalytic activity of Pd_1/ZnO(10-10) toward methanol partial oxidation: A DFT+kMC study.*

12. **T. B. Rawal**, M. Smerieri, J. Pal, S. Hong, M. Alatalo, T. S. Rahman, L. Savio, L. Vattuone, and M. Rocca, *STM and DFT study of low-temperature dissociation of O_2 on Ag(110) in the vanishing coverage limit.*

LIST OF REFERENCES

[1] K. S. Novoselov, A. K. Geim, S. V. Morozov, D. Jiang, Y. Zhang, S. V. Dubonos, I. V. Grigorieva, and A. A. Firsov, Science **306**, 666 (2004).

[2] K. S. Novoselov, D. Jiang, F. Schedin, T. J. Booth, V. V. Khotkevich, S. V. Morozov, and A. K. Geim, Proc. Nat. Aca. Sci. **102**, 10451 (2005).

[3] A. K. Geim and K. S. Novoselov, Nat. Mater. **6**, 183 (2007).

[4] K. F. Mak, C. Lee, J. Hone, J. Shan, and T. F. Heinz, Phys. Rev. Lett. **105** (2010).

[5] B. Radisavljevic, A. Radenovic, J. Brivio, V. Giacometti, and A. Kis, Nat. Nanotech. **6**, 147 (2011).

[6] H. S. S. R. Matte, A. Gomathi, A. K. Manna, D. J. Late, R. Datta, S. K. Pati, and C. N. R. Rao, Angew. Chem. Int. Ed. **49**, 4059 (2010).

[7] B. Radisavljevic, M. B. Whitwick, and A. Kis, ACS Nano **5**, 9934 (2011).

[8] H. Fang, S. Chuang, T. C. Chang, K. Takei, T. Takahashi, and A. Javey, Nano Lett. **12**, 3788 (2012).

[9] D.-S. Tsai, K.-K. Liu, D.-H. Lien, M.-L. Tsai, C.-F. Kang, C.-A. Lin, L.-J. Li, and J.-H. He, ACS Nano **7**, 3905 (2013).

[10] W. Zhang, P. Zhang, Z. Su, and G. Wei, Nanoscale **7**, 18364 (2015).

[11] Q. H. Wang, K. Kalantar-Zadeh, A. Kis, J. N. Coleman, and M. S. Strano, Nat. Nanotech. **7**, 699 (2012).

[12] L. S. Byskov, J. K. Nørskov, B. S. Clausen, and H. Topsøe, J. Catal. **187**, 109 (1999).

[13] D. Le, T. B. Rawal, and T. S. Rahman, J. Phys. Chem. C **118**, 5346 (2014).

[14] T. F. Jaramillo, K. P. Jørgensen, J. Bonde, J. H. Nielsen, S. Horch, and I. Chorkendorff, Science **317**, 100 (2007).

[15] H. T. Wang *et al.*, Proc. Nat. Acad. Sci. **110**, 19701 (2013).

[16] D. Voiry, M. Salehi, R. Silva, T. Fujita, M. W. Chen, T. Asefa, V. B. Shenoy, G. Eda, and M. Chhowalla, Nano Lett. **13**, 6222 (2013).

[17] D. Voiry *et al.*, Nat. Mater. **12**, 850 (2013).

[18] A. Ciesielski and P. Samor, Adv. Mater. **28**, 6030 (2016).

[19] H. T. Wang, H. T. Yuan, S. S. Hong, Y. B. Li, and Y. Cui, Chem Soc Rev **44**, 2664 (2015).

[20] M. Chhowalla, H. S. Shin, G. Eda, L. J. Li, K. P. Loh, and H. Zhang, Nat. Chem. **5**, 263 (2013).

[21] A. Ruban, B. Hammer, P. Stoltze, H. L. Skriver, and J. K. Norskov, J. Mol. Catal. Chem. **115**, 421 (1997).

[22] J. Greeley, J. K. Nørskov, and M. Mavrikakis, Ann. Rev. Phys. Chem. **53**, 319 (2002).

[23] J. K. Norskov, F. Abild-Pedersen, F. Studt, and T. Bligaard, Proc. Natl. Acad. Sci. U.S.A. **108**, 937 (2011).

[24] F. E. Kruis, H. Fissan, and A. Peled, J. Aero. Sci. **29**, 511 (1998).

[25] M. C. Daniel and D. Astruc, Chem. Rev. **104**, 293 (2004).

[26] B. Hvolbæk, T. V. W. Janssens, B. S. Clausen, H. Falsig, C. H. Christensen, and J. K. Nørskov, Nano Today **2**, 14 (2007).

[27] M. Haruta, Cattech **6**, 102 (2002).

[28] P. K. Jain, K. S. Lee, I. H. El-Sayed, and M. A. El-Sayed, J. Phys. Chem. B **110**, 7238 (2006).

[29] J. Jones *et al.*, Science **353**, 150 (2016).

[30] X.-F. Yang, A. Wang, B. Qiao, J. Li, J. Liu, and T. Zhang, Acc. Chem. Res. **46**, 1740 (2013).

[31] B. Qiao, A. Wang, X. Yang, L. F. Allard, Z. Jiang, Y. Cui, J. Liu, J. Li, and T. Zhang, Nat. Chem. **3**, 634 (2011).

[32] W. Kohn and L. Sham, Phys. Rev. **140**, A1133 (1965).

[33] A. Tkatchenko, Adv. Func. Mater. **25**, 2054 (2015).

[34] K. Reuter, D. Frenkel, and M. Scheffler, Phys. Rev. Lett. **93**, 116105 (2004).

[35] K. Reuter and M. Scheffler, Phys. Rev. B **73**, 045433 (2006).

[36] K. Reuter, Catal Lett **146**, 541 (2016).

[37] G. Binnig and H. Rohrer, Surf. sci. **126**, 236 (1983).

[38] M. Born and R. Oppenheimer, Ann. Phys. **389**, 457 (1927).

[39] L. H. Thomas, Proc. Cambridge Phil. Soc. **23**, 542 (1927).

[40] E. Fermi, Z. Physik **48**, 73 (1928).

[41] P. Hohenberg and W. Kohn, Phys. Rev. **136**, B864 (1964).

[42] A. D. Becke, Phys. Rev. A **38**, 3098 (1988).

[43] J. P. Perdew, K. Burke, and M. Ernzerhof, Phys. Rev. Lett. **77**, 3865 (1996).

[44] J. P. Perdew and Y. Wang, Phys. Rev. B **45**, 13244 (1992).

[45] Z. Wu and R. E. Cohen, Phys. Rev. B **73**, 235116 (2006).

[46] J. Heyd and G. E. Scuseria, J. Chem. Phys. **121**, 1187 (2004).

[47] M. Dion, H. Rydberg, E. Schröder, D. C. Langreth, and B. I. Lundqvist, Phys. Rev. Lett. **92**, 246401 (2004).

[48] J. P. Perdew and A. Zunger, Phys. Rev. B **23**, 5048 (1981).

[49] A. D. Becke, J. Chem. Phys. **140** (2014).

[50] K. Lejaeghere *et al.*, Science **351**, 1415 (2016).

[51] J. Hubbard, Proc. Royal Soc. London Series: A. Math. Phys. Sci. **296**, 100 (1967).

[52] J. Hubbard, Proc. Royal Soc. London : Math. Phys. Eng. Sci. **276**, 238 (1963).

[53] V. I. Anisimov, F. Aryasetiawan, and A. I. Lichtenstein, J. Phys.: Condens. Matt. **9**, 767 (1997).

[54] Vladimir Anisimov and Y. Izyumov, *Electronic Structure of Strongly Correlated Materials* (Springer, 2010), 2010 edn., Vol. 163, Springer Series in Solid-State Sciences, p.^pp. 291.

[55] B. Himmetoglu, A. Floris, S. de Gironcoli, and M. Cococcioni, Int J Quantum Chem **114**, 14 (2014).

[56] S. H. Vosko, L. Wilk, and M. Nusair, Can J Phys **58**, 1200 (1980).

[57] J. P. Perdew and Y. Wang, Phys. Rev. B **45**, 13244 (1992).

[58] J. P. Perdew, Phys. Rev. Lett. **55**, 1665 (1985).

[59] J. P. Perdew and W. Yue, Phys. Rev. B **33**, 8800 (1986).

[60] J. P. Perdew, Phys. Rev. B **33**, 8822 (1986).

[61] J. P. Perdew, J. A. Chevary, S. H. Vosko, K. A. Jackson, M. R. Pederson, D. J. Singh, and C. Fiolhais, Phys. Rev. B **48**, 4978 (1993).

[62] S. Grimme, J. Comp. Chem. **25**, 1463 (2004).

[63] S. Grimme, J. Comp. Chem. **27**, 1787 (2006).

[64] A. D. Becke, J. Chem. Phys. **107**, 8554 (1997).

[65] S. Grimme, J. Antony, S. Ehrlich, and H. Krieg, J. Chem. Phys. **132**, 154104 (2010).

[66] G. Román-Pérez and J. M. Soler, Phys. Rev. Lett. **103**, 096102 (2009).

[67] K. Lee, É. D. Murray, L. Kong, B. I. Lundqvist, and D. C. Langreth, Phys. Rev. B **82**, 081101 (2010).

[68] J. Klimeš, D. R. Bowler, and A. Michaelides, Phys. Rev. B **83**, 195131 (2011).

[69] J. Klimeš, D. R. Bowler, and A. Michaelides, J. Phys.: Condens. Matt. **22**, 022201 (2010).

[70] D. Hamann, M. Schlüter, and C. Chiang, Phys. Rev. Lett. **43**, 1494 (1979).

[71] D. Vanderbilt, Phys. Rev. B **41**, 7892 (1990).

[72] P. E. Blöchl, Phys. Rev. B **50**, 17953 (1994).

[73] G. Kresse and D. Joubert, Phys. Rev. B **59**, 1758 (1999).

[74] J. D. Pack and H. J. Monkhorst, Phys. Rev. B **16**, 1748 (1977).

[75] C. L. Fu and K. M. Ho, Phys. Rev. B **28**, 5480 (1983).

[76] M. Methfessel and A. T. Paxton, Phys. Rev. B **40**, 3616 (1989).

[77] R. F. W. Bader, *Atoms in Molecules: A Quantum Theory* (Oxford University Press: New York, 1990).

[78] G. Henkelman, A. Arnaldsson, and H. Jónsson, Comp. Mater. Sci. **36**, 354 (2006).

[79] E. Sanville, S. D. Kenny, R. Smith, and G. Henkelman, J. Comp. Chem. **28**, 899 (2007).

[80] J. Tersoff and D. R. Hamann, Phys. Rev. Lett. **50**, 1998 (1983).

[81] J. Tersoff and D. R. Hamann, Phys. Rev. B **31**, 805 (1985).

[82] R. M. Pick, M. H. Cohen, and R. M. Martin, Phys. Rev. B **1**, 910 (1970).

[83] S. Baroni, S. de Gironcoli, A. Dal Corso, and P. Giannozzi, Rev. Mod. Phys. **73**, 515 (2001).

[84] G. Mills, H. Jonsson, and G. K. Schenter, Surf. Sci. **324**, 305 (1995).

[85] G. Mills and H. Jónsson, Phys. Rev. Lett. **72**, 1124 (1994).

[86] G. Henkelman and H. Jonsson, J. Chem. Phys. **113**, 9978 (2000).

[87] E. Bitzek, P. Koskinen, F. Gahler, M. Moseler, and P. Gumbsch, Phys. Rev. Lett. **97** (2006).

[88] W. H. Press, S. A. Teukolsky, W. T. Vetterling, and B. P. Flannery, *Numerical Recipes* (Cambridge University Press: New York, 2007), South African Journal of Chemistry.

[89] D. C. Liu and J. Nocedal, Mathmatical Programming **45**, 503 (1989).

[90] D. Sheppard, R. Terrell, and G. Henkelman, J. Chem. Phys. **128** (2008).

[91] G. Henkelman, B. P. Uberuaga, and H. Jonsson, J. Chem. Phys. **113**, 9901 (2000).

[92] G. H. Vineyard, J. Phys. Chem. Solids **3**, 121 (1957).

[93] K. Reuter, *First-principles kinetic Monte Carlo simulations for heterogeneous catalysis: Concepts, status, and frontiers* (From the Molecular Process to the Technical System, edited by O. Deutschmann (Wiley-VCH, Weinberg, 2010), 2011).

[94] A. B. Bortz, M. H. Kalos, and J. L. Lebowitz, J. Comp. Phys. **17**, 10 (1975).

[95] T. Fujita *et al.*, Nat. Mater. **11**, 775 (2012).

[96] K. Fuku, R. Hayashi, S. Takakura, T. Kamegawa, K. Mori, and H. Yamashita, Angew. Commun. **52**, 7446 (2013).

[97] W. Zhu, R. Michalsky, Ö. Metin, H. Lv, S. Guo, C. J. Wright, X. Sun, A. A. Peterson, and S. Sun, J. Am. Chem. Soc. **135**, 16833 (2013).

[98] H. Falsig, B. Hvolbaek, I. S. Kristensen, T. Jiang, T. Bligaard, C. H. Christensen, and J. K. Norskov, Angew. Chem. Int. Ed. **47**, 4913 (2008).

[99] S. Karanjit, K. Bobuatong, R. Fukuda, M. Ehara, and H. Sakurai, Int. Jour. Quant. Chem. **113**, 428 (2013).

[100] P. Liu and J. A. Rodriguez, J. Chem. Phys. **126**, 164705 (2007).

[101] G. Vile and J. Perez-Ramirez, Nanoscale **6**, 13476 (2014).

[102] S. K. Das, T. Parandhaman, N. Pentela, A. K. M. Maidul Islam, A. B. Mandal, and M. Mukherjee, J. Phys. Chem. C **118**, 24623 (2014).

[103] J. Luo *et al.*, Adv. Mater. **20**, 4342 (2008).

[104] Z. Wang, L. Xin, X. Zhao, Y. Qiu, Z. Zhang, O. A. Baturina, and W. Li, Renew. Energy **62**, 556 (2014).

[105] O. Y. Gutiérrez, S. Singh, E. Schachtl, J. Kim, E. Kondratieva, J. Hein, and J. A. Lercher, ACS Catal. **4**, 1487 (2014).

[106] T. F. Jaramillo, K. P. Jorgensen, J. Bonde, J. H. Nielsen, S. Horch, and I. Chorkendorff, Science **317**, 100 (2007).

[107] J. V. Lauritsen *et al.*, J. Catal. **249**, 220 (2007).

[108] X. Huang, Z. Zeng, S. Bao, M. Wang, X. Qi, Z. Fan, and H. Zhang, Nat. Commun. **4**, 1444 (2013).

[109] L. Yuwen *et al.*, Nanoscale **6**, 5762 (2014).

[110] H. Sun, J. Chao, X. Zuo, S. Su, X. Liu, L. Yuwen, C. Fan, and L. Wang, RSC Adv. **4**, 27625 (2014).

[111] U. Bhanu, M. R. Islam, L. Tetard, and S. I. Khondaker, Sci. Rep. **4**, 5575 (2014).

[112] J. Kim, S. Byun, A. J. Smith, J. Yu, and J. Huang, J. Phys. Chem. Lett. **4**, 1227 (2013).

[113] S. Su, H. Sun, F. Xu, L. Yuwen, and L. Wang, Electroanalysis **25**, 2523 (2013).

[114] J. Huang *et al.*, Mater. Res. Bull. **48**, 4544 (2013).

[115] A. J. Cheah, W. S. Chiu, P. S. Khiew, H. Nakajima, T. Saisopa, P. Songsiriritthigul, S. Radiman, and M. A. A. Hamid, Catal. Sci. & Tech. **5**, 4133 (2015).

[116] L. Yang *et al.*, ACS Nano **8**, 6979 (2014).

[117] X. Xia, Z. Zheng, Y. Zhang, X. Zhao, and C. Wang, Sens. and Actuat. B: Chemical **192**, 42 (2014).

[118] S. Su, W. Cao, C. Zhang, X. Han, H. Yu, D. Zhu, J. Chao, C. Fan, and L. Wang, RSC Adv. **6**, 76614 (2016).

[119] P. Zhang, X. Lu, Y. Huang, J. Deng, L. Zhang, F. Ding, Z. Su, G. Wei, and O. G. Schmidt, J. Mater. Chem. A **3**, 14562 (2015).

[120] Z. Yin, B. Chen, M. Bosman, X. Cao, J. Chen, B. Zheng, and H. Zhang, Small **10**, 3537 (2014).

[121] M. Chen and D. W. Goodman, Acc. Chem. Res. **39**, 739 (2006).

[122] C. T. Campbell, Nat. Chem. **4**, 597 (2012).

[123] M. S. Chen and D. W. Goodman, Science **306**, 252 (2004).

[124] Z. Duan and G. Henkelman, ACS Catal. **5**, 1589 (2015).

[125] T. Fujitani and I. Nakamura, Angew. Chem. Int. Ed. **50**, 10144 (2011).

[126] D. Widmann and R. J. Behm, Acc. Chem. Res. **47**, 740 (2014).

[127] I. X. Green, W. Tang, M. Neurock, and J. T. Yates, Acc. Chem. Res. **47**, 805 (2013).

[128] L. M. Molina and B. Hammer, Phys. Rev. Lett. **90**, 206102 (2003).

[129] H. Y. Kim, H. M. Lee, and G. Henkelman, J. Am. Chem. Soc. **134**, 1560 (2012).

[130] L. M. Liu, B. McAllister, H. Q. Ye, and P. Hu, J. Am. Chem. Soc. **128**, 4017 (2006).

[131] Y.-G. Wang, Y. Yoon, V.-A. Glezakou, J. Li, and R. Rousseau, J. Am. Chem. Soc. **135**, 10673 (2013).

[132] K. Okazaki, S. Ichikawa, Y. Maeda, M. Haruta, and M. Kohyama, App. Catal. A: General **291**, 45 (2005).

[133] J. A. Rodriguez, P. Liu, J. Hrbek, J. Evans, and M. Pérez, Angew. Chem. **119**, 1351 (2007).

[134] J. A. Rodríguez, P. Liu, J. Hrbek, M. Pérez, and J. Evans, J. Mol. Catal. A: Chemical **281**, 59 (2008).

[135] J. A. Rodriguez, P. Liu, X. Wang, W. Wen, J. Hanson, J. Hrbek, M. Pérez, and J. Evans, Catal. Today **143**, 45 (2009).

[136] H.-T. Chen, J.-G. Chang, S.-P. Ju, and H.-L. Chen, J. Comp. Chem. **31**, 258 (2010).

[137] J. A. Rodriguez, P. Liu, J. Hrbek, J. Evans, and M. Pérez, Angew. Chem. Int. Ed. **46**, 1329 (2007).

[138] J. Zhao, Z. Zhang, S. Yang, H. Zheng, and Y. Li, J. Alloy. Comp. **559**, 87 (2013).

[139] J. Klimeš, D. Bowler, and A. Michaelides, Phys. Rev. B **83**, 195131 (2011).

[140] J. Klimeš, D. R. Bowler, and A. Michaelides, J. Phys.: Conden. Matt. **22**, 022201 (2010).

[141] G. Kresse and J. Furthmuller, Comp. Mater. Sci. **6**, 15 (1996).

[142] S. Hong and T. S. Rahman, J. Am. Chem. Soc. **135**, 7629 (2013).

[143] M. Farnesi Camellone, J. Zhao, L. Jin, Y. Wang, M. Muhler, and D. Marx, Angew. Chem. Int. Ed. **52**, 5780 (2013).

[144] H. Over, Y. D. Kim, A. P. Seitsonen, S. Wendt, E. Lundgren, M. Schmid, P. Varga, A. Morgante, and G. Ertl, Science **287**, 1474 (2000).

[145] M. Boronat, A. Leyva-Pérez, and A. Corma, Acc. Chem. Res. **47**, 834 (2014).

[146] T. B. Rawal, S. Hong, A. Pulkkinen, M. Alatalo, and T. S. Rahman, Phys. Rev. B **92**, 035444 (2015).

[147] B. K. Min and C. M. Friend, Chem. Rev. **107**, 2709 (2007).

[148] R. A. Sheldon, M. Wallau, I. W. Arends, and U. Schuchardt, Acc. Chem. Res. **31**, 485 (1998).

[149] T. V. W. Janssens, B. S. Clausen, B. Hvolbæk, H. Falsig, C. H. Christensen, T. Bligaard, and J. K. Nørskov, Top. Catal. **44**, 15 (2007).

[150] N. Weiher, A. M. Beesley, N. Tsapatsaris, L. Delannoy, C. Louis, J. A. van Bokhoven, and S. L. M. Schroeder, J. Am. Chem. Soc. **129**, 2240 (2007).

[151] Z. Yang, R. Wu, and D. W. Goodman, Phys. Rev. B **61**, 14066 (2000).

[152] B. White, M. Yin, A. Hall, D. Le, S. Stolbov, T. Rahman, N. Turro, and S. O'Brien, Nano Lett. **6**, 2095 (2006).

[153] M. Haruta, T. Kobayashi, H. Sano, and N. Yamada, Chem. Lett. **16**, 405 (1987).

[154] M. Haruta, S. Tsubota, T. Kobayashi, H. Kageyama, M. J. Genet, and B. Delmon, J. Catal. **144**, 175 (1993).

[155] N. Lopez, T. V. W. Janssens, B. S. Clausen, Y. Xu, M. Mavrikakis, T. Bligaard, and J. K. Nørskov, J. Catal. **223**, 232 (2004).

[156] S. Lee, C. Fan, T. Wu, and S. L. Anderson, J. Am. Chem. Soc. **126**, 5682 (2004).

[157] D. C. Meier and D. W. Goodman, J. Am. Chem. Soc. **126**, 1892 (2004).

[158] S. H. Overbury, V. Schwartz, D. R. Mullins, W. Yan, and S. Dai, J. Catal. **241**, 56 (2006).

[159] N. Lopez and J. K. Nørskov, J. Am. Chem. Soc. **124**, 11262 (2002).

[160] C. Lemire, R. Meyer, S. Shaikhutdinov, and H.-J. Freund, Angew. Chem. Int. Ed. **43**, 118 (2004).

[161] T. V. W. Janssens, A. Carlsson, A. Puig-Molina, and B. S. Clausen, J. Catal. **240**, 108 (2006).

[162] B. Yoon, H. Häkkinen, U. Landman, A. S. Wörz, J.-M. Antonietti, S. Abbet, K. Judai, and U. Heiz, Science **307**, 403 (2005).

[163] D. Ricci, A. Bongiorno, G. Pacchioni, and U. Landman, Phys. Rev. Lett. **97**, 036106 (2006).

[164] M. Farnesi Camellone and D. Marx, J. Phys. Chem. C **118**, 20989 (2014).

[165] D. W. Goodman, Catal Lett **99**, 1 (2005).

[166] M. Comotti, W.-C. Li, B. Spliethoff, and F. Schüth, J. Am. Chem. Soc. **128**, 917 (2006).

[167] H. Häkkinen, S. Abbet, A. Sanchez, U. Heiz, and U. Landman, Angew. Chem. Int. Ed. **42**, 1297 (2003).

[168] V. Subramanian, E. E. Wolf, and P. V. Kamat, J. Am. Chem. Soc. **126**, 4943 (2004).

[169] M. Valden, X. Lai, and D. W. Goodman, Science **281**, 1647 (1998).

[170] T. Hayashi, K. Tanaka, and M. Haruta, J. Catal. **178**, 566 (1998).

[171] G. Mul, A. Zwijnenburg, B. van der Linden, M. Makkee, and J. A. Moulijn, J. Catal. **201**, 128 (2001).

[172] J. Jia, K. Haraki, J. N. Kondo, K. Domen, and K. Tamaru, J. Phys. Chem. B **104**, 11153 (2000).

[173] T. V. Choudhary, C. Sivadinarayana, A. K. Datye, D. Kumar, and D. W. Goodman, Catal Lett **86**, 1 (2003).

[174] C. Milone, R. Ingoglia, L. Schipilliti, C. Crisafulli, G. Neri, and S. Galvagno, J. Catal. **236**, 80 (2005).

[175] S. Schimpf, M. Lucas, C. Mohr, U. Rodemerck, A. Brückner, J. Radnik, H. Hofmeister, and P. Claus, Catal. Today **72**, 63 (2002).

[176] M. Okumura, T. Akita, and M. Haruta, Catal. Today **74**, 265 (2002).

[177] Y. Hartadi, D. Widmann, and R. J. Behm, J. Catal. **333**, 238 (2016).

[178] J. Strunk, K. Kähler, X. Xia, M. Comotti, F. Schüth, T. Reinecke, and M. Muhler, App. Catal. A: General **359**, 121 (2009).

[179] Q. Fu, H. Saltsburg, and M. Flytzani-Stephanopoulos, Science **301**, 935 (2003).

[180] M. M. Schubert, S. Hackenberg, A. C. van Veen, M. Muhler, V. Plzak, and R. J. Behm, J. Catal. **197**, 113 (2001).

[181] S. Carrettin, P. Concepcion, A. Corma, J. M. Lopez Nieto, and V. F. Puntes, Angew. Chem. Int. Ed. **43**, 2538 (2004).

[182] Z.-P. Liu, X.-Q. Gong, J. Kohanoff, C. Sanchez, and P. Hu, Phys. Rev. Lett. **91**, 266102 (2003).

[183] I. N. Remediakis, N. Lopez, and J. K. Norskov, Angew. Chem. Int. Ed. **44**, 1824 (2005).

[184] L. B. Vilhelmsen and B. Hammer, ACS Catalysis **4**, 1626 (2014).

[185] I. X. Green, W. Tang, M. Neurock, and J. T. Yates, Science **333**, 736 (2011).

[186] T. S. Sreeprasad, P. Nguyen, N. Kim, and V. Berry, Nano Lett. **13**, 4434 (2013).

[187] T. B. Rawal, D. Le, and T. S. Rahman, J. Phys. Chem. C **121**, 7282 (2017).

[188] Y. Shi, J.-K. Huang, L. Jin, Y.-T. Hsu, S. F. Yu, L.-J. Li, and H. Y. Yang, Sci. Rep. **3**, 1839 (2013).

[189] T. W. Scharf, R. S. Goeke, P. G. Kotula, and S. V. Prasad, ACS Appl. Mater. & Inter. **5**, 11762 (2013).

[190] J. Shakya, A. S. Patel, F. Singh, and T. Mohanty, Appl. Phys. Lett. **108**, 013103 (2016).

[191] D. Y. Chung *et al.*, Nanoscale **6**, 2131 (2014).

[192] M. A. Lukowski, A. S. Daniel, F. Meng, A. Forticaux, L. Li, and S. Jin, J Am Chem Soc **135**, 10274 (2013).

[193] C. T. Tye and K. J. Smith, Top. Catal. **37**, 129 (2006).

[194] J. Hong *et al.*, Nat. Commun. **6**, 6293 (2015).

[195] H.-P. Komsa, J. Kotakoski, S. Kurasch, O. Lehtinen, U. Kaiser, and A. V. Krasheninnikov, Phys. Rev. Lett. **109**, 035503 (2012).

[196] A. Gazsi, T. Bánsági, and F. Solymosi, Catal Lett **131**, 33 (2009).

[197] E. Hernández-Ramírez, J. A. Wang, L. F. Chen, M. A. Valenzuela, and A. K. Dalai, App. Surf. Sci. **399**, 77 (2017).

[198] I. X. Green, W. Tang, M. Neurock, and J. T. Yates, Angew. Chem. Int. Ed. **50**, 10186 (2011).

[199] S. Nosé, J. Chem. Phys. **81**, 511 (1984).

[200] W. G. Hoover, Phys. Rev. A **31**, 1695 (1985).

[201] G. Shafai, S. Hong, M. Bertino, and T. S. Rahman, J. Phys. Chem. C **113**, 12072 (2009).

[202] G. Shafai, M. A. Ortigoza, and T. S. Rahman, J. Phys.: Condens. Matt. **24**, 104026 (2012).

[203] C. M. Chang and M. Y. Chou, Phys. Rev. Lett. **93**, 133401 (2004).

[204] J. Wang, G. Wang, and J. Zhao, Phys. Rev. B **66**, 035418 (2002).

[205] M. Boronat, F. Illas, and A. Corma, J. Phys. Chem. A **113**, 3750 (2009).

[206] Y. Shi, J.-K. Huang, L. Jin, Y.-T. Hsu, S. F. Yu, L.-J. Li, and H. Y. Yang, Sci. Rep. **3**, 1839 (2013).

[207] M. Behrens, S. Kissner, F. Girsgdies, I. Kasatkin, F. Hermerschmidt, K. Mette, H. Ruland, M. Muhler, and R. Schlogl, Chem. Commun. **47**, 1701 (2011).

[208] M. Behrens *et al.*, Science **336**, 893 (2012).

[209] M. Behrens, S. Zander, P. Kurr, N. Jacobsen, J. Senker, G. Koch, T. Ressler, R. W. Fischer, and R. Schlogl, J. Am. Chem. Soc. **135**, 6061 (2013).

[210] Y. Choi and P. Liu, J. Am. Chem. Soc. **131**, 13054 (2009).

[211] T. P. Goumans, C. R. Catlow, and W. A. Brown, J. Chem. Phys. **128**, 134709 (2008).

[212] F. Guder, E. Frei, U. M. Kucukbayrak, A. Menzel, R. Thomann, R. Luptak, B. Hollaender, I. Krossing, and M. Zacharias, ACS App. Mater. Inter. **6**, 1576 (2014).

[213] I. Kasatkin, P. Kurr, B. Kniep, A. Trunschke, and R. Schlogl, Angew. Chem. Int. Ed. **46**, 7324 (2007).

[214] Y. Xiang, V. Chitry, P. Liddicoat, P. Felfer, J. Cairney, S. Ringer, and N. Kruse, J. Am. Chem. Soc. **135**, 7114 (2013).

[215] H. Yue, X. Ma, and J. Gong, Acc. Chem. Res. **47**, 1483 (2014).

[216] P. Forzatti, E. Tronconi, and I. Pasquon, Catal. Rev. **33**, 109 (1991).

[217] S. Mawson, M. S. Mccutchen, P. K. Lim, and G. W. Roberts, Energy & Fuels **7**, 257 (1993).

[218] A. Medford, A. Lausche, F. Abild-Pedersen, B. Temel, N. Schjødt, J. Nørskov, and F. Studt, Top. Catal. **57**, 135 (2014).

[219] J. J. Spivey and A. Egbebi, Chem Soc Rev **36**, 1514 (2007).

[220] D. Mei *et al.*, J. Catal. **271**, 325 (2010).

[221] G. Prieto *et al.*, Angew. Chem. Int. Ed. **53**, 6397 (2014).

[222] R. G. Herman, Catal. Today **55**, 233 (2000).

[223] U. Eberle, M. Felderhoff, and F. Schuth, Angew. Chem. Int. Ed. **48**, 6608 (2009).

[224] G. B. Kauffman, Found. Chem. **15**, 239 (2013).

[225] G. A. Olah, Angew. Chem. Int. Ed. **44**, 2636 (2005).

[226] R. K. Niven, Renew. Sustain. Ener. Rev. **9**, 535 (2005).

[227] A. Al-Hasan, Energy Conver. Manag. **44**, 1547 (2003).

[228] J. T. Sun, I. S. Metcalfe, and M. Sahibzada, Ind. Eng. Chem. Res. **38**, 3868 (1999).

[229] Y. X. Yang, J. Evans, J. A. Rodriguez, M. G. White, and P. Liu, Phys. Chem. Chem. Phys. **12**, 9909 (2010).

[230] M. V. Twigg and M. S. Spencer, App. Catal. A: General **212**, 161 (2001).

[231] T. R. Miles, T. R. Miles, L. L. Baxter, R. W. Bryers, B. M. Jenkins, and L. L. Oden, Biomass Bioenerg **10**, 125 (1996).

[232] T. Y. Park, I. S. Nam, and Y. G. Kim, Ind. Eng. Chem. Res. **36**, 5246 (1997).

[233] V. P. Santos *et al.*, ACS Catal. **3**, 1634 (2013).

[234] R. Andersson, M. Boutonnet, and S. Järås, Fuel **115**, 544 (2014).

[235] M. T. Claure, S. H. Chai, S. Dai, K. A. Unocic, F. M. Alamgir, P. K. Agrawal, and C. W. Jones, J. Catal. **324**, 88 (2015).

[236] H. J. Qi, D. B. Li, C. Yang, Y. G. Ma, W. H. Li, Y. H. Sun, and B. Zhong, Catal Commun **4**, 339 (2003).

[237] N. W. Ashcroft and N. D. Mermin, *Solid State Physics* 2003), 1 edn., p.^pp. 848.

[238] J. Ye, C. Liu, D. Mei, and Q. Ge, ACS Catalysis **3**, 1296 (2013).

[239] Y.-F. Zhao, R. Rousseau, J. Li, and D. Mei, J. Phys. Chem. C **116**, 15952 (2012).

[240] L. C. Grabow and M. Mavrikakis, ACS Catalysis **1**, 365 (2011).

[241] Y. Choi and P. Liu, J. Am. Chem. Soc. **131**, 13054 (2009).

[242] W.-L. Dai, Q. Liu, Y. Cao, and J.-F. Deng, App. Catal. A: General **175**, 83 (1998).

[243] L. Savio, A. Gerbi, L. Vattuone, M. Rocca, F. Vecchiocattivi, D. Cappelletti, and F. Pirani, Chem. Phys. Lett. **404**, 336 (2005).

[244] J. G. Serafin, A. C. Liu, and S. R. Seyedmonir, J. Mol. Catal. A: Chemical **131**, 157 (1998).

[245] C. T. Campbell and M. T. Paffett, Surf. Sci. **139**, 396 (1984).

[246] L. Vattuone, M. Rocca, C. Boragno, and U. Valbusa, J. Chem. Phys. **101**, 713 (1994).

[247] P. A. Gravil, J. A. White, and D. M. Bird, Surf. Sci. **352**, 248 (1996).

[248] D. A. Outka, J. Stöhr, W. Jark, P. Stevens, J. Solomon, and R. J. Madix, Phys. Rev. B **35**, 4119 (1987).

[249] U. Burghaus and H. Conrad, Surf. Sci. **364**, 109 (1996).

[250] J. R. Hahn and W. Ho, Phys. Rev. Lett. **87**, 166102 (2001).

[251] M. A. Barteau and R. J. Madix, J. Am. Chem. Soc. **105**, 344 (1983).

[252] J. R. Hahn and W. Ho, Phys. Rev. Lett. **87**, 196102 (2001).

[253] J. V. Barth and T. Zambelli, Surf. Sci. **513**, 359 (2002).

[254] J. V. Barth, T. Zambelli, J. Wintterlin, and G. Ertl, Chem. Phys. Lett. **270**, 152 (1997).

[255] Y. Kuk and L. C. Feldman, Phys. Rev. B **30**, 5811 (1984).

[256] B. W. Busch and T. Gustafsson, Surf. Sci. **407**, 7 (1998).

[257] J.-K. Hansen, J. Bremer, and O. Hunderi, Surf. Sci. **418**, L58 (1998).

[258] K. C. Prince, G. Paolucci, and A. M. Bradshaw, Surf. Sci. **175**, 101 (1986).

[259] F. Bartolucci, R. Franchy, J. C. Barnard, and R. E. Palmer, Phys. Rev. Lett. **80**, 5224 (1998).

[260] L. Vattuone, P. Gambardella, U. Valbusa, and M. Rocca, Surf. Sci. **377–379**, 671 (1997).

[261] L. Vattuone, M. Rocca, P. Restelli, M. Pupo, C. Boragno, and U. Valbusa, Phys. Rev. B **49**, 5113 (1994).

[262] M. A. Barteau and R. J. Madix, J. Chem. Phys. **74**, 4144 (1981).

[263] W. W. Pai, N. C. Bartelt, M. R. Peng, and J. E. Reutt-Robey, Surf. Sci. **330**, L679 (1995).

[264] L. Yang, T. S. Rahman, G. Bracco, and R. Tatarek, Phys. Rev. B **40**, 12271 (1989).

[265] M. Canepa, P. Cantini, F. Fossa, L. Mattera, and S. Terreni, Phys. Rev. B **47**, 15823 (1993).

[266] D. J. Coulman, J. Wintterlin, R. J. Behm, and G. Ertl, Phys. Rev. Lett. **64**, 1761 (1990).

[267] S. R. Parkin, H. C. Zeng, M. Y. Zhou, and K. A. R. Mitchell, Phys. Rev. B **41**, 5432 (1990).

[268] V. Pouthier, C. Ramseyer, C. Girardet, P. Zeppenfeld, V. Diercks, and R. Halmer, Phys. Rev. B **58**, 9998 (1998).

[269] X. Duan, O. Warschkow, A. Soon, B. Delley, and C. Stampfl, Phys. Rev. B **81**, 075430 (2010).

[270] P. Cabrera-Sanfelix, C. Lin, A. Arnau, and D. Sánchez-Portal, J. Phys. : Condens. Matt. **25**, 135003 (2013).

[271] J. R. Hahn and W. Ho, J. Chem. Phys. **123**, 214702 (2005).

[272] P. A. Gravil, D. M. Bird, and J. A. White, Phys. Rev. Lett. **77**, 3933 (1996).

[273] F. E. Olsson, N. Lorente, and M. Persson, Surf. Sci. **522**, L27 (2003).

[274] P. J. Van Den Hoek and E. J. Baerends, Surf. Sci. **221**, L791 (1989).

[275] S. Monturet, M. Alducin, and N. Lorente, Phys. Rev. B **82**, 085447 (2010).

[276] J. R. Hahn and W. Ho, J. Chem. Phys. **122**, 244704 (2005).

[277] P. Walker and W. H. Tarn, *CRC Handbook of Metal Etchants* (CRC Press: New York, 1990).

[278] L. Vattuone, U. Valbusa, and M. Rocca, Surf. Sci. **317**, L1120 (1994).

[279] C. Åkerlund, I. Zorić, B. Kasemo, A. Cupolillo, F. B. de Mongeot, and M. Rocca, Chem. Phys. Lett. **270**, 157 (1997).

[280] S. Roy, V. Mujica, and M. A. Ratner, J. Chem. Phys. **139**, 074702 (2013).

[281] D. M. Bird and P. A. Gravil, Surf. Sci. **377**, 555 (1997).

[282] J. R. Hahn, H. J. Lee, and W. Ho, Phys. Rev. Lett. **85**, 1914 (2000).

[283] H. J. Freund, G. Meijer, M. Scheffler, R. Schlogl, and M. Wolf, Angew. Chem. Int. Ed. **50**, 10064 (2011).

[284] B. L. M. Hendriksen and J. W. M. Frenken, Phys. Rev. Lett. **89**, 046101 (2002).

[285] J. Lin *et al.*, Angew. Chem. Int. Ed. **51**, 2920 (2012).

[286] I. N. Remediakis, N. Lopez, and J. K. Norskov, Angew. Chem. Int. Ed. **44**, 1824 (2005).

[287] U. Burghaus and H. Conrad, Surf. Sci. **338**, L869 (1995).

[288] U. Burghaus and H. Conrad, Surf. Sci. **370**, 17 (1997).

[289] L. S. Byskov, B. Hammer, J. K. Nørskov, B. S. Clausen, and H. Topsøe, Catal Lett **47**, 177 (1997).

[290] T. Sueyoshi, T. Sasaki, and Y. Iwasawa, Journal of Physical Chemistry **100**, 1048 (1996).

[291] H. Over, A. P. Seitsonen, E. Lundgren, M. Schmid, and P. Varga, J. Am. Chem. Soc. **123**, 11807 (2001).

[292] Y. D. Kim, H. Over, G. Krabbes, and G. Ertl, Top. Catal. **14**, 95 (2000).

[293] S. Wendt, M. Knapp, and H. Over, J. Am. Chem. Soc. **126**, 1537 (2004).

[294] M. Smerieri, L. Savio, L. Vattuone, and M. Rocca, J. Phys. : Condens. Matt. **22**, 304015 (2010).

[295] J. Pal, T. B. Rawal, M. Smerieri, S. Hong, M. Alatalo, L. Savio, L. Vattuone, T. S. Rahman, and M. Rocca, Phys. Rev. Lett. **118**, 226101 (2017).

[296] J. Agrell, K. Hasselbo, K. Jansson, S. G. Järås, and M. Boutonnet, App. Catal. A: General **211**, 239 (2001).

[297] M. L. Cubeiro and J. L. G. Fierro, J. Catal. **179**, 150 (1998).

[298] Y.-H. Chin, R. Dagle, J. Hu, A. C. Dohnalkova, and Y. Wang, Catal. Today **77**, 79 (2002).

[299] R. Jiang, W. Guo, M. Li, D. Fu, and H. Shan, J. Phys. Chem. C **113**, 4188 (2009).

[300] R. Jiang, W. Guo, M. Li, X. Lu, J. Yuan, and H. Shan, Phys. Chem. Chem. Phys. **12**, 7794 (2010).

[301] J. H. Kwak, J. Hu, D. Mei, C.-W. Yi, D. H. Kim, C. H. F. Peden, L. F. Allard, and J. Szanyi, Science **325**, 1670 (2009).

[302] M. F. Camellone and S. Fabris, J. Am. Chem. Soc. **131**, 10473 (2009).

[303] B. Meyer and D. Marx, Phys. Rev. B **67**, 035403 (2003).

[304] O. Dulub, B. Meyer, and U. Diebold, Phys. Rev. Lett. **95**, 136101 (2005).

[305] S. Desgreniers, Phys. Rev. B **58**, 14102 (1998).

[306] U. Rössler (Editor) *et al.*, *Landolt-Börnstein: Numerical Data and Functional Relationships in Science and Technology* (Springer, 1999).

[307] G. Kresse and J. Furthmüller, Comp. Mater. Sci. **6**, 15 (1996).

[308] S. Hong, A. Karim, T. S. Rahman, K. Jacobi, and G. Ertl, J. Catal. **276**, 371 (2010).

[309] T. P. Schulze, J. Comp. Phys. **227**, 2455 (2008).

[310] H. Iddir, S. Öğüt, N. D. Browning, and M. M. Disko, Phys. Rev. B **72**, 081407 (2005).

[311] L. Giordano, J. Goniakowski, and G. Pacchioni, Phys. Rev. B **64**, 075417 (2001).

[312] J. Lin *et al.*, J. Am. Chem. Soc. **135**, 15314 (2013).

[313] C. T. Vo, L. K. Huynh, J. Y. Hung, and J.-C. Jiang, App. Surf. Sci. **280**, 219 (2013).

[314] R. G. S. Pala and H. Metiu, J. Catal. **254**, 325 (2008).

[315] X. Guo, L. Hanley, and J. T. Yates, J. Am. Chem. Soc. **111**, 3155 (1989).

[316] J. Greeley and M. Mavrikakis, J. Am. Chem. Soc. **126**, 3910 (2004).

[317] J. Greeley and M. Mavrikakis, J. Catal. **208**, 291 (2002).

[318] J. Greeley and M. Mavrikakis, J. Am. Chem. Soc. **124**, 7193 (2002).

[319] N. Kruse, M. Rebholz, V. Matolin, G. Chuah, and J. Block, Surf. Sci. **238**, L457 (1990).

[320] M. L. Cubeiro and J. L. G. Fierro, Appl. Catal. A: General **168**, 307 (1998).

[321] Y. H. Chin, R. Dagle, J. L. Hu, A. C. Dohnalkova, and Y. Wang, Catal Today **77**, 79 (2002).

[322] F. Tao, private communication (2015).

[323] Y. Usami, K. Kagawa, M. Kawazoe, Y. Matsumura, H. Sakurai, and M. Haruta, Appl. Catal. A-General **171**, 123 (1998).

[324] Y. Matsumura, M. Okumura, Y. Usami, K. Kagawa, H. Yamashita, M. Anpo, and M. Haruta, Catal Lett **44**, 189 (1997).

[325] D. S. Adipranoto, F. Shikanai, M. Yonemura, K. Mori, J. G. Park, K. Itoh, and T. Kamiyama, Solid State Ionics **180**, 492 (2009).

[326] P. Gao, M. Gu, X. L. Liu, B. Liu, and S. M. Huang, App. Phys. Lett. **95**, 221904 (2009).

[327] A. N. Gruzintsev and W. N. Zagorodnev, Semiconductors+ **46**, 149 (2012).

[328] Y. Y. Zhou, M. K. Lu, G. J. Zhou, S. M. Wang, and S. F. Wang, Mater. Lett. **60**, 2184 (2006).

[329] I. Tanaka, D. Kim, M. Nakayama, and H. Nishimura, J. Lumin. **87–89**, 257 (2000).

[330] H. Ichida, Y. Kanematsu, T. Shimomura, K. Mizoguchi, D. Kim, and M. Nakayama, Phys. Rev. B **72** (2005).

[331] Z. Zheng, A. R. Liu, S. M. Wang, B. J. Huang, K. W. Wong, X. T. Zhang, S. K. Hark, and W. M. Lau, J. Mater. Chem. **18**, 852 (2008).

[332] H. L. Kang, R. Liu, K. L. Chen, Y. F. Zheng, and Z. D. Xu, Electrochim. Acta **55**, 8121 (2010).

[333] K. Tennakone, G. R. R. A. Kumara, A. R. Kumarasinghe, K. G. U. Wijayantha, and P. M. Sirimanne, Semicond. Sci. Tech. **10**, 1689 (1995).

[334] M. Rusop, T. Soga, T. Jimbo, and M. Umeno, Sur. Rev. Lett. **11**, 577 (2004).

[335] G. R. A. Kumara, S. Kaneko, M. Okuya, and K. Tennakone, Langmuir **18**, 10493 (2002).

[336] V. P. S. Perera and K. Tennakone, Sol. Ener. Mater. Sol. Cells **79**, 249 (2003).

[337] A. Konno, T. Kitagawa, H. Kida, G. R. Asoka Kumara, and K. Tennakone, Curr. App. Phys. **5**, 149 (2005).

[338] P. Stakhira, V. Cherpak, D. Volynyuk, F. Ivastchyshyn, Z. Hotra, V. Tataryn, and G. Luka, Thin Solid Films **518**, 7016 (2010).

[339] I. Tanaka and M. Nakayama, J. App. Phys. **92**, 3511 (2002).

[340] Yang and Q. Gao, Langmuir **21**, 6866 (2005).

[341] Nash J D, Siddhanti A D, Penabade A R, Bertrad K, Andino A, Rosario K, H. S, and B. G. R, in preparation.

[342] P. Giannozzi *et al.*, J. Phys.: Condens. Matt. **21**, 395502 (2009).

[343] D. Huang, Y. J. Zhao, S. Li, C. S. Li, J. J. Nie, X. H. Cai, and C. M. Yao, J. Phys. D App. Phys. **45**, 145102 (2012).

[344] J. G. Gross, M. Fliyou, S. Lewonczuk, J. Ringeissen, and R. Pinchaux, Phys. Rev. B **37**, 3068 (1988).